EUROPEAN COMMISSION

Community research

PEBS

(Contract Number: FP7 249681)

PROYECT DERIVERABLE 3.4-1:

Report on testing multiple-continua THC(m) models with laboratory and large-scale tests

Author(s):

Javier Samper, Alba Mon, Luis Montenegro,
Bruno Pisani & Acacia Naves

UDC

Reporting period: **01/03/10 – 28/02/14**

Date of issue of this report: first draft **09/2013;** final version **08/2014**

Start date of project: **01/03/10** Duration: **48** Months

Project co-funded by the European Commission under the Seventh Euratom Framework Programme for Nuclear Research &Training Activities (2007-2011)		
Dissemination Level		
PU	Public	**PU**
RE	Restricted to a group specified by the partners of the [acronym] project	
CO	Confidential, only for partners of the [acronym] project	

EURATOM


EURATOM

DISTRIBUTION LIST

Name	Number of copies	Comments

Report on testing multiple-continua THC(m) models with laboratory and large-scale tests

Summary

An Engineered Barrier System (EBS) is foreseen for backfilling and sealing of radioactive waste repositories. Quantifying the time evolution of the EBS requires the use of coupled thermal (T), hydrodynamic (H), chemical (C) and mechanical (M) models. Such models are also needed to interpret laboratory experiments of canister corrosion, corrosion-bentonite interactions and concrete-bentonite interactions. PEBS (Long-term Performance of the Engineered Barrier System, EBS) is an European Research Euratom Project which aims at evaluating the sealing and barrier performance of the EBS with time, through the development of a comprehensive approach involving experiments, models and the consideration of the potential impacts on long-term safety functions.

UDC has developed advanced multiple-continua models for clay barriers by improving the previous THC(m) models. Such improvements include:

1) Accounting for different types of waters (free, adsorbed and interlayer) in clays and different types of pores (macropores, Interaggregate and Interaggregate pores) in multiple-continua models.
2) Incorporating mechanical and geochemical couplings to account for porosity changes caused by swelling phenomena. This leads to fully coupled THMC models.
3) Improvements in the chemistry of gaseous species such as $O_2(g)$, $CO_2(g)$ and $H_2(g)$.

Model improvements were implemented in the INVERSE-FADES-CORE code developed at the University of A Coruña (Zheng et al., 2010).

The improved multiple-continua THC(m) models have been tested with both small- and large-scale tests. Such tests include tests performed within the NFPRO

project that were not modelled previously and tests performed by Ciemat within the PEBS project. These tests include:

1) The FEBEX mock-up test
2) Heating and hydration tests on 60 cm long cells
3) Heating and hydration corrosion tests
4) Heating and hydration tests with concrete and bentonite
5) Heating and hydration tests with two interphases: magnetite-bentonite and concrete-bentonite

This report presents the testing of the improved coupled THCM models with data from the FEBEX mock-up test and the various heating and hydration experiments performed at the Ciemat facilities. These models were solved with the INVERSE-FADES-CORE code.

The testing of the FEBEX mock up test shows that the computed water intake reproduces the measured intake data. A slight deviation is observed at t = 5000 days. The computed relative humidities reproduce the measured data at the external sensors (r = 0.55 and r = 0.70 m), but underestimate the measured data after 1500 days at the internal sensors (r = 0.22 and r = 0.37 m). A double porosity model could overcome these discrepancies.

Model predictions have been compared to temperature, water content, porosity and porewater chemical data from heating and hydration infiltration tests performed by Ciemat on cylindrical samples (60 cm long and 7 cm in diameter) of compacted FEBEX bentonite. These tests were performed on several columns, which were dismantled after durations ranging from 0.5 to 7.6 years. The numerical model of the 60-cm long heating and hydration tests reproduces the observed temperature, saturation degrees, porosities and dissolved and exchanged chemical data. Geochemical predictions improve when the changes in porosity caused by swelling are considered and when some parameters such as vapor tortuosity, heat dissipation and cation selectivities are estimated.

The experiments involving canister-bentonite and concrete-bentonite interfaces were performed with different sample lengths (25 mm for double interface experiments

and small corrosion cells and 100 mm for the HB and FB experiments) and temperatures (25º, 50º, 60º and 100ºC). The small corrosion cells include a 21 mm thick layer of compacted bentonite and a 4 mm thick layer of Fe powder. The FB3 experiment includes a sample of 87 mm length of bentonite and a 13 mm layer of Fe powder in contact with the heater. The so-called double interface experiments, 2-I experiments, include a 3 mm thick layer of cement mortar which is in contact with the hydration system, a 18 mm thick layer of bentonite and a 2 mm layer of powdered magnetite. The HB experiments, on the other hand, include a 30 mm layer of concrete which is in contact with the hydration system and a 71.5 mm thick layer of bentonite. The corrosion cells were hydrated with Grimsel granitic water. The concrete-bentonite cells were hydrated with a Reference Argillaceous Formation water. The bentonite samples have an initial porosity of 0.40 and a gravimetric water content of 14% which corresponds to a saturation degree of 56.8 % and a suction of $1.29 \cdot 10^{8}$ Pa. The mortar of the 2I cells has a porosity of 0.3. The concrete of the HB cell has a porosity of 0.125 and an initial gravimetric water content of 2.6 %.The initial gas pressure is equal to the atmospheric pressure.

The experiments were modelled with a THCM model using 1D finite element grids. A uniform liquid pressure was adopted at the injection boundary. Hydrodynamic, thermal and solute transport parameters were taken from those calibrated previously from previous heating and hydration experiments. The hydration boundary was modelled with a zero-vertical displacement, a Cauchy condition for the energy equation and a Neuman condition for solute transport with the solute flux equal to the product of the water flux times the solute concentration of the inflow water. The effective diffusion coefficient is equal to $2 \cdot 10^{-10}$ m^2/s and is the same for the all the dissolved species except for Cl^- which has an effective diffusion coefficient of $9 \cdot 10^{-11}$ m^2/s. The initial chemical composition of the bentonite was taken from Fernández et al. (2001). The chemical system is defined in terms of the following primary species: H_2O, H^+, Ca^{2+}, Mg^{2+}, Na^+, K^+, Cl^-, SO_4^{2-}, Fe^{2+}, HCO_3^-, $O_2(aq)$, Al^{3+} and $SiO_2(aq)$. The model accounts for homogeneous reactions (acid-base, aqueous complexation and redox reactions) and heterogeneous reactions such as mineral dissolution/precipitation, cation exchange and surface complexation. Calcite, gypsum/anhydrite, cristobalite, and portlandite, brucite, ettringite, sepiolite, anorthite, C0.8SH and C1.8SH were considered for the concrete-bentonite experiments. Calcite, gypsum/anhydrite, cristobalite, magnetite, siderite, goethite, and $Fe(OH)_2(s)$ were considered for the

bentonite-canister experiments. Cation exchange of Ca^{2+}, Mg^{2+}, Na^{+}, K^{+} and Fe^{2+} was modelled with the Gaines-Thomas convention. Surface complexation reactions take place at the following three types of protolysis sites: $S^{S}OH$, $S^{W1}OH$ and $S^{W2}OH$. Canister corrosion is modeled with a constant corrosion rate. Magnetite precipitation is kinetically controlled.

Several hypotheses were tested with the numerical models to explain the observed mineral phases. The models of the corrosion tests were calibrated with the water content and dry density data measured at the end of the experiments and temperature and relative humidity measured during the experiments. The kinetic parameters of magnetite precipitation were calibrated with measured Fe weight content data which are representative of the precipitation of $Fe(OH)_2(s)$. Model results of the small cell corrosion experiments indicate that:

1) Magnetite and $Fe(OH)_2(s)$ precipitate and compete for Fe^{2+} precipitation. These corrosion products penetrate a few mm into the bentonite.
2) Fe^{2+} is sorbed by surface complexation.
3) Fe^{2+} cation exchange is less relevant than Fe^{2+} sorption.
4) The numerical results fit the measured data of the iron weight for the tests performed at 25º, 50º and 100ºC.

Concrete-bentonite interface experiments were modelled to: 1) Analyze the alterations observed at a millimetric scale and 2) Identify the relevant secondary minerals, such as CSH gels. Double interface (2I) model were performed to study the interactions of the bentonite with the corrosion products and with the mortar. The coupled THCm numerical models of these tests capture the main observed trends of mineral dissolution-precipitation. The HB4 model, however, does not reproduce the ettringite and CSH precipitation. For these phases, the numerical model predicts much less precipitation than the observed values. The numerical model of the 2I3 cellshows some discrepancies for ettringite in the mortar and in the bentonite and for brucite precipitation at the mortar-bentonite interface and in the bentonite (not observed in the test). The model did not account for CASH phase due to the lack of thermodynamic data for these phases.

Content

List of Figures

List of Tables

1 Introduction

A large number of hydrodynamic, geochemical and thermal data have been collected for compacted bentonites during the last 30 years to characterize their properties and evaluate the feasibility of compacted bentonite for the Engineered Clay Barrier (EBS) of a high level radioactive waste repository. Various laboratory and in situ heating and hydration experiments were performed within the FEBEX and NFPRO Projects (ENRESA, 2000; 2006a; 2006b; 2006c). Hydration and heating experiments on bentonite long cells were performed during the FEBEX Project. During the NFPRO project, corrosion tests were performed also. Tests involving the concrete-bentonite and concrete-bentonite-corrosion interfaces were performed also during NFPRO and PEBS projects.

1.1 Objectives

The main objectives of this report include:

1) The development of advanced multiple-continua models for clay barriers by improving the previous THC(m) models. Such improvements include:
   a. Accounting for different types of waters (free, adsorbed and interlayer) in clays and different types of pores (macropores, Interaggregate and Interaggregate pores) in multiple-continua models.
   b. Incorporating mechanical and geochemical couplings to account for porosity changes caused by swelling phenomena. This leads to fully coupled THMC models.
   c. Improvements in the chemistry of gaseous species such as $O_2(g)$, $CO_2(g)$ and $H_2(g)$.
2) The implementation of the model improvements in the INVERSE-FADES-CORE code developed at the University of A Coruña (Zheng et al., 2010)
3) The testing of the improved multiple-continua THC(m) models with small- and large-scale tests. Such tests include:
   a. The FEBEX mock-up test

b. Heating and hydration tests on 60 cm long cells

c. Heating and hydration corrosion tests

d. Heating and hydration tests with concrete and bentonite

e. Heating and hydration tests with two interphases: magnetite-bentonite and concrete-bentonite

This report presents the testing of the improved coupled THCM models with data from the FEBEX mock-up test and the various heating and hydration experiments performed at the Ciemat facilities.

1.2 Scope

Chapter 2 describes the improvements in the models and in the code carried out during the PEBS Project. Then, the updated model of the FEBEX Mok-up test is presented in Chapter 3. Chapter 4 describes the THC(M) model of the 60-cm long cells, CG cells. Chapter 5 presents the THC(m) models of the corrosion tests, including the small (SC cells) and the medium size corrosion cells (FB cells). The THC(m) model of the concrete bentonite cell, HB4 cell, is described in Chapter 6. Chapter 7 describes the THC(m) model of the double interface concrete/bentonite/corrosion tests. Finally, Chapter 8 contains the main conclusions.

Appendix A contains the list of parameters and chemical reactions and constants of the models. Appendix B contains the plots of the model results for the corrosion tests. Appendix C includes the model results of the concrete-bentonite HB4 test. The the model results of the double interface tests are included in Appendix D.

2 Numerical model and code improvements

2.1 Mathematical THMC formulation

Water mass balance is given by (Navarro and Alonso, 2000):

$$\frac{D_s m^w}{Dt} + m^w \nabla \cdot v^s + \nabla \cdot \left(\rho^l X_l^w q^l + \rho^g X_g^v q^g + j_v\right) = 0 \quad (1)$$

where $\frac{D_s}{Dt}$ is the material derivative with respect to the solid particles which move with a velocity vector v_s (m/s), $\nabla \cdot()$ is the divergence operator, $\rho^l$and ρ^g are the bulk densities of the liquid and gaseous phases (kg/m^3), respectively, X_l^w is the mass fraction of water in the liquid phase, X_g^v the mass fraction of the vapour in the gas phase, q^l is the vector of volumetric liquid flux (m/s) which is given by Eq. (15), q^g is the vector of volumetric gas flux (m/s) which is given by Eq. (16), j_v is the dispersive mass flux of vapour with respect to the mean gas velocity (kg/m^2/s) which is given by Eq. (17), and m^w is the mass of water per unit volume of porous medium (kg/m^3) which is given by

$$m^w = \emptyset\left[\rho^l X_l^w S_l + \rho^g X_g^v (1 - S_l)\right] \quad (2)$$

where $\emptyset$ is the porosity and S_l is the liquid saturation degree.

The air mass balance equation is given by (Navarro and Alonso, 2000):

$$\frac{D_s m^a}{Dt} + m^a \nabla \cdot v^s + \nabla \cdot \left(\rho^g X_g^a q^g + \rho^l X_l^a q^l\right) = 0 \quad (3)$$

where X_g^a is the mass fraction of air in the gaseous phase, X_l^a is the mass fraction of air in the liquid phase, and m^a is the mass of air per unit volume of porous medium (kg/m^3) which is given by:

$$m^a = \emptyset\left[\rho^g X_g^a (1 - S_l) + \rho^l X_l^a S_l\right] \quad (4)$$

The solid mass balance is given by (Navarro and Alonso, 2000):

$$\frac{D_s \rho^d}{Dt} + \rho^d \nabla \cdot v^s = 0 \quad (5)$$

where ρ^d is the dry density of the medium which is equal to $\rho^s(1 - \emptyset)$, where ρ^s is the density of the solid particles (kg/m^3). If the coefficient of the thermal expansion of the solid particles (1/ºC), C_T^s , is considered and the mechanical compressibility of the particles is disregarded, then Eq. (5) becomes:

$$\frac{D_s \emptyset}{Dt} = (1 - \emptyset)\left[\nabla \cdot v_s - C_T^s \frac{D_s T}{Dt}\right] \quad (6)$$

where T is the temperature (ºC).

The formulation assumes that all phases are at local thermal equilibrium and therefore they are all at the same temperature. Hence, the energy balance is described in terms of an equation of internal energy which is defined by the following balance of enthalpy:

$$\frac{D_s h}{Dt} + h\nabla \cdot v^s + \nabla \cdot (-\Lambda \cdot \nabla T + I^e) = 0 \tag{7}$$

where h is the average specific enthalpy of the soil (J/kg) which in turn is given by:

$$\begin{aligned} h = {} & \rho^l X_l^w \emptyset S_l h^w + \rho^l X_l^a \emptyset S_l h^a + \rho^g X_g^v \emptyset (1 - S_l) h^v + \rho^g X_g^a \emptyset (1 - S_l) h^a \\ & + \rho^l X_l^a \emptyset S_l h^a + \rho^s (1 - \emptyset) h^s \end{aligned} \tag{8}$$

where h^w, h^v, h^a and h^s are the specific enthalpies of free water, vapour, air and solid particles respectively, which are assumed to depend linearly on temperature and specific heat (Navarro and Alonso, 2000) and I^e is the vector of convective energy flux which is given by:

$$I^e = \rho^l X_l^w h^w q^l + \rho^g X_g^v h^v q^v + \rho^g X_g^a h^a q^g \tag{9}$$

where q^g is the vector of volumetric vapour flux (m/s) which is given by the last terms of Eq. (1), that is, $q^v = \rho^g X_g^v q^g + j^v$ and Λ is the bulk thermal conductivity tensor (W/mºC) which for unsaturated bentonite is computed as a volume-weighted average of the conductivities of the components according to:

$$\Lambda = \emptyset S_l \Lambda^w + X_l^a \emptyset S_l \Lambda^a + \emptyset (1 - S_l)(\Lambda^v + \Lambda^a) + (1 - \emptyset)\Lambda^s \tag{10}$$

where Λ^{w}, Λ^{v}, Λ^{a} and Λ^{s} are the thermal conductivities of water, vapour, air and solid, respectively. This equation is inspired in the formulation of De Vries's (1963) which according to Tang et al. (2008) provides the best fit to measured thermal conductivity data for several bentonites, including FEBEX bentonite. The formulation in Eq. (10), however, may not be the appropriate for courser porous materials.

According to Soler (2001), the Dufour effect is negligible compared to thermal conduction and therefore can be disregarded.

The following incremental formulation of the equilibrium equation of Navarro and Alonso (2000) is used:

$$\nabla \cdot (\Delta \sigma' + \Delta P^g \delta) + \Delta \rho g k = 0 \tag{11}$$

where $\Delta\rho$ is the increment of the average soil density, g is the gravitational acceleration (m/s^2), k is the unit vector in the gravity direction, δ is the vector

expression of Kronecker's delta, ΔP^g is the increment in gas pressure (Pa) which for saturated conditions should be replaced by the increment in the liquid pressure (Pa), ΔP^l, and $\Delta\sigma'$ is the vector of increments of effective stress (Pa) which is related to the vector of increments of total stress $\Delta\sigma$ (Pa) in unsaturated conditions through:

$$\Delta\sigma' = \Delta\sigma - \Delta P^g \delta \tag{12}$$

while for saturated conditions the previous equation is replaced by $\Delta\sigma' = \Delta\sigma - \Delta P^l \delta$ (Fredlund and Rahardjo, 1993).

Solute transport processes include advection, molecular diffusion, and mechanical dispersion. Each of them produces a solute flux per unit surface and unit time. There are as many transport equations as primary chemical species in the system. The mass balance equation for the jth primary species is given by (Zheng and Samper, 2008a):

$$m_l^w \frac{\partial C_j}{\partial t} + \frac{\partial\left(m_l^w P_j\right)}{\partial t} + \frac{\partial\left(m_l^w W_j\right)}{\partial t} + \frac{\partial\left(m_l^w Y_j\right)}{\partial t} = L^*\left(C_j\right) + r_i\left(C_j^0 - C_j\right) \quad j = 1,2,\dots,N_c \tag{13}$$

C_j is the total dissolved concentration of the of jth species (mol/L), m_l^w is the mass of liquid water per unit volume of medium (kg/m^3) which is equal to $\rho^l X_l^w \theta$, where $\theta = S_l \emptyset$ is the volumetric watercontent (m3/m3), P_j, Y_j and W_j are the total precipitated, sorbed and exchanged concentrations (mol/L), respectively, of the jth primary species, r_i is the sink term (kg/m^2/s), C_j^0 is the dissolved concentration of jth species (mol/L) in the sink term r_i, N_C is the number of primary species. L*() is the following transport operator:

$$L^*() = \nabla \cdot \left[m_l^w D^j \cdot \nabla()\right] - m_l^w q^l \cdot \nabla() + (r_e - r_c)() \tag{14}$$

where D^j is the dispersion coefficient (m^2/s), and r_c and r_e are the condensation and evaporation rates (kg/m^2/s), respectively.

Coupled transport phenomena such as thermal and chemical osmosis may be important for compacted bentonites (Keijzeret al., 1999; Keijzer and Loch, 2001; Soler, 2001). The volumetric liquid flux, q^l, includes the classical Darcian term together with the chemical and thermal osmotic terms:

$$q^l = -\frac{K^{il} k^{rl}}{\mu^l}(\nabla p^l + \rho^l g \nabla z) - k_T \nabla T + \sigma \frac{K^{il} k^{rl}}{\mu^l} \nabla \pi_h \tag{15}$$

where p^l is the liquid pressure (Pa), K^{il} is the intrinsic permeability tensor of the liquid (m2), k^{rl} is the relative permeability of the liquid, μ^l is the viscosity of the liquid

(kg/m/s), z is the elevation, k_T is the thermal-osmotic permeability (m^2/K/s), π_h is the osmotic pressure (Pa), and σ is a dimensionless reflection coefficient for chemical osmosis which measures the non-ideality of a membrane and is defined as the ratio of the applied osmotic pressure to the developed hydraulic pressure at equilibrium. An ideal membrane has a reflection coefficient of 1 whereas it varies between 0 and 1 for non-ideal membranes.

The volumetric gas flux, q^g, is given by:

$$q^g = -\frac{K^{ig} k^{rg}}{\mu^g}(\nabla p^g + \rho^g g \nabla z) \tag{16}$$

where K^{ig} is the intrinsic permeability tensor of the gas (m^2), k^{rg} is the relative permeability of gas, μ^g and is the viscosity of the gas phase (kg/m/s).

The dispersive mass flux of vapour, j^v, is calculated by Fick's law:

$$j^v = -\rho^g D^v \nabla X_g^v \tag{17}$$

where D^v is the hydrodynamic dispersion tensor for vapour (m^2/s) which includes the effects of mechanical dispersion and molecular diffusion. The effective molecular diffusion coefficient for the vapour, D_e^v , (m^2/s) is calculated from (Pollock, 1986):

$$D_e^v = \frac{5.9 \cdot 10^{-6} \tau^v (T + 273.15)^{2.3}}{p^g} \tag{18}$$

where τ^v is the vapour tortuosity (dimensionless).

The mechanical law is given by:

$$d\varepsilon = C d\sigma' + \beta d\Psi + \alpha dT \tag{19}$$

where ε is the strain vector, C is the elastic matrix (1/Pa), β is a vector of coefficients (1/Pa) which account for the deformation caused by changes in suction Ψ, $\Psi = (p^l - p^g)$, and α is a vector of thermal expansion coefficients (1/ºC). The standard sign convention used in Soil Mechanics is adopted here according to which compressions are positive.

To overcome the difficulties of the different mechanical models, some researchers have resorted to simpler models such as the state-surface approach to simulate bentonite swelling. Nguyen et al. (2005) used successfully the state-surface approach to interpret a swelling pressure test. The following state-surface expression of Lloret and Alonso (1995) is adopted here to model bentonite swelling:

$$e = A + B ln\sigma' + C ln(\Psi + p^a) + D ln\sigma' \ln(\Psi + p^a) \tag{20}$$

where e is the void ratio which is equal to the volume of voids divided by the volume of the solids; p^a is the atmospheric pressure in Pa, σ' is the mean effective stress in Pa; Ψ is suction in Pa, and A, B, C and D are empirical constants which for FEBEX compacted bentonite are A=0.76, B=-0.052446, C=-0.0406413 and D= 0.00479977 (Nguyen et al., 2005).

The chemical model for compacted bentonite accounts for the following reactions: aqueous complexation, acid/base, cation exchange, surface complexation and mineral dissolution/precipitation. The chemical system is defined in terms of the concentrations of the following primary species: H_2O, H^+, Ca^{2+}, Mg^{2+}, Na^+, K^+, Cl^-, SO_4^{2-} , HCO_3^-, $SiO_{2(aq)}$, Al^{3+} and Fe^{2+}. The concentrations of secondary species are computed from concentrations of primary species through appropriate mass action laws (Xu et al.,1999). The concentrations of precipitated, exchanged and adsorbed species are computed using similar equations. A detailed description of calculations of chemical reactions can be found in Xuet al. (1999). Aqueous complexes were identified from speciation runs performed with EQ3/6 (Wolery, 1992). The Gaines–Thomas convention is used for cation exchange. Surface complexation is modelled using three types of protonation/deprotonation sites, S^SOH, $S^{W1}OH$ and $S^{W2}OH$, as proposed by Bradbury and Baeyens (1997).

The equilibrium constants for aqueous complexes and minerals change with temperature under non-isothermal conditions. They are calculated with the following expression which is valid for temperatures between 0 and 300 ºC:

$$logK(T) = \frac{b_1}{T^2} + \frac{b_2}{T} + b_3 lnT + b_4 + b_5 T \qquad (21)$$

where b_1 to b_5 are coefficients which are derived by fitting Eq. (21) to measured $logK$ values at 0, 25, 60, 100 and 300ºC (Wolery, 1992).The thermodynamic database of EQ3/6 (Wolery, 1992) is used for aqueous complexes and minerals.

2.2 Code improvements

The following improvements were implemented in INVERSE-FADES-CORE:

1. Accounting for different types of water (free, adsorbed and interlayer) in clays and different types of pores (macropores, interaggregate and interaggregate pores) in multiple-continuous models.

2. Incorporating mechanical and geochemical couplings to account for porosity changes caused by swelling phenomena. This leads to fully coupled THMC models.
3. Improving the chemistry of gaseous species such as $O_2(g)$, $CO_2(g)$ and $H_2(g)$.
4. Debugging programming errors:
    a. The correction of a bug in the reading and writing of sorption data. This bug did not affect the calculations involving sorption reactions and was relevant only when such reactions were not considered. It has been fixed.
    b. The correction of the calculation of the kinetic rate, r, of mineral dissolution/precipitation. In the previous version of the code the rate r was expressed as “mol of mineral per dm^3 of medium“. However, the rate r should be expressed in terms of “mol of mineral per kg of soil”. This correction has been implemented in the code.

2.3 Computer code

INVERS-FADES-CORE is a finite element code for modelling nonisothemal multiphase flow, heat transport and multicomponent reactive solute transport under both chemical equilibrium and kinetics conditions. The code takes into account the mass balance of water, air, solid and energy; the transport of solids and mechanical equilibrium. INVERSE-FADES-CORE solves both forward and inverse multiphase flow and multicomponent reactive transport problems in 1-, 2- and 3-D axi-symmetric porous and fractured media (Zheng and Samper, 2004, 2005). This code is the result of integrating the capabilities of FADES (Navarro, 1997), $CORE^{2D}$ (Samper et al., 2003), FADES-CORE (ENRESA 2000a) and INVERSE-CORE (Dai and Samper, 2004). State variables of the forward model include liquid and gas pressures and temperature which are solved by a Newton–Raphson method. A sequential iteration method is used to solve reactive transport equations. The inverse problem is solved by minimizing a generalized least-squares criterion with a Gauss-Newton–Levenberg–Marquardt method (Dai and Samper, 2004). The forward routines of INVERSE-FADES-CORE have been widely verified with analytical solutions and tested with THM and THC problems (Navarro and Alonso, 2000; ENRESA, 2000a;

Samper et al., 2008a) as well as with THMC processes (Zheng, 2006; Zheng and Samper, 2004). Codes of CORE^{2D} series have been used to model FEBEX laboratory tests (Samper et al., 2006, 2008b; Zheng et al., 2010), in situ tests (Zhang et al., 2008; Zheng et al., 2011), field case studies (Molinero et al., 2004; Dai and Samper, 2004; Molinero and Samper, 2006; Dai and Samper, 2006; Dai et al., 2006), evaluate the long-term geochemical evolution of radioactive waste repositories in clay (Yang et al., 2008) and granite (Yang et al.,2007), analyze stochastic transport and multicomponent competitive cation exchange in aquifers (Samper and Yang, 2006) and study concrete degradation (Galíndez et al., 2006). The main applications of INVERSE-FADES-CORE include:

1) The THC model of the FEBEX in situ test (Samper et al., 2008a)
2) The THCM model of the FEBEX in situ test (Zheng et al., 2011)
3) The THCM model of the FEBEX mock up test (Zheng and Samper, 2008)
4) The THCM model of a heating and hydration lab experiment performed on compacted FEBEX bentonite (Zheng et al., 2010)
5) The THC model of the Ventilation experiment on Opalinus Clay (Zheng et al., 2008b)

3 Model testing with data from the FEBEX mock-up test

The mock-up test replicates at almost full scale the Spanish reference concept for radioactive waste disposal in granite (ENRESA, 2005). The components of the mock-up test include: two electric heaters, a 0.64 m-thick clay barrier, instrumentation, automatic control of heaters, and a data acquisition system. In the mock-up test the buffer is confined in a steel structure which ensures a uniform temperature and water pressure around the external surface of the buffer. Heating and hydration of the clay buffer started in February 1997 and has continued uninterruptedly at the Ciemat facilities in Madrid (Martín and Barcala, 2005; Martín et al., 2006).

A THC model of the FEBEX mock-up test was performed within the FEBEX project (see Zheng and Samper, 2008). This model was constructed with data from t = 0 until t = 3000 days. Here this model has been tested with data collected from t = 3000 days to t = 5000 days.

The computed cumulative water intake reproduces the measured water intake data (Figure 3-1). Some deviations are observed at t = 5000 days. The computed volume is smaller than the measured volume. The computed relative humidities reproduce the measured data at 0.22 m (Figure 3-2) until 1500 days. However, the computed relative humidities are smaller than the measured data after 1500 days. Measured data are 10% larger than computed humidities at the sensors located at 0.37 m from the heater at 5000 days (Figure 3-3). The computed relative humidities fit well the measured data at a distance of 0.55 m (Figure 3-4). The computed relative humidities are slightly larger than the measured data at 0.70 m from the heater (Figure 3-5).

In summary, the computed relative humidities reproduce the measured data at the external sensors (r = 0.55 and r = 0.70 m), but underestimate the measured data after 1500 days at the internal sensors (r = 0.22 and r = 0.37 m). A double porosity model could overcome these discrepancies.

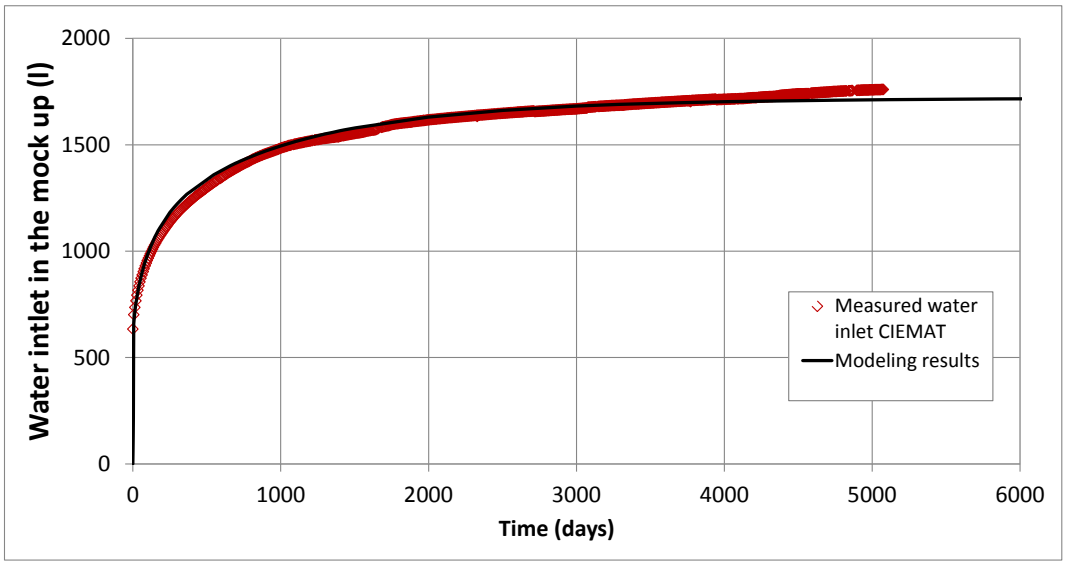

Figure 3-1. Computed (line) and measured (symbols) water intake for the FEBEX mock-up test.

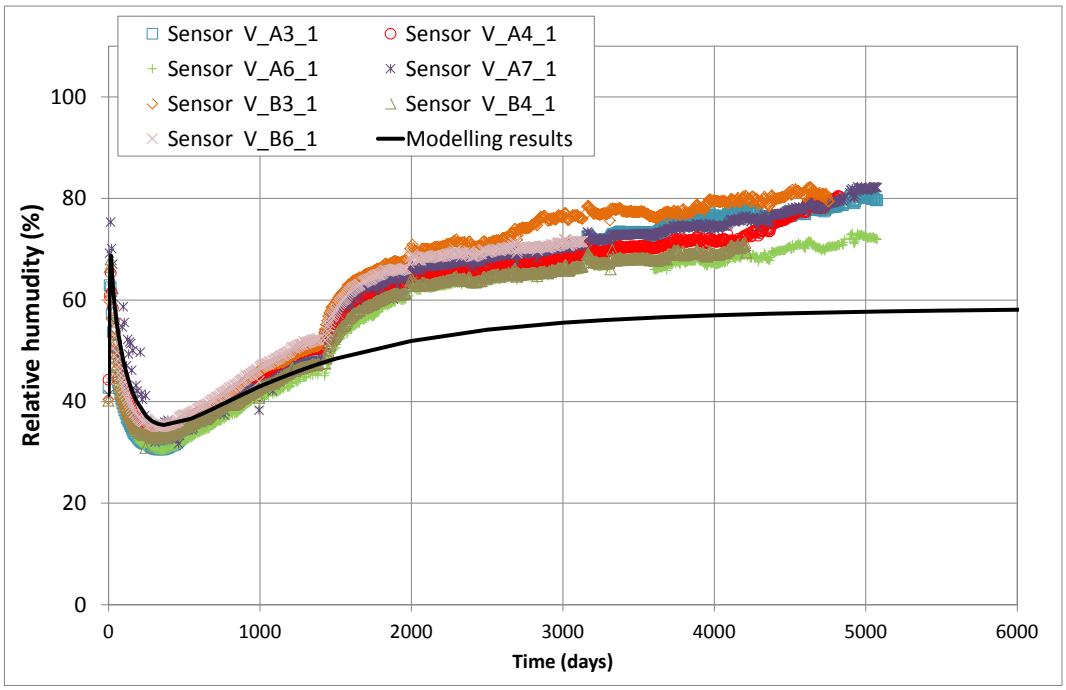

Figure 3-2. Computed (line) and measured (symbols) relative humidity in the sensors located at 0.22 m from the heater for the FEBEX mock-up test.

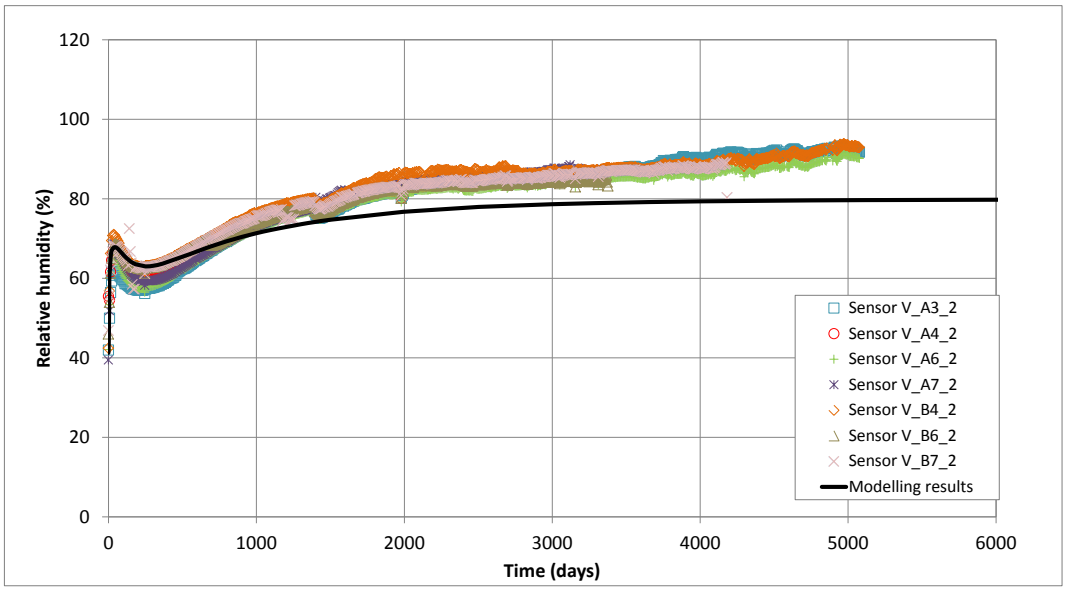

Figure 3-3. Computed (lines) and measured (symbols) relative humidity in the sensors located at 0.37 m from the heater for the FEBEX mock-up test.

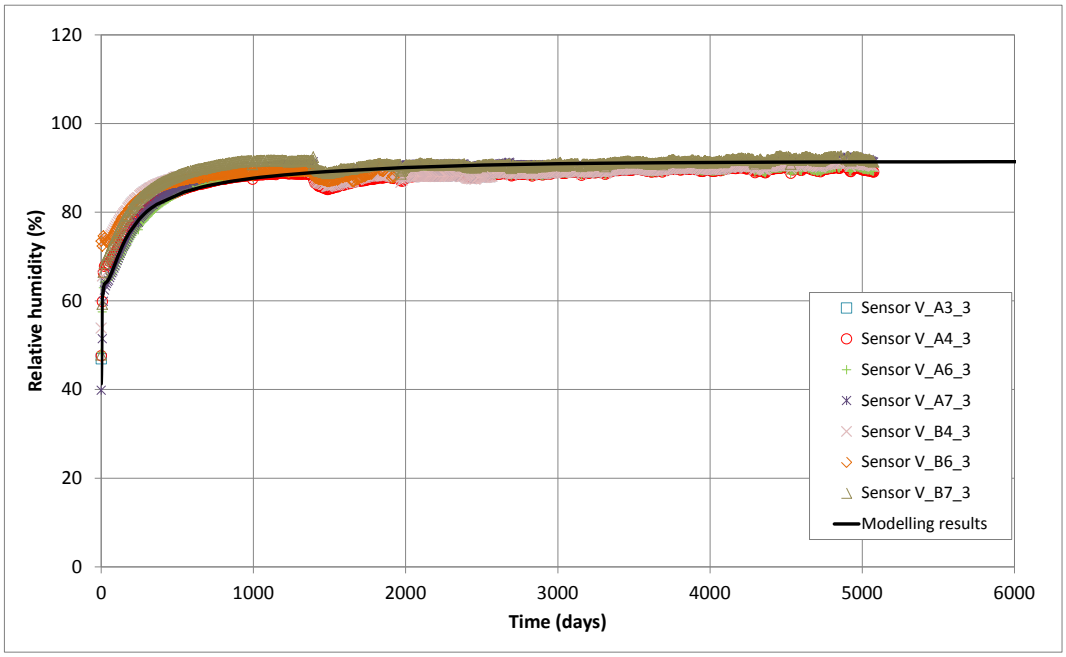

Figure 3-4. Computed (lines) and measured (symbols) relative humidity in the sensors located at 0.55 m from the heater for the FEBEX mock-up test.

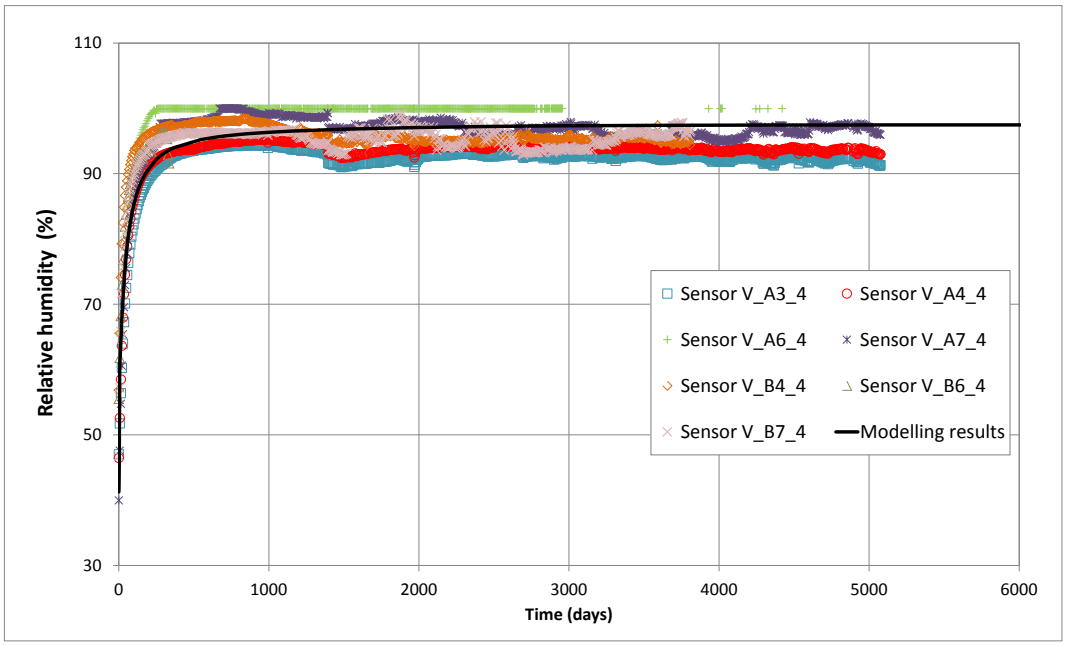

Figure 3-5. Computed (lines) and measured (symbols) relative humidity in the sensors located at 0.70 m from the heater for the FEBEX mock-up test.

4 THC(m) models of the heating and hydration tests on 60 cm long cells

4.1 Introduction

Model predictions have been compared to temperature, water content, porosity and porewater chemical data from heating and hydration infiltration tests performed by Ciemat on cylindrical samples (60 cm long and 7 cm in diameter) of compacted FEBEX bentonite. These tests were performed on several columns, which were dismantled after durations ranging from 0.5 to 7.6 years. These tests are denoted as CG tests. Measured mineralogical data show no mineralogical changes at the end of the tests (Villar et al., 2008a). Dry density, water content, saturation, temperature and chemical composition were measured at the end of the tests.

The updated THMC model developed from data of other heating and hydration tests was tested with data from the CG cell tests.

4.2 Test description

A series of hydration and heating tests were performed during the FEBEX Project on cylindrical bentonite samples 60 cm long and 7 cm in diameter. These tests lasted from 0.5 to 7.6 years (Villar et al., 2008a). They are denoted, FQ1/2 (CG1), HI1/2 (CG1), FQ2 (CG2) and CG3. The following notation has been adopted to shorten the names of the CG tests. The tests lasting half a year are denoted as CG0.5 for FQ1/2(CG1) and CG0.5b for HI1/2(CG1), respectively. The tests with a duration of 1 year are denoted as CG1 for FQ1 (CG5) and CG1b for HI1 (CG6), respectively. The tests with a duration of 2 years are denoted as CG2 for FQ2(CG2) and CG2b for HI2(CG4). Finally, the test on the CG3 cell which lasted 7.6 years, is denoted as CG7.6.

Sample columns were prepared with FEBEX bentonite blocks compacted to a dry density of 1.65 g/cm^3 with an initial water content of 14%. The cells were installed in a Teflon cover to prevent lateral heat conduction and bentonite deformation. The hydration system maintained the water pressure at 1.2 MPa at the top of the cell. A heater was installed at the bottom of the cell to ensure a temperature of 100ºC (Figure 4-1). The samples were hydrated with granitic water. Its chemical composition is listed in Table A2-1. The cells were instrumented with thermocouples. Temperatures and water intake were monitored during the tests. The cells were dismantled at the end of the tests to measure dry density, water content, soluble

salts, exchanged cations and mineralogical content. Table 4-1 lists the main features of the tests including their duration, and the available water intake, dry density, water content, soluble salts and exchanged cation data.

Table 4-1. Main features of the 60 cm heating and hydration tests.

Reference	Test Code	Duration (days)	Available measured data					
			Water intake	Temperature	Water content	Dry density	Soluble salts	Exchanged cations
FQ1/2 CG1	CG0.5	188	YES	YES	YES	YES	YES	NO
HI1/2 CG1	CG0.5b	214	YES	YES	YES	YES	YES	YES
FQ1 CG5	CG1	370	NO	YES	YES	YES	YES	NO
HI1 CG6	CG1b	440	NO	YES	YES	YES	YES	YES
FQ2 CG2	CG2	762	NO	YES	YES	YES	YES	NO
HI2 CG4	CG2b	747	YES	YES	YES	YES	YES	YES
CG3	CG7.6	2775	YES	NO	YES	YES	YES	NO

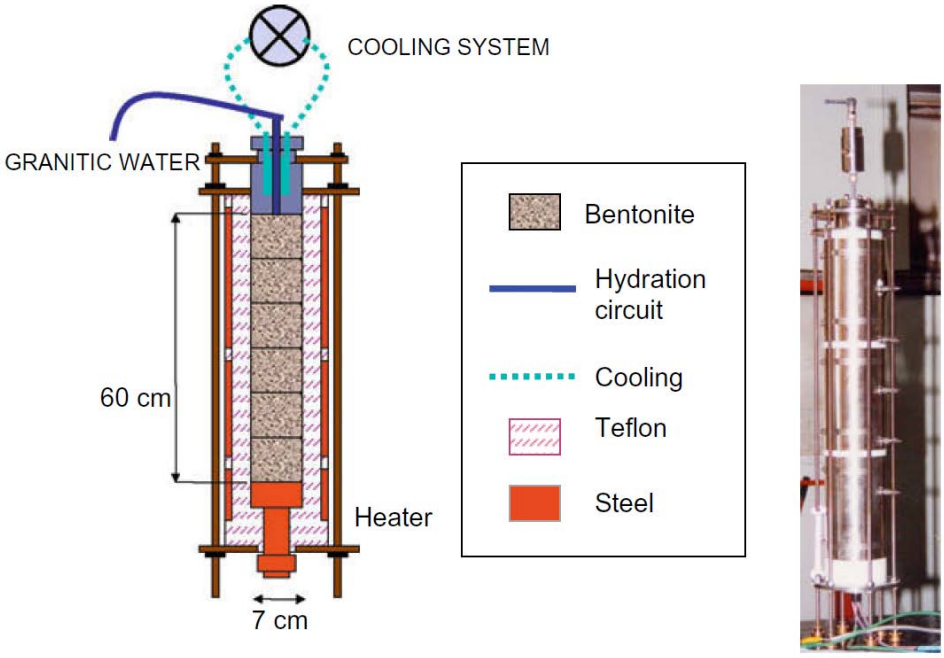

Figure 4-1. Experimental setup of CG tests (Villar et al., 2008a).

4.3 Analysis of available data

Available water intake data from CG cells were analysed in the Deliverable 3.5-1 (Samper et al., 2011). Water intake was obtained from the water uptake online measurements during the tests. The water intake calculated from the difference between the final and the initial bentonite weight is 15% smaller than the measured

on line water intake data. Therefore, the water uptake of was corrected by a factor of 0.85 (see Table 2 of Villar et a., 2008b). Figure 4-2 shows the raw water uptake data for CG cells. The corrected water intake data were used for model testing and calibration. The cumulative water intake of the CG 0.5b test is smaller than the intake of the other cells. This difference is due to the fact that the CG0.5b cell was the first test to be performed. This test had no provisions for thermal isolation. The data from the CG0.5b test were not considered for model testing.

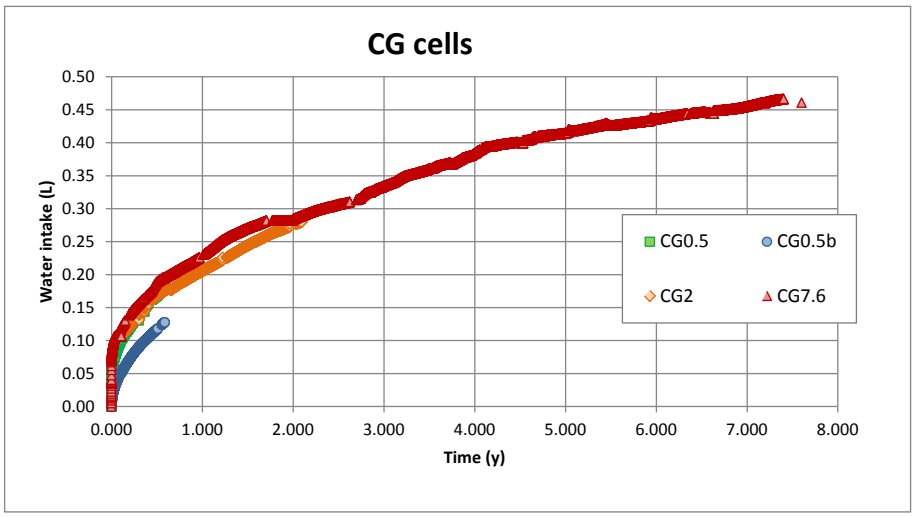

Figure 4-2. Raw cumulative water inake for CG cells versus time.

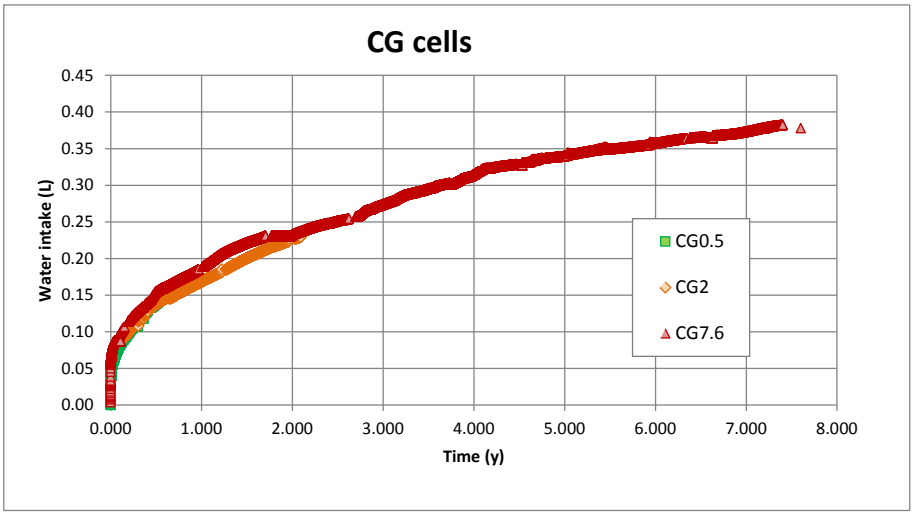

Figure 4-3. Corrected cumulative water uptake for CG cells versus time.

The Chapman's method was used to obtain the concentration of exchanged cations for CG0.5, CG0.5b, CG1, CG1b, CG2 and CG2b tests. In this method, soluble salts are washed first. Then, the exchanged cations of the bentonite were extracted by successive displacements with a buffered solution of 1M ammonium acetate at pH 7 (Fernández and Villar, 2010). The exchanged cations in the CG7.6 test were measured with the $CsNO_3$ method according to which Cs^+ is used to

displace the exchanged cations. This method is considered to be more accurate than that of Chapman method because it does not overestimate the concentration of the divalent cations at the interlayers. The average measured sum of concentrations of exchanged cations for the CG0.5, CG1 and CG2 tests is about 90 meq/100 g while such sum is 101 meq/100g for the CG7.6 test. This sum is smaller than the CEC of the FEBEX bentonite (102 meq/100 g) used in the chemical model because the method used to measure the exchanged cations has interpretation errors. The measured concentrations of exchanged data which have are smaller than the CEC by more than 10% were discarded for model testing and calibration.

Figure 4-4 shows the raw and filtered concentrations of exchanged cations for the CG0.5 tests. The average sum of these data is 91 meq/100g and is slightly smaller than the CEC of the FEBEX bentonite (ENRESA, 2004). The measured data at x = 0.01 m are not considered for the model calibration. The average sum of concentrations of exchanged cations in the CG1 tests is 91.3 meq/100g. The measured sum at x = 0.36 m is 10% smaller than the CEC and has not been considered for model testing (Figure 4-5). The measured sum of concentrations data at x = 0.2 m is larger than the average of the CG2 test. This value was not considered for model testing (Figure 4-6). Figure 4-7 shows the concentrations of exchanged cations in the CG7.6 test. Measured data from x = 0.4 m to x = 0.6 m are smaller than the CEC and were not considered for model testing.

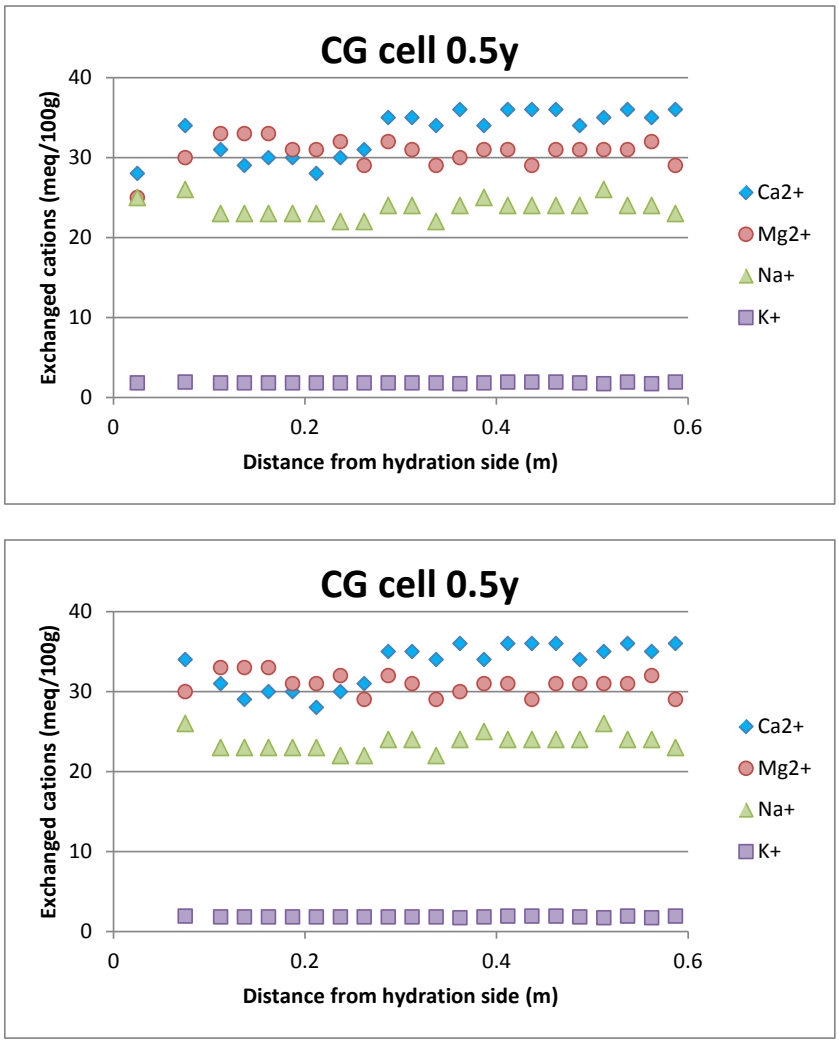

Figure 4-4. Row (top) and filtered (bottom) measured concentrations of exchanged cations for the CG0.5 test.

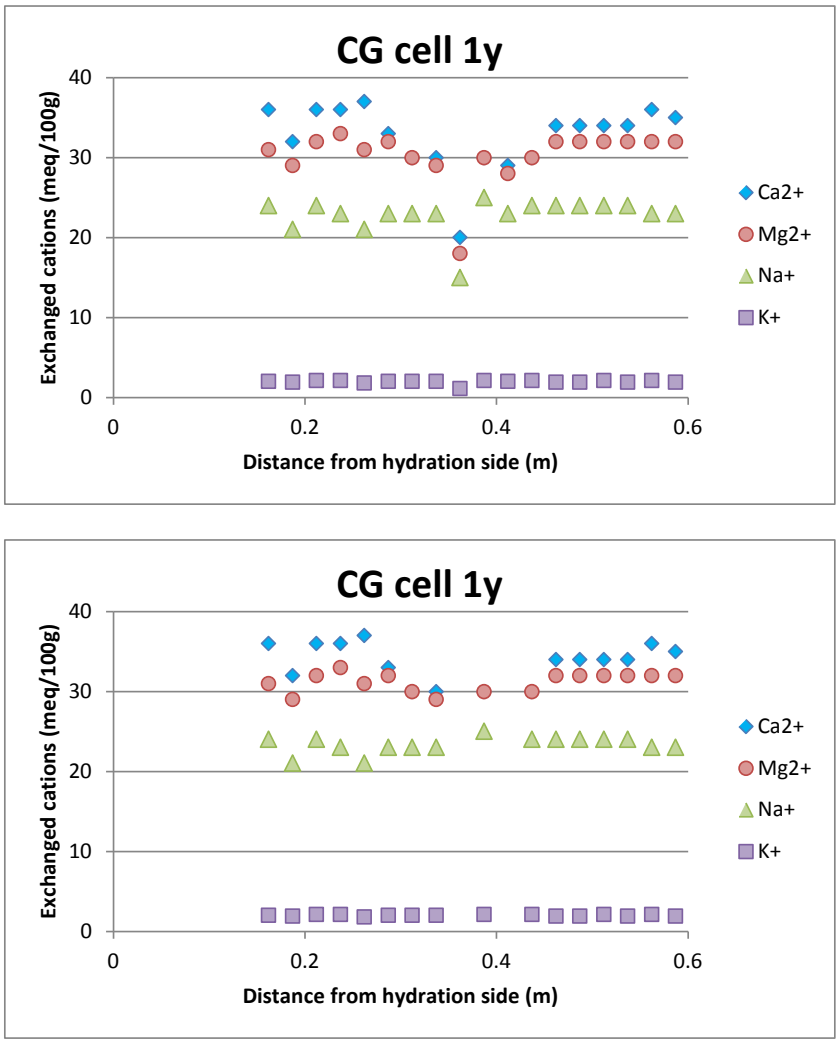

Figure 4-5. Row (top) and filtered (bottom) measured concentrations of exchanged cations for the CG1 test.

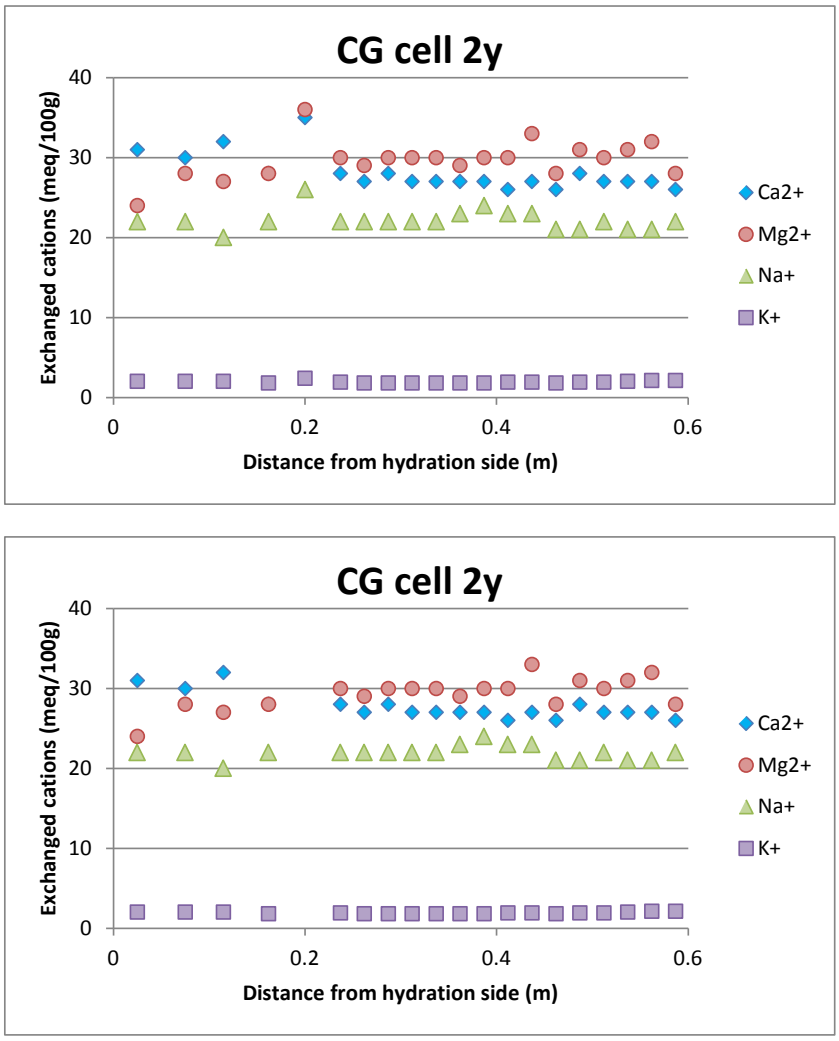

Figure 4-6. Row (top) and filtered (bottom) measured concentrations of exchanged cations for the CG2 test.

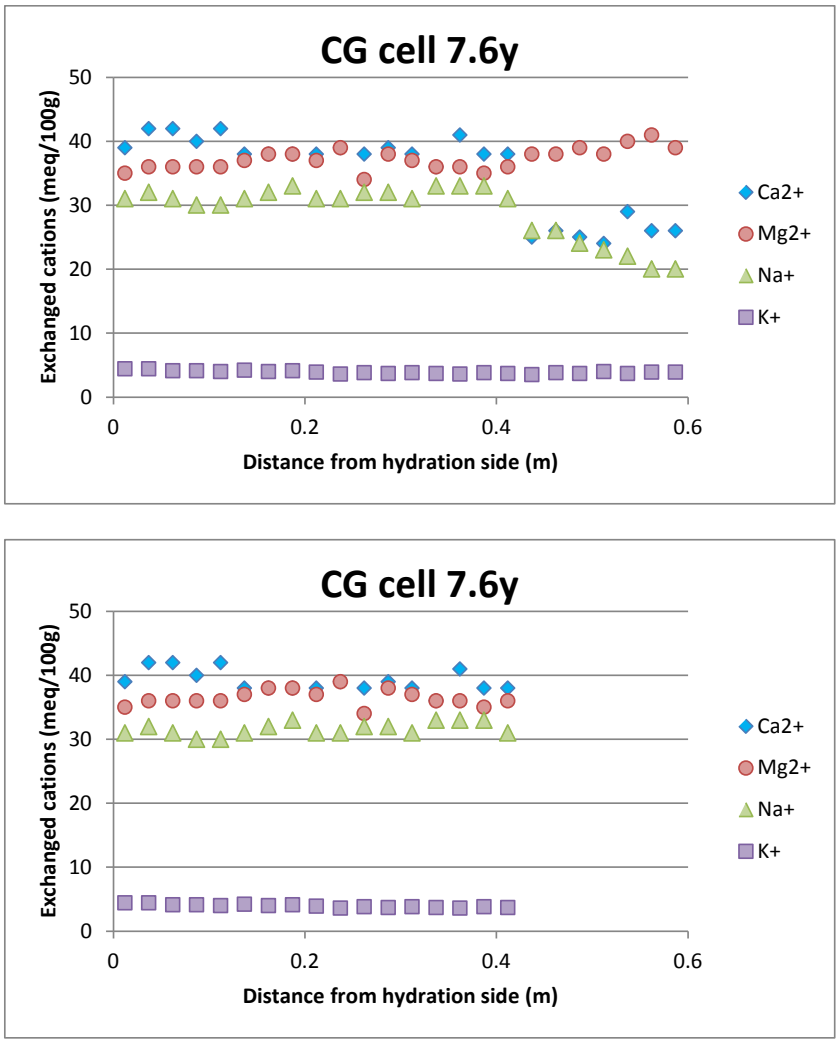

Figure 4-7. Row (top) and filtered (bottom) measured concentrations of exchanged cations for the CG7.6 test.

The chemical composition of the bentonite pore water can be estimated with the squeezing or the aqueous extract methods (Fernández and Villar, 2010).

The squeezing involves the extraction of the interstitial pore water from a nearly saturated sample of bentonite. The volume of water extracted depends on the water content, the squeezing pressure and the time.

The aqueous extract method is used to quantify the soluble salts of clay samples. An 1:R aqueous extract consists on adding a mass of distilled water equal to R times M_s to a mass M_s of powdered clay sample (Zheng et al., 2010). The solid to liquid ratio for CG cells is 1:4 (10 g of clay in 40 ml of water). The clay sample and the water are stirred for two days, thus allowing for the equilibration of water and clay samples. Squeezing was used for some bentonite samples. The concentration of conservative species in the clay pore water, c_i, can be derived from the concentration

of aqueous extract, c_{ae}, performed on a clay sample of mass M_s, from the species mass balance. The gravimetric water content of aqueous extract, w_{ae}, is related to the gravimetric water content of clay sample, w_i, through:

$$w_{ae} = w_i + R(w_i + 1) \tag{22}$$

The dilution factor, F, which relates c_i to c_{ae} is given by:

$$F = \frac{c_i}{c_{ae}} = 1 + R + \frac{R}{w_i} \tag{23}$$

The dilution factor was calculated for each section using the water content measured at the end of the test.

The concentration c_i of the conservative species Cl^- was calculated for the CG cells. Measured and computed Cl^- concentrations were compared for CG0.5, CG0.5b, CG1, CG1b, CG2 and CG2b tests.

For other chemical species such as Ca^{2+} or Na^+ the dissolved concentrations should be derived by solving an inverse model which is time consuming. CIEMAT performed a geochemical model of the geochemical data of the CG7.6 test (Fernández and Villar, 2010). The computed concentrations of the chemical species of this test were compared with the results of the Ciemat geochemical model for the dissolved concentrations of Ca^{2+}, Mg^{2+}, K^+, Na^+, SO_4^{2-} and HCO_3^-.

Figure 4-8, Figure 4-9 and Figure 4-10 show the measured Cl^- concentration with aqueous extract and squeezing for the CG0.5, CG0.5b, CG1, CG1b, CG2 and CG2b tests. Some squeezing data are much smaller than the aqueous extract Cl^- data and are deemed to be erroneous. These figures show the raw and filtered data.

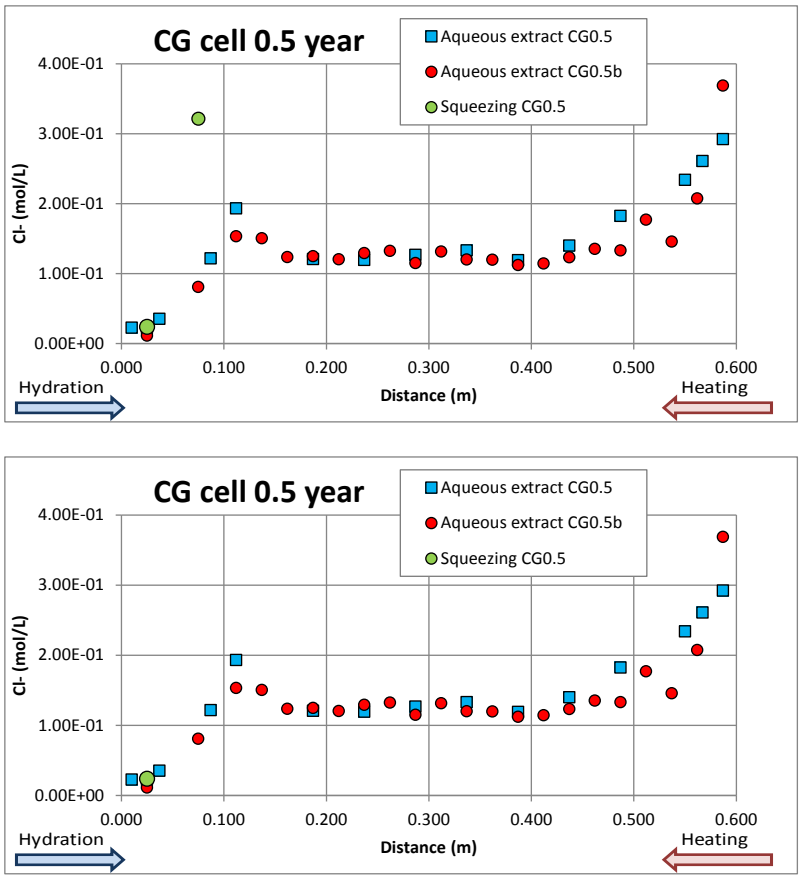

Figure 4-8. Row (top) and filtered (bottom) concentrations of dissolved Cl^- derived from aqueous extract and squeezing methods for the CG0.5 and CG0.5b tests.

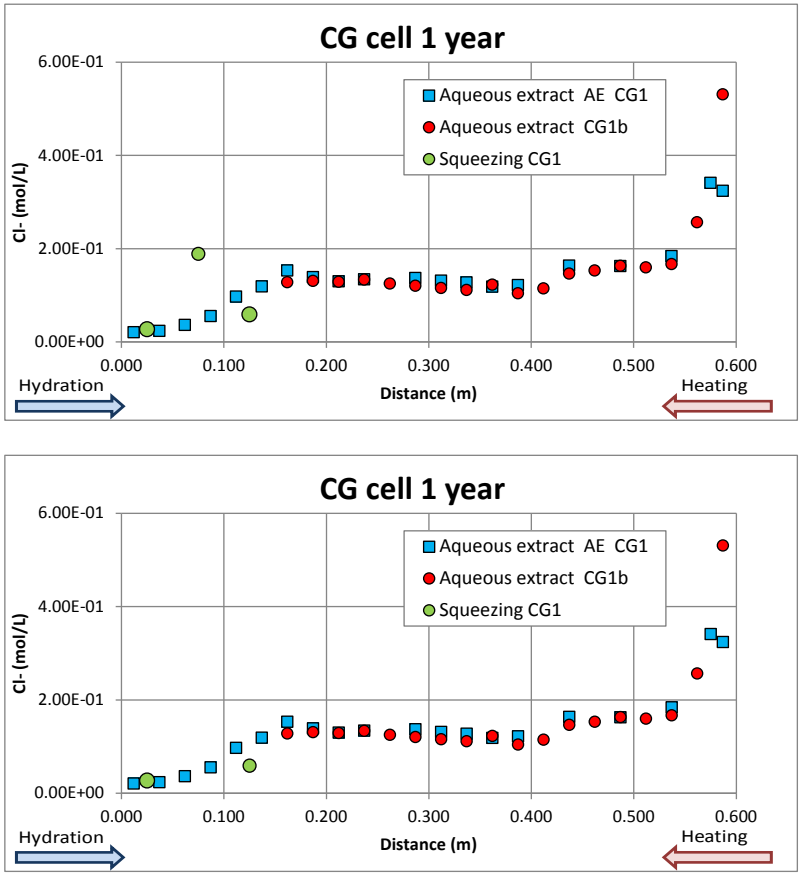

Figure 4-9. Row (top) and filtered (bottom) concentrations of dissolved Cl^- derived from aqueous extract and squeezing methods for the CG1 and CG1b tests.

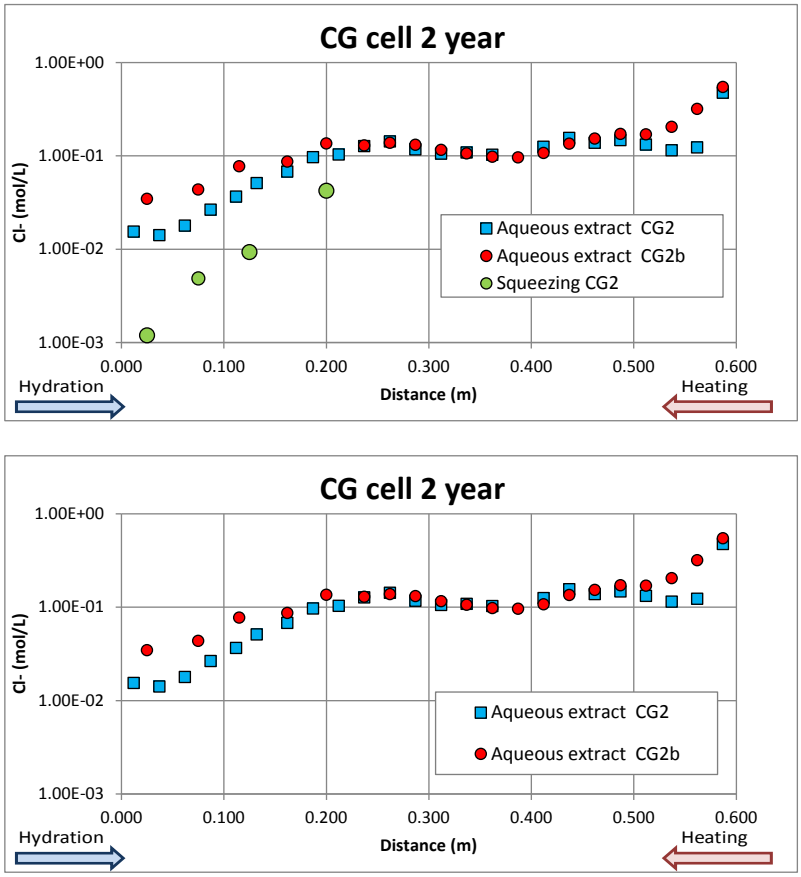

Figure 4-10. Row (top) and filtered (bottom) concentrations of dissolved Cl^- derived from aqueous extract and squeezing methods for the CG2 and CG2b tests.

4.4 Model description

The numerical models were performed in two stages: testing and calibration. The THMC model parameters were taken from the previous model of Zheng et al. (2010).

The numerical model was performed with a one-dimensional finite element mesh (Figure 4-11). The liquid pressure at the top of the cell is fixed at 1.2 MPa. The temperature is 22ºC at the top of the cell and 100ºC at the bottom of the cell in the contact with the heater. Heating and hydration tests were simulated with four models: a model of 0.5 years (188 days), a model of 1 year (440 days), a model for 2 years (747 days) and a model for the 7.6 years (2775 days). The numerical models account for the heating as well as for the cooling during two days. The THMC parameters of the bentonite are the same for the 4 simulations. They are listed in Table A1-1 to Table A1-4 in Appendix A. Some parameters such as intrinsic permeability of the liquid were taken from laboratory experiments (ENRESA, 2006a). Other bentonite

parameters, such as relative permeability of the liquid and the gas, vapour tortuosity, the reflection coefficient and the thermo-osmotic permeability were taken from those of previous heating and hydration tests (Zheng et al., 2010). The vertical displacement was disabled at the top of the cell. The total stress was fixed to 250 kPa. Initially, the bentonite has a porosity of 0.4 and a gravimetric water content of 14%, which corresponds to a saturation of 57% and a suction of $1.27 \cdot 10^5$ kPa. The initial temperature is equal to 22ºC. The initial gas pressure is equal to the atmospheric pressure. Heat dissipation from the bentonite was not considered initially. A Cauchy condition was used for the energy equation at the hydration and at the thermocouple sensors, according to which the heat flux, Q_c, is computed from:

$$Q_c = \alpha_T (T - T^*) \tag{24}$$

where α_T is the thermal coefficient which was calibrated to a value of 1016 W/ºC and T* is the external temperature which is equal to the mean temperature measured in the sensors.

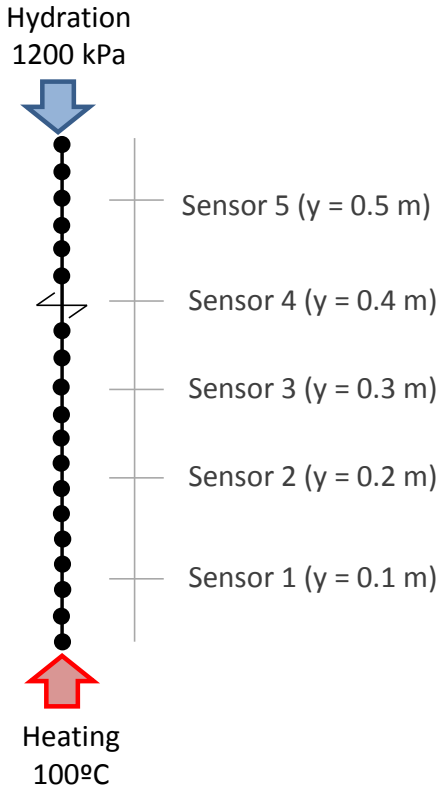

Figure 4-11. One dimensional finite element mesh used for the numerical model of the 60 cm long cells.

A Neuman boundary condition was used for solute transport at the hydration boundary according to which the solute flux is equal to the product of the water flux

times the solute concentration of the inflow water. The hydration water in these tests is granitic water (Table A2-1). The initial concentrations of the primary species of the bentonite pore water were taken from Fernández et al. (2001) (Table A2-1). The effective diffusion coefficient, D_e, was s assumed to be the same for all species and equal to $2 \cdot 10^{-10}$ m^2/s. The effective diffusion coefficient for Cl^- was estimated from a heating and hydration experiment by Zheng et al. (2010) to be equal to $2 \cdot 10^{-11}$ m^2/s.

The chemical system is defined in terms of the following primary species: H_2O, H^+, Na^+, K^+, Ca^{2+}, Mg^{2+}, HCO_3^-, Cl^-, SO_4^{2-} and SiO_2(aq). The cation exchange and surface complexation parameters of the bentonite are listed in Table A2-6 and Table A2-7. The model accounts for the cation exchange of Na^+, K^+, $Ca^{2+}$and Mg^{2+} in the bentonite. The cation exchange capacity is 102 meq/100g (Fernández et al., 2004). The previous model of Zheng et al. (2010) was used for model testing. However, the selectivity coefficients were calibrated during the calibration stage.

The initial mineral volume fractions are listed in Table 4-2. The bentonite contains initially 1% of calcite, 4.5% of chalcedony and 0.08% of gypsum. All these minerals are assumed at equilibrium. The dissolution of the montmorillonite is not considered in the model because smectite dissolution is slow and is not expected to be relevant. The relevant aqueous complexes were identified with EQ3NR (Wolery, 1992). The equilibrium constant of the aqueous complexation, mineral dissolution/precipitation, surface complexation and cation exchange reactions are listed in Table A2-4 to A2-7 in Appendix A.

Table 4-2. Initial mineral volume fractions (%) of CG tests (ENRESA, 2006a).

Minerals	Calcite	Gypsum	Anhydrite	Chalcedony
Bentonite	1.0	0.08	0.0	4.5

4.5 Model testing

A numerical model was performed using the THMC parameters and the geochemical system taken from the previous model of Zheng et al. (2010). The results of the model are compared to measured data. Such comparison reveals the need to calibrate some model parameters.

4.5.1 Thermo-hydro-mechanical results of CG cells

Water content, saturation and dry density were measured at the end of the tests. Measured porosity was calculated from the measured dry density according to:

$$\emptyset = 1 - \rho_d/\rho_s \quad (25)$$

where $\emptyset$ is the porosity, ρ_d is the dry density and ρ_s is the solid density which is equal to 2.65 kg/dm^3.

4.5.1.1 CG0.5 and CG0.5b cells

Figure 4-12 shows the spatial distribution of the computed porosity after 188 days of heating and after the cooling stage for the CG0.5 and CG0.5b tests. The computed results match the measured data. The porosity near the hydration boundary is larger than the initial value due to the bentonite swelling. Near the heater, the porosity is smaller than the initial value.

The post mortem analyses of the tests show that the diameter of the saturated bentonite samples increased and the bentonite cell deformed (Fernández and Villar, 2010). The computed gravimetric water content and the saturation degree fit the measured data. The computed gravimetric water content reproduces the measured data near the hydration boundary (Figure 4-13). There are some discrepancies which could be related to discrepancies in the temperature. If the temperature is decreased between 0.4 and 0.5 m the water content and the saturation degree will increase.

The computed water cumulative volume is larger than measured water intake for the CG0.5 test (Figure 4-15). It should be noticed that the measured cumulative water intake of the CG 0.5b test is much smaller than the intake of the other cells because the CG0.5b cell was the first test to be performed and had no thermal isolation. The data from the CG0.5b test were not considered for model testing.

Figure 4-16 shows the mean measured temperature, the temperature range (maximum and the minimum) and the computed final temperature for the CG0.5 and CG0.5b tests. The computed temperature reproduces the temperature at the heater and near the hydration boundary. However, the computed temperature is larger than the temperature measured at the sensors, possibly due to heat dissipation through the lateral surface of the cells.

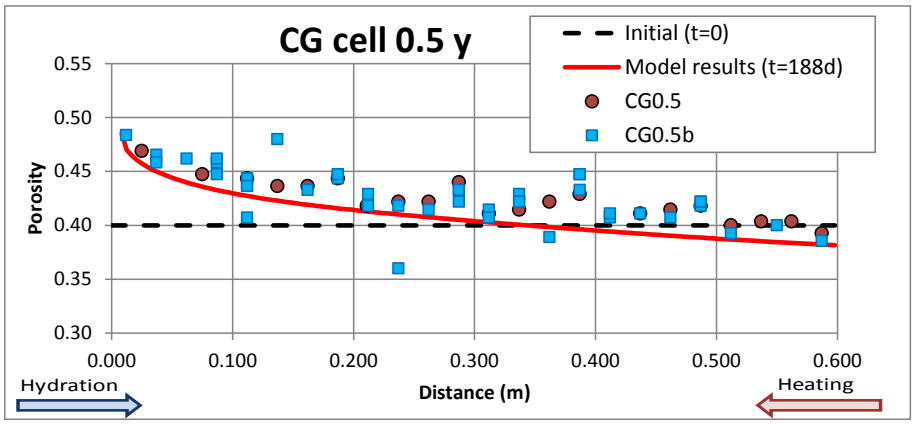

Figure 4-12. Spatial distribution of the measured (symbols) and the computed (line) porosity at the end of the CG0.5 and CG0.5b tests.

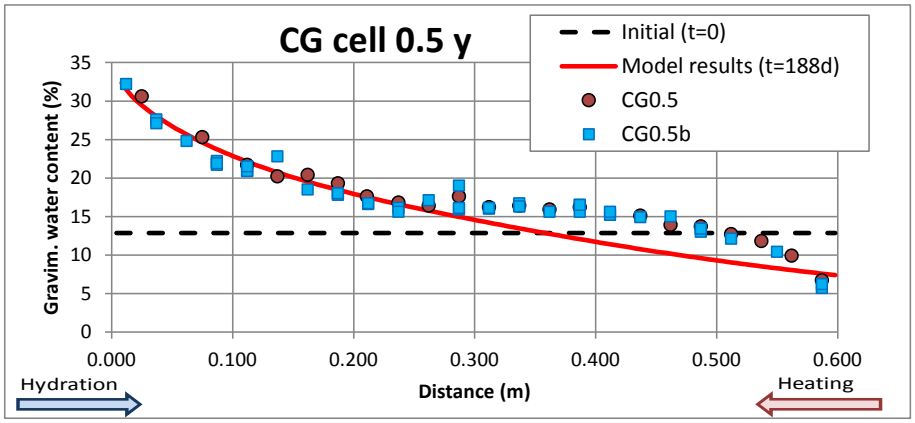

Figure 4-13. Spatial distribution of the measured (symbols) and the computed (line) gravimetric water content at the end of the CG0.5 and CG0.5b tests.

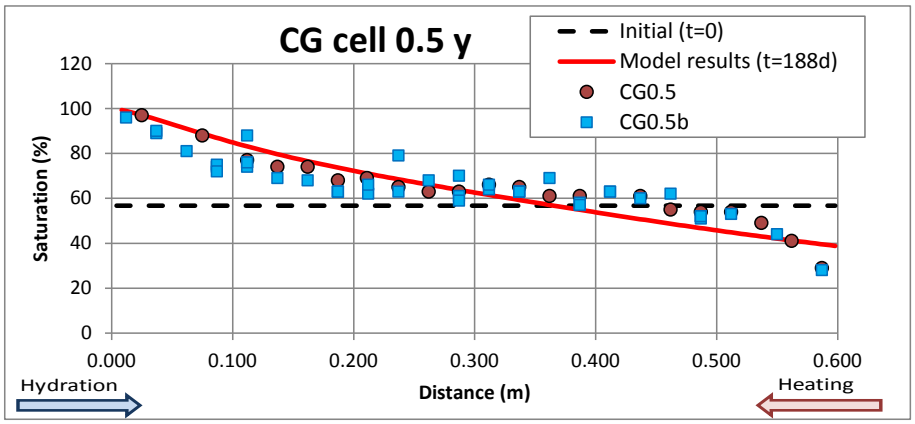

Figure 4-14. Spatial distribution of the measured (symbols) and the computed (line) saturation degree at the end of the CG0.5 and CG0.5b tests.

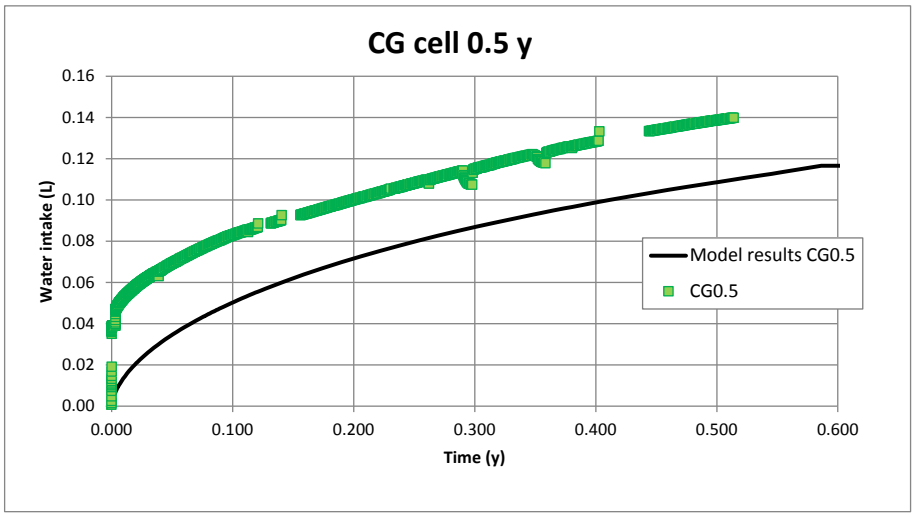

Figure 4-15. Time evolution of the measured (symbols) and the computed (line) water intake for the CG0.5 test.

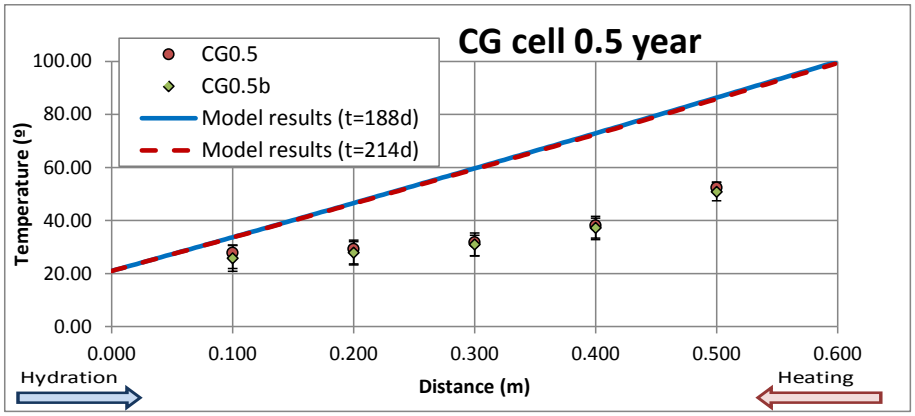

Figure 4-16. Spatial distribution of the mean measured (symbols) and the computed (lines) temperatures at the end of the CG0.5 and CG0.5b tests.

4.5.1.2 CG1 and CG1b cells

The numerical results obtained for the CG1 model are similar to those of the CG0.5 cells. Figure 4-17 shows the measured and computed porosity. The computed porosity is smaller than that measured. The model reproduces the measured water content and saturation degree of cells CG1 and CG1b better than the measured data of CG0.5 and CG0.5b tests (Figure 4-18 and Figure 4-19). The computed water content after a year is larger than that after half a year.

There are no cumulative water intake data for the CG1 cells. The computed water intake for the CG1 cells is compared to the measured cumulative water intake for the the CG0.5 test in Figure 4-20. The computed water intake is larger than

measured data for CG0.5 test. It should be noticed that the measured cumulative water intake of the CG 0.5b test is much smaller than the intake of the other cells because the CG0.5b cell was the first test to be performed and had no thermal isolation. The data from the CG0.5b test were not considered for model testing.

Similar to the CG0.5 test, the computed temperatures do not reproduce the measured temperatures in the sensors in the CG1 tests (Figure 4-21).

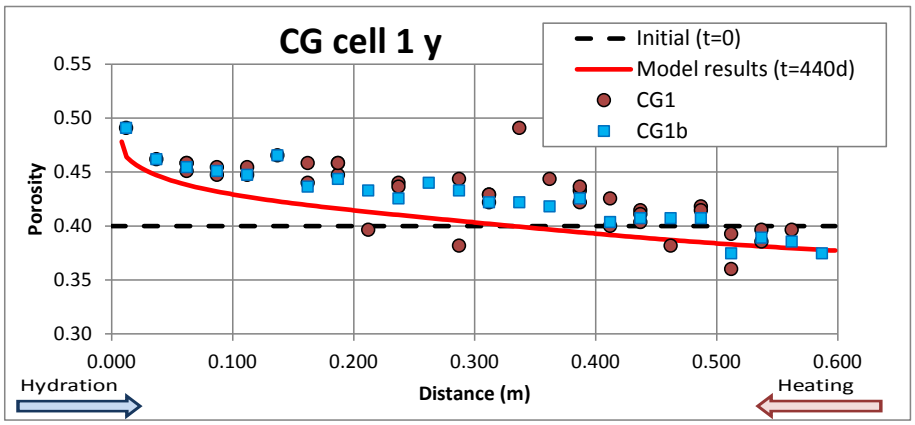

Figure 4-17. Spatial distribution of the measured (symbols) and the computed (lines) porosity at the end of the CG1 and CG1b tests.

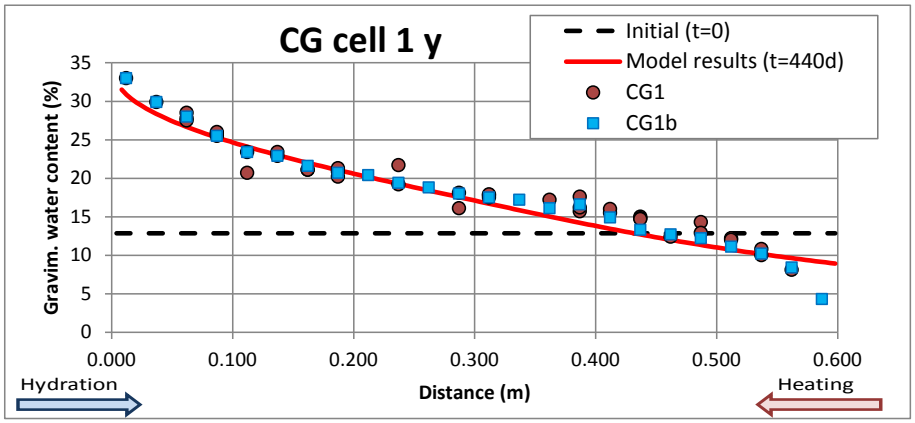

Figure 4-18. Spatial distribution of measured (symbols) and the computed (lines) gravimetric water content at the end of the CG1 and CG1b tests.

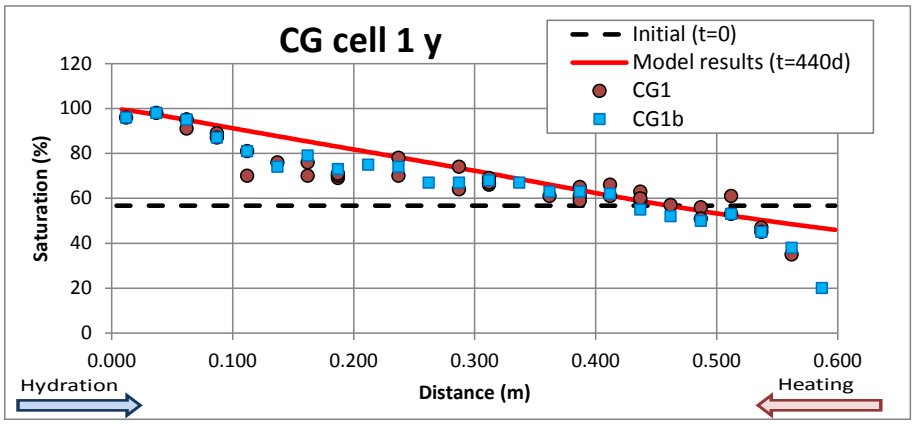

Figure 4-19. Spatial distribution of measured (symbols) and the computed (lines) saturation degree at the end of the CG1 and CG1b tests.

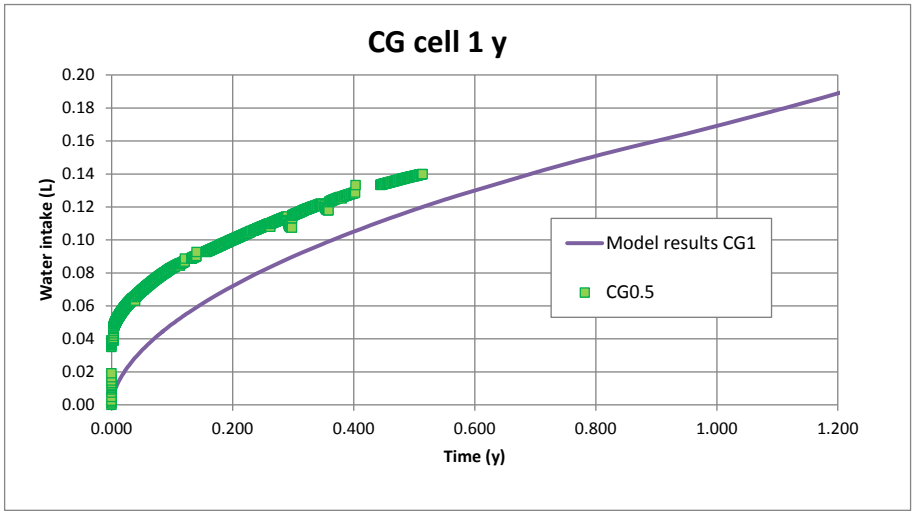

Figure 4-20. Time evolution of the computed (line) cumulative water intake for the CG1 and CG1b tests and the measured (symbols) water intake in the CG0.5 tests.

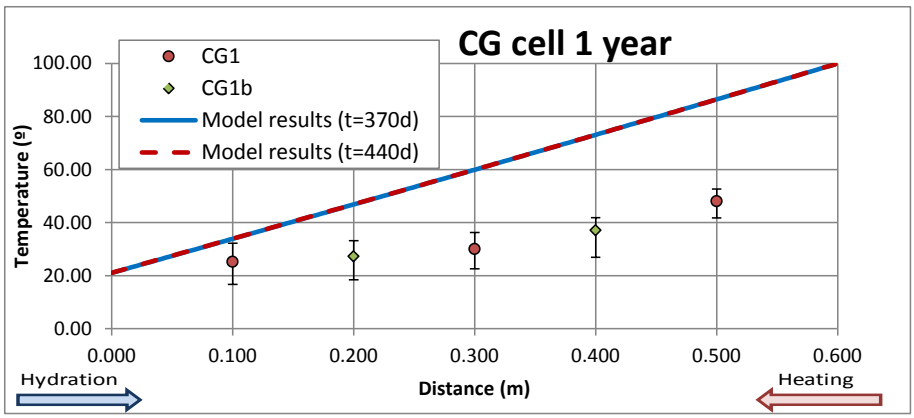

Figure 4-21. Spatial distribution of the mean measured (symbols) and the computed (lines) temperatures at the end of the CG1 and CG1b tests.

4.5.1.3 CG2 and CG2b cells

The numerical results obtained for the CG1 model are similar to those of the CG0.5 cells. Figure 4-17 shows the measured and computed porosity. The computed porosity is smaller than that measured. The model reproduces the measured water content and saturation degree of cells CG1 and CG1b better than the measured data of CG0.5 and CG0.5b tests (Figure 4-18 and Figure 4-19). The computed water content after a year is larger than that after half a year.

The numerical results obtained for the CG2 test are similar to those of the CG0.5 and CG1 tests. The computed porosity after two years of saturation is smaller than the measured porosity (Figure 4-22). On the other hand, the computed water content and saturation degree fit the measured data (Figure 4-23 and Figure 4-24) except near the heater probably due to deficiencies in vapour transport. It will be shown later that the calibration of the vapour tortuosity improves the fit of the saturation degree near the heater.

Figure 4-25 shows the measured water intake of the CG0.5 and CG2 tests and the computed water intake for the CG2 test. The computed water intake does not reproduce the final value of the measured cumulative intake.

The computed temperatures are larger than the values measured in the sensors (Figure 4-26). Clearly, there is a need to account for the lateral loss of heat.

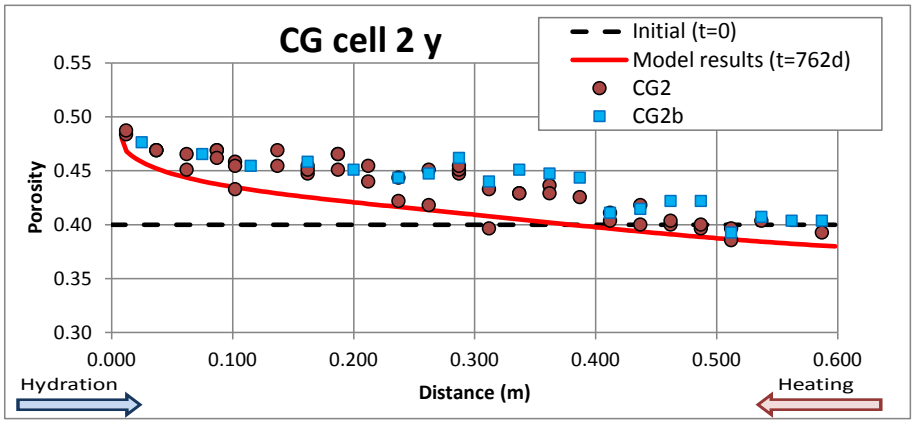

Figure 4-22. Spatial distribution of the measured (symbols) and the computed (line) porosity at the end of the CG2 and CG2b tests.

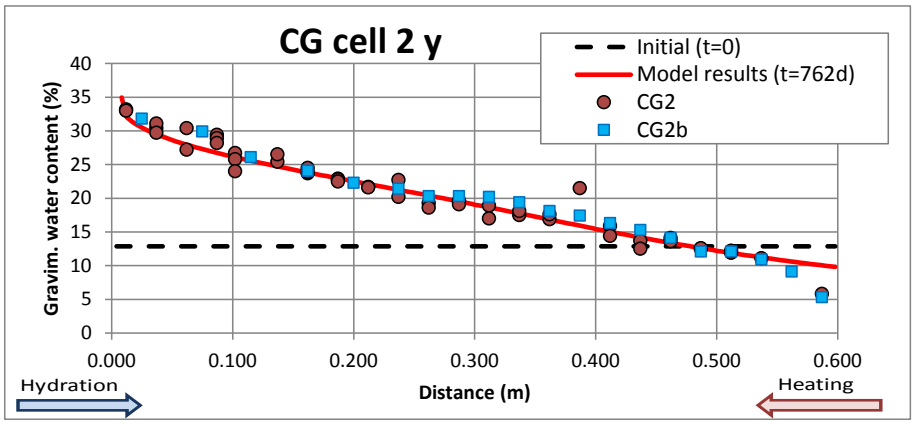

Figure 4-23. Spatial distribution of the measured (symbols) and the computed (line) gravimetric water content at the end of the CG2 and CG2b tests.

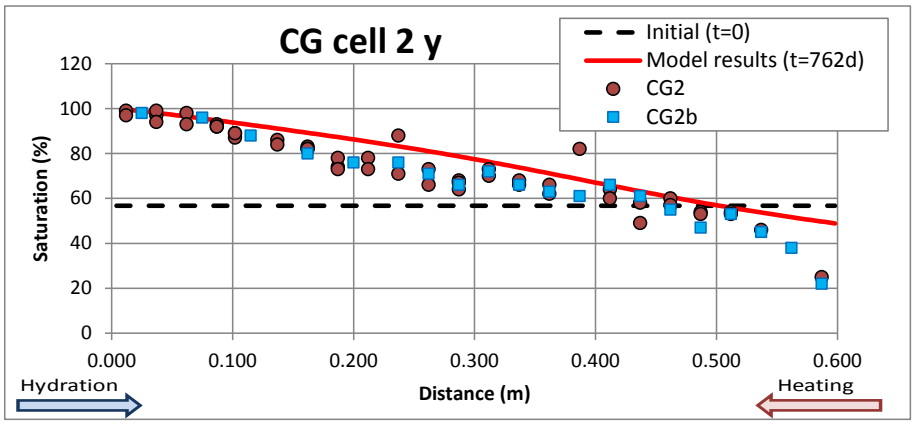

Figure 4-24. Spatial distribution of the measured (symbols) and the computed (line) saturation degree at the end of the CG2 and CG2b tests.

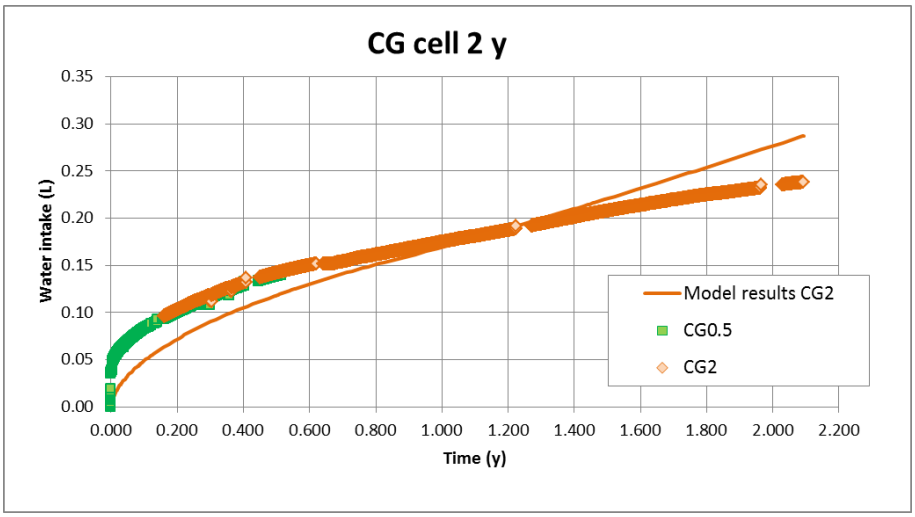

Figure 4-25. Time evolution of the measured (symbols) and computed (line) water intake for the CG2 and CG2b tests.

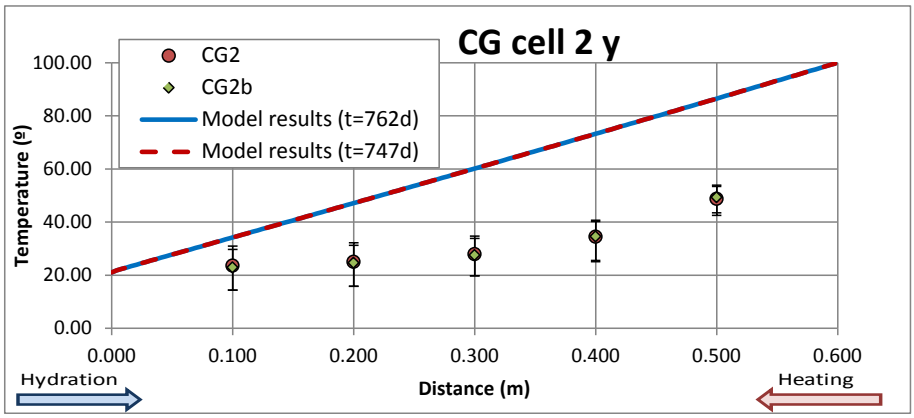

Figure 4-26. Spatial distribution of the mean measured (symbols) and the computed (lines) temperatures at the end of the CG2 and CG2b tests.

4.5.1.4 CG7.6 cell

The numerical results obtained for the CG7.6 test are similar to those of the CG0.5, CG1 and CG2 tests. The computed porosity is smaller than the measured porosity (Figure 4-27). The computed water content and the saturation degree fit well the measured data (Figure 4-28 and Figure 4-29). Figure 4-30 shows the measured cumulative water intake of the CG0.5, CG2 and CG7.6 tests and the computed water intake for the CG7.6 cell. The computed water intake reproduces the measured values for t < 2 years. However, the computed water intake predicts the measured data at 7.6 years.

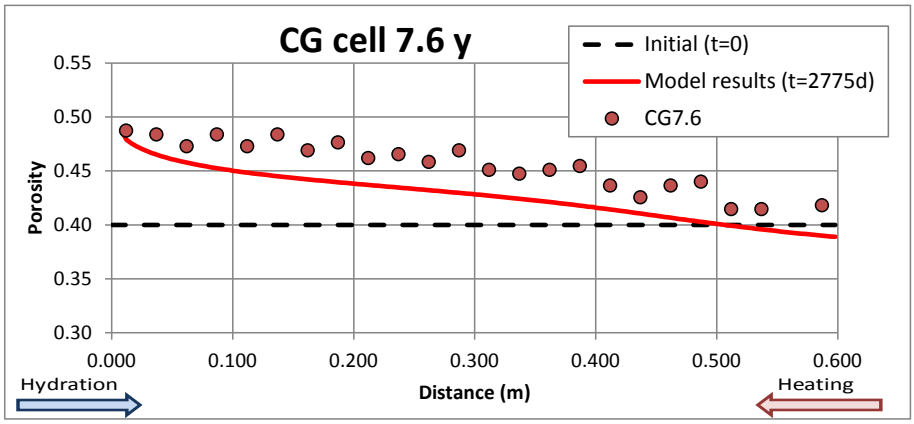

Figure 4-27. Spatial distribution of the measured (symbols) and the computed (line) porosity at the end of the CG7.6 test.

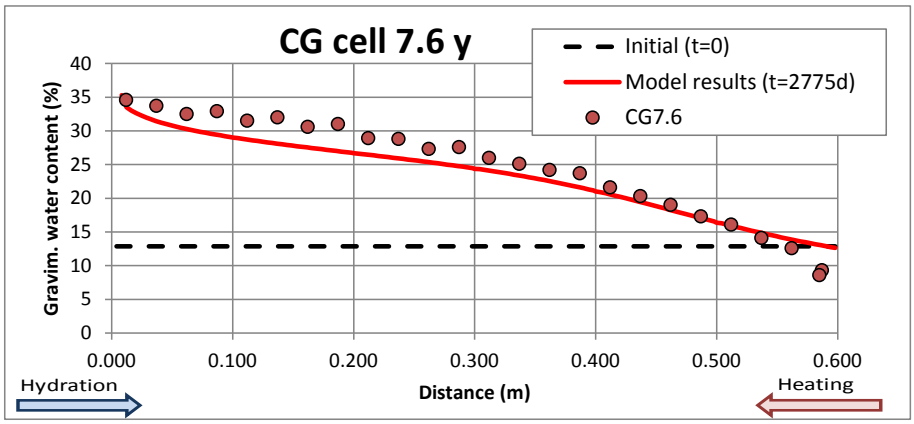

Figure 4-28. Spatial distribution of the measured (symbols) and the computed (line) gravimetric water content at the end of the CG7.6 test.

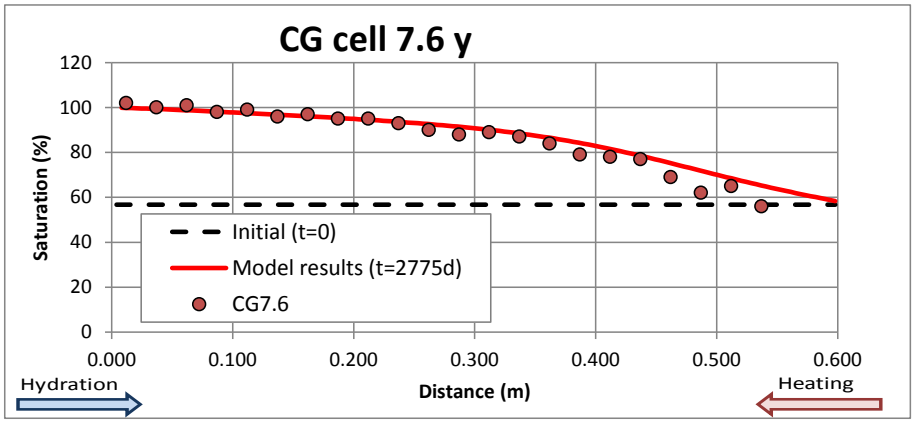

Figure 4-29. Spatial distribution of the measured (symbols) and the computed (line) saturation degree at the end of the CG7.6 test.

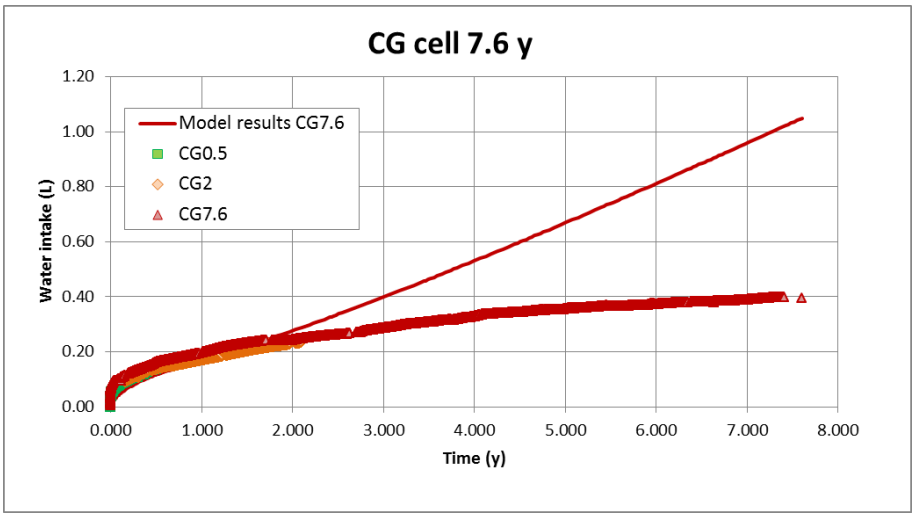

Figure 4-30. Time evolution of the measured (symbols) and computed (line) cumulative water intake for the CG7.6 test.

4.5.2 Testing with geochemical data

4.5.2.1 CG0.5 and CG0.5b cells

Figure 4-31 shows the measured aqueous extract, squeezing and computed concentration of Cl^-. Computed results fit the measured aqueous extract data. The concentration of Cl^- decreases near the hydration side due to the dilution caused by the water inflow which is more diluted. Cl^- remains constant and equal to the initial value of 0.16 mol/l, for 0.15 < x < 0.5 m. The concentration of Cl^- increases near the heater due to the evaporation.

Figure 4-32 to Figure 4-35 show the measured and computed concentrations of the exchanged cations, Na^+, K^+, Ca^{2+} and Mg^{2+} for the CG0.5b test. The error bars of ±20% of measured data are also shown. In general, the computed cation concentrations are within the error bars except for Mg^{2+}.

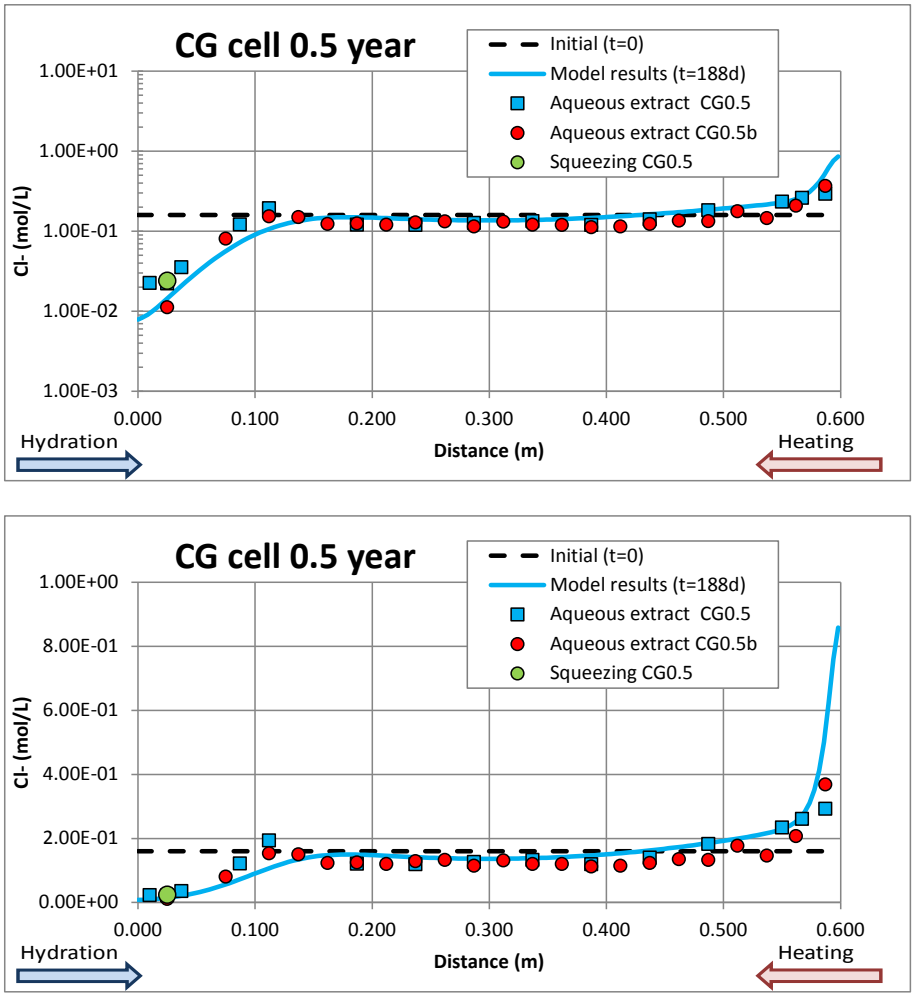

Figure 4-31. Spatial distribution of the measured (symbols) and the computed (line) Cl^- concentrations at the end of the CG0.5 and CG0.5b tests. Measured data include aqueous extract and squeezing data. Logarithmic scale (top) and natural scale (bottom).

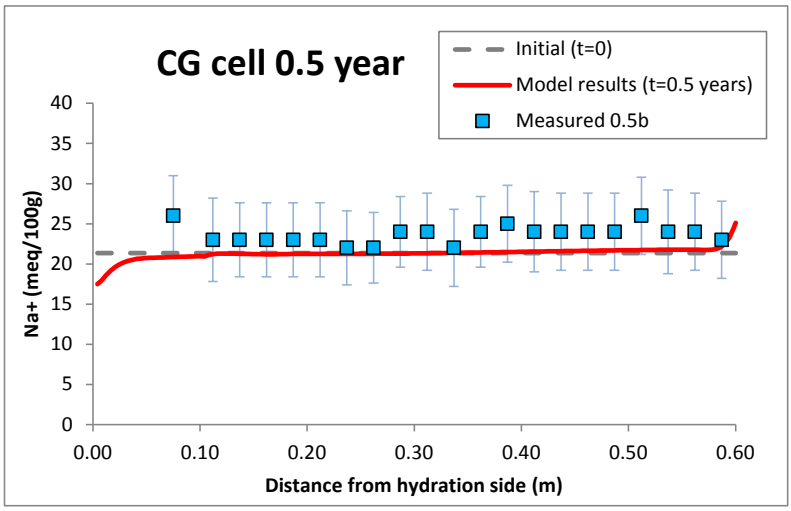

Figure 4-32. Spatial distribution of the measured (symbols) and the computed (line) concentrations of exchanged Na^+ at the end of the CG0.5b test.

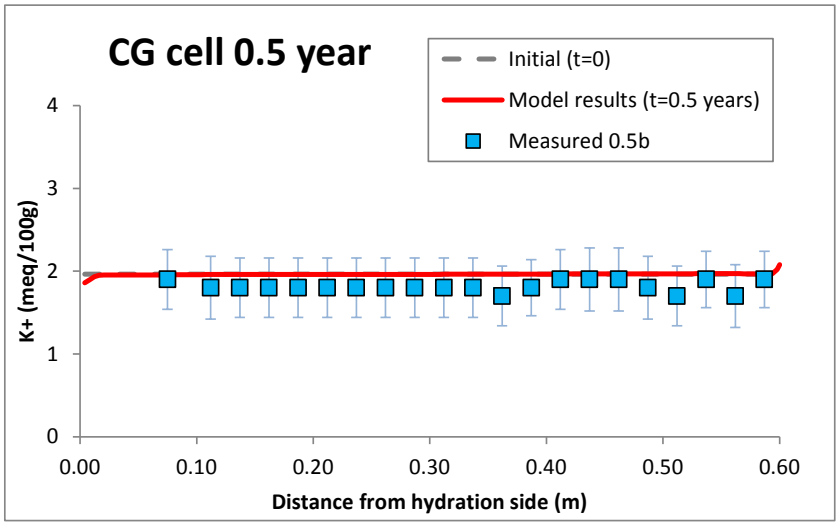

Figure 4-33. Spatial distribution of the measured (symbols) and the computed (line) concentrations of exchanged K^+ at the end of the CG0.5b test.

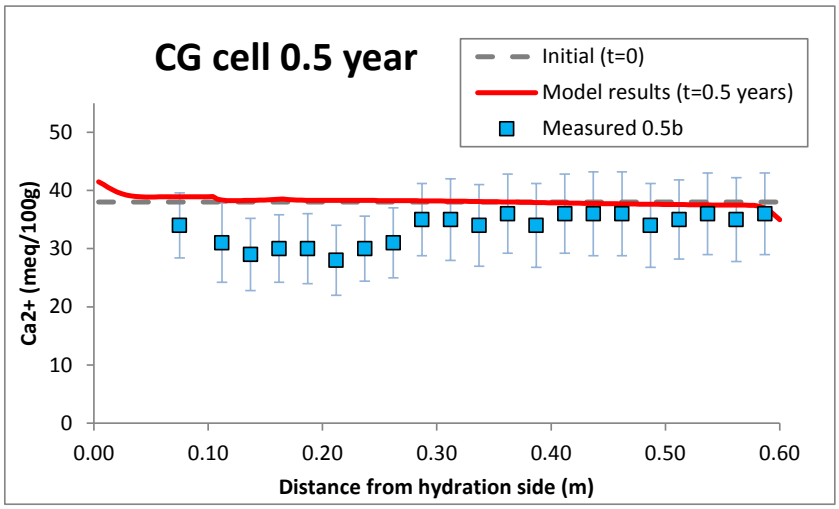

Figure 4-34. Spatial distribution of the measured (symbols) and the computed (line) concentrations of exchanged Ca^{2+} at the end of the CG0.5b test.

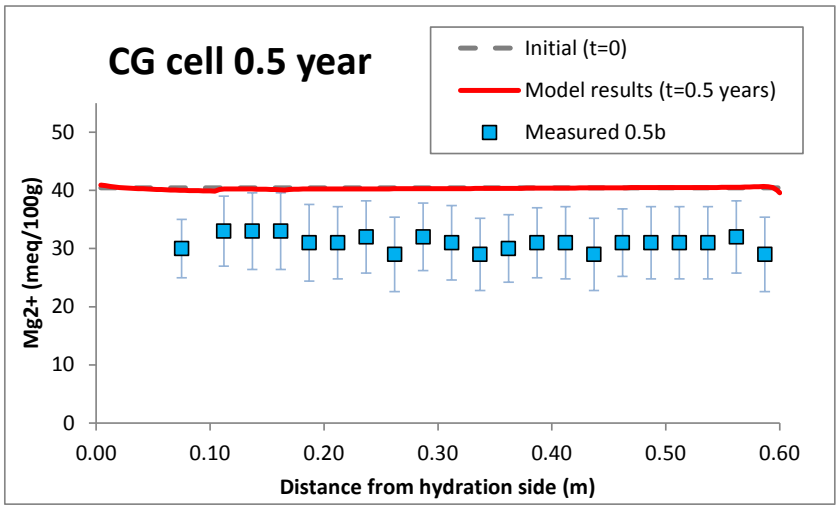

Figure 4-35. Spatial distribution of the measured (symbols) and the computed (line) concentrations of exchanged Mg^{2+} at the end of the CG0.5b test.

4.5.2.2 CG1 and CG1b cells

Figure 4-36 show the measured aqueous extract, squeezing and computed concentration of Cl^- for the CG1 and CG1b tests. Computed results fit chloride measured data.

Figure 4-37 to Figure 4-40 show the measured and computed concentrations of the exchanged cations Na^+, K^+, Ca^{2+} and Mg^{2+} for the CG1b test. The error bars of ±20% of measured data are also shown. In general, the computed cation concentrations are within the error bars except for Mg^{2+}. The computed concentrations of the exchanged Ca^{2+} increases near the hydration side due to the dissolution of calcite which increases the concentration of dissolved Ca^{2+}. Near the heater calcite precipitates, the concentration of dissolved Ca^{2+} decreases and therefore the concentrations of the exchanged Ca^{2+} decreases. Ca^{2+} in the exchanger exchanges mostly with the dissolved Na^+.

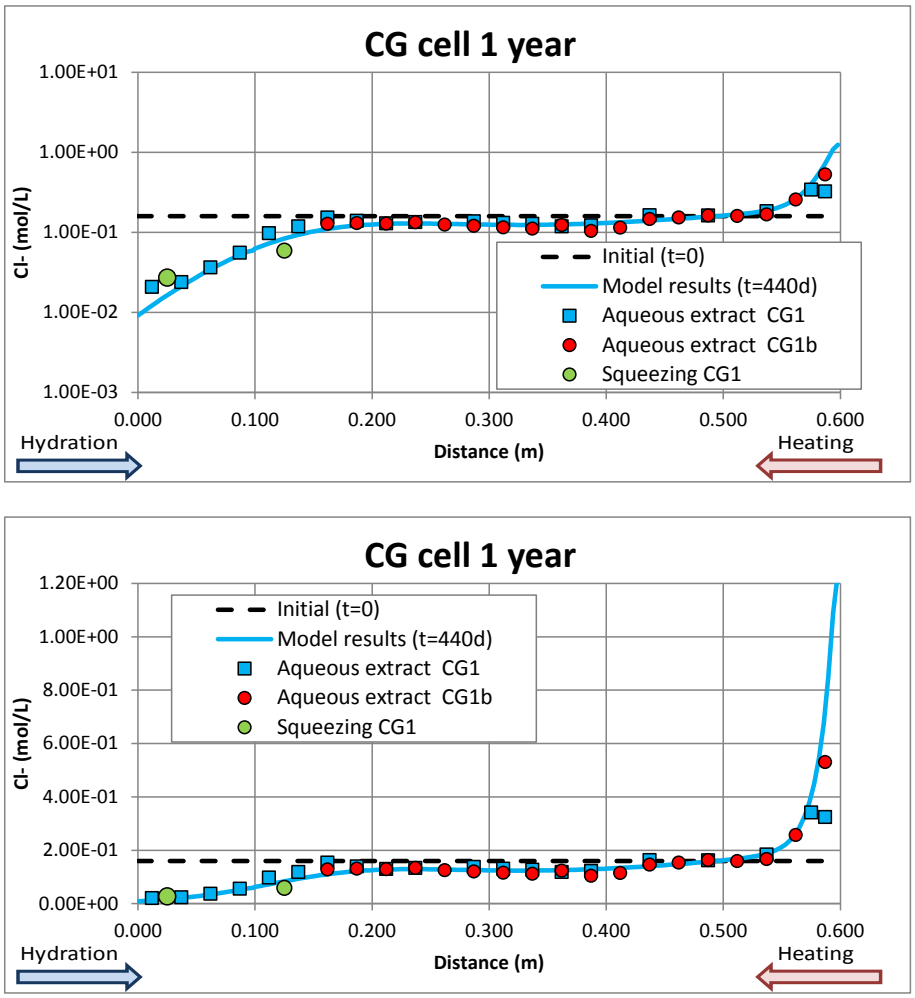

Figure 4-36. Spatial distribution of the measured (symbols) and the computed (line) Cl^- concentrations at the end of the CG1 and CG1b tests. Measured data include aqueous extract and squeezing data. Logarithmic scale (top) and natural scale (bottom).

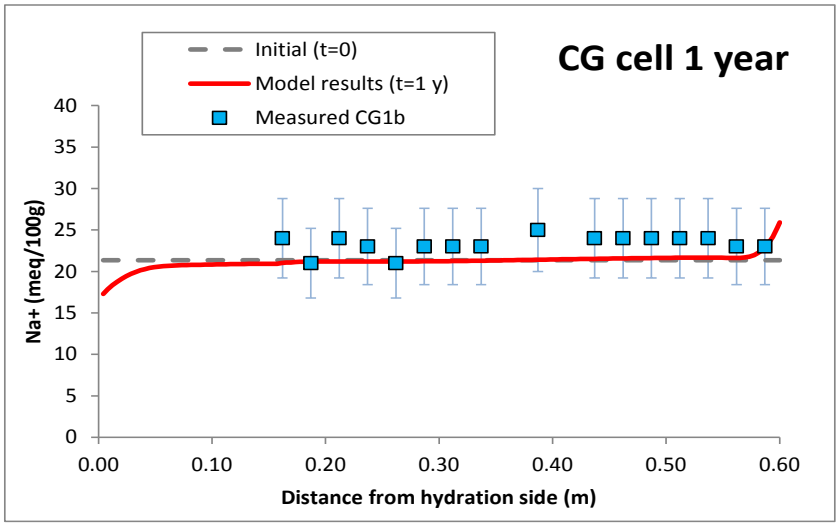

Figure 4-37. Spatial distribution of the measured (symbols) and the computed (line) concentrations of exchanged Na^+ at the end of the CG1b test.

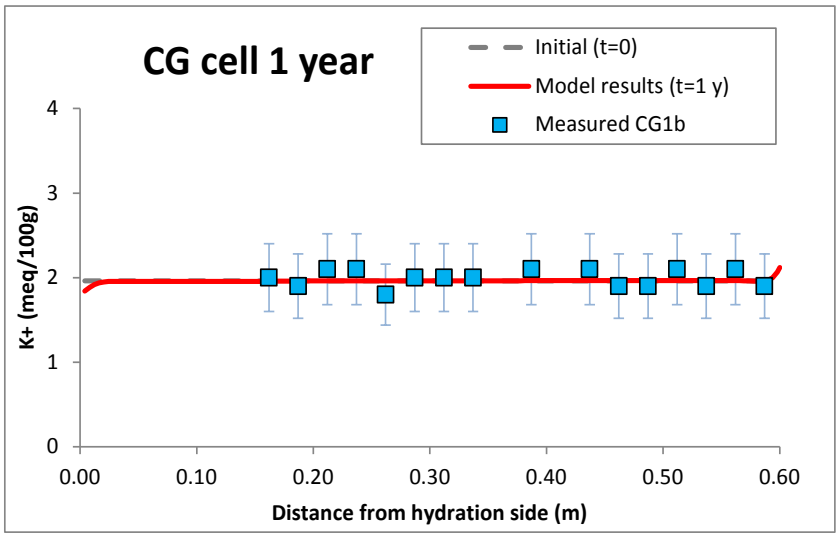

Figure 4-38. Spatial distribution of the measured (symbols) and the computed (line) concentrations of exchanged K^+ at the end of the CG1b test.

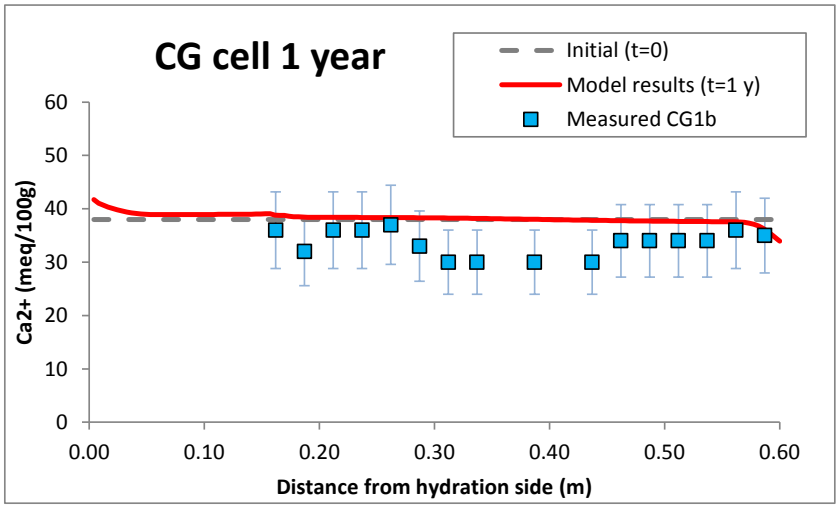

Figure 4-39. Spatial distribution of the measured (symbols) and the computed (line) concentrations of exchanged Ca^{2+} at the end of the CG1b test.

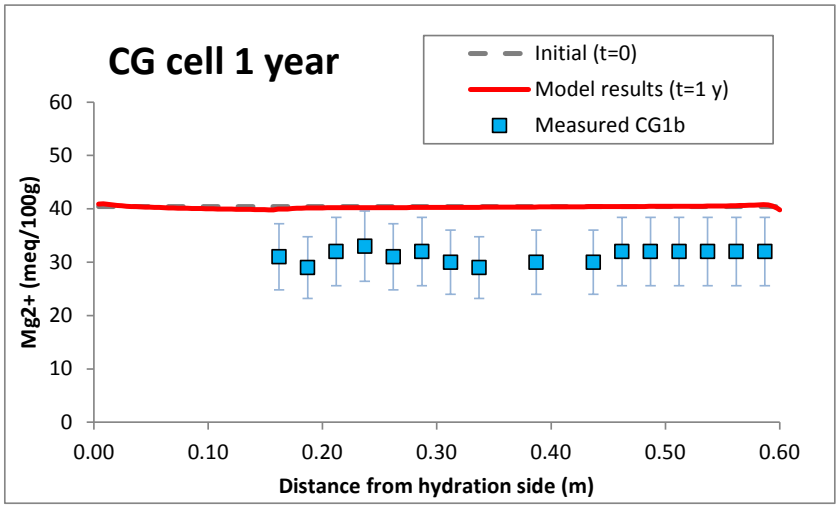

Figure 4-40. Spatial distribution of the measured (symbols) and the computed (line) concentrations of exchanged Mg^{2+} at the end of CG1b test.

4.5.2.3 CG2 and CG2b cells

The computed chloride concentrations for these tests show similar trends to those of the CG0.5, CG0.5b, CG1 and CG1b tests. Figure 4-41 shows the measured aqueous extract data and the computed concentrations of Cl^- for the CG2 and CG2b tests. The computed concentrations fit the measured Cl^- data. The fit of the measured Cl^- data of the CG2 tests is better than that of the CG2b test near the hydration side.

Figure 4-42 to Figure 4-45 show the measured and the computed concentrations of the exchanged cations Na^+, K^+, Ca^{2+} and Mg^{2+} for the CG1b test. The error bars of ±20% of measured data are also shown. In general, the computed cation concentrations are within the error bars except for Ca^{2+} and Mg^{2+}.

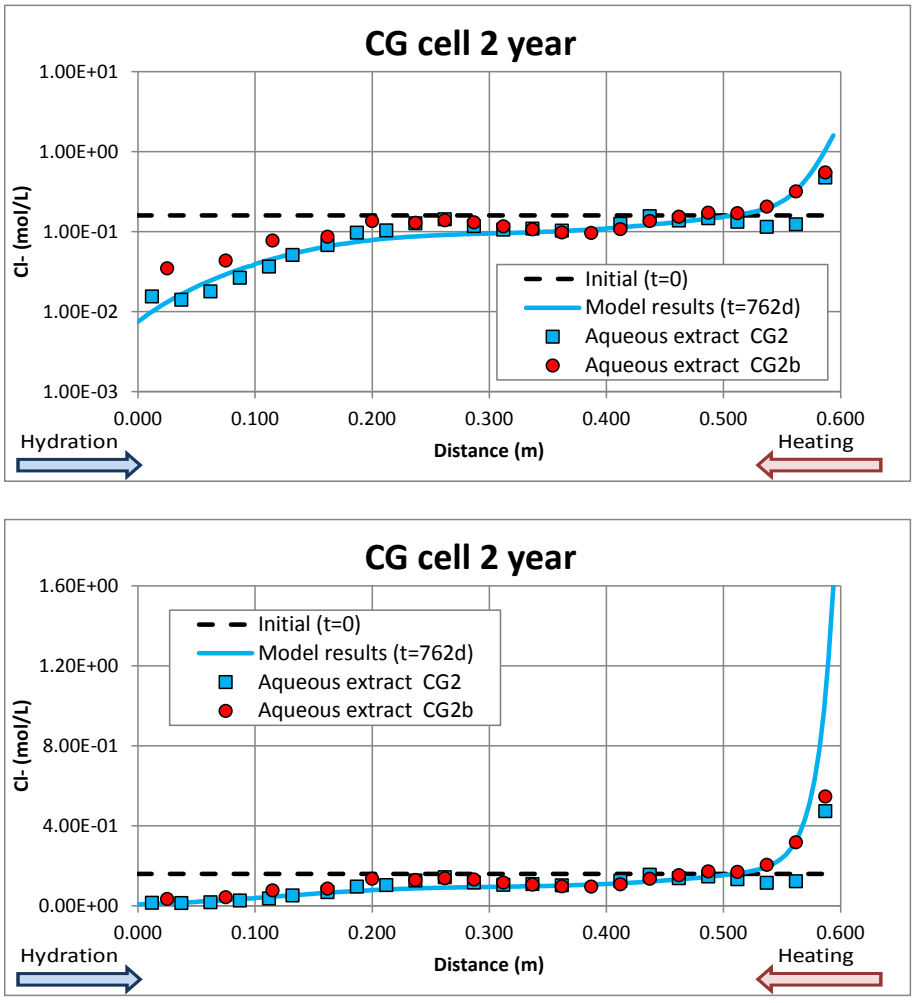

Figure 4-41. Spatial distribution of the measured (symbols) and the computed (line) Cl^- concentrations at the end of the CG2 and CG2b tests. Measured data include aqueous extract and squeezing data. Logarithmic scale (top) and natural scale (bottom).

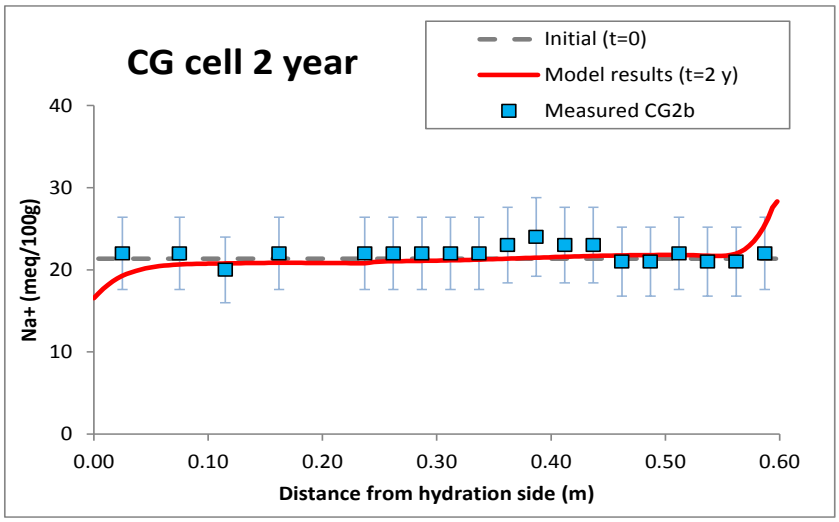

Figure 4-42. Spatial distribution of the measured (symbols) and the computed (line) concentrations of exchanged Na^+ at the end of the CG2b test.

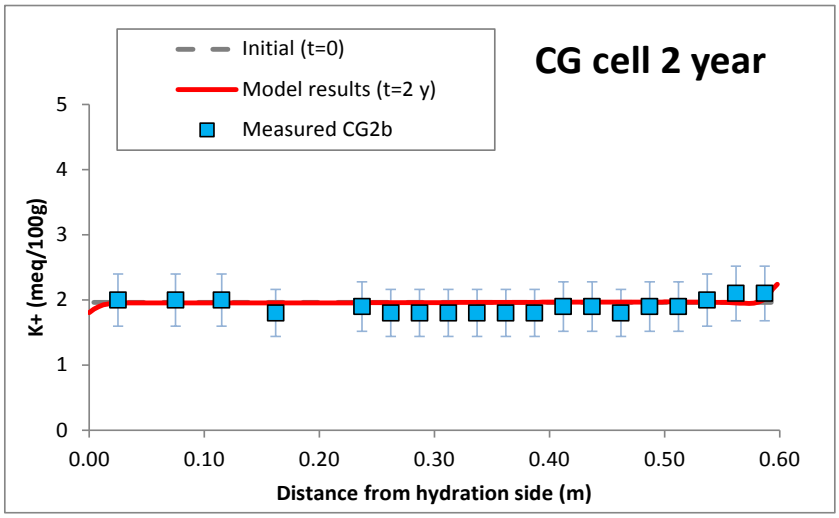

Figure 4-43. Spatial distribution of the measured (symbols) and the computed (line) concentrations of exchanged K^+ at the end of the CG2b test.

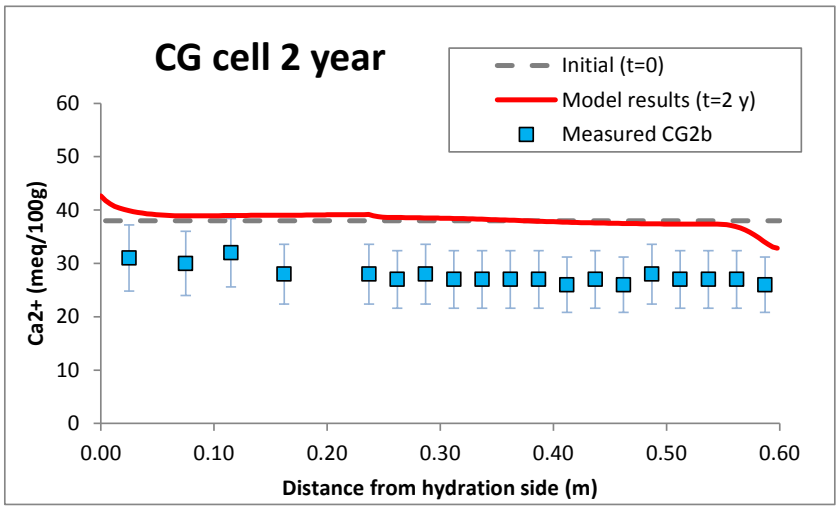

Figure 4-44. Spatial distribution of the measured (symbols) and the computed (line) concentrations of exchanged Ca^{2+} at the end of the CG2b test.

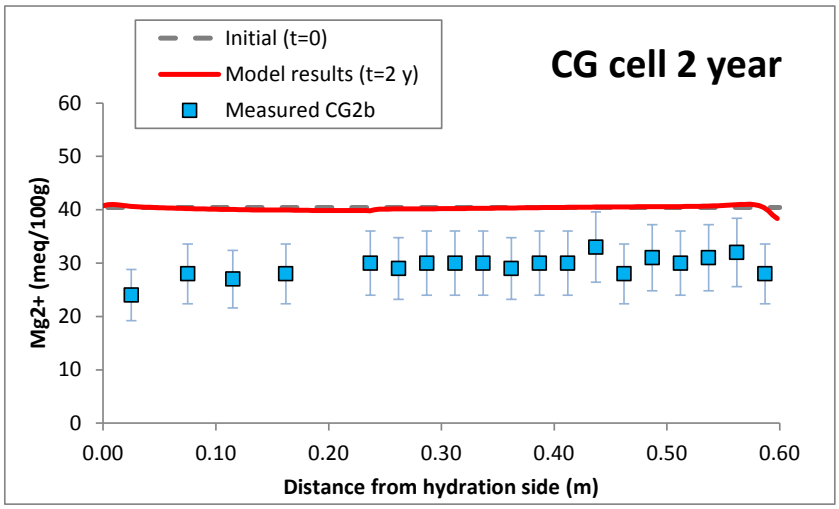

Figure 4-45. Spatial distribution of the measured (symbols) and the computed (line) concentrations of exchanged Mg^{2+} at the end of the CG2b test.

4.5.2.4 CG7.6 cell

Figure 4-46 shows the comparison the computed concentrations of Cl^- with the concentrations obtained by Ciemat with a geochemical model for the CG7.6 test. Computed Cl^- concentrations are significantly smaller than the concentrations obtained with the geochemical model which coincide with the aqueous extract corrected data. This discrepancy could be due to the model discrepancies in the cumulative water intake.

Figure 4-47 to Figure 4-50 show the comparison of the computed concentrations of dissolved Ca^{2+}, Mg^{2+}, Na^+ and K^+, with the concentrations of the Ciemat geochemical model. The Ciemat geochemical model concentrations are larger than the computed concentrations which may be affected by the too large water intake. Computed concentrations reproduce the measured values near the heater. The trend of sulphate concentrations is different because the concentrations of the geochemical model are smaller than the computed sulphate concentrations (Figure 4-51). It should be noticed that the sulphate concentration depends on the precipitation/dissolution of gypsum and anhydrite.

The concentration HCO_3^- increases in the bentonite during the test due to the dissolution of the calcite. However, it decreases near the heater due to the precipitation of calcite. Computed concentrations show a trend similar to the concentrations of the Ciemat geochemical model (Figure 4-52).

The computed pH is shown in Figure 4-53. The initial pH is 7.72 and decreases slightly at the end of the test. The results of the numerical model agree well with the pH of the Ciemat geochemical model.

Figure 4-54, Figure 4-55, Figure 4-56 and Figure 4-57 show the measured and computed concentrations of the exchanged cations. The error bars of ±10% of measured data are also shown. In general, the fit of the computed cation concentrations of Mg^{+2} and Ca^{2+} is acceptable while there are significant discrepancies for K^{+} and Na^{+}.

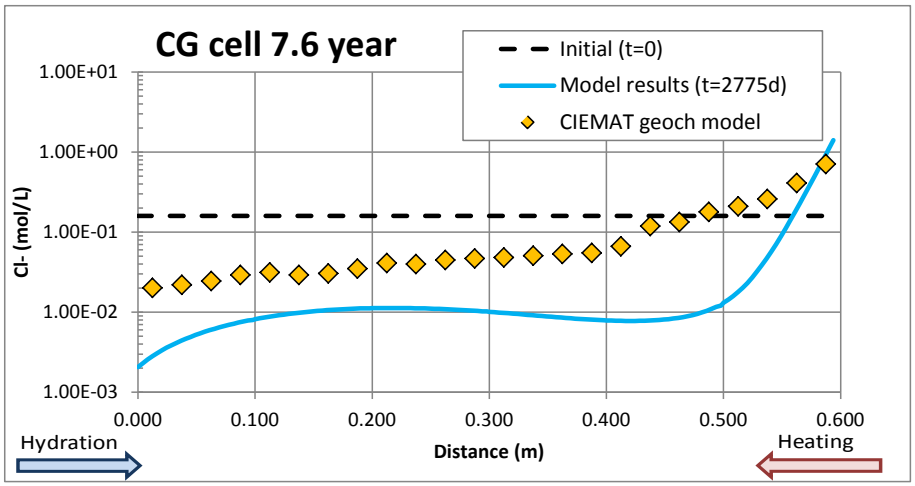

Figure 4-46. Comparison of the Cl^{-} concentrations of the Ciemat geochemical model (symbols) and the computed (line) Cl^{-} concentrations at the end of the CG7.6 test.

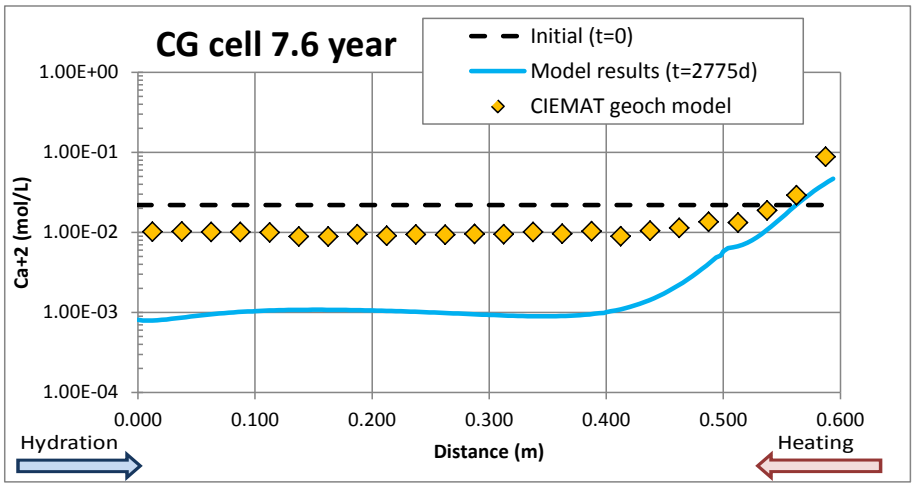

Figure 4-47. Comparison of the Ca^{2+} concentrations of the Ciemat geochemical model (symbols) and the computed (line) Ca^{2+} concentrations at the end of the CG7.6 test.

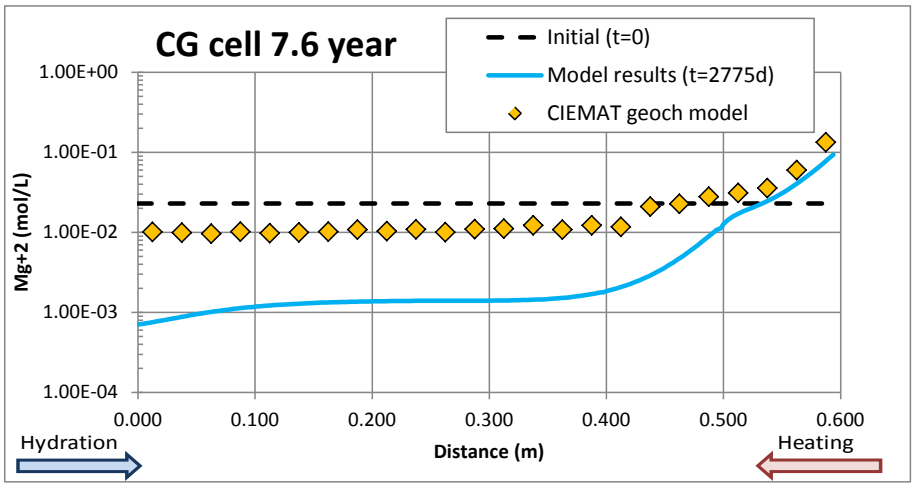

Figure 4-48. Comparison of the Mg^{2+} concentrations of the Ciemat geochemical model (symbols) and the computed (line) Mg^{2+} concentrations at the end of the CG7.6 test.

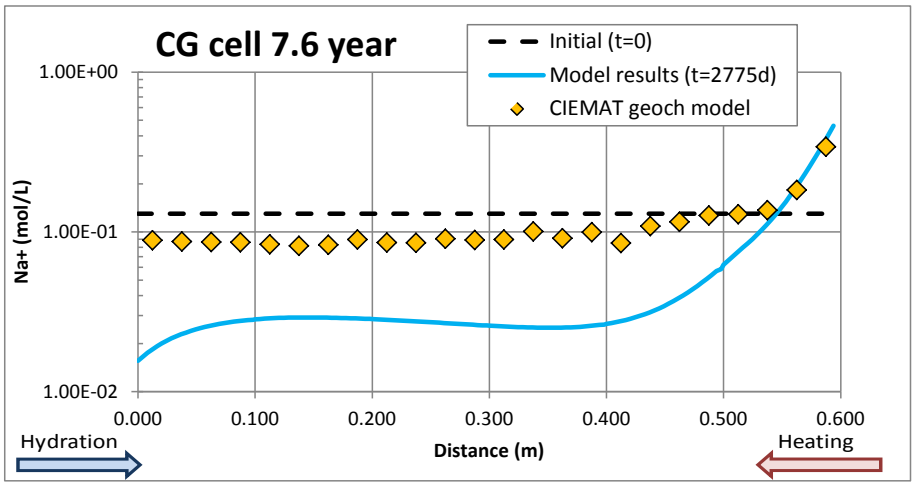

Figure 4-49. Comparison of the Na^{+} concentrations of the Ciemat geochemical model (symbols) and the computed (line) Na^{+} concentrations at the end of the CG7.6 test.

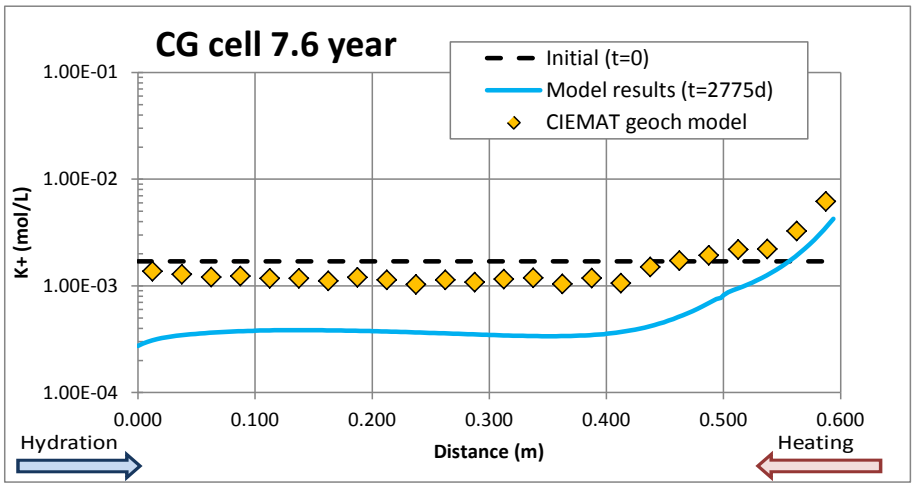

Figure 4-50. Comparison of the K^{+} concentrations of the Ciemat geochemical model (symbols) and the computed (line) K^{+} concentrations at the end of the CG7.6 test.

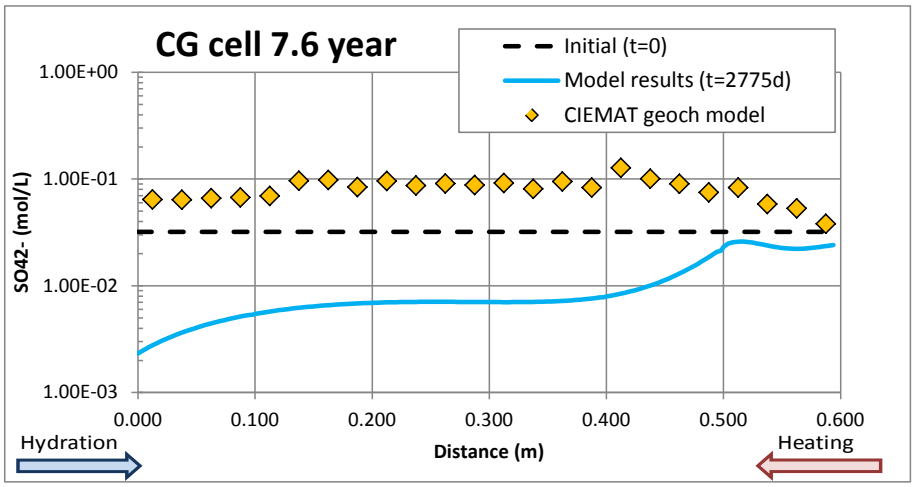

Figure 4-51. Comparison of the SO_4^{2-} concentrations of the Ciemat geochemical model (symbols) and the computed (line) SO_4^{2-} concentrations at the end of the CG7.6 test.

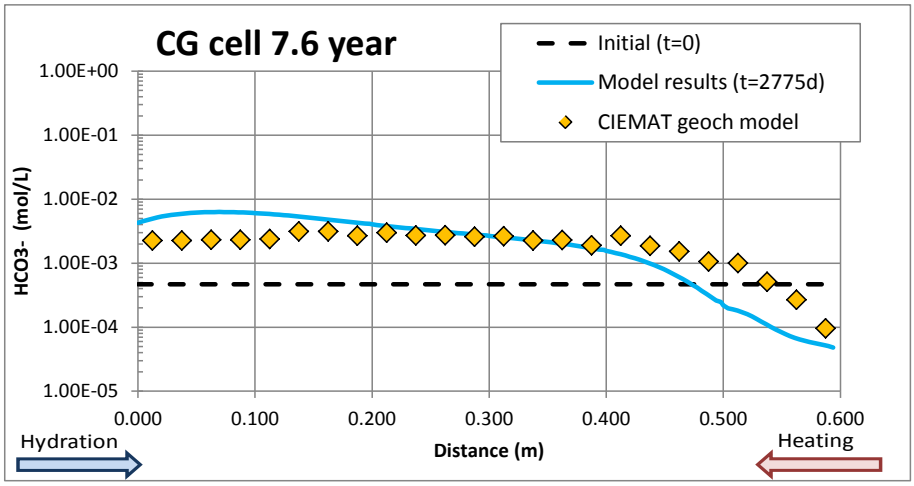

Figure 4-52. Comparison of the HCO_3^- concentrations of the Ciemat Geochemical model (symbols) and the computed (line) HCO_3^- concentrations at the end of the CG7.6 test.

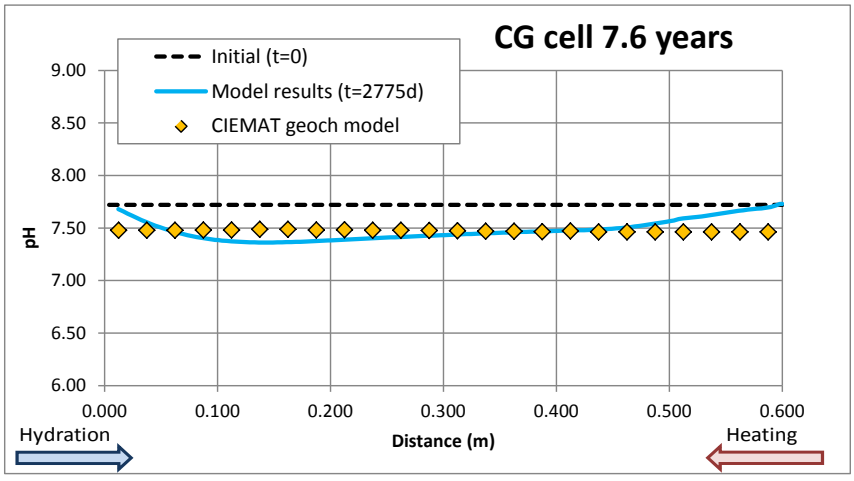

Figure 4-53. Comparison of the pH of the Ciemat geochemical model (symbols) and the computed (line) pH at the end of the CG7.6 test.

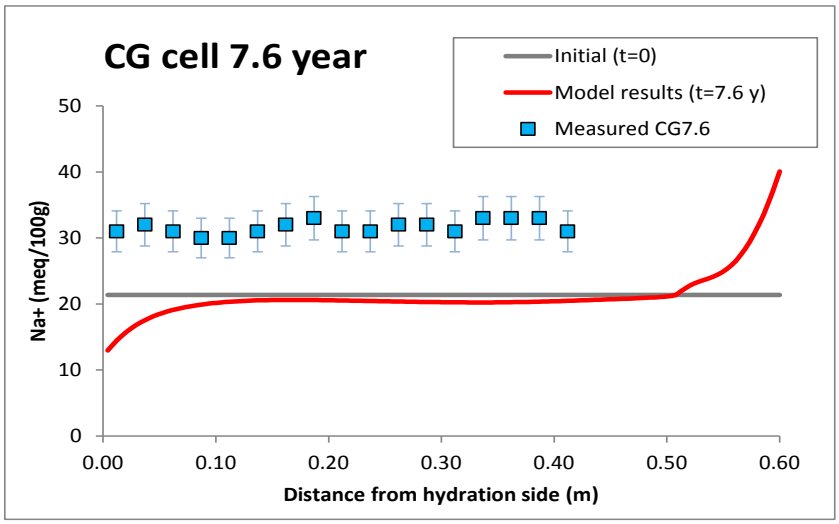

Figure 4-54. Spatial distribution of the measured (symbols) and the computed (line) concentration of exchanged Na^+ at the end of the CG7.6 test.

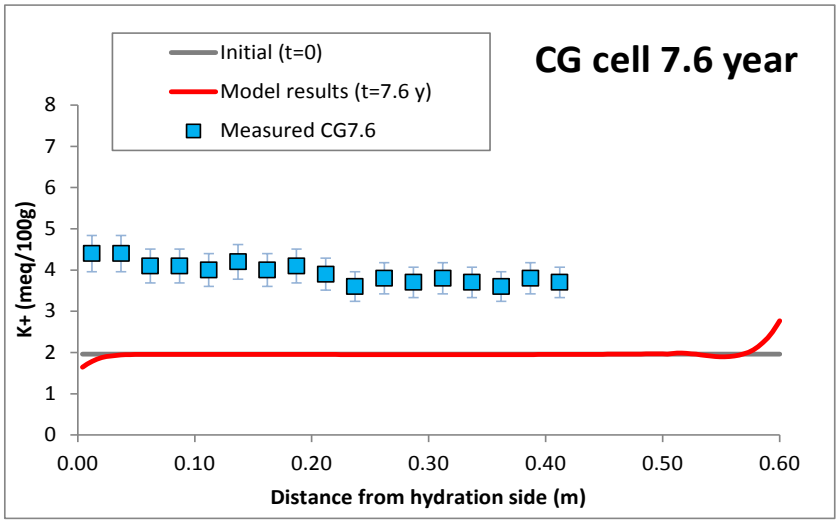

Figure 4-55. Spatial distribution of the measured (symbols) and the computed (line) concentration of exchanged K^+ at the end of the CG7.6 test.

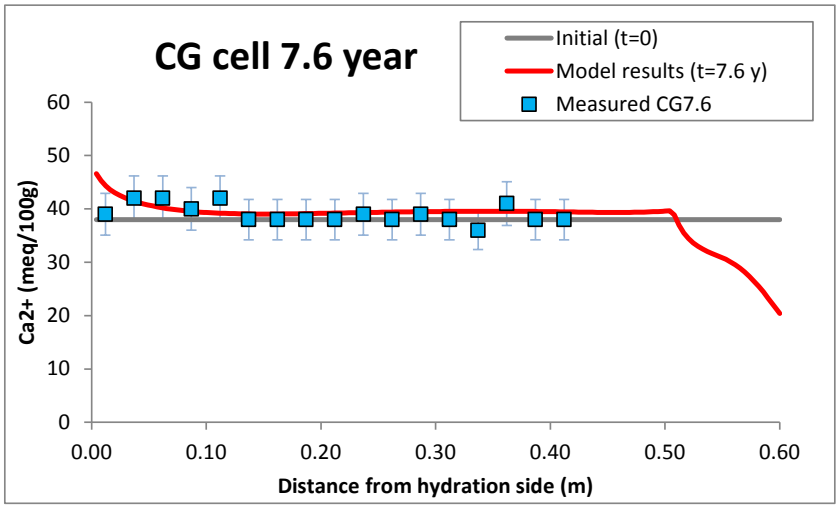

Figure 4-56. Spatial distribution of the measured (symbols) and the computed (line) concentration of exchanged for Ca^{2+} at the end of the CG7.6 test.

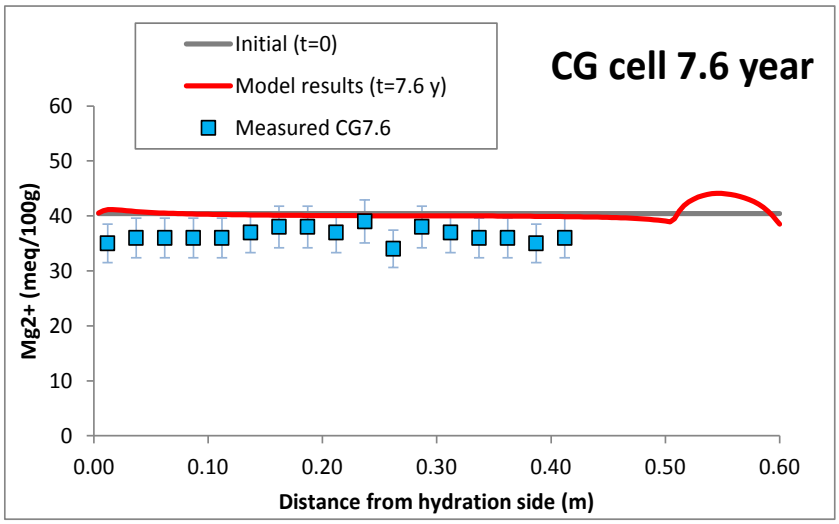

Figure 4-57. Spatial distribution of the measured (symbols) and the computed (line) concentration of exchanged Mg^{2+} at the end of the CG7.6 test.

4.5.3 Conclusions of the model testing

The testing of the THMC models with data from the CG cells show that the model captures the main trends of the measured data of the CG0.5, CG0.5b, CG1, CG1b, CG2 and CG2b tests. However, model results show some discrepancies which include:

1) The computed porosity is slightly smaller than measured data for the CG0.5, CG1, CG2 and CG7.6 tests
2) The computed gravimetric water content and saturation degree fit well the measured data except near the heater
3) The compted temperatures are larger than the measured temperatures in the sensors due to heat dissipation along the lateral surface of cells
4) The computed water intake overestimates the measured data in all the tests
5) The computed concentrations of Cl^- fit the measured aqueous extract data of the CG0.5, CG1 and CG2 tests with some discrepancies in the intermediate cells.
6) The computed concentrations of Cl^-, Ca^{2+}, Mg^{2+}, Na^+, K^+ and SO_4^{2-} are smaller than the concentrations of the Ciemat geochemical model.
7) The computed concentrations of exchanged Ca^{2+}, Na^+ and K^+ reproduce the measured data for the CG0.5 and C1 tests. The computed exchanged concentrations of Mg^{2+} are larger than measured data for the CG0.5 and C1

tests. The computed exchanged concentration of Ca^{2+} and Mg^{2+} do not reproduce the measured data for the CG7.6 cell.

The results of the model testing indicate the need to calibrate some model parameters in order to overcome these discrepancies.

4.6 Model calibration

Vapour tortuosity was the first parameter to be adjusted. It was changed from 0.3 to 0.4 for the CG0.5, CG1 and CG2 tests and from 0.3 to 0.2 for the CG7.6 test.

A Cauchy condition was used for temperatures along the lateral surface to reproduce the lateral heat loss in the cells CG0.5, CG1 and CG2. The external temperature was assumed equal to mean of the measured temperatures in the sensors. A thermal coefficient of 1000 W/ºC was used.

The selectivity coefficients were updated to match the concentrations of the exchanged cations of the FEBEX bentonite. The initial and the calibrated selectivity coefficients are listed in Table 4-3.

The previous model considered a lax deformation in the hydration nodes. This assumption leads to a large water volume in the cells, especially in the CG7.6 test. In the model calibration, the hydration point was treated in a manner similar to other bentonite points.

Table 4-3. Selectivity coefficients for cation exchange reactions for the model of the CG tests.

Cation	Initial selectivity coefficient	Calibrated selectivity coefficient
Ca^{2+}	0.292	0.333
Mg^{2+}	0.281	0.373
Na^{+}	1.000	1.000
K^{+}	0.138	0.146

4.6.1 Thermo-hydro-mechanical results of CG cells after model calibration

4.6.1.1 CG0.5 and CG0.5b cells

Figure 4-58 shows the spatial distribution of the computed porosity after 188 days of heating and after the cooling phase. for the CG0.5 and CG0.5b tests after model calibration. Numerical results reproduce the measured porosities. Near the

hydration boundary the porosity is larger than the initial value due to bentonite swelling. Near the heater, the porosity is smaller than the initial value. Post mortem analyses show that the diameter of the saturated bentonite sample increased and the bentonite cell deformed (Villar et al., 2008a).

The computed gravimetric water content and saturation degree and fit to the measured data are shown Figure 4-59 and Figure 4-60. Computed values fit well the measured data.

Figure 4-61 shows the measured and computed total cumulative water intake. The numerical results reproduce the measured water intake of the CG0.5 cell.

The prescribed temperature of the heater was decreased from 100ºC to 90ºC in order to reproduce the observed temperatures at the sensors and the measured concentration of the Cl^- near the heater which depends on the evaporation rate. The computed temperatures and the mean temperatures measured at the thermocouple sensors are plotted in Figure 4-62.

The simulation of the temperature was performed with the average conditions of the external temperature which changes seasonally. Figure 4-63 shows the fluctuations of the temperatures measured in the sensors and the computed mean temperatures at the sensors.

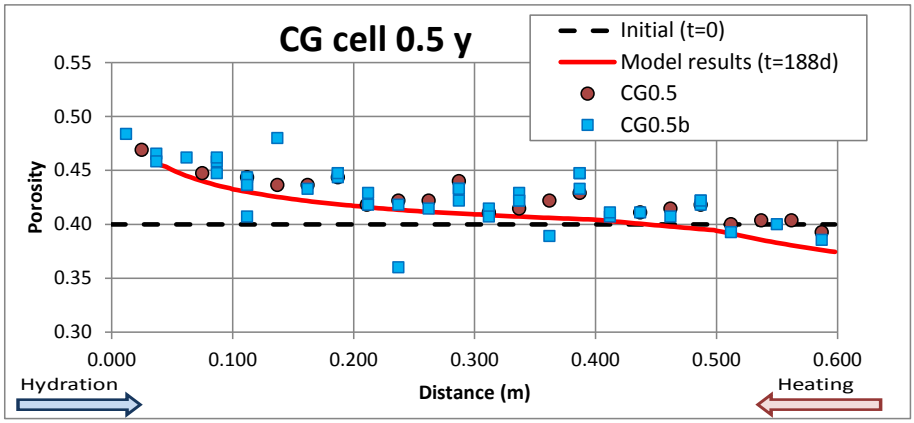

Figure 4-58. Spatial distribution of the measured (symbols) and the computed (line) porosity at the end of the CG0.5 and CG0.5b tests after model calibration.

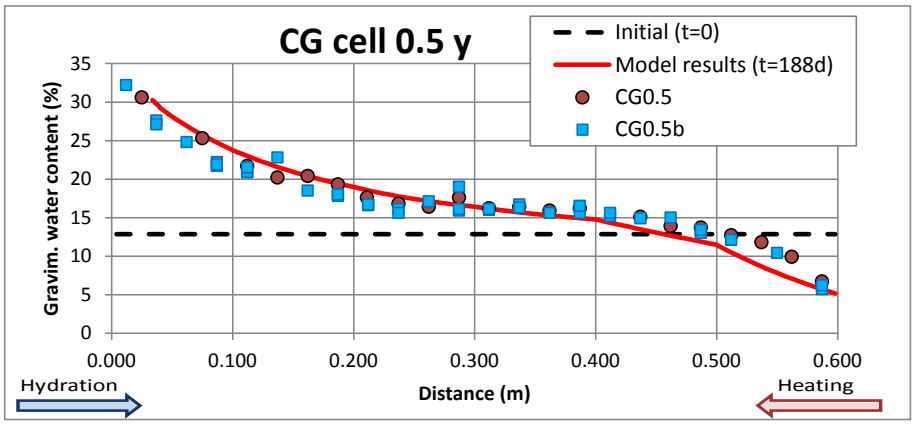

Figure 4-59. Spatial distribution of the measured (symbols) and computed (line) gravimetric water content at the end of the CG0.5 and CG0.5b tests after model calibration.

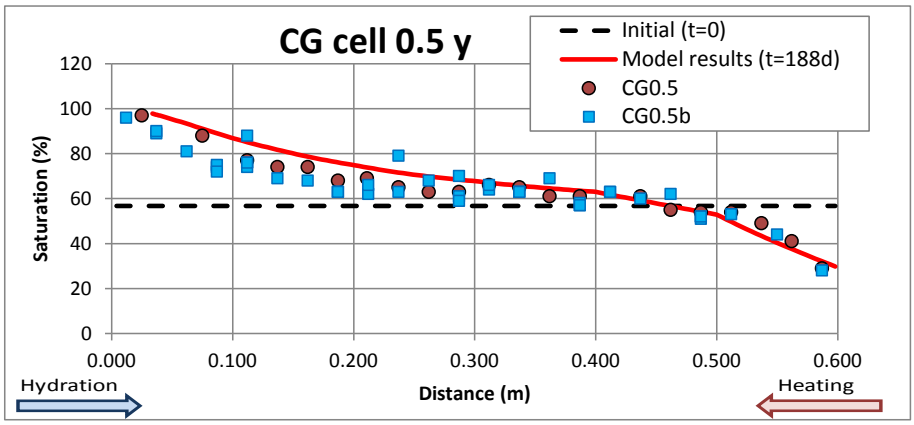

Figure 4-60. Spatial distribution of the measured (symbols) and the computed (line) saturation degree at the end of the CG0.5 and CG0.5b tests after model calibration.

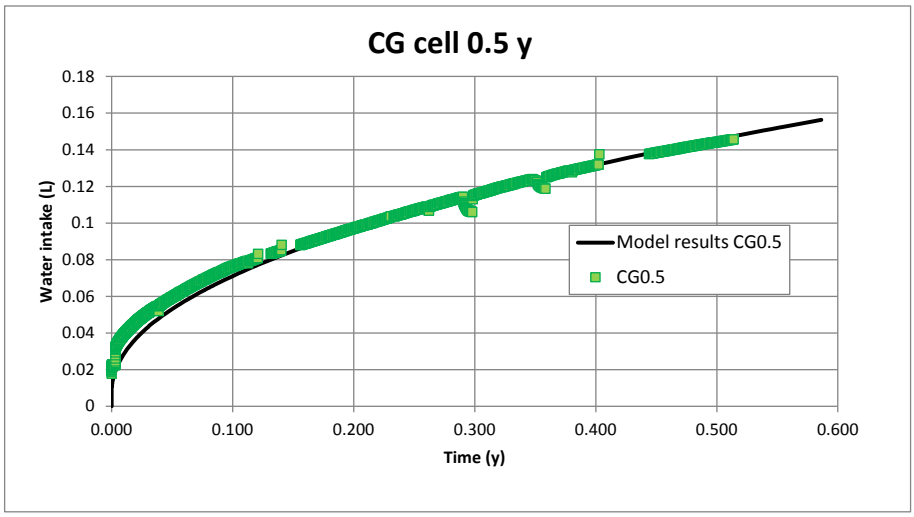

Figure 4-61. Time evolution of the measured (symbols) and computed (line) cumulative water intake for the CG0.5 and CG0.5b tests after model calibration.

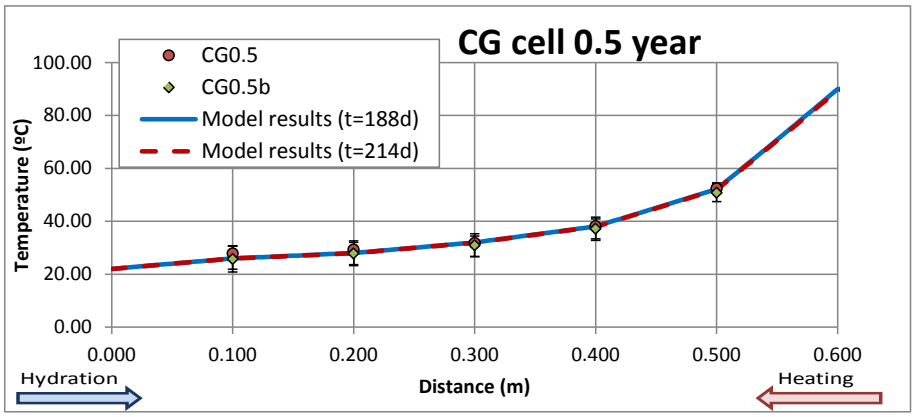

Figure 4-62. Spatial distribution of the mean measured (symbols) and computed (lines) temperatures at the end of the CG0.5 and CG0.5b tests after the calibration of the heat released at the lateral surface of the cells.

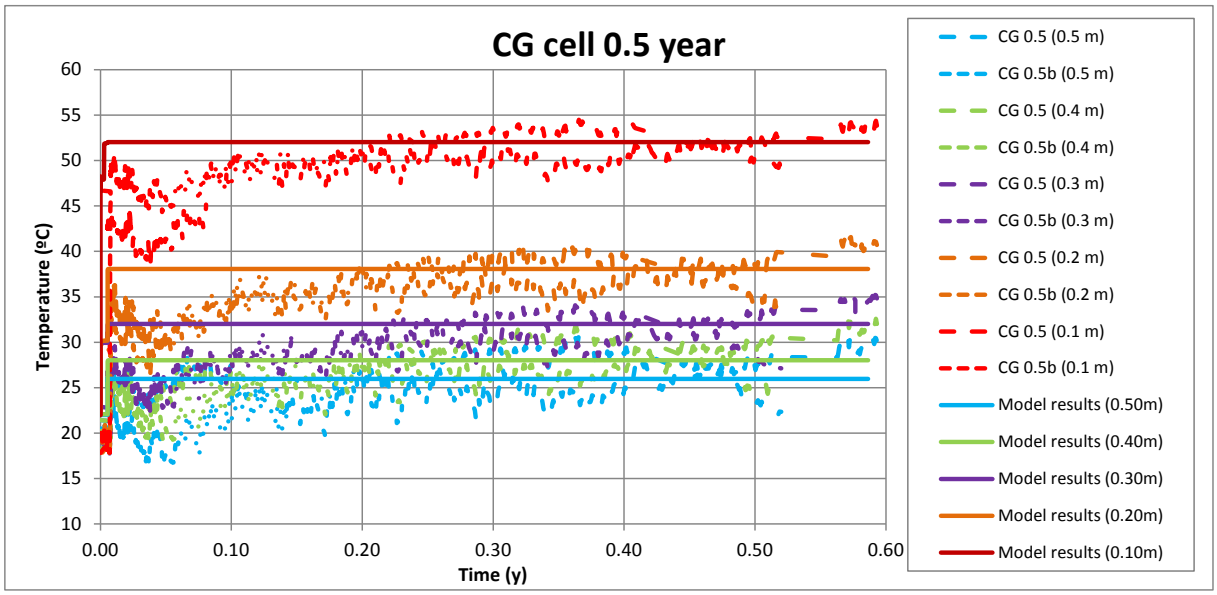

Figure 4-63. Time evolution of the measured (discontinuous lines) and computed (continuous lines) temperatures at the sensors located at x = 0.1, 0.2, 0.3, 0.4 and 0.5 m from the heaters of the CG0.5 and CG0.5b tests after the calibration of the heat released at the lateral surface.

4.6.1.2 CG1 and CG1b cells

After model calibration the computed gravimetric water content and water saturation degree reproduce the measured data better than those of the model before calibration especially near the heater (compare Figure 4-65 and Figure 4-66 to Figure 4-18 and Figure 4-19).

Figure 4-67 shows the computed cumulative water intake for the CG0.5 and CG1 tests and the measured data for the CG0.5 and CG0.5b tests. The computed water intake follows the same trend as that of the CG0.5 cell.

Figure 4-68 shows the spatial distribution of mean temperatures in the sensors of the CG1 cell as well as the maximum and minimum measured temperatures. The computed temperatures reproduce the measured temperatures in the sensors. Figure 4-69 shows the measured temperature in the sensors and the computed temperature. Computed temperature fits the mean temperature of the sensors during the tests.

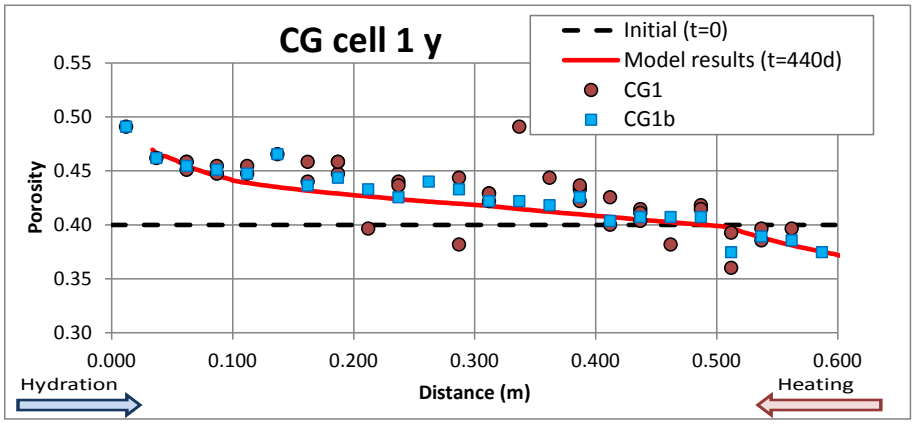

Figure 4-64. Spatial distribution of the measured (symbols) and the computed (line) porosity at the end of the CG1 and CG1b tests after model calibration.

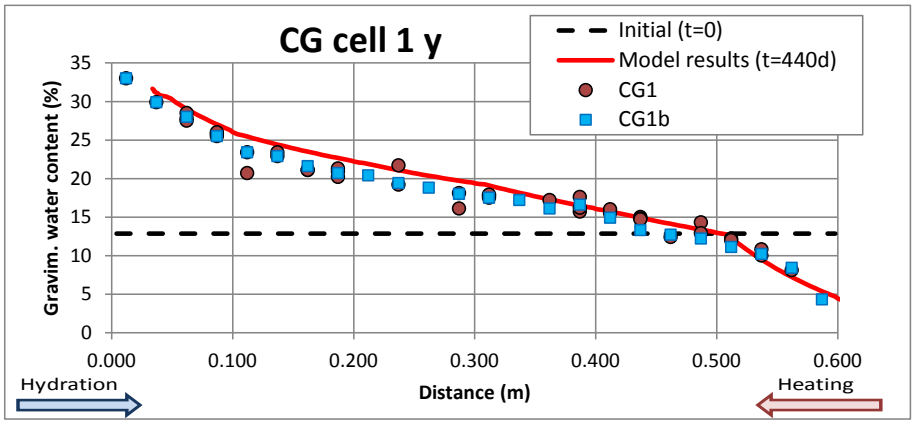

Figure 4-65. Spatial distribution of measured (symbols) and computed (line) gravimetric water content at the end of the CG1 and CG1b tests after model calibration.

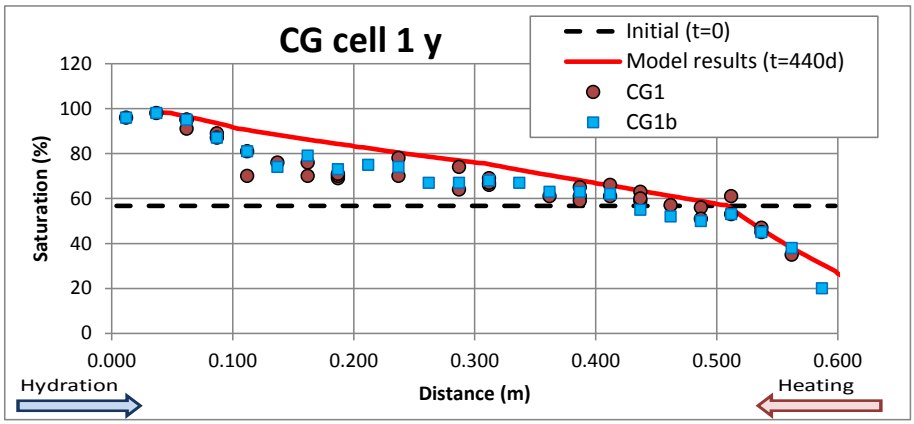

Figure 4-66. Spatial distribution of the measured (symbols) and the computed (line) saturation degree at the end of the CG1 and CG1b tests after model calibration.

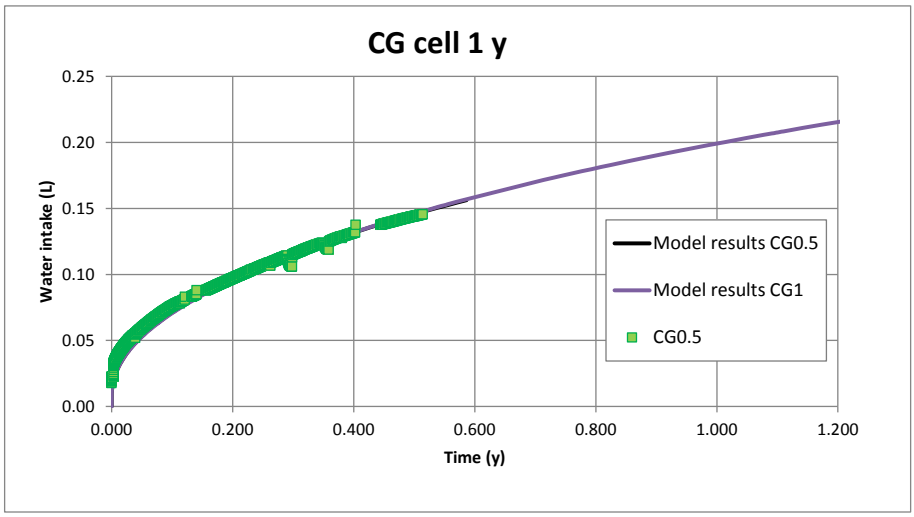

Figure 4-67. Time evolution of the measured (symbols) cumulative water intake for the CG0.5 test and computed (lines) water intake for the CG0.5, CG1 and CG1b tests after model calibration.

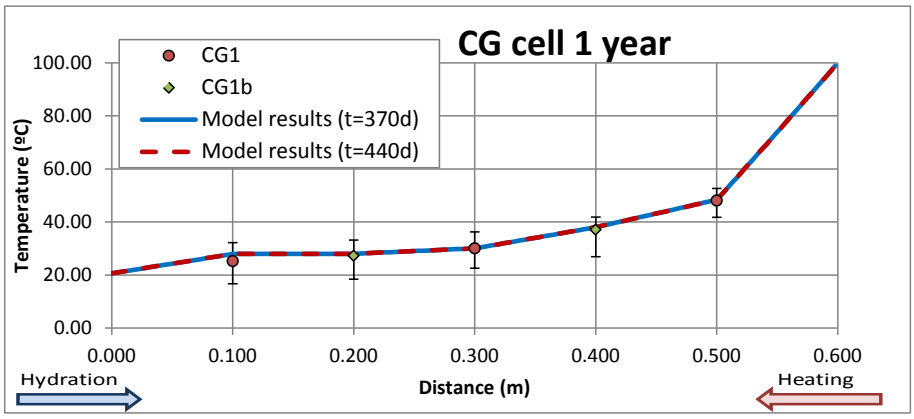

Figure 4-68. Spatial distribution of the mean measured (symbols) and computed (lines) temperatures at the end of the CG1 and CG1b tests after the calibration of the heat released at the lateral surface of the cells.

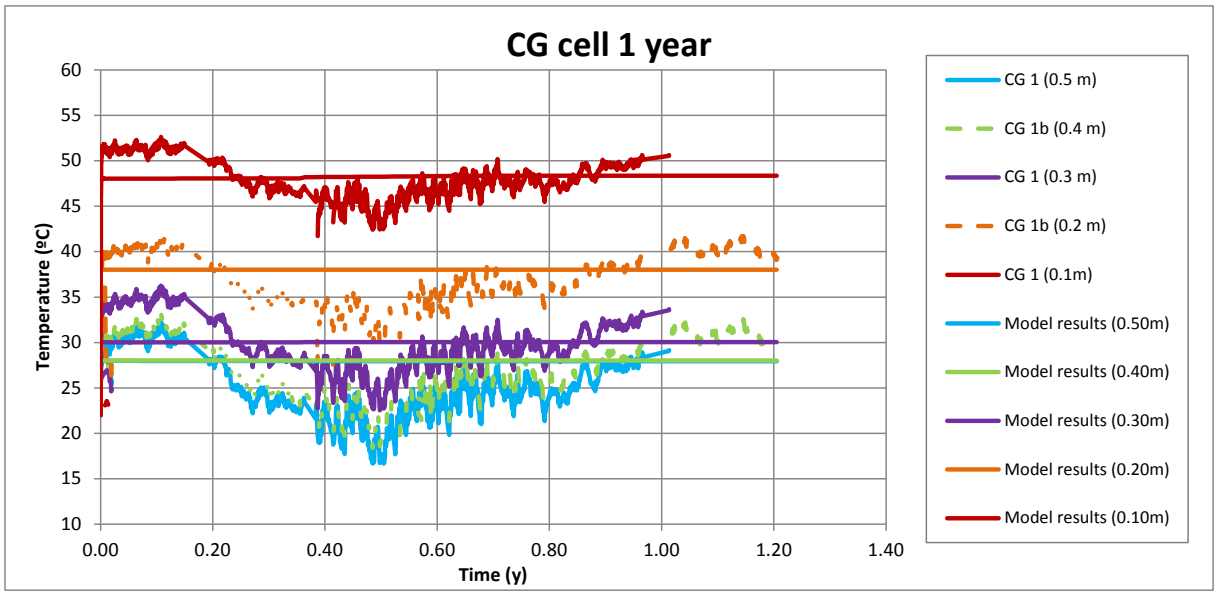

Figure 4-69. Time evolution of the measured (discontinuous lines) and computed (continuous lines) temperatures at the sensors located at x = 0.1, 0.2, 0.3, 0.4 and 0.5 m from the heaters for CG1 and CG1b tests after the calibration of the heat released at the lateral surface.

4.6.1.3 CG2 and CG2b cells

The computed porosity is slightly smaller than the measured data for the CG2 test (Figure 4-70). The computed porosity after model calibration does not improve the porosity results.

The computed gravimetric water content reproduces the measured data (Figure 4-71). The differences between the computed values before and after model calibration are largest near the heater where the computed gravimetric water content reproduces the measured data.

The computed saturation is slightly larger than measured data (Figure 4-72).

Figure 4-73 shows the computed cumulative water intake for the CG0.5, CG1 and CG2 tests and measured data for the CG0.5, CG0.5b and CG2b tests. The computed water intake reproduces the measured water intake data and the final cumulative volume.

The computed spatial distribution of the temperatures reproduces the mean temperatures measured at the sensors (Figure 4-74 and Figure 4-75).

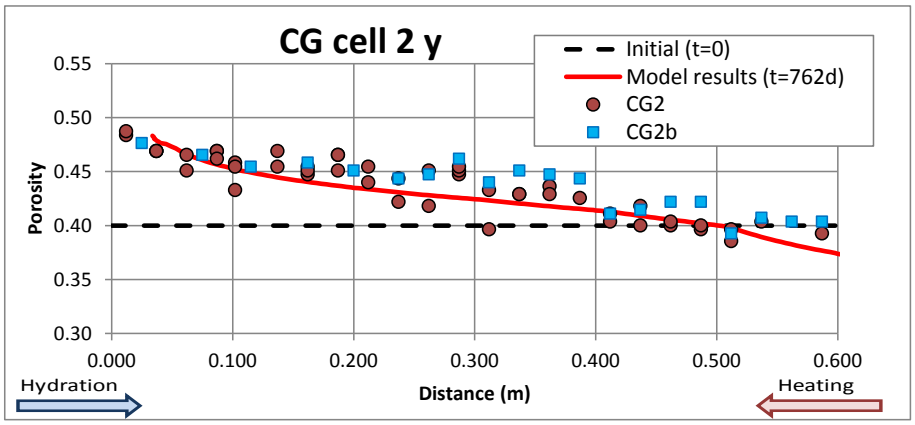

Figure 4-70. Spatial distribution of the measured (symbols) and the computed (line) porosity at the end of the CG2 and CG2b tests after model calibration.

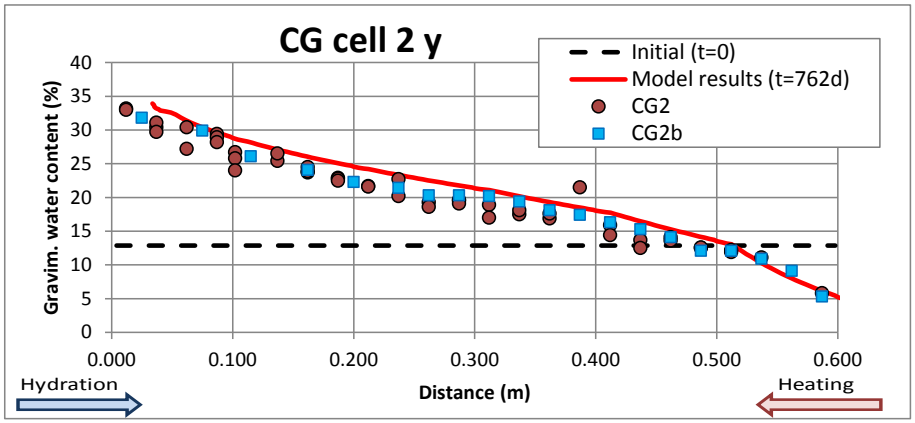

Figure 4-71. Spatial distribution of the measured (symbols) and the computed (line) gravimetric water content at the end of the CG2 and CG2b tests after model calibration.

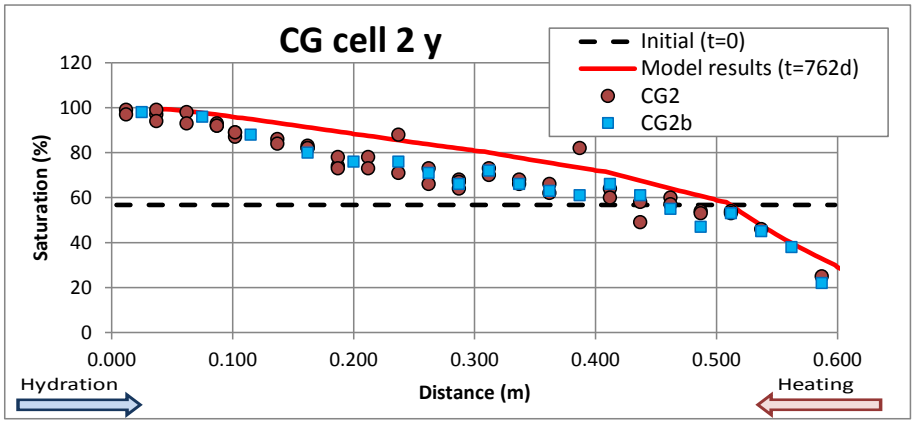

Figure 4-72. Spatial distribution of the measured (symbols) and the computed (line) saturation degree at the end of the CG2 and CG2b tests after model calibration.

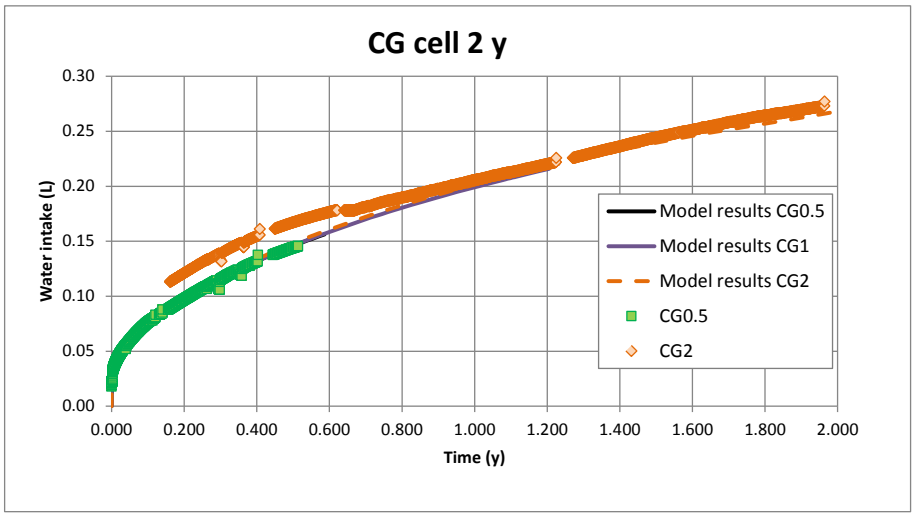

Figure 4-73. Time evolution of the measured water intake (symbols) for the CG0.5 and CG2 tests and computed water intake (lines) for the CG0.5, CG1 and CG2 tests after model calibration.

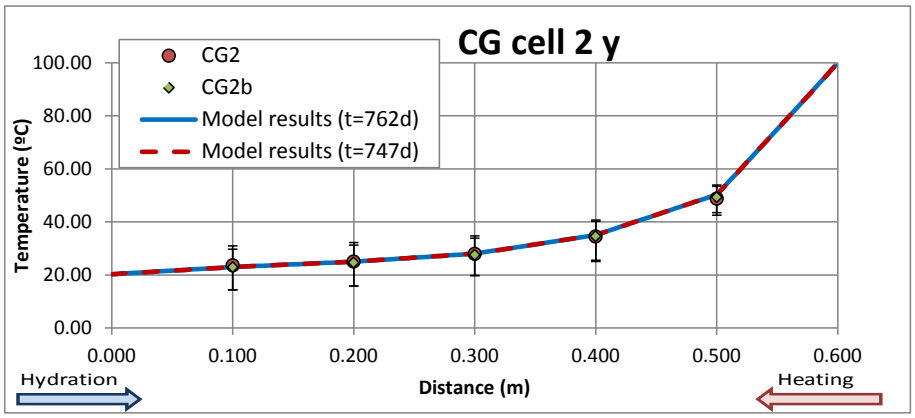

Figure 4-74. Spatial distribution of the mean measured (symbols) and the computed (lines) temperatures at the end of the CG2 and CG2b tests after the calibration of the heat released at the lateral surface.

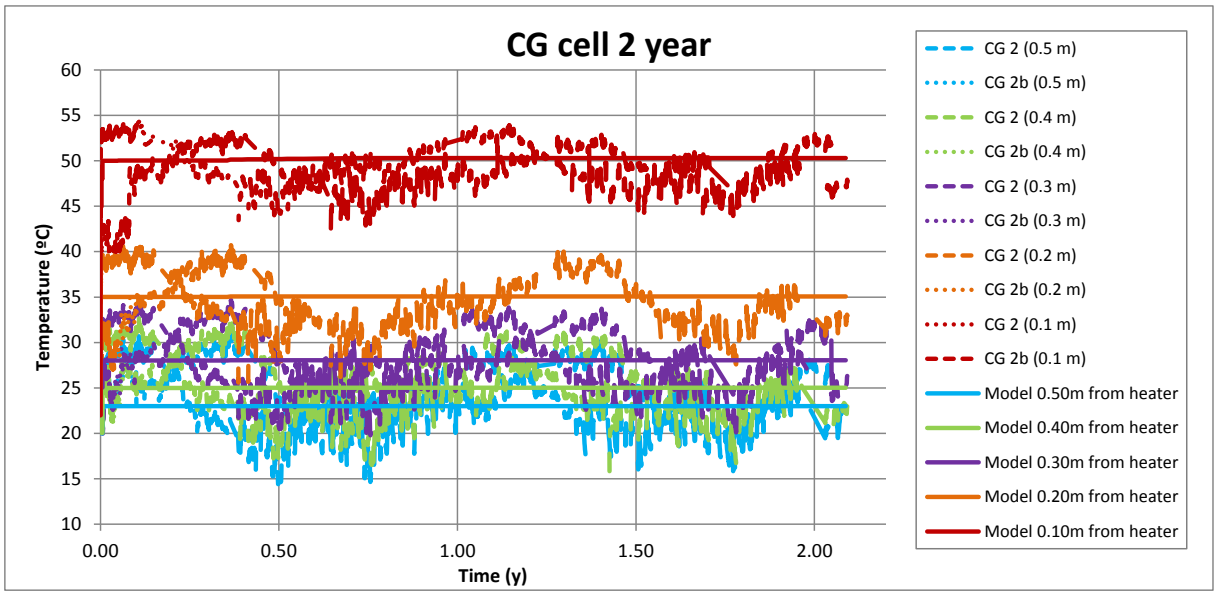

Figure 4-75. Time evolution of the measured (discontinuous lines) and computed (continuous lines) temperatures at the sensors located at x = 0.1, 0.2, 0.3, 0.4 and 0.5 m from the heaters for CG2 and CG2b tests after the calibration of the heat released at the lateral surface.

4.6.1.4 CG7.6 cell

The model calibration improves the computed porosity in the intermediate zone of the bentonite sample (Figure 4-76).

The computed gravimetric water content and water saturation degree reproduce the measured data (Figure 4-77 and Figure 4-78).

Figure 4-79 shows the computed cumulative water intake for the CG0.5, CG1, CG2 and CG7.6 cells. The computed cumulative water intake reproduces the measured water intake better than the previous model.

Temperature reaches 100ºC in the heater and 25ºC in the hydration side (Figure 4-80). Given the lack of temperature data in this test, the temperatures at intermediate points were taken from those measured in the sensors of the CG 2 cell.

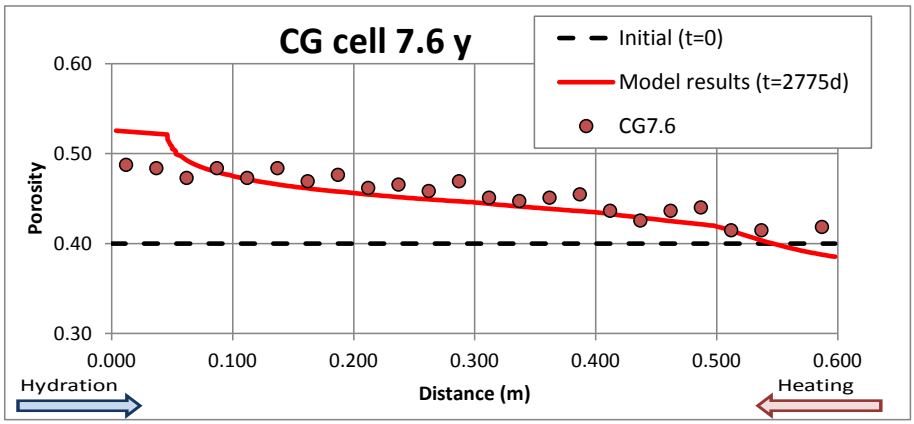

Figure 4-76. Spatial distribution of the measured (symbols) and the computed (line) porosity at the end of the CG7.6 test after model calibration.

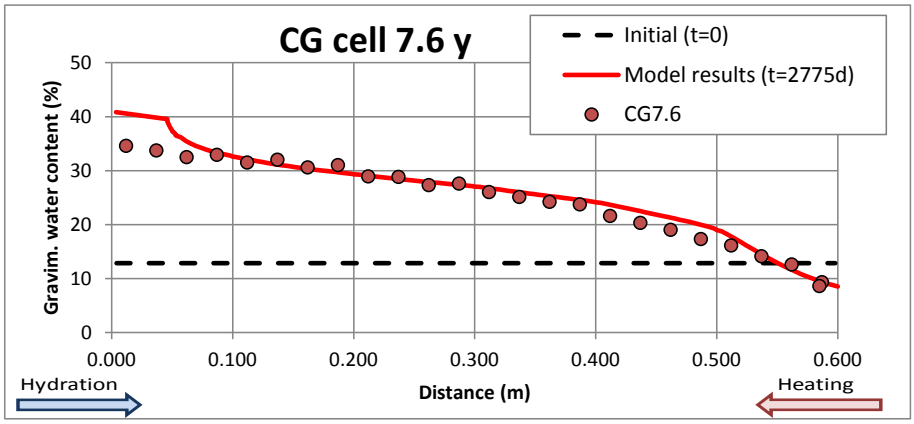

Figure 4-77. Spatial distribution of the measured (symbols) and the computed (line) gravimetric water content at the end of the CG7.6 test after model calibration.

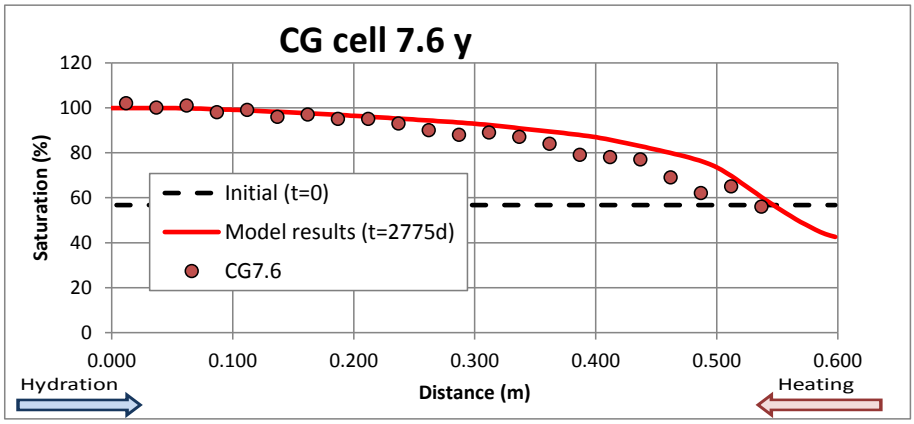

Figure 4-78. Spatial distribution of the measured (symbols) and the computed (line) saturation degree at the end of the CG7.6 test after model calibration.

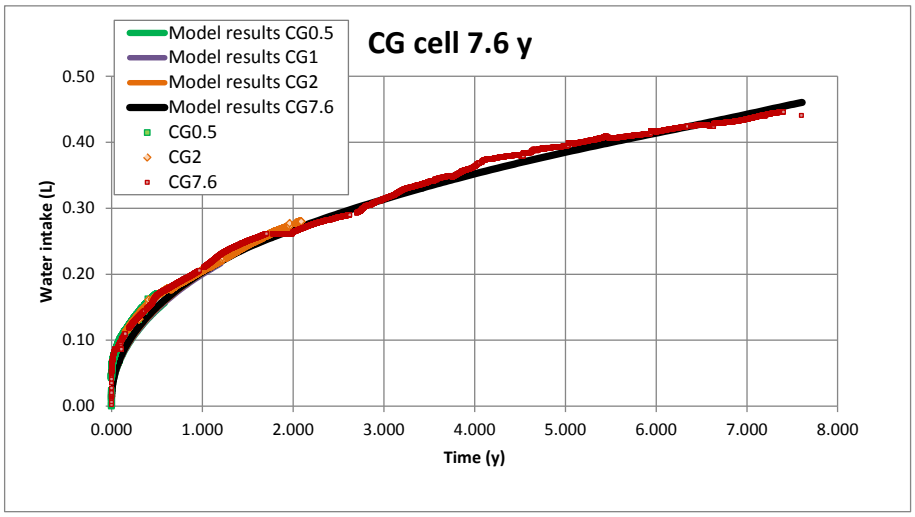

Figure 4-79. Time evolution of the measured water intake (symbols) for the CG0.5, CG2 and CG7.6 tests and computed cumulative water intake (lines) for the CG0.5, CG1, CG2 and CG7.6 tests.

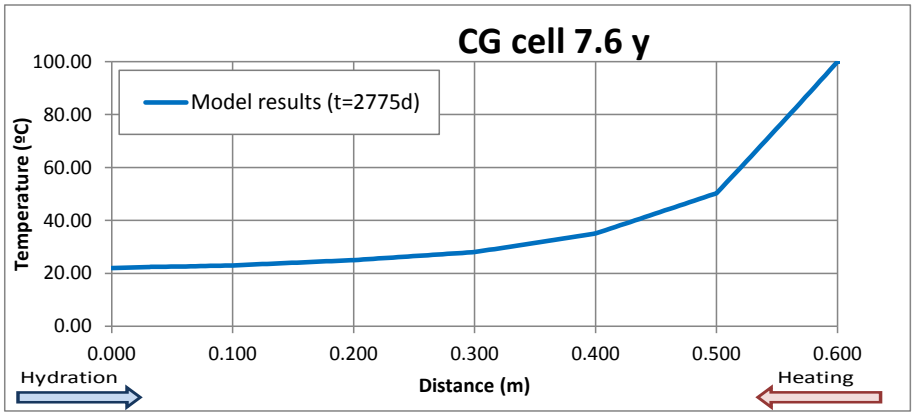

Figure 4-80. Spatial distribution of the computed temperature at the end of the CG7.6 test after model calibration.

4.6.2 Chemical results of the CG cells

4.6.2.1 CG0.5 and CG0.5b cell

The computed concentration of dissolved Cl^- reproduces the measured data (Figure 4-81). The calibrated model reproduces the Cl^- concentration data near the heater better than the previous model (Figure 4-31). However, the model underpredicts the measured data near the hydration boundary.

Figure 4-82 to Figure 4-85 show the computed and measured concentrations of exchanged cations. For the most part computed exchanged cations are within the error bands of measured data.

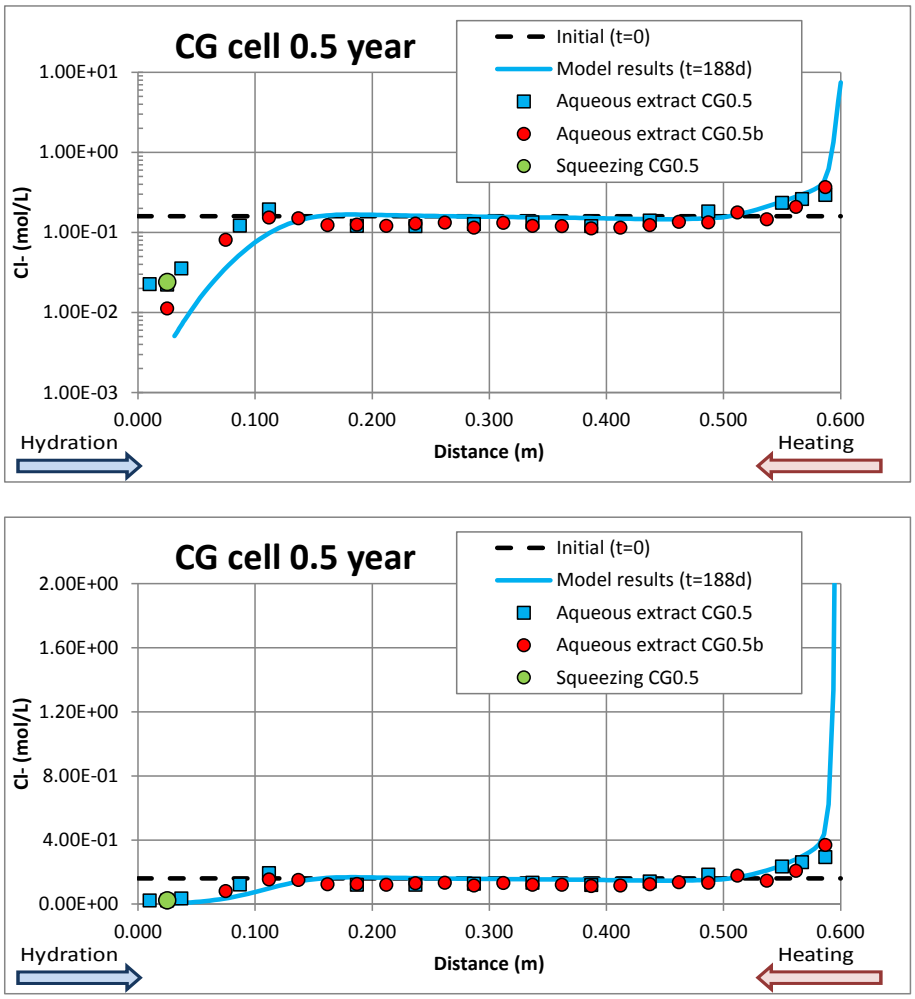

Figure 4-81. Spatial distribution of the measured (symbols) and the computed (line) Cl^- concentrations at the end of the CG0.5 and CG0.5b tests after model calibration. Measured data include aqueous extract and squeezing data. Logarithmic scale (top) and natural scale (bottom).

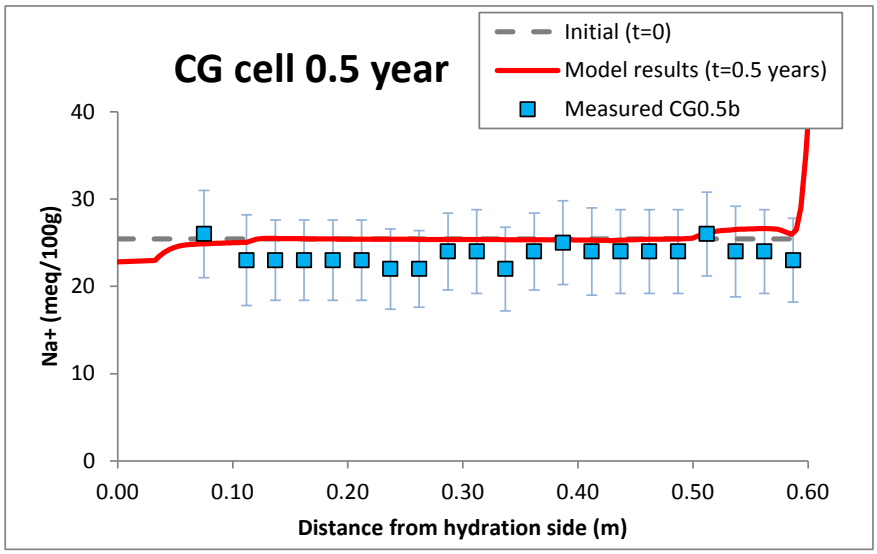

Figure 4-82. Spatial distribution of the measured (symbols) and the computed (line) concentration of exchanged Na^+ at the end of the CG0.5b test after model calibration.

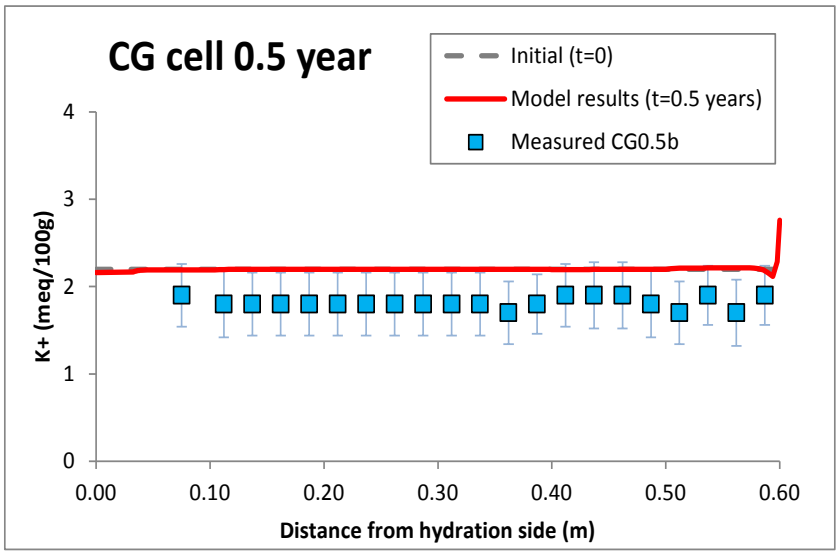

Figure 4-83. Spatial distribution of the measured (symbols) and the computed (line) concentration of exchanged K^+ at the end of the CG0.5b test after model calibration.

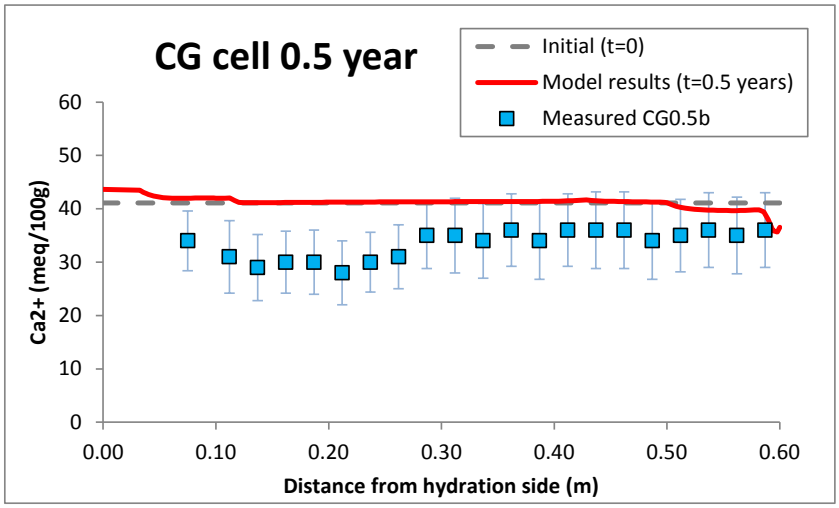

Figure 4-84. Spatial distribution of the measured (symbols) and the computed (line) concentration of exchanged Ca^{2+} at the end of the CG0.5b test after model calibration.

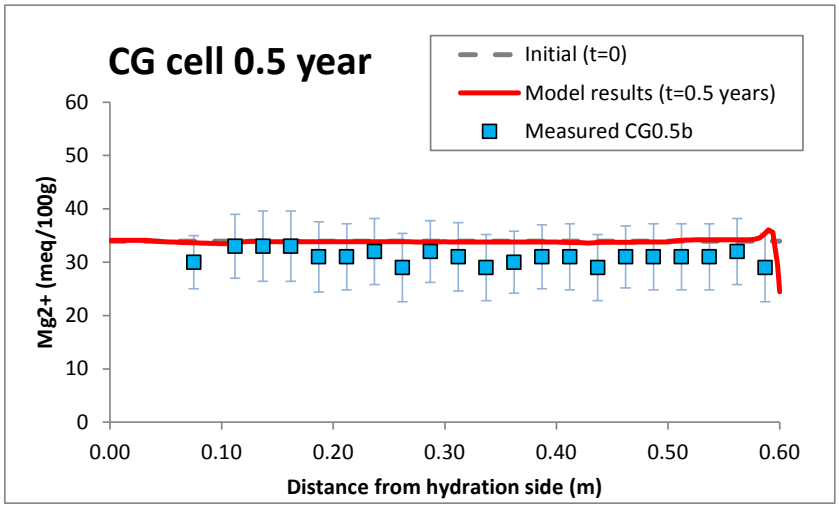

Figure 4-85. Spatial distribution of the measured (symbols) and the computed (line) concentration of exchanged Mg^{2+} at the end of the CG0.5b test after model calibration.

4.6.2.2 CG1 and CG1b cells

Figure 4-86 shows the computed concentrations of dissolved Cl^- as well as the measured aqueous extract and squeezing Cl^- data and for the CG1 and CG1b tests. Computed results fit the Cl^- measured data, especially near the heater. However, the computed concentrations are smaller than the measured values near the hydration side.

Figure 4-87 to Figure 4-90 show the measured and computed concentration of the exchanged cations Na^+, K^+, Ca^{2+} and Mg^{2+} for the CG1 and CG1b tests. In general, the computed concentrations reproduce the measured data.

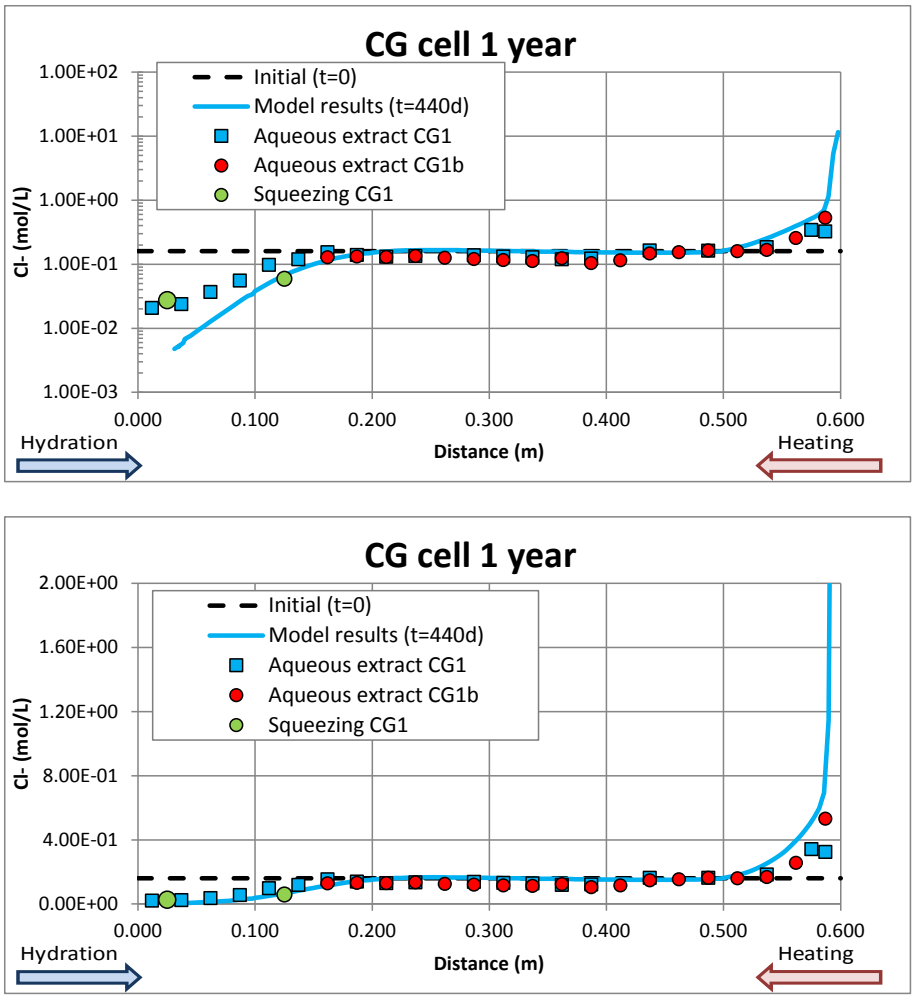

Figure 4-86. Spatial distribution of the measured (symbols) and the computed (line) Cl^- concentrations at the end of the CG1 and CG1b tests after model calibration. Measured data include aqueous extract and squeezing data. Logarithmic scale (top) and natural scale (bottom).

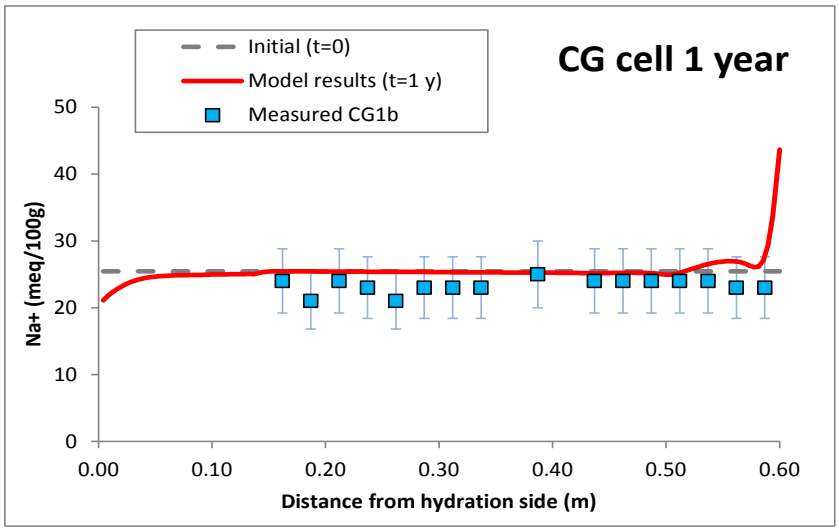

Figure 4-87. Spatial distribution of the measured (symbols) and the computed (line) concentration of exchanged Na^+ at the end of the CG1b test after model calibration.

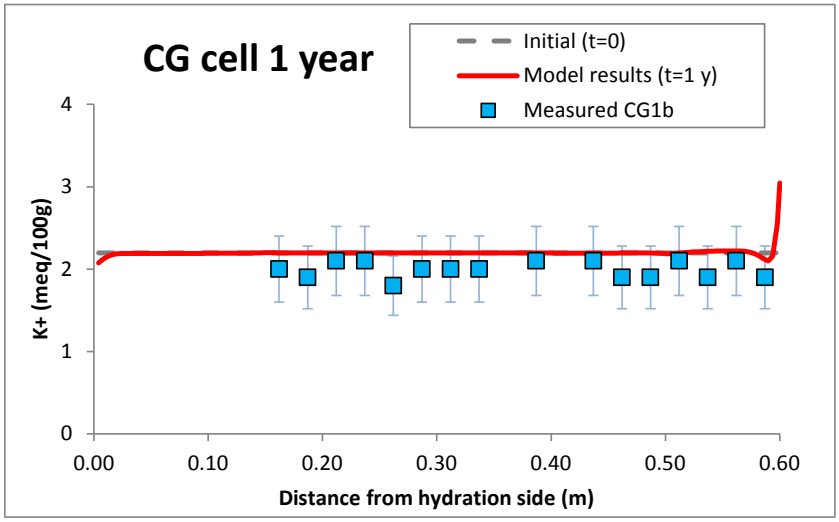

Figure 4-88. Spatial distribution of the measured (symbols) and the computed (line) concentration of exchanged K^+ at the end of the CG1b test after model calibration.

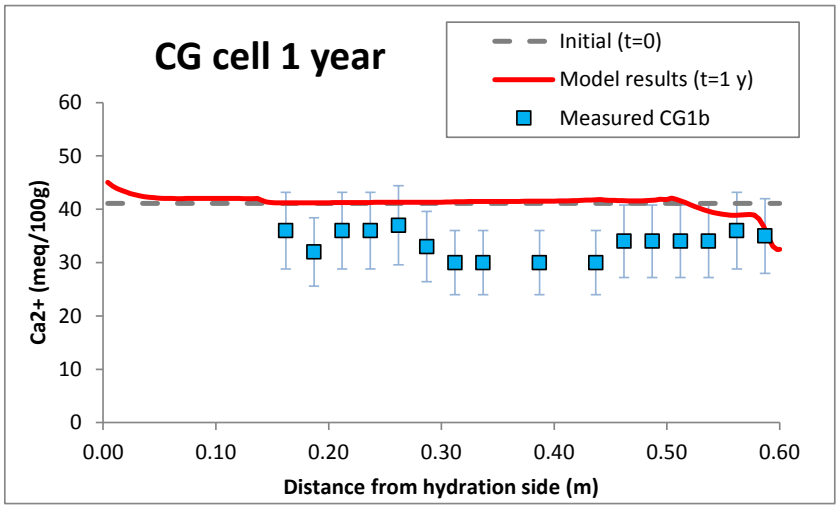

Figure 4-89. Spatial distribution of the measured (symbols) and the computed (line) concentration of exchanged Ca^{2+} at the end of the CG1b test after model calibration.

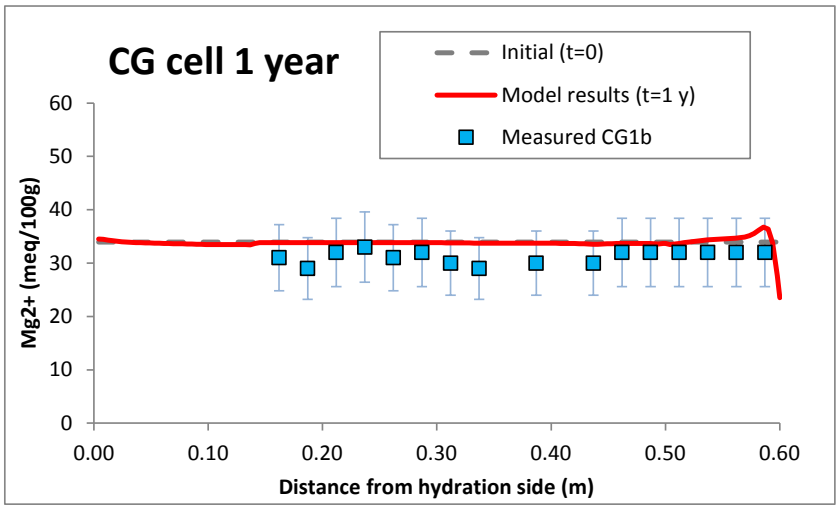

Figure 4-90. Spatial distribution of the measured (symbols) and the computed (line) concentration of exchanged Mg2+ at the end of the CG1b test after model calibration.

4.6.2.3 CG2 and CG2b cells

Figure 4-91 shows the computed concentration of Cl^- for the CG2 and CG2b tests together with the aqueous extract measured data. The computed values reproduce the measured data near the hydration boundary. Computed results are slightly higher than measured data near the heater. The computed concentrations fit the measured data of the CG2b test better than those of the CG2 test.

The computed concentrations of the exchanged cations reproduce the measured data for Na^+, K^+ and Mg^{2+} (Figure 4-92, Figure 4-93 and Figure 4-95). The computed concentrations of exchanged Ca^{2+} are larger than the measured data (Figure 4-94).

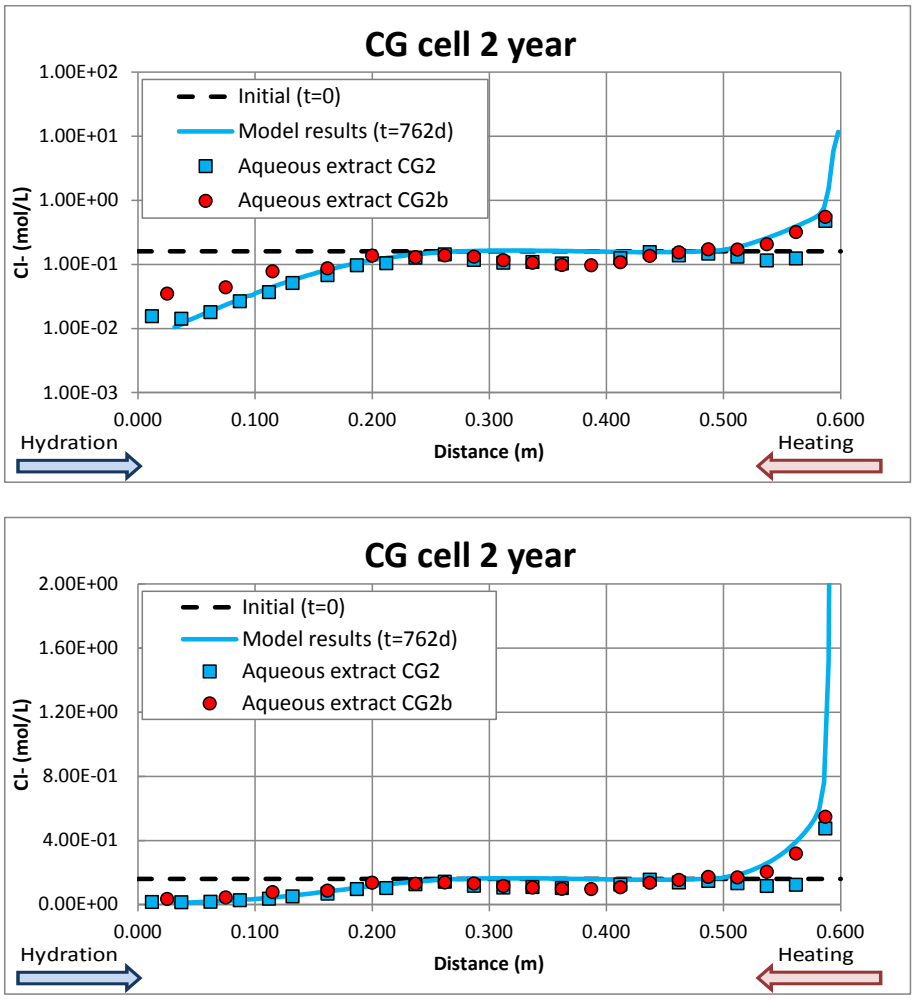

Figure 4-91. Spatial distribution of the measured (symbols) and the computed (line) Cl^- concentrations at the end of the CG2 and CG2b tests after model calibration. Measured data include aqueous extract and squeezing data. Logarithmic scale (top) and natural scale (bottom).

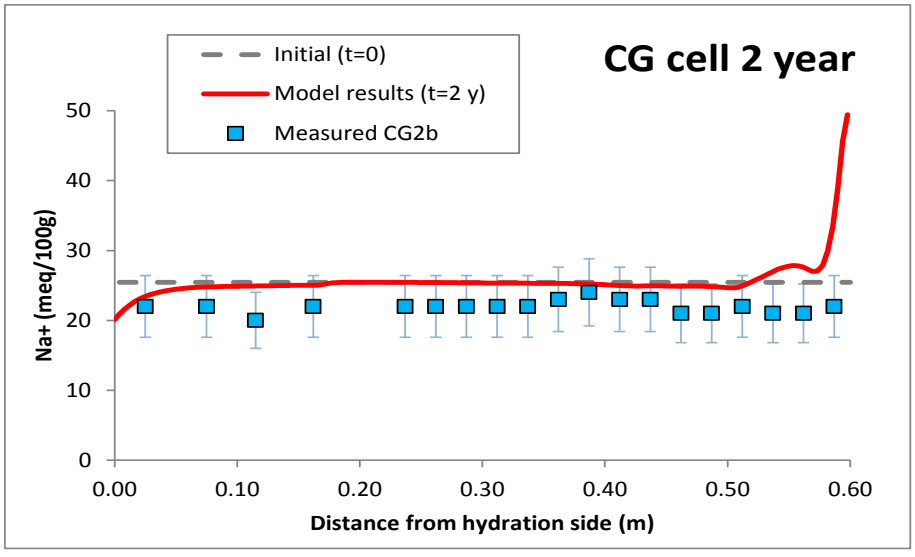

Figure 4-92. Spatial distribution of the measured (symbols) and the computed (line) concentration of exchanged Na^+ at the end of the CG2 and CG2b test after model calibration.

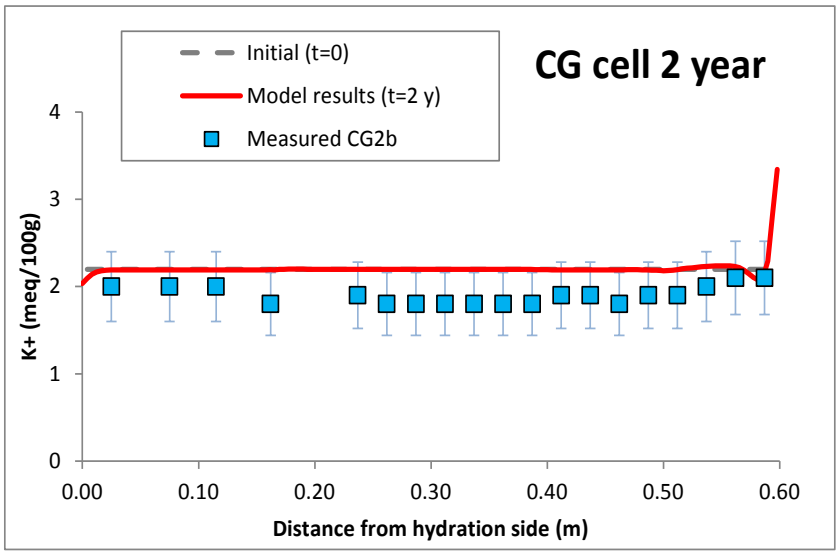

Figure 4-93. Spatial distribution of the measured (symbols) and the computed (line) concentration of exchanged K^+ at the end of the CG2 and CG2b test after model calibration.

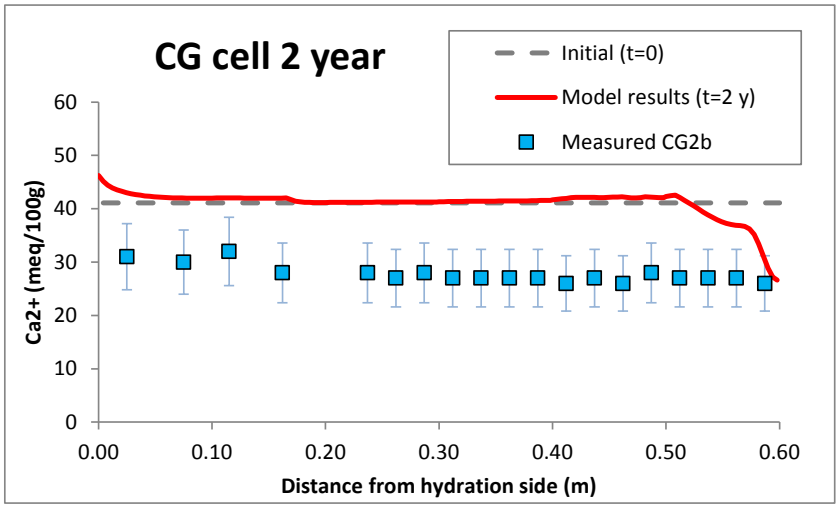

Figure 4-94. Spatial distribution of the measured (symbols) and the computed (line) concentration of exchanged Ca^{2+} at the end of the CG2 and CG2b test after model calibration.

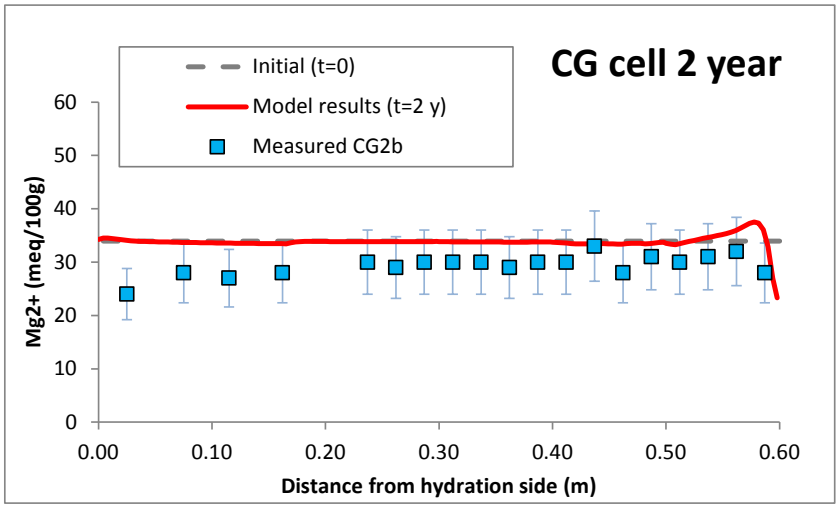

Figure 4-95. Spatial distribution of the measured (symbols) and the computed (line) concentration of exchanged Mg^{2+} at the end of the CG2 and CG2b test after model calibration.

4.6.2.4 CG7.6 cell

Figure 4-96 shows the comparison of the computed concentration of Cl^- and the concentration of the Ciemat geochemical model (CGM). Computed concentrations reproduce the concentration of the CGM better than the previous model. The computed concentration of Cl^- is smaller than the concentration of the CGM near the heater. Both concentrations coincide in the range 0 cm < x < 50 cm.

The concentrations of dissolved Ca^{2+}, Mg^{2+}, Na^+ and K^+ show trends similar to those of Cl^- (Figure 4-97 to Figure 4-100). The computed concentrations fit the concentrations of the CGM, except for the Ca^{2+} concentration near the heater.

The computed concentration of sulphate is smaller than the concentration of the CGM results, except near the heater where the computed concentrations are larger than the concentrations of the CGM (Figure 4-101).

The computed concentration of HCO_3^- coincides with the concentration of the CGM (Figure 4-102).

Figure 4-103 shows the computed concentration of SiO_2(aq) which increases from its initial value due to the dissolution of chalcedony (Figure 4-108). The change in the slope of the dissolved SiO_2(aq) is due to the local precipitation of chalcedony near the heater.

The computed pH and the pH of the CGM are similar and equal to 7.5, except near the heater (Figure 4-96).

Calcite dissolves near the hydration boundary and precipitates in a front which starts at x = 5 cm at t = 0.5 years and reaches x = 10 cm after 7.6 years. Then, calcite precipitates in the intermediate zones of the bentonite sample (10 cm < x < 60 cm) and it continues precipitating near the heater at 7.6 years (Figure 4-105). Mineralogical analyses indicated the presence of carbonates at distances ranging from 3 to 17 cm from the hydration boundary for the CG0.5 and CG7.6 tests, respectively (Fernández and Villar, 2010). These observations are reproduced by the computed calcite concentrations after 0.5 and 7.6 years.

Gypsum dissolves in the bentonite. During the cooling phase, gypsum dissolves in the bentonite and precipitates near the heater (Figure 4-106). Anhydrite precipitates near the heater with time (40 cm < x < 60 cm) and it dissolves during the cooling (Figure 4-107). The mineralogical analyses observed evidences of Ca-sulphate precipitates at x = 8 cm for the CG0.5 test, at x = 19 cm for the CG1 test and at x = 16 cm and x = 40 cm for the CG7.6 test. These observations are

approximately reproduced by the computed values of gypsum precipitation after the cooling phase.

Chalcedony dissolves in the bentonite except near the heater (Figure 4-108). The mineralogical observations found silica gel at x = 21 cm and x = 51 cm from the hydration side for the CG1 and CG7.6 tests, respectively. Chalcedony precipitation is mild between x = 50 cm and x = 60 cm from the hydration side. This result is coherent with the observations at 7.6 years.

Figure 4-109 to Figure 4-112 show the measured and computed concentrations of exchanged cations. After model calibration the computed concentrations of Mg^{+2} and Ca^{2+} reproduce the measured data. However, those of K^{+} and Na^{+} do not fit the data.

Figure 4-113 to Figure 4-115 show the concentration of main sorption species for the strong, weak 1 and weak 2 sites. The dominant sorbed species at the strong sites is S_sOH which increases in the intermediate part of the bentonite sample and decreases near the hydration side and near the heater. $S_{w2}OH$ is the main species in the weak 2 sites.

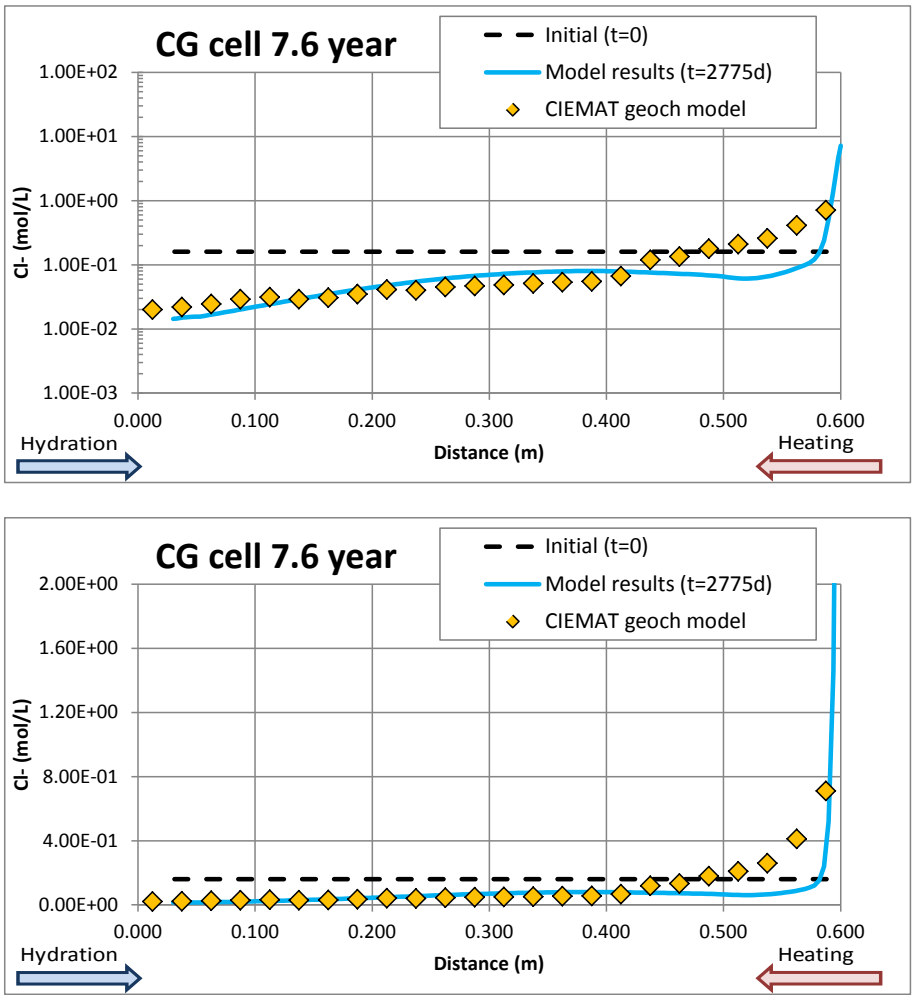

Figure 4-96. Comparison of the Cl^- concentrations of the Ciemat geochemical model (symbols) and the computed (line) Cl^- concentrations at the end of the CG7.6 test after model calibration. Logarithmic scale (top) and natural scale (bottom).

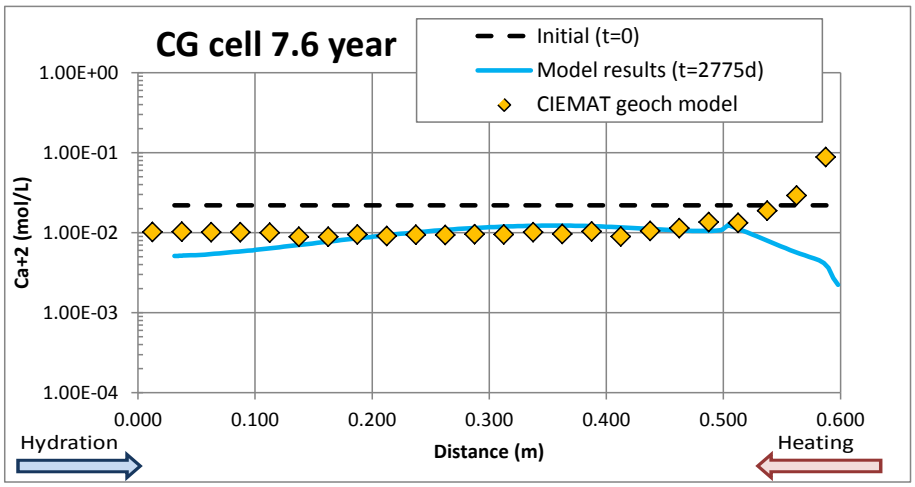

Figure 4-97. Comparison of the Ca^{2+} concentrations of the Ciemat geochemical model (symbols) and the computed (line) Ca^{2+} concentrations at the end of the CG7.6 test after model calibration.

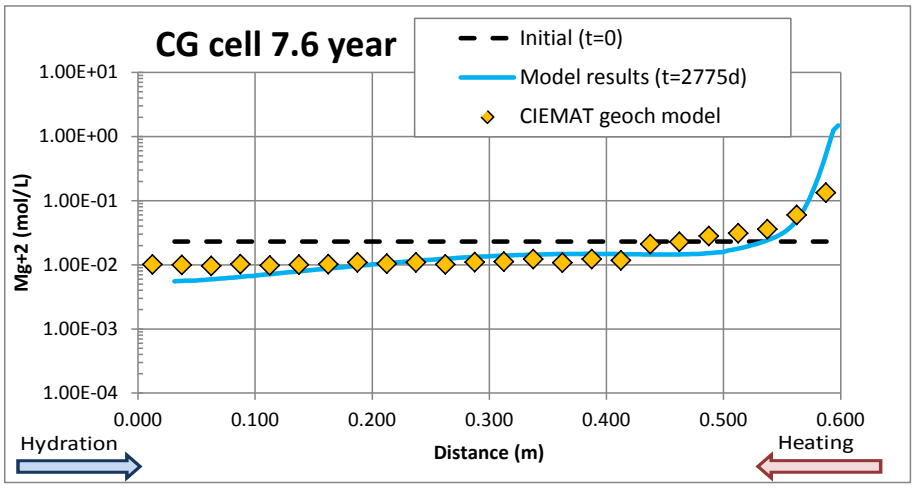

Figure 4-98. Comparison of the Mg^{2+} concentrations of the Ciemat geochemical model (symbols) and the computed (line) Mg^{2+} concentrations at the end of the CG7.6 test after model calibration.

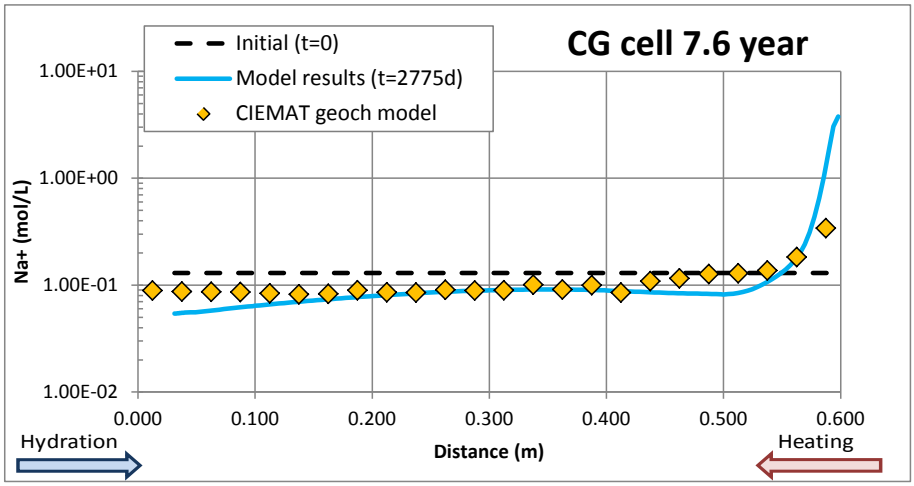

Figure 4-99. Comparison of the Na^{+} concentrations of the Ciemat geochemical model (symbols) and the computed (line) Na^{+} concentrations at the end of the CG7.6 test after model calibration.

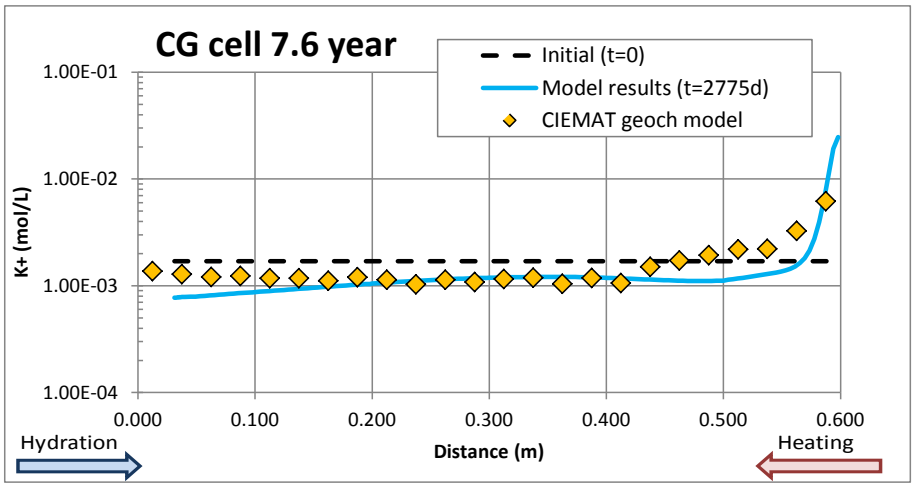

Figure 4-100. Comparison of the K^{+} concentrations of the Ciemat geochemical model (symbols) and the computed (line) K^{+} concentrations at the end of the CG7.6 test after model calibration.

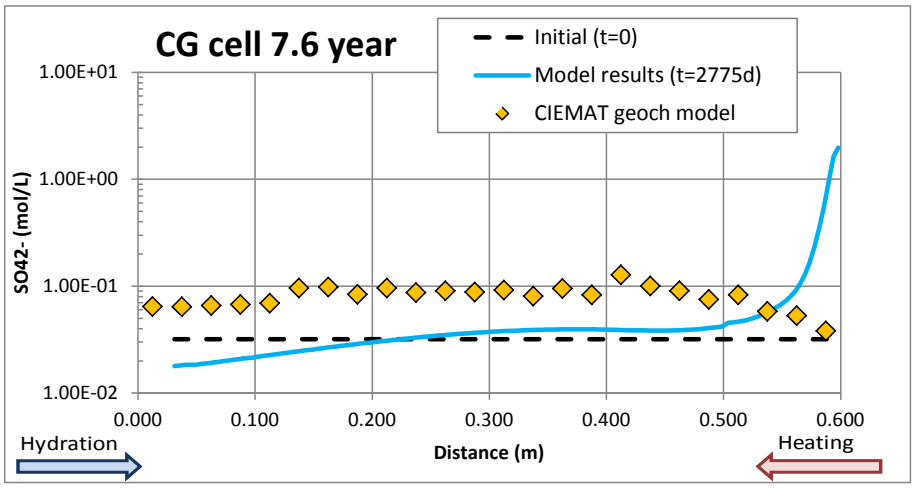

Figure 4-101. Comparison of the SO_4^{2-} concentrations of the Ciemat geochemical model (symbols) and the computed (line) SO_4^{2-} concentrations at the end of the CG7.6 test after model calibration.

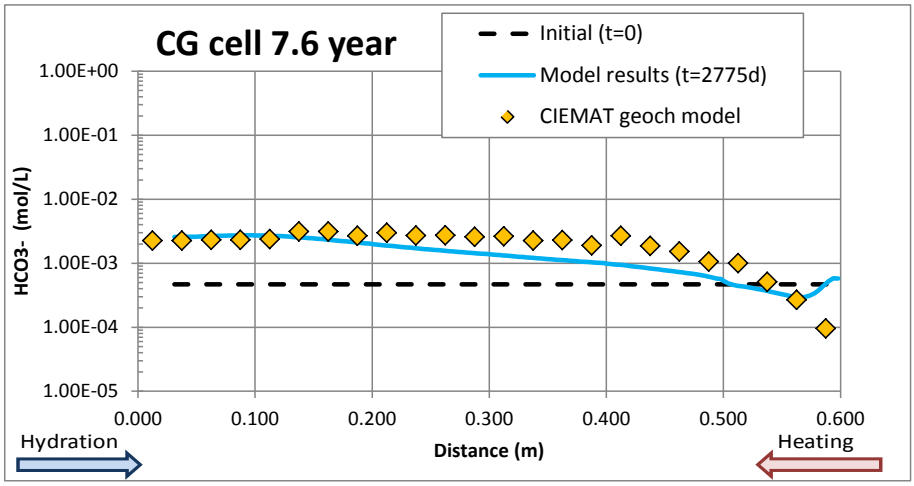

Figure 4-102. Comparison of the HCO_3^- concentrations of the Ciemat geochemical model (symbols) and the computed (line) HCO_3^- concentrations at the end of the CG7.6 test after model calibration.

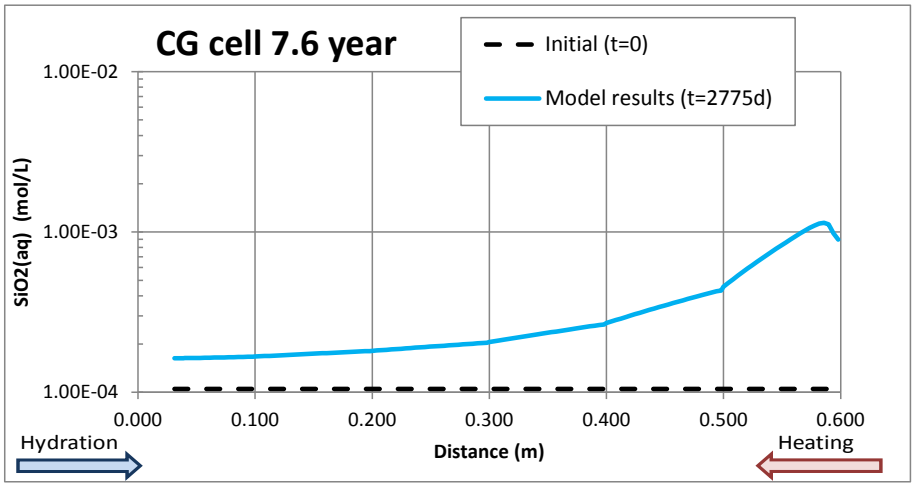

Figure 4-103. Spatial distribution of the computed SiO_2(aq) concentrations at the end of the CG7.6 test after model calibration.

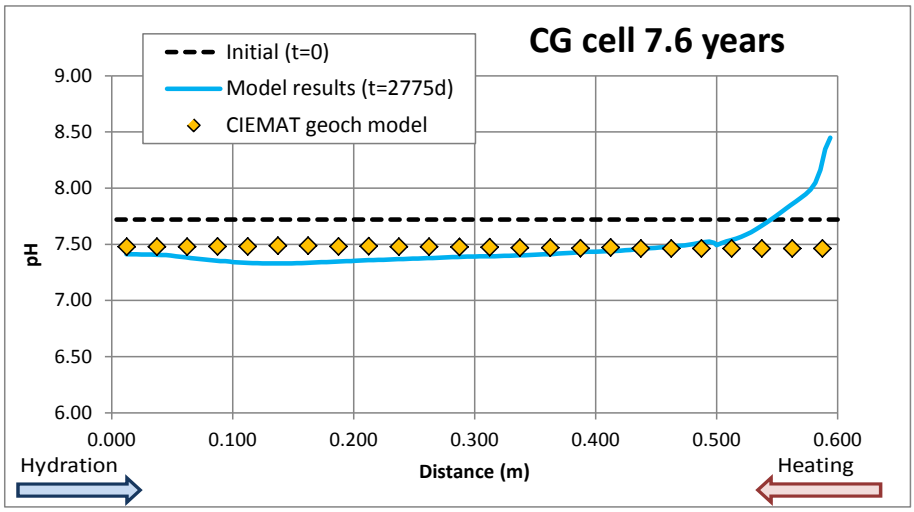

Figure 4-104. Comparison of the pH of the Ciemat geochemical model (symbols) and the computed (line) pH at the end of the CG7.6 test after model calibration.

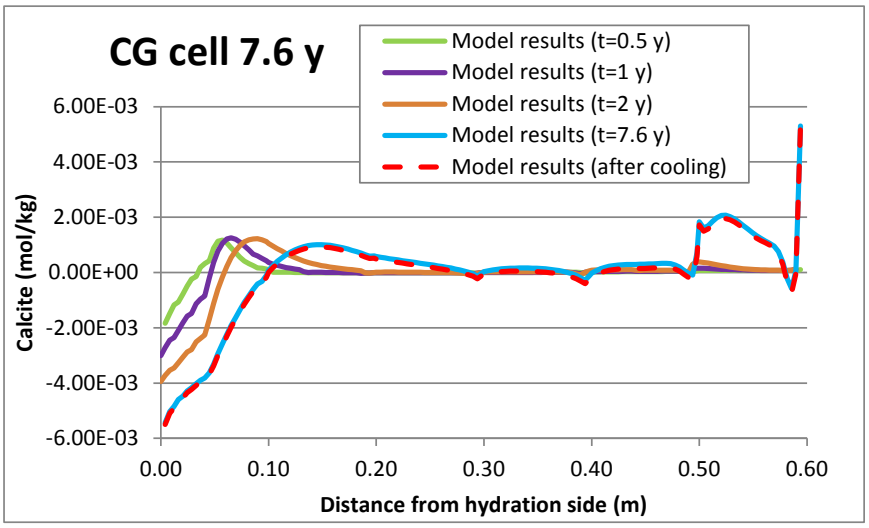

Figure 4-105. Spatial distribution of the cumulative dissolution/precipitation of calcite for the CG7.6 test at several times after model calibration. Positive values for precipitation and negative for dissolution.

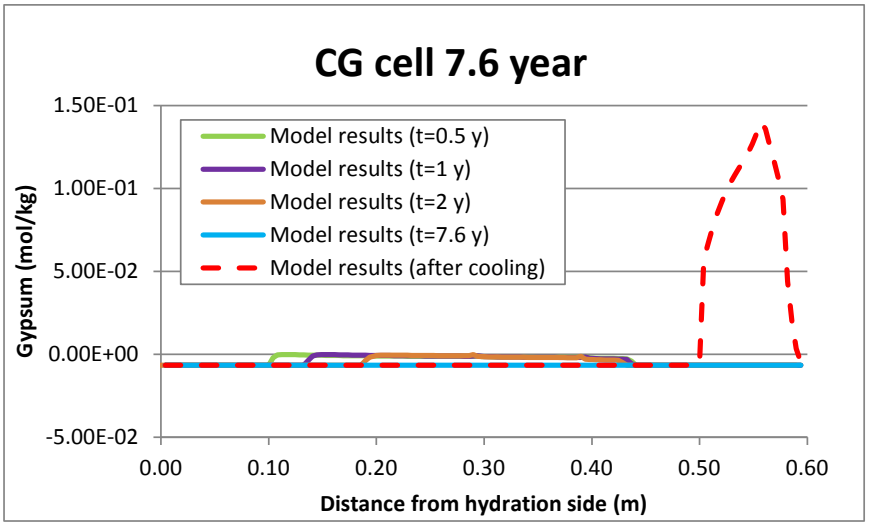

Figure 4-106. Spatial distribution of the cumulative dissolution/precipitation of gypsum for the CG7.6 test at several times after model calibration. Positive values for precipitation and negative for dissolution.

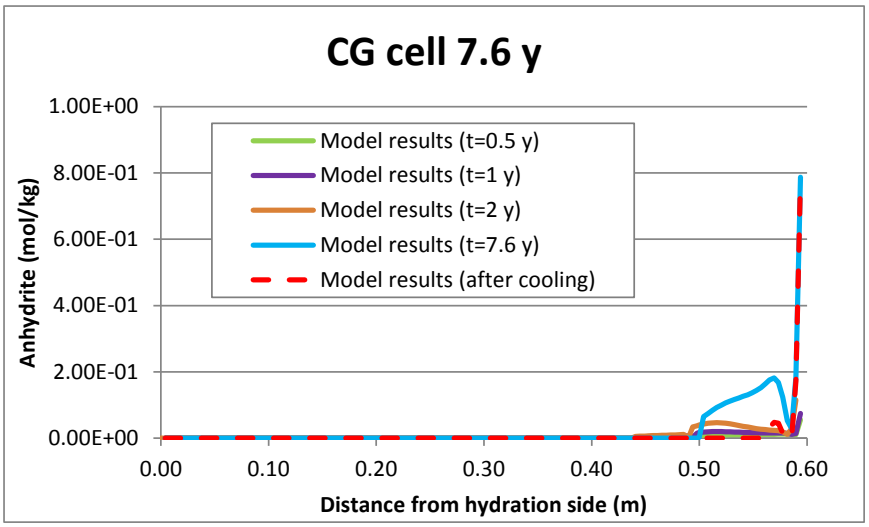

Figure 4-107. Spatial distribution of the cumulative dissolution/precipitation of anhydrite for the CG7.6 test at several times after model calibration. Positive values for precipitation and negative for dissolution.

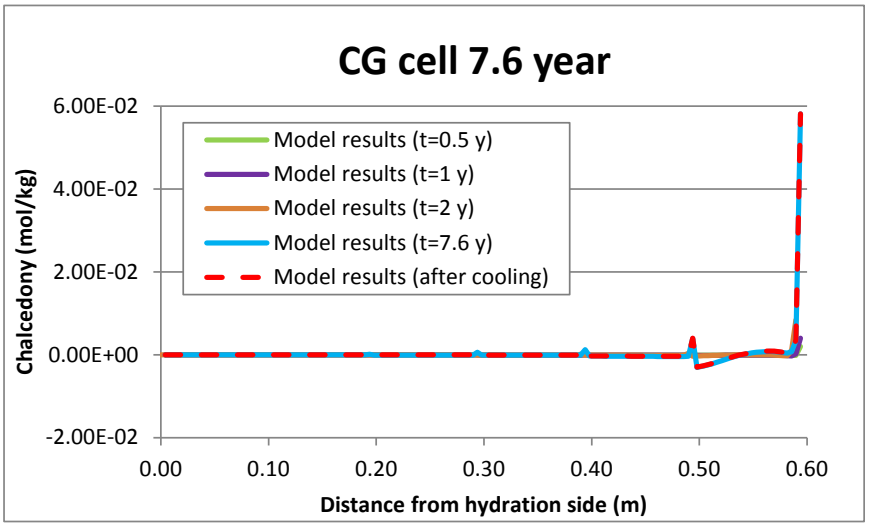

Figure 4-108. Spatial distribution of the cumulative dissolution/precipitation of chalcedony for the CG7.6 test at several times after model calibration. Positive values for precipitation and negative for dissolution.

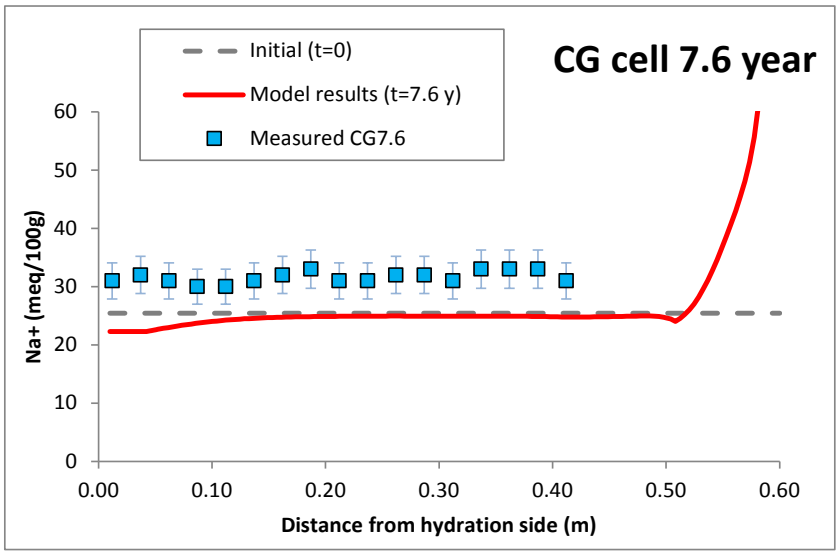

Figure 4-109. Spatial distribution of the measured (symbols) and the computed (line) concentration of exchanged Na^+ at the end of the CG7.6 test after model calibration.

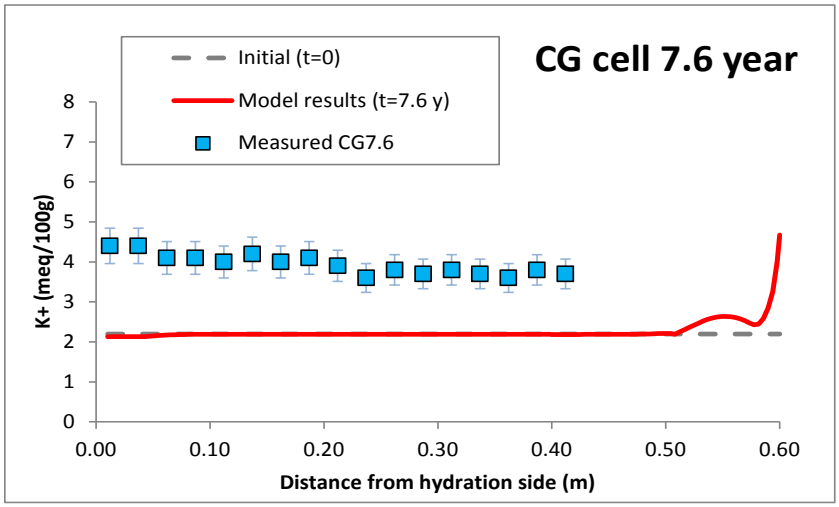

Figure 4-110. Spatial distribution of the measured (symbols) and the computed (line) concentration of exchanged K^+ at the end of the CG7.6 test after model calibration.

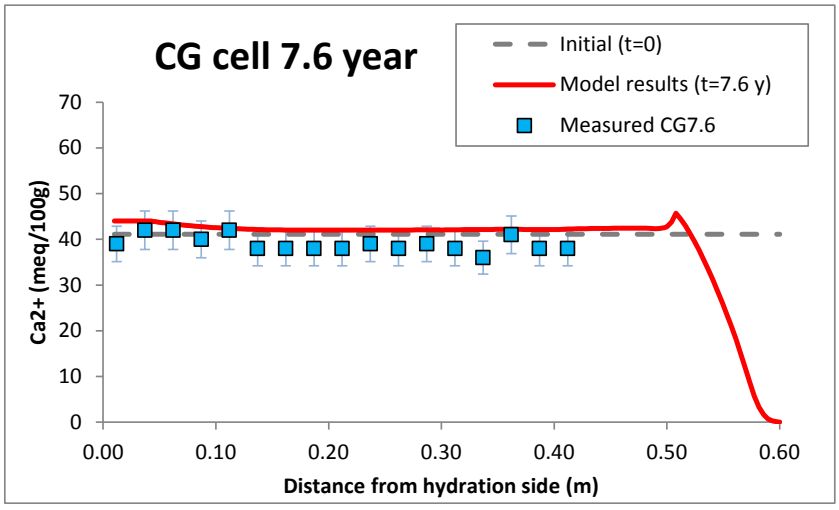

Figure 4-111. Spatial distribution of the measured (symbols) and the computed (line) concentration of exchanged Ca^{2+} at the end of the CG7.6 test after model calibration.

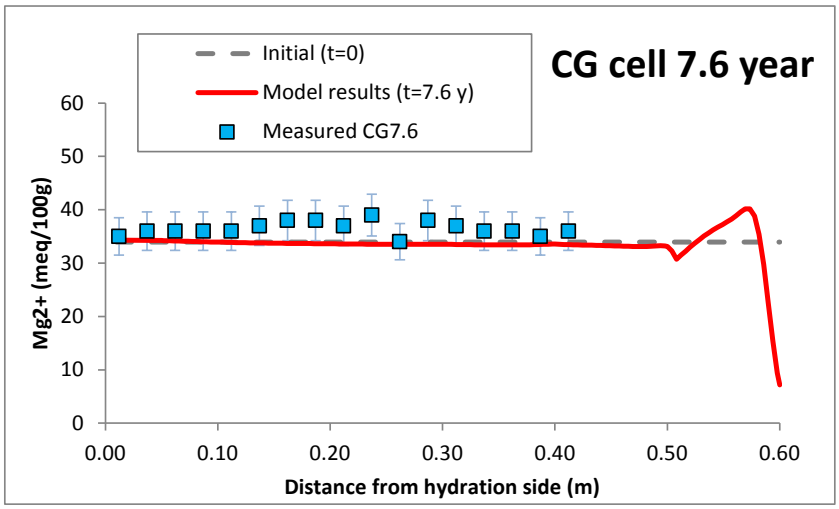

Figure 4-112. Spatial distribution of the measured (symbols) and the computed (line) concentration of exchanged Mg^{2+} at the end of the CG7.6 test after model calibration.

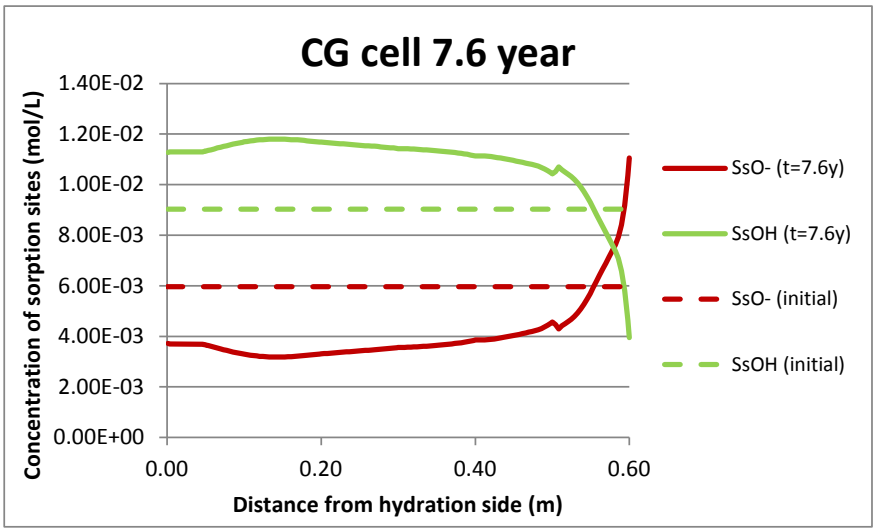

Figure 4-113. Spatial distribution of the concentrations of the sorbed species on strong sites at the end of the CG7.6 test after model calibration.

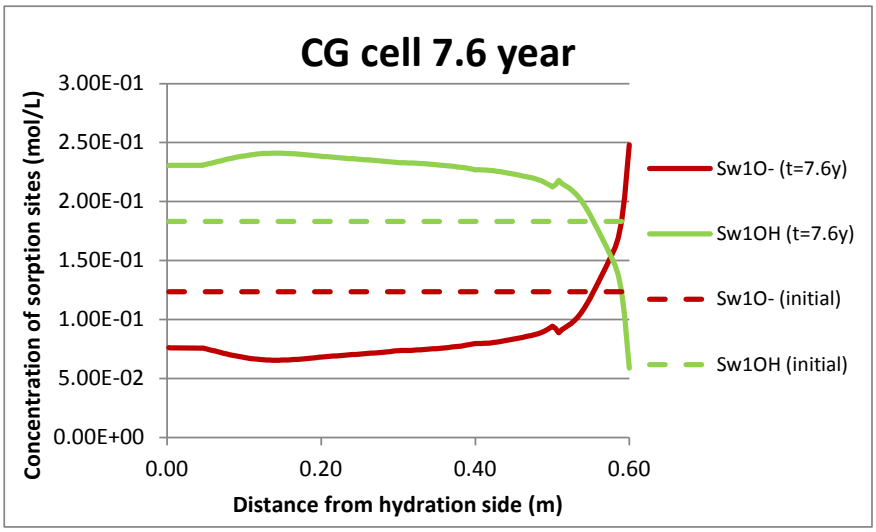

Figure 4-114. Spatial distribution of the concentrations of the sorbed species on weak 1 sites at the end of the CG7.6 test after model calibration.

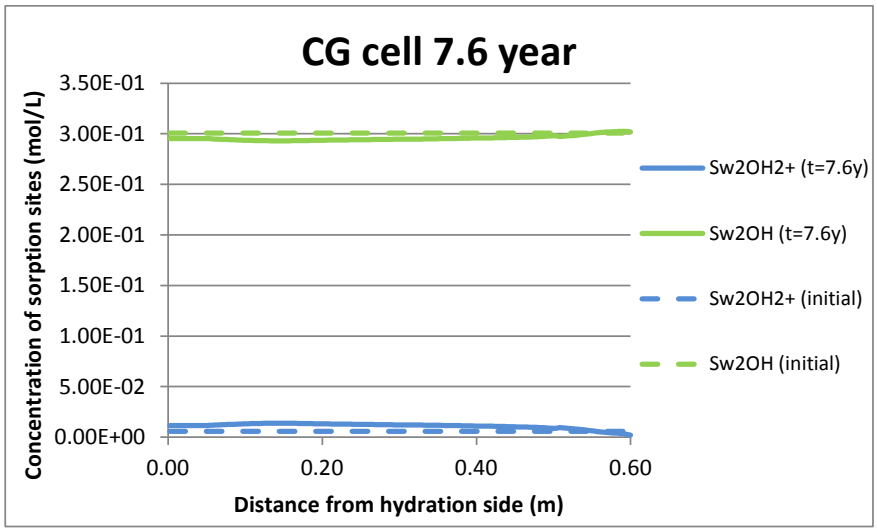

Figure 4-115. Spatial distribution of the concentrations of the sorbed species on the weak 2 sites at the end of the CG7.6 test after model calibration.

4.6.3 Conclusion of the model calibration

The numerical model of the 60-cm long heating and hydration tests reproduces the observed temperature, saturation degrees, porosities and dissolved an exchanged chemical data. Geochemical predictions improve when the changes in porosity caused by swelling are considered and when some parameters such as vapor tortuosity, heat dissipation and cation selectivities are estimated.

5 THC(m) models of the corrosion tests

5.1 Introduction

Corrosion tests were performed to ascertain the effects of the corrosion products in the bentonite. The tests were performed within the NFPRO and PEBS projects to study the interactions of bentonite and the corrosion products. Two types of tests were performed:

(1) The so-called small cell experiments (SC cells), with a length of 25 mm, which were designed to reproduce the repository conditions prevailing 3000 years after the emplacement of the waste when the bentonite is fully saturated;

(2) The medium cells tests (HB), with a length of 10 cm, which were performed to simulate the operational, early post-closure and transient phases of the repository before achieving full saturation of the EBS which is characterized by oxic to suboxic conditions.

The tests were performed under anoxic conditions to mimic the conditions of the repository once the O_2(g) is consumed. Corrosion under reducing conditions will occur according to thermodynamic predictions.

This chapter presents the numerical models of several types of heating and hydration experiments performed by Ciemat on compacted FEBEX bentonite to study the interactions of iron-bentonite under repository conditions and analyze how such interactions affect the bentonite properties. These experiments were performed at several temperatures and on samples of different lengths. The small cells (SC cells) are 25 mm tests performed by Ciemat with bentonite and Fe powder. These tests were hydrating and heating with a fixed temperature of 25º, 50º and 100ºC. These tests were performed during the NFPRO project (Torres et al; 2008).The experiments were modelled with INVERSE-FADES-CORE. Fe powder was used in the corrosions tests. H_2O is assumed to be the oxidizing agent of the canister. Fe powder is treated as a porous mineral made of Fe(s), which dissolves according to:

$$Fe(s) + 2H^+ + 0.5O_2 \Leftrightarrow Fe^{2+} + H_2O \quad (26)$$

The following general kinetic rate expression has been used for mineral dissolution/precipitation:

$$r_m = k_m e^{-\frac{Ea}{RT}} (\Omega_m{}^{\theta} - 1)^{\eta} \quad (27)$$

where r_m is the dissolution/precipitation rate (mol/m^2/s); k_m is the kinetic rate constant (mol/m^2/s) at 25ºC, Ω_m is the ratio between the ion activity product and the equilibrium constant (dimensionless) and θ and η are parameters of the kinetic law; $e^{-\frac{Ea}{RT}}$ is the thermodynamic factor, which takes into account the apparent activation energy of the reaction, Ea, and R and T are the gas constant and the absolute temperature, respectively. Fe powder corrosion is modelled by using a constant kinetic rate. Magnetite is a mineral phase which may precipitate with a kinetic law depending on the mineral saturation index. The kinetic parameters for magnetite were taken from De Windt and Torres (2009). The corrosion rate, r_c, in µm/year is calculated from:

$$r_c = \frac{r_m M_w}{\rho} \tag{28}$$

where ρ is the density of the iron, M_w is the molecular weight and r_m is the corrosion rate in mol/m^2/s.

5.2 Small corrosion cells

5.2.1 Introduction

The small cells (SC cells) are 25 mm tests performed by Ciemat with bentonite and Fe powder to study the interactions of the corrosion products and bentonite. These tests were performed at a fixed temperature. Tests were performed at the following temperatures: 25º, 50º and 100ºC. These tests were performed during the NFPRO project (Torres et al; 2008).

5.2.2 Test description

The corrosion tests on small cells were performed in hermetic cylindrical cells in the Ciemat facilities. The cells contained 21 mm of compacted bentonite and 4 mm of carbon-steel powder (Figure 5-1). The tests were performed with unsaturated Febex bentonite. The external cylindrical cell was made out of Teflon to prevent the deformation. Tests were performed at the following temperatures: 25º, 50º and 100ºC. The bentonite blocks were compacted to a dry density of 1.65 g/cm^3 and an initial gravimetric water content of 0.14. The hydration water was injected by a steel distribution plate at a pressure of 100 kPa. The hydration water was Grimsel water. The main features of the small tests performed by Ciemat are listed in Table 5-1.

Numerical models were developed for the tests performed on small cells a1, a2 and a3 which lasted 6 months. The iron source was Fe powder. The hydration water is a reduced Grimsel groundwater. Initially the cells were unsaturated. It is estimated that bentonite samples got fully saturated after 2 weeks.

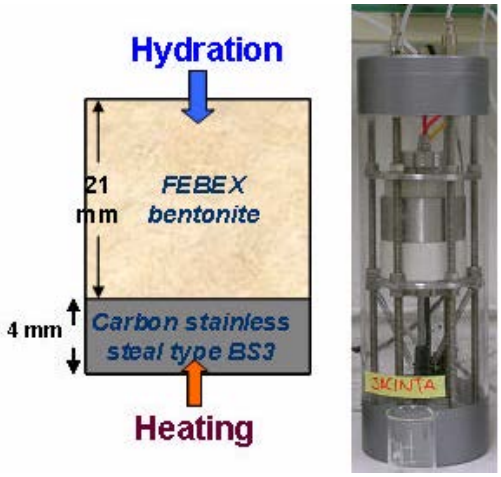

Figure 5-1. Sketch of the corrosion test on small cells (Torres et al., 2008).

Table 5-1. Main features of the corrosion tests on small cells (Torres et al., 2008).

Test code	Temperature (ºC)	Duration (months)	Iron source	Hydration water	Saturation (%)	Penetration of the corrosion front (mm)
a1	25	6	Fe powder	RGW (reduced Grimsel groundwater)	100	4
a2	50	6	Fe powder	RGW (reduced Grimsel groundwater)	100	4
a3	100	6	Fe powder	RGW (reduced Grimsel groundwater)	100	6
a3	100	12	Steel fillings	BGW (commercial granitic water)	100	2
a3	100	12	Steel fillings	SCW (synthetic concrete water)	72	

After the dismantling, most of the corrosion cells showed a sequence of colours: white, greenish-blue, orange and black (Torres et al., 2008) which was interpreted as the stages of the transformation of $Fe(OH)_2(s)$ into magnetite. There was a co-existence of several iron oxides and oxyhydroxides in all the experiments due to the transformation of the initial $Fe(OH)_2(s)$. The following iron oxides and oxyhydroxides were found: goethite, lepidocrocite and magnetite.

5.2.3 Analysis of available data

Bentonite dry density, water content and saturation degree were measured at the end of the tests. These data were used for the calibration of the thermo- hydro-mechanical model.

There no data on the concentration of the bentonite pore water after the tests. The penetration of the corrosion front into the bentonite is known and was used for the model calibration. The measured weight content of $Fe(OH)_2(s)$ was used to calibrate the penetration of the corrosion products into the bentonite.

5.2.4 Model description

A reactive transport model of the corrosion small cells was performed by De Wint and Torres (2009). We used their kinetic parameters for our THMC model.

The THMC numerical model includes the bentonite and the Fe powder. A one-dimensional finite element mesh (Figure 5-2). A liquid pressure of 100 kPa and a temperature of 22ºC were prescribed at the top of the cell. The temperature at the heater was fixed at the following temperatures 25º, 50º and 100ºC.

The model simulates the heating and hydration during 180 days. The main THMC model parameters of the bentonite and Fe powder are listed in Table A1-1 to Table A1-4 in the Appendix A. Some parameters such as the intrinsic permeability of the liquid of the bentonite were taken from laboratory experiments (ENRESA, 2000a and ENRESA, 2000b). The parameters of the bentonite, such as the relative permeability of the liquid and the gas, the reflection coefficient and the thermo-osmotic permeability were taken from Zheng et al. (2010).

As an educated guess, the thermal and physical parameters for the Fe powder were taken from those of the iron. The retention curve, the relative permeability of the liquid and the intrinsic and relative permeability of the gas for the Fe powder were assumed equal to those of the bentonite. The intrinsic permeability of the liquid was assumed to be 100 times larger than that for the bentonite. The vertical displacement was disabled at the top of the cell. A light deformation was imposed in the Fe powder. The total stress was fixed to 250 kPa.

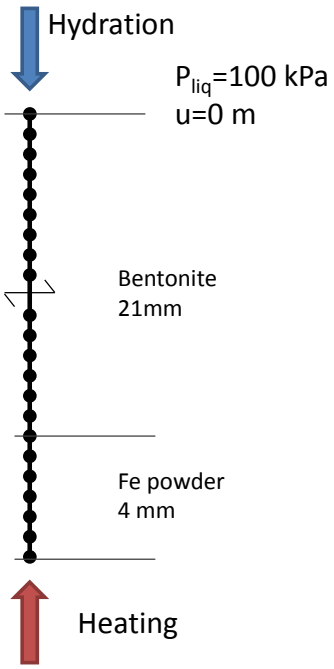

Figure 5-2. Finite element mesh and boundary conditions for the numerical model of the corrosion tests in small cells.

Bentonite has an initial porosity of 0.4 and an initial gravimetric water content of 14%, which corresponds to a saturation of 57% and a suction of $1.27 \cdot 10^5$ kPa. The initial temperature is equal to 22ºC throughout the cell. The initial gas pressure is equal to the atmospheric pressure.

A Neuman boundary condition was used for solute transport according to which solute flux is equal to the product of water flux times solute concentration of inflow water. The hydration water in this experiment was Grimsel groundwater. Its composition is listed in Table A2-1. The initial concentration of the primary species of the bentonite pore water was taken from Fernández et al. (2001) (see Table A2-1 in the Appendix A). The effective diffusion coefficient, D_e, is assumed to be the same for all species and equal to $2 \cdot 10^{-10}$ m^2/s. The effective diffusion coefficient for Cl^- was taken from Zheng et al. (2010) which is equal to $9 \cdot 10^{-11}$ m^2/s. The chemical system is defined in terms of the following primary species: H_2O, $O_2(aq)$, H^+, Na^+, K^+, Ca^{2+}, Mg^{2+}, Fe^{2+}, HCO_3^-, Cl^-, SO_4^{2-} and $SiO_2(aq)$.Table A2-2 and Table A2-3 show the parameters and initial conditions for surface complexation and cation exchange in the bentonite. The cation exchange is not considered in the Fe powder, however the sorption is allowed. The initial volume fractions of the minerals are listed in Table 5-2. The bentonite contains initially 1% of calcite, 1% of quartz and 0.08% of gypsum. The Fe powder is assumed to be 100% Fe(s). The following secondary minerals are

allowed to precipitate: gypsum, anhydrite, magnetite, goethite, siderite and $Fe(OH)_2$(s). The relevant aqueous complexes were identified with EQ3NR (Wolery, 1992). The equilibrium constants of the homogeneous reactions, minerals, surface complexation and sorption are listed in Table A2-4, Table A2-5, Table A2-6 and Table A2-7.

Table 5-2. Initial mineral volume fractions (%) considered in the the small cells models.

Minerals	Quartz	Calcite	Gypsum	Iron
Bentonite	1.0	1.0	0.08	-
Fe powder	-	-	-	100

Table 5-3. Kinetic parameters of carbon steel and magnetite used in the small cells models (De Wint and Torres, 2009).

Mineral	Activation energy (kJ/mol)	$K_{25ºC}$ (mol/m^2/s)	θ	η	Specific surface (m^2/ m^3 medium)
Fe (s)	11.0	$-4.0\cdot10^{-10}$	1	0	$2.15\cdot10^{5}$
Magnetite	20.0	$9.53\cdot10^{-11}$	0.1	1	$1.0\cdot10^{5}$

5.2.5 Model results of the SC cells

This section presents the main thermo-hydro-mechanical and chemical computed results for the model of the a3 cell which had a heater temperature of 100ºC.

5.2.5.1 Thermo-hydro-mechanical results

There is a measurement of water content and saturation degree of the bentonite sample at the end of the test (180 days). The computed water content reproduces the measured value. The water content is largest in the hydration side. It decreases towards the interface of Fe powder/bentonite (Figure 5-3). The bentonite becomes nearly fully saturated after 180 days (Figure 5-4). The saturation degree in the interface and in the Fe powder is about 70%.

The computed porosity is slightly smaller than the measured data (Figure 5-5). The computed porosity is largest in the hydration side and decreases towards the Fe powder.

The computed temperature profile reaches steady state in a few minutes. The temperature in the Fe powder is 100ºC. Figure 5-6 shows the computed temperature profiles for the SC cells corrosion tests on small cells at 25ºC, 50ºC and 100ºC.

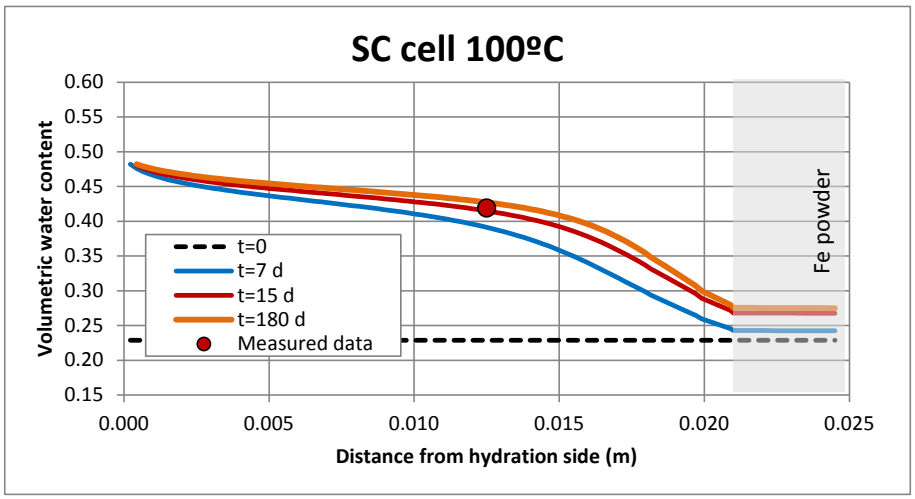

Figure 5-3. Spatial distribution of the computed (lines) and the measured (symbol) volumetric water content in the small-cell corrosion test at 100ºC.

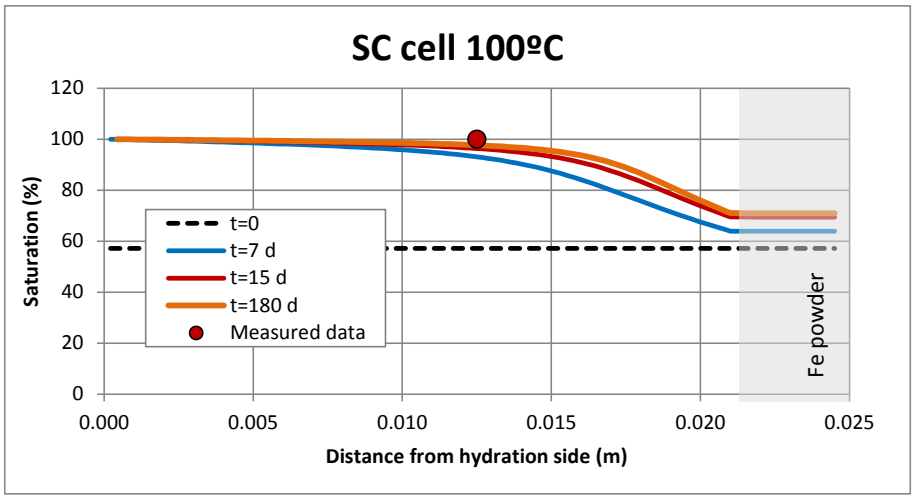

Figure 5-4. Spatial distribution of the computed (lines) and the measured (symbol) saturation degree in the small-cell corrosion test at 100ºC.

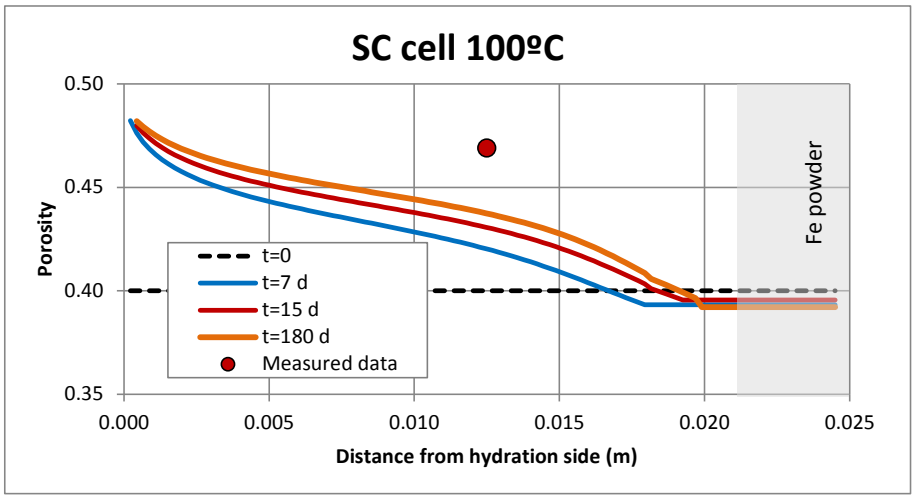

Figure 5-5. Spatial distribution of the computed (lines) and the measured (symbol) porosity in the small-cell corrosion test at 100ºC.

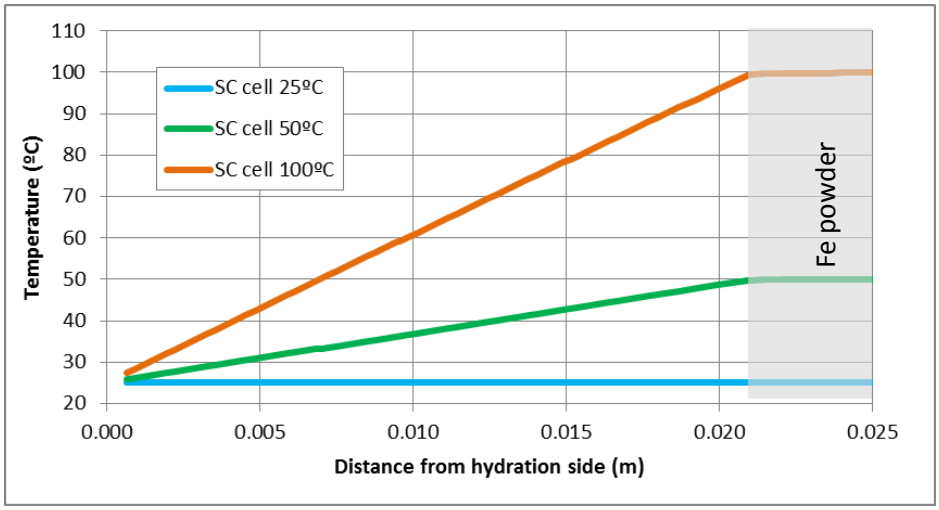

Figure 5-6. Spatial distribution of the computed temperature in the small-cell corrosion tests at with temperatures 25ºC, 50ºC and 100ºC.

5.2.5.2 Chemical results

Figure 5-7 shows the computed spatial distribution of the Cl^- concentration. Cl^- concentrations in the Fe powder are larger than in the bentonite after 7 days. Later, the Cl^- concentrations decrease in the Fe powder. The initial increase in concentrations is due to the evaporation near the heater. Vapour diffuses into the bentonite and condensates. The final Cl^- concentration is largest in the Fe powder and smallest near the hydration side because the water content is largest in the hydration side and smallest in the Fe powder.

The spatial distribution of the computed concentrations of dissolved Na^+, K^+, Ca^{2+}, Mg^{2+}, HCO_3^-, SO_4^{2-} and SiO_2(aq) are shown in Appendix B (from Figure B1-1 to

Figure B1-7). The computed concentrations of Ca^{2+}, Mg^{2+}, Na^{+} and K^{+} show similar trends to those of Cl^{-}. In addition to diffusion, these species are subjected to mineral dissolution/precipitation and cation exchange reactions. The spatial distribution of the dissolution/precipitation of calcite, gypsum, anhydrite and quartz are shown in Appendix B (from Figure B1-8 to Figure B1-11).

The concentration of HCO_3^{-} in the bentonite is larger than in the Fe powder because calcite dissolves in the bentonite especially near the hydration side and precipitates in the Fe powder and in the bentonite-Fe powder interface (Figure B1-8).

The concentration of sulphate is affected by the dissolution/precipitation sulphate minerals (Figure B1-6). Gypsum dissolves instantaneously in the bentonite. Anhydrite precipitates near the heater at 7 days and then it dissolves.

The spatial distribution of computed silica is controlled by the solubility of the quartz which depends on the temperature (Figure B1-7).

The concentration of the dissolved iron decreases in the bentonite and in the Fe powder at early times due to the precipitation of magnetite and $Fe(OH)_2$(s) (Figure 5-8). The concentration of dissolved Fe^{2+} increases in the bentonite and in the Fe powder after 30 days (Figure 5-9). There is a local decreasing at in the interface bentonite-iron due to the precipitation of corrosion products.

The dissolved concentration of Na^{+} and K^{+} decreases in the bentonite and in the Fe powder with time (Figure B1-1 and Figure B1-2). The concentrations of exchanged Na^{+} and K^{+} decrease in bentonite.

Calcite dissolves in the bentonite and precipitates at the interface bentonite-iron (Figure B1-8). The concentration of the exchanged Ca^{2+} decreases.

The concentration of the dissolved Mg^{2+} increases in the bentonite and even more in the Fe powder due to the decrease of the concentration of exchanged Mg^{2+}.

The corrosion of steel releases Fe^{2+} and causes the precipitation of magnetite and $Fe(OH)_2$(s). Fe powder corrodes at a constant rate of 0.2 μm/year. Figure 5-10 shows the spatial distribution of Fe powder dissolution at different times. Magnetite precipitates with a kinetic control in the Fe powder and in the bentonite-iron interface (Figure 5-11). $Fe(OH)_2$(s) also precipitates at the same places as magnetite (Figure 5-12). Goethite precipitates before 30 days and then dissolves (Figure 5-14). It should be noticed that siderite does not precipitate. Figure 5-13 shows the comparison of the spatial distribution of the computed and measured precipitated iron at the end of the tests. The weight of iron was measured as the amount of $Fe(OH)_2$(s)

present in the cell. The computed results reproduce the measured iron weight data. Our values are similar to those of De Wint and Torres (2009 and 2010).

Figure 5-15 shows the spatial distribution of the computed pH at different times. The initial pH in the bentonite and in the Fe powder is 7.72. At early times, the pH decreases in the bentonite-iron interface and increases in the Fe powder due to corrosion. At the end of the test, the pH tends to a nearly uniform value of 7.5.

Figure 5-16 shows the spatial distribution of the computed Eh at different times. The Eh decreases initially due to the increasing in temperature and it decreases even more due to the corrosion. The final value of -0.65V is similar to that obtained by De Wint and Torres (2009).

The computed exchanged concentrations of cations are shown in Figure 5-17 and Figure 5-18. Exchanged cations were measured at the end of the test only at the bentonite/iron powder interface. The results of the numerical model at 180 days do not reproduce exactly the measured data but are within the 20% error bar.

Figure B1-12, Figure B1-13 and Figure B1-14 in the Appendix B show the spatial distribution of the concentration of the sorbed species. The most important species sorbed in the strong sites is $S^{s}OFe^{+}$. The most important surface complexes in the weak 1 and weak 2 sites are $S^{w1}OH$ and $S^{w2}OH$, respectively.

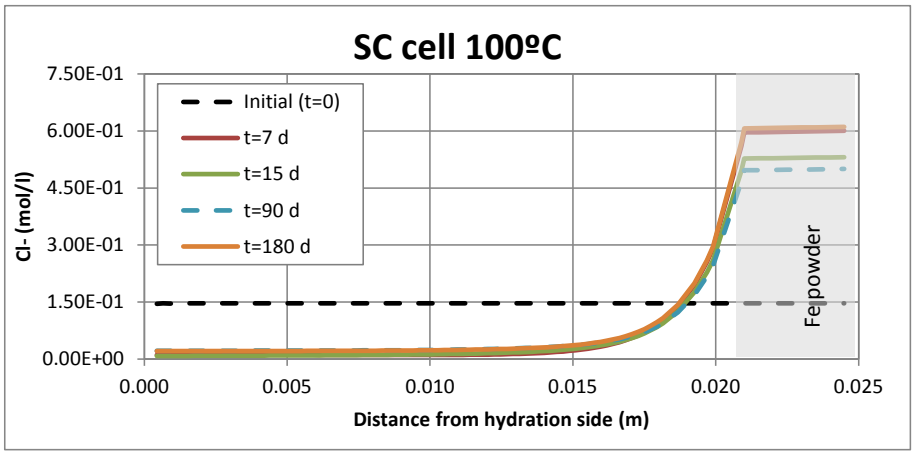

Figure 5-7. Spatial distribution of the computed concentration of dissolved Cl^- in the small-cell corrosion test at 100ºC.

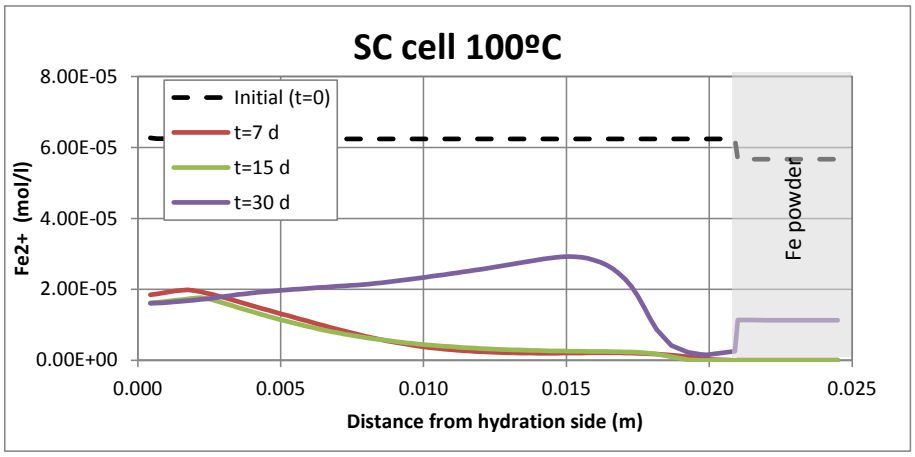

Figure 5-8. Spatial distribution of the computed concentration of dissolved Fe^{2+} in in the small-cell corrosion test at 100ºC between 0 and 30 days.

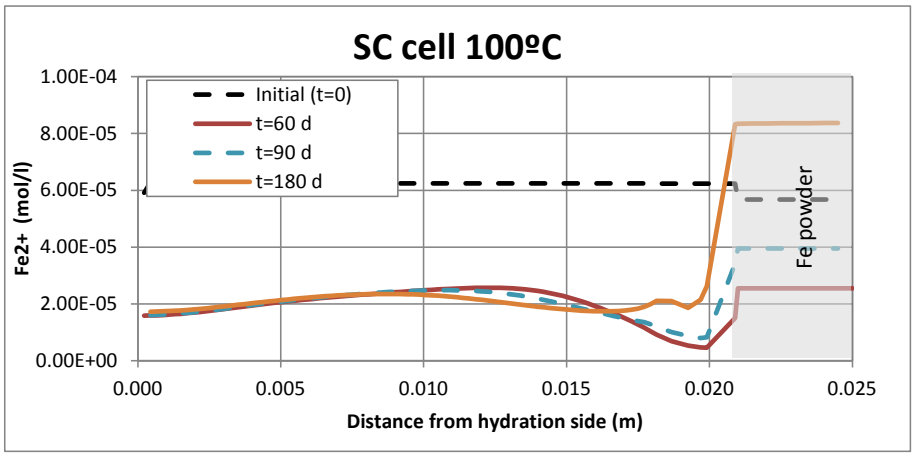

Figure 5-9. Spatial distribution of the computed concentration of dissolved Fe^{2+} in the small-cell corrosion test at 100ºC between 60 and 180 days.

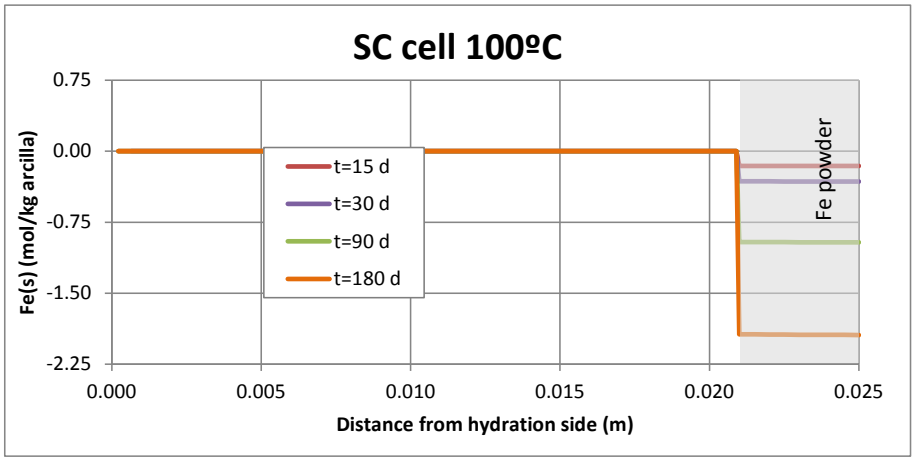

Figure 5-10. Spatial distribution of the computed cumulative dissolution for iron in the small-cell corrosion test at 100ºC.

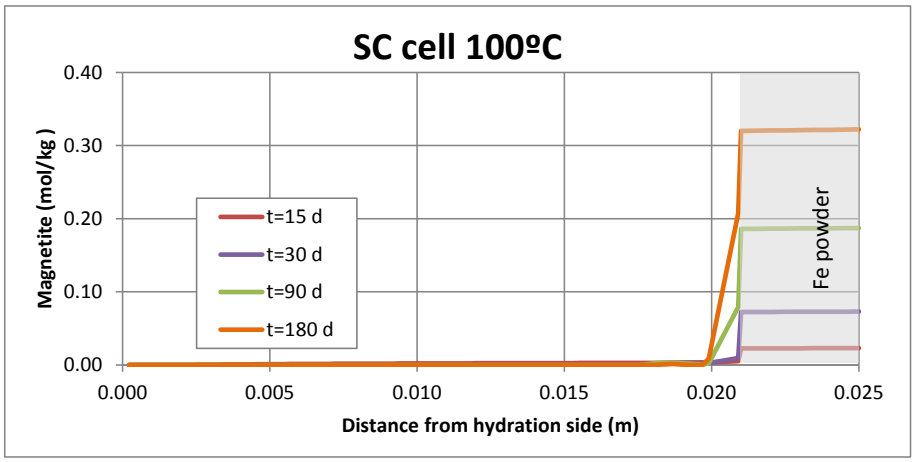

Figure 5-11. Spatial distribution of the computed cumulative precipitation/dissolution for magnetite in the small-cell corrosion test at 100ºC.

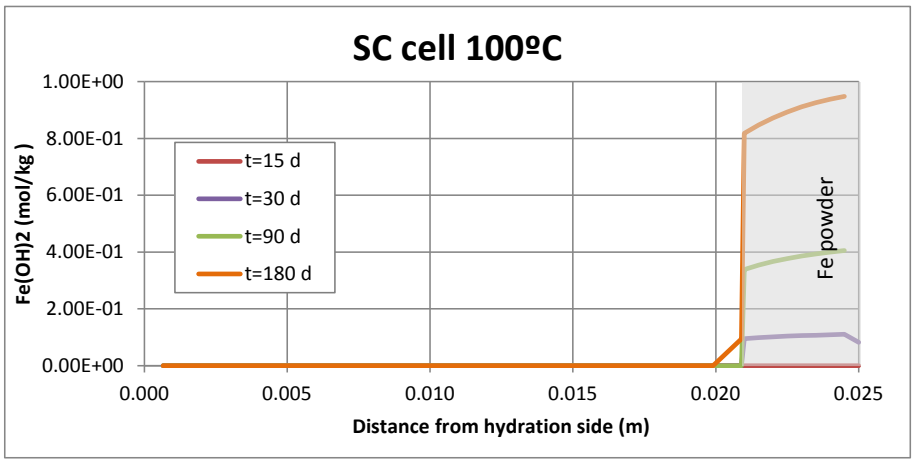

Figure 5-12. Spatial distribution of the computed cumulative precipitation/dissolution of $Fe(OH)_2(s)$ in the small-cell corrosion test at 100ºC.

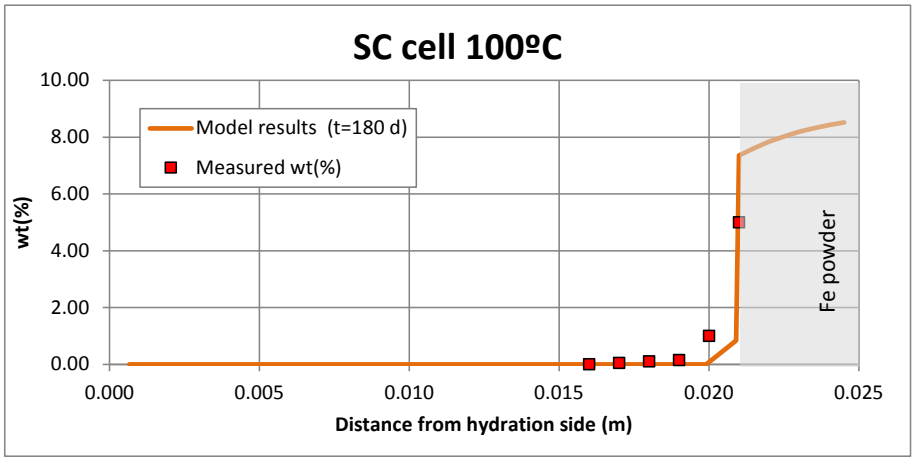

Figure 5-13. Measured (symbol) and computed (line) weight of iron in the small-cell corrosion test at 100ºC.

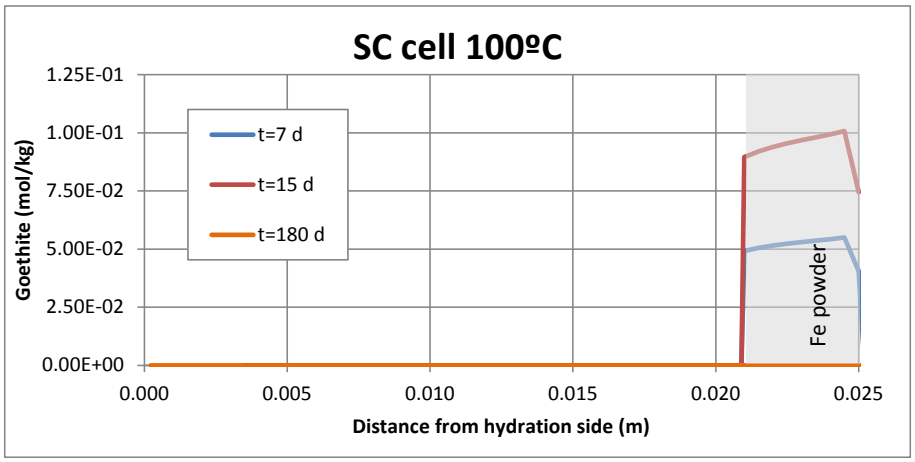

Figure 5-14. Spatial distribution of the computed cumulative precipitation/dissolution for goethite in the small-cell corrosion test at 100ºC.

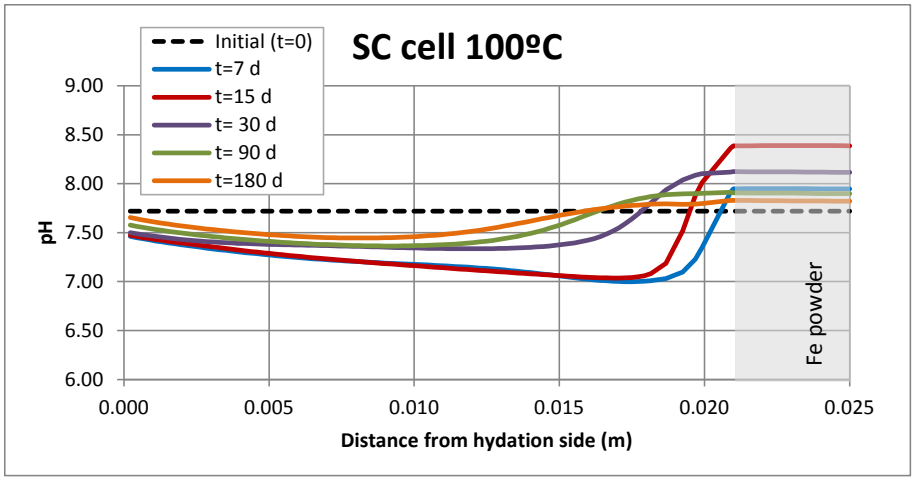

Figure 5-15. Spatial distribution of the computed pH in corrosion test in the small-cell corrosion test at 100ºC.

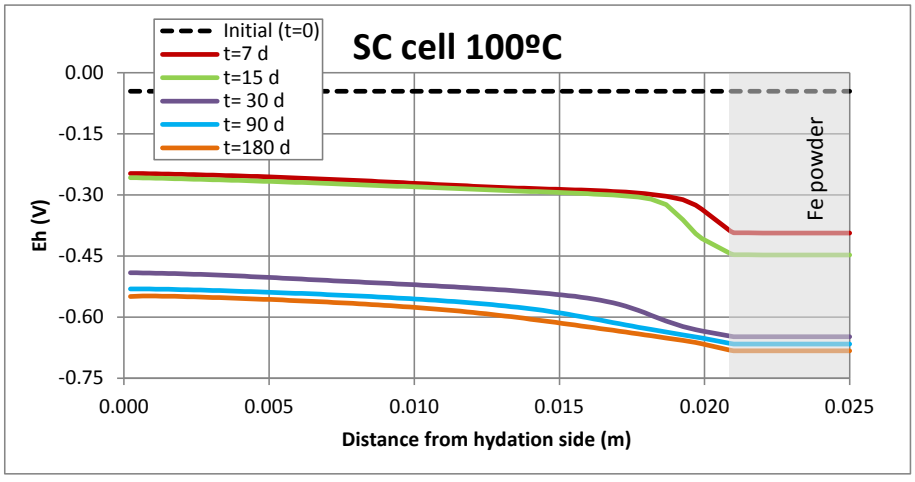

Figure 5-16. Spatial distribution of the computed Eh in the small-cell corrosion test at 100ºC.

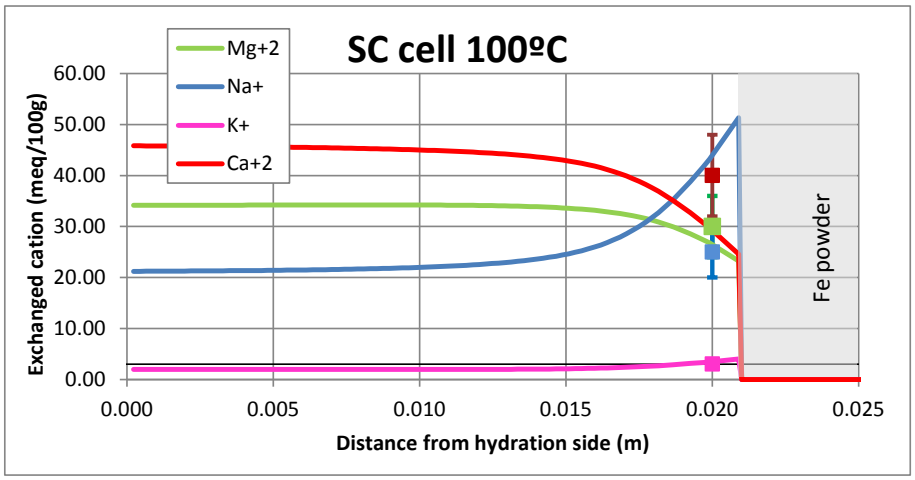

Figure 5-17. Spatial distribution of the computed concentration (lines) and measured (symbols) of the exchanged cations in the small-cell corrosion test at 100ºC.

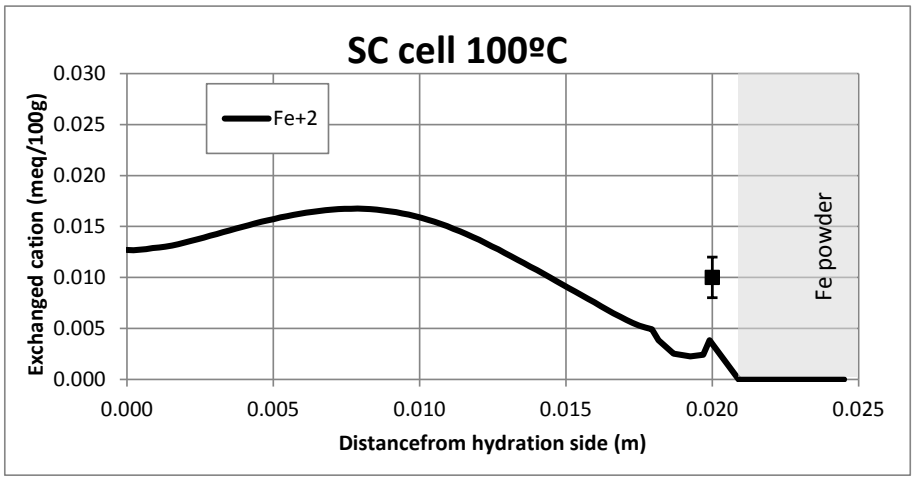

Figure 5-18. Spatial distribution of the computed (line) and measured (symbol) of the concentration of the exchanged Fe^{2+} in the small-cell corrosion test at 100ºC.

Corrosion tests were performed also at 25º and 50ºC. Table 5-4 shows the kinetic parameters used for the three temperatures. The values of the rate constants, k, were taken from De Wint and Torres (2009) (see Table 3-3 in their report). The rate constant at 25ºC is equal to $9.53 \cdot 10^{-11}$ mol/m^2/s. The constant for the model at 50ºC was calibrated between the range proposed by De Windt and Torres, (2009) in order to fit the measured iron weight data. This discrepancy is acceptable given the large uncertainty in the kinetic parameters and rate constants of iron phases.

Table 5-4. Calibrated values of the kinetic parameters for the magnetite of the SC cell model at 25º, 50º and 100ºC.

SC cells model	$k_{25ºC}$ (mol/m^2/s)	θ	η	E_a (kJ/mol)	Specific surface (m^2/ m^3 medium)
SC cell at 25ºC	$9.53 \cdot 10^{-11}$	0.1	1	20.0	$1.0 \cdot 10^5$
SC cell at 50ºC	$2.00 \cdot 10^{-11}$	0.1	1	20.0	$1.0 \cdot 10^5$
SC cell at 100ºC	$9.53 \cdot 10^{-11}$	0.1	1	20.0	$1.0 \cdot 10^5$

Figure 5-19 shows the spatial distribution of the concentration of dissolved Fe^{2+} at the end of the tests of temperatures of 25ºC, 50ºC and 100ºC. The general trend is similar for the three tests. The largest concentrations occur in the Fe powder. Concentrations are uniform in the bentonite with a local decrease near the interface.

The computed pH for the tests at 25ºC and 50º C are larger than that of the test of 100ºC (Figure 5-20).

Figure 5-21 shows the computed dissolution of the iron at 25ºC, 50ºC and 100ºC. The corrosion rate increases with temperature. The largest corrosion of Fe(s) corresponds to the test performed at 100ºC.

Both magnetite and $Fe(OH)_2$(s) precipitate and compete for Fe^{2+} precipitation. The precipitation of magnetite is largest for the test at 100ºC and smallest for the test at 50ºC because the kinetic rate constant of magnetite is the smallest for 50ºC (Figure 5-22). Figure 5-23 shows the spatial distribution of precipitation of the $Fe(OH)_2$(s). The numerical results fit the measured data of the iron weight for the tests performed at 50ºC and 100ºC (Figure 5-24).

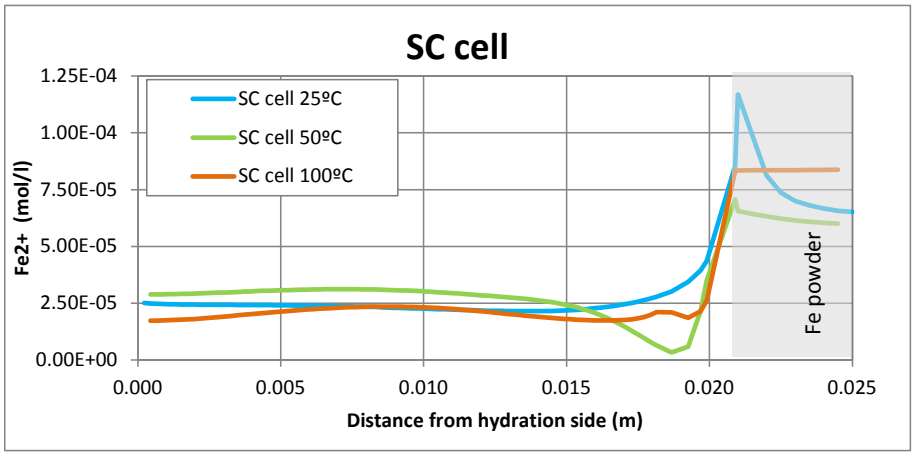

Figure 5-19. Spatial distribution of the computed concentration of dissolved Fe^{2+} at the end of the tests in the corrosion tests on small cells at 25, 50 and 100ºC.

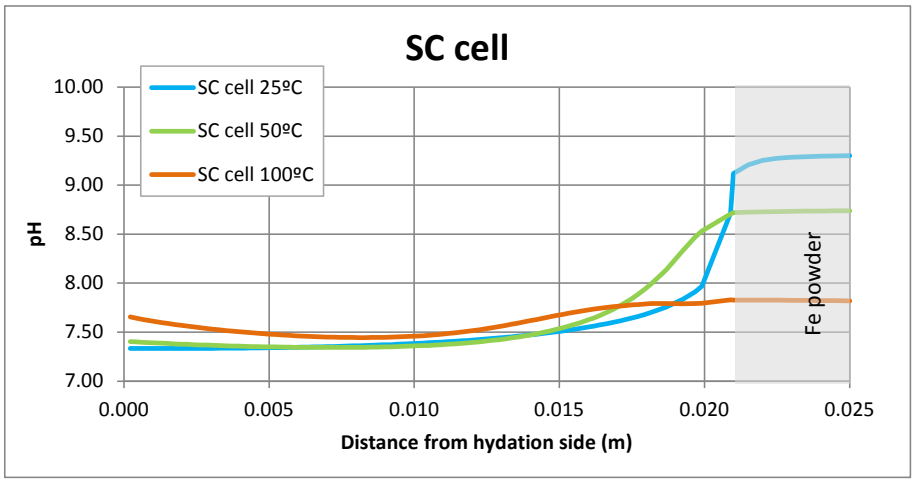

Figure 5-20. Spatial distribution of the computed pH at the end of the tests in the corrosion tests on small cells at 25, 50 and 100ºC.

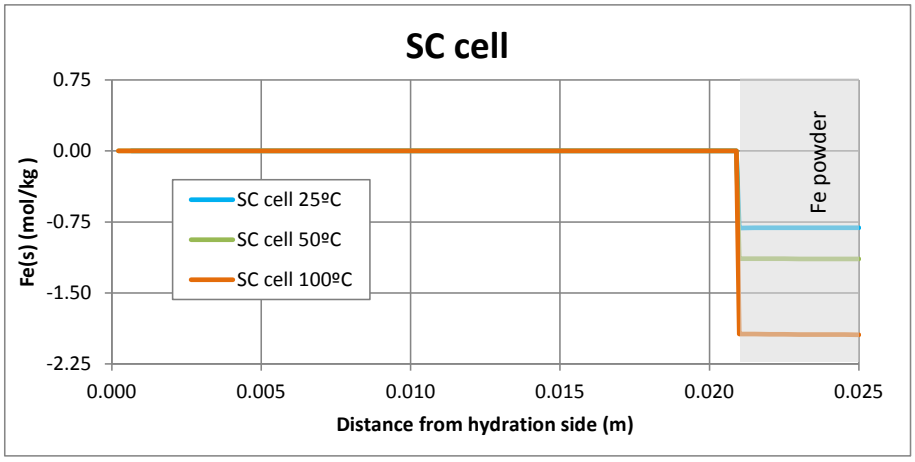

Figure 5-21. Spatial distribution the computed cumulative dissolution for iron at the end of the tests in the corrosion tests on small cells at 25, 50 and 100ºC.

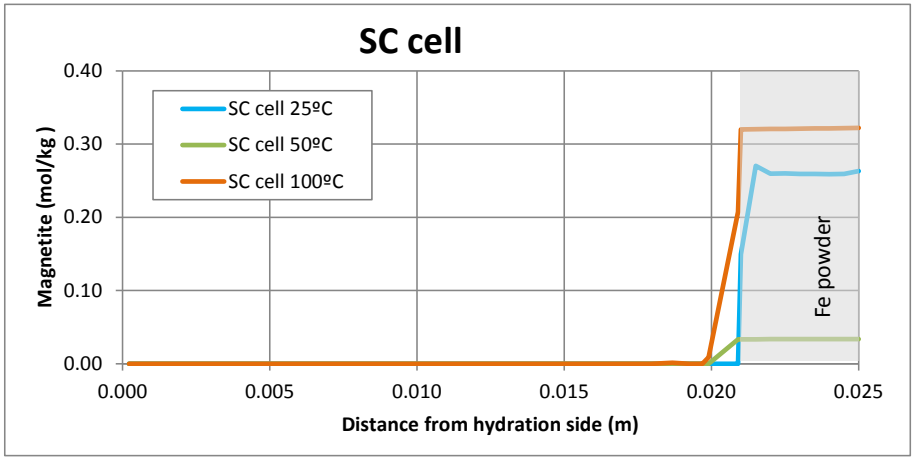

Figure 5-22. Spatial distribution of the computed magnetite cumulative precipitation at the end of the tests in the corrosion tests on small cells at 25, 50 and 100ºC.

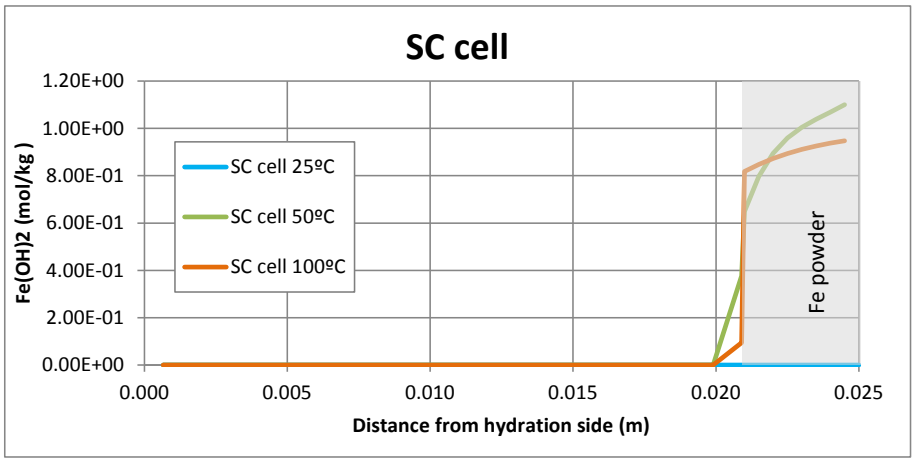

Figure 5-23. Spatial distribution of the computed $Fe(OH)_2(s)$ cumulative precipitation at the end of the tests in the corrosion tests on small cells at 25, 50 and 100ºC.

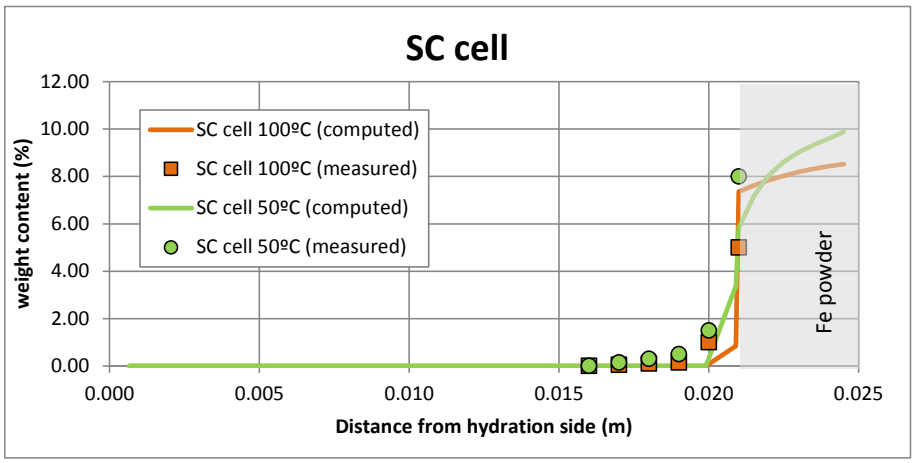

Figure 5-24. Spatial distribution of the computed (lines) and the measured (symbols) iron weight at the end of the tests in the corrosion tests on small cells at 50 and 100ºC.

5.3 Medium size corrosion test

5.3.1 Introduction

The medium-size cells for corrosion studies, FB, are 10 cm long. These tests were performed by Ciemat with bentonite and Fe powder.

The bentonite samples were hydrated and heated at 100ºC. These tests were performed during the NFPRO and PEBS projects.

A THC(m) model was performed for one of the FB cells, the FB3 cell. This test lasted 4 years and was dismantled within the PEBS project.

5.3.2 Test description

The corrosion tests on medium cells, FB cells, were performed at the Ciemat facilities and were dismantled during the PEBS project. The cell contains a 86.8 mm long sample of compacted FEBEX bentonite and a layer of 13 mm of carbon-steel powder (Figure 5-25). The external cylindrical cell was made out of Teflon to prevent the deformation. The tests were performed at anoxic conditions for several durations ranging from 6 months to 4.5 years. FB1 (6 months) and FB2 (15 months) were dismantled during the NFPRO Project while FB3 cell was dismantled within PEBS Project. Contrary to the SC cells, FB cells did not reach saturation at the end of the test.

A hydration system was installed on the top of the cell to maintain the temperature of the water at 22ºC. A heater plane at the bottom of the cell fixed the temperature at 100ºC. The hydration water was injected by a steel distribution plate at a pressure of 600 kPa. The bentonite blocks were initially compacted to a dry density of 1.65 g/cm^3 and had an initial gravimetric water content of 0.14.

The hydration water was Grimsel water. Its chemical composition is listed in Table A2-1.

The relative humidity and the temperature were measured on line in two sensors located at 18 mm and 74 mm from the heater. Bentonite samples were taken at the end of the test to measure water content, dry density, exchanged cations and soluble salts.

The interactions of the bentonite-corrosion products are different for a saturation or dry situation of the Fe powder. The relative humidity plays an important role in the Fe oxidation (Torres et al., 2013). High relative humidity allows the formation of more crystalline phases. In the 6-month test (FB1 cell) goethite was formed; in the 15-month test (FB2 cell) hematite precipitated; and in the 52-months test (FB3 cells) lepidocrocite, goethite, akaganeite and magnetite were found at the bentonite-iron contact. In summary, goethite precipitates at early times in the absence of water. Then, hematite precipitates due to the degradation of the goethite. This corrosion mechanism is produced by the water vapor as the oxidizing agent. Finally, the magnetite, the more stable phase, precipitates.

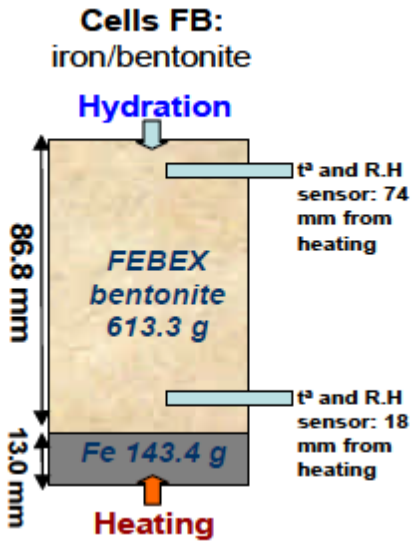

Figure 5-25. Scheme of the corrosion tests on medium cells (Turrero et al., 2011).

5.3.1 Available data

Available data include: 1) Porosity, temperature, relative humidity and concentrations of the soluble salts and pH at the end of the tests; and2) Time evolution of temperature and relative humidity in the sensors.

Measured relative humidity in the sensor located near the heater could have measurement errors due to the leakage of vapour through the sensor gap.

5.3.2 Model description

The numerical model was performed with a one-dimensional finite element mesh (Figure 5-26). The model includes the bentonite and the Fe powder. A liquid pressure of 600 kPa and a temperature of 22ºC were prescribed at the top of the cell. A temperature of 100ºC was fixed at the heater. The model simulates the heating and hydration during 1593 days.

The main THMC model parameters of the bentonite and Fe powder are listed in Table A1-1, Table A1-2, Table A1-3 and Table A1-4 in Appendix A. The vertical displacement was disabled at the top of the cell. The total stress is fixed to 250 kPa.

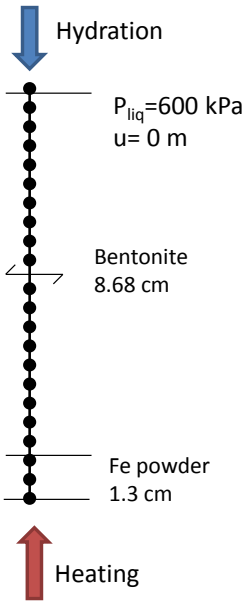

Figure 5-26. One dimensional finite element mesh for the numerical model of the corrosion test on the FB3 cell.

Bentonite has an initial porosity of 0.4 and an initial gravimetric water content of 14%, which corresponds to a saturation of 57% and a suction of $1.27 \cdot 10^5$ kPa. As an educated guess, the Fe powder is assumed to have an initial porosity of 0.38 and a saturation of 31%. The initial temperature in the cell is equal to 22ºC. The initial gas pressure is equal to the atmospheric pressure. The transport boundary conditions, the diffusion coefficients and the geochemical data are similar to those of the SC cell model.

The mineral precipitation/dissolution was considered at chemical equilibrium except for the corrosion of Fe(s). The following secondary minerals were considered in the model: magnetite, goethite, siderite and $Fe(OH)_2$(s). Magnetite is the most relevant corrosion product in these tests. Fe(s) corrodes with a constant kinetic rate of $-4 \cdot 10^{-12}$ mol/m^2/s which corresponds to 0.15 µ/year which is similar to that of the SC cells. The specific surface of the iron powder is $2.15 \cdot 10^5$ m^2/m^3.

5.3.3 Model results of the FB3 cell

5.3.3.1 Thermo-hydro-mechanical results

Figure 5-27 to Figure 5-30 show the spatial evolution of measured and computed volumetric water content, porosity, temperature and relative humidity at the end of the test (1593 days). The computed volumetric water content is smaller than

the measured data in the hydration side and slightly higher in the Fe powder (Figure 5-27).

The computed porosity is smaller than the porosity measured data (Figure 5-28). Water content near the hydration side is larger than near the heater because because porosity increases near the hydration zone (Figure 5-27 and Figure 5-28). Water evaporates near the heater. The vapour diffuses and condensates in a colder location.

The computed relative humidity and temperature reproduce the measured data at the end of the test (Figure 5-29 and Figure 5-30).

Figure 5-31 shows the time evolution of the computed and measured temperature in the sensors. The computed temperature is slightly larger than measured data in the sensors. The evolution of the computed relative humidity in the sensor near the heater does not reproduce the measured relative humidity data (Figure 5-32). This discrepancy could be due to problems in the water injection system during the tests or vapour leakage through the sensors.

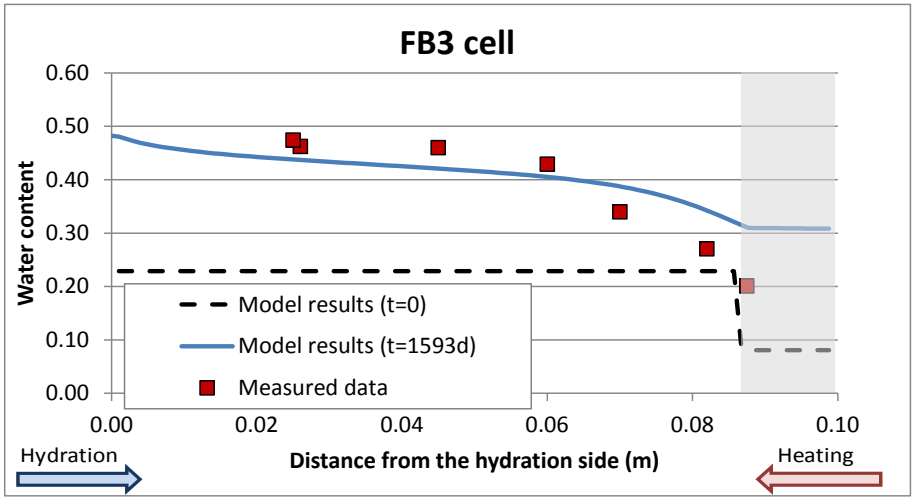

Figure 5-27. Spatial distribution of the measured (symbols) and the computed (line) volumetric water content at the end of the corrosion test on FB3 cell.

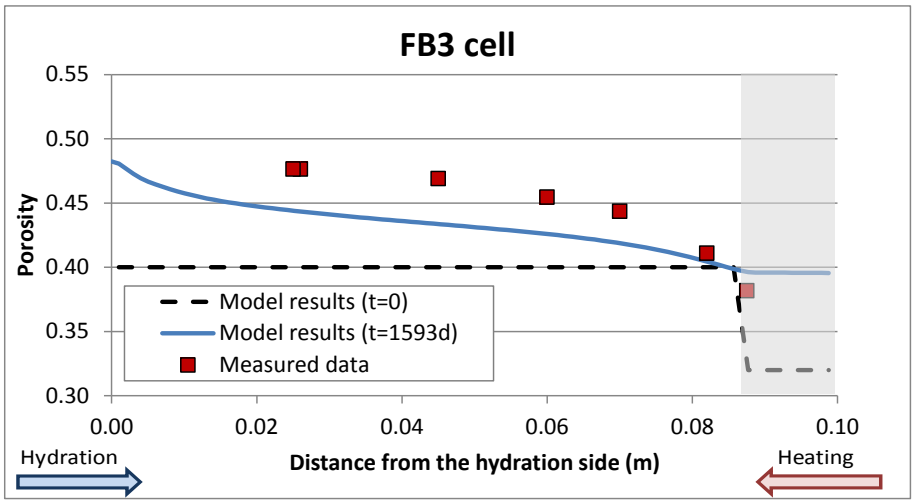

Figure 5-28. Spatial distribution of the measured (symbols) and the computed (line) porosity at the end of the corrosion test on FB3 cell.

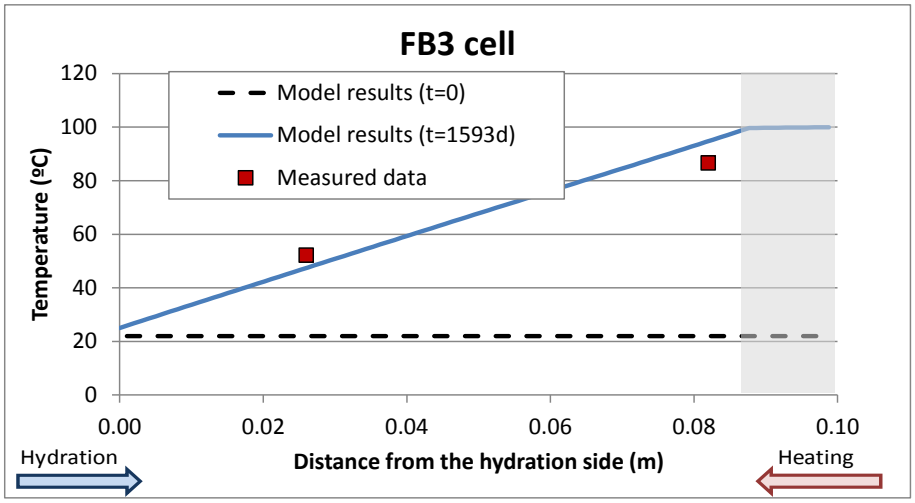

Figure 5-29. Spatial distribution of the measured (symbols) and the computed (line) temperature at the end of the corrosion test on FB3 cell.

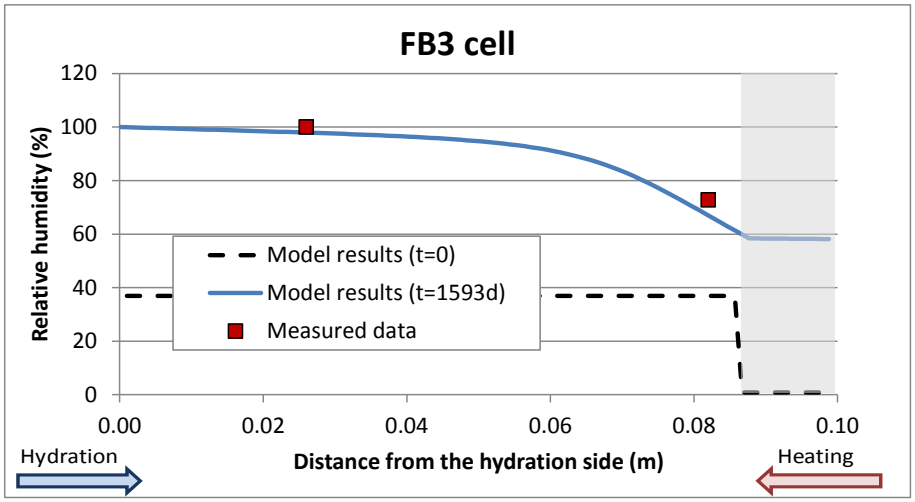

Figure 5-30. Spatial distribution of the measured (symbols) and the computed (line) relative humidity at the end of the corrosion test on FB3 cell.

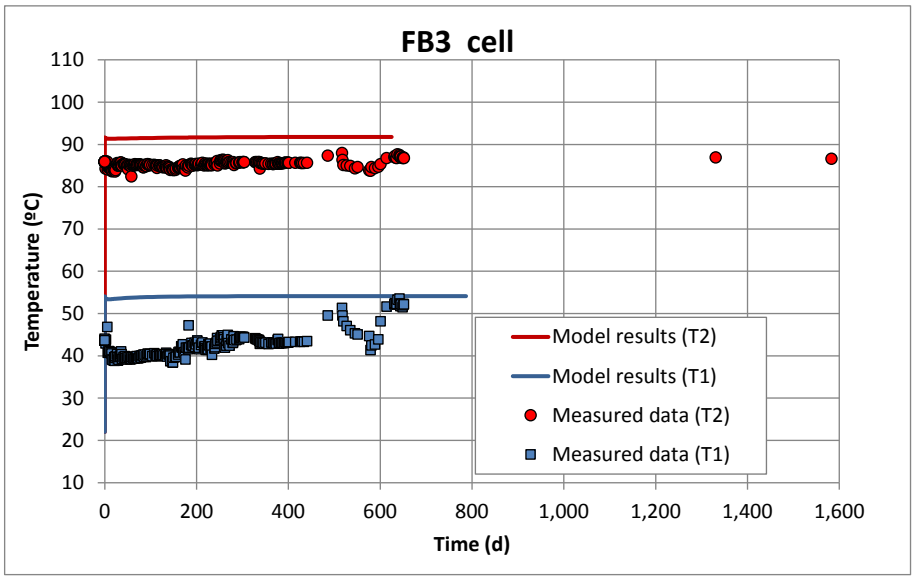

Figure 5-31. Time evolution of the computed (lines) and the measured (symbols) temperature in the sensors T2 (18 mm from heater) and T1 (74 mm from heater) in the corrosion test on FB3 cell.

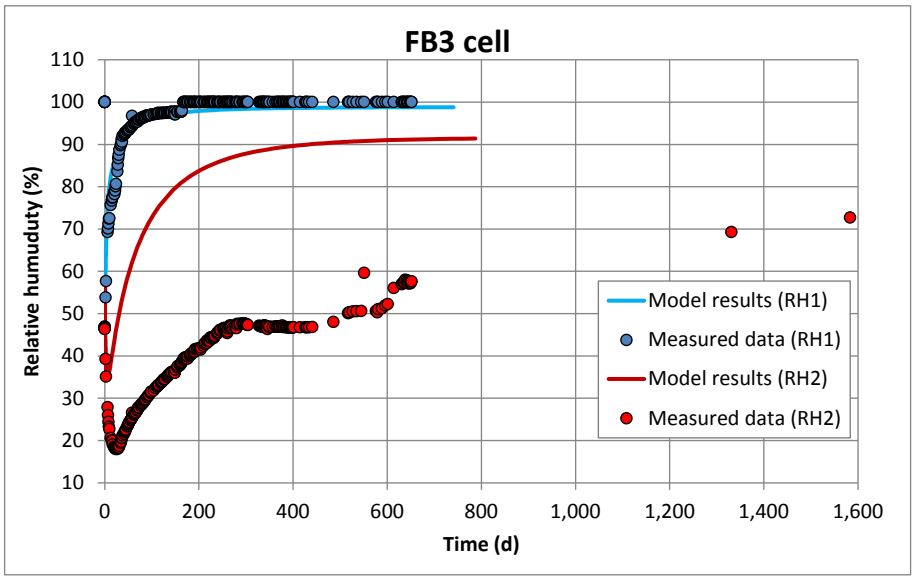

Figure 5-32. Time evolution of the computed (lines) and the measured (symbols) relative humidity in the sensors RH2 (18 mm from heater) and RH1 (74 mm from heater) in the corrosion test on FB3 cell.

5.3.3.2 Chemical results

Figure 5-33 shows the spatial distribution of the computed Cl^- concentration at some selected times. The concentration of Cl^- decreases in the bentonite and it increases near the heater due to water evaporation. The dissolved concentrations of Na^+, K^+, Mg^{2+} and Ca^{2+} show similar patterns (see Figure B2-1 to Figure B2-4 in the Appendix B.2). The concentrations decrease near the hydration boundary and increase near the heater due to the evaporation before 100 days.

The concentration of dissolved sulphate is affected by the dissolution/precipitation of gypsum and anhydrite (Figure B2-5). Gypsum dissolves in the bentonite (Figure B2-9). Anhydrite precipitates near the heater (Figure B2-10).

The concentration of HCO_3^- increases near the hydration side and decreases at the bentonite-iron interface (Figure B2-6). This trend is related to the behaviour of calcite which dissolves near the hydration and precipitates at the interface (Figure B2-8).

The concentration of dissolved silica increases in the bentonite and even more in the Fe powder (Figure B2-7). Quartz dissolves in the bentonite (Figure B2-9). The dissolved SiO_2 moves into the Fe powder where it accumulates.

Figure 5-34 shows the evolution of the concentration of the dissolved Fe^{2+}. The dissolved concentration of Fe^{2+} decreases initially in the Fe powder due to magnetite precipitation. The concentration of Fe^{2+} increases at the final times due to Fe(s) corrosion.

pH is initially equal to 7.72. It decreases in the bentonite before 10 days. Finally pH is about 7.5 in the bentonite and the Fe powder (Figure 5-35).

Figure 5-36 shows the computed Eh. The initial Eh is -0.01 V, and then Eh decreases to a value of -0.6 V.

Fe(s) corrodes at a constant corrosion rate of 0.15 μm/year in the Fe powder (Figure 5-37). Magnetite precipitates in the Fe powder. Magnetite precipitation does not penetrate into bentonite as indicated by the experimental observations (Figure 5-38). Siderite, goethite and $Fe(OH)_2$(s) do not precipitate.

Figure 5-39 shows the computed and measured concentrations of the exchanged Ca^{2+}, Mg^{2+}, Na^+ and K^+ at the end of the test. In general, the computed concentrations of exchanged cations are within the error bands except for Mg^{2+}. The concentration of exchanged Fe^{2+} decreases from its initial value (Figure B2-12). Figure B2-13, Figure B2-14 and Figure B2-15 show the concentrations of sorbed species on strong, weak 1 and weak 2 sites. Fe^{2+} sorption is most important in the strong and weak 1 sites.

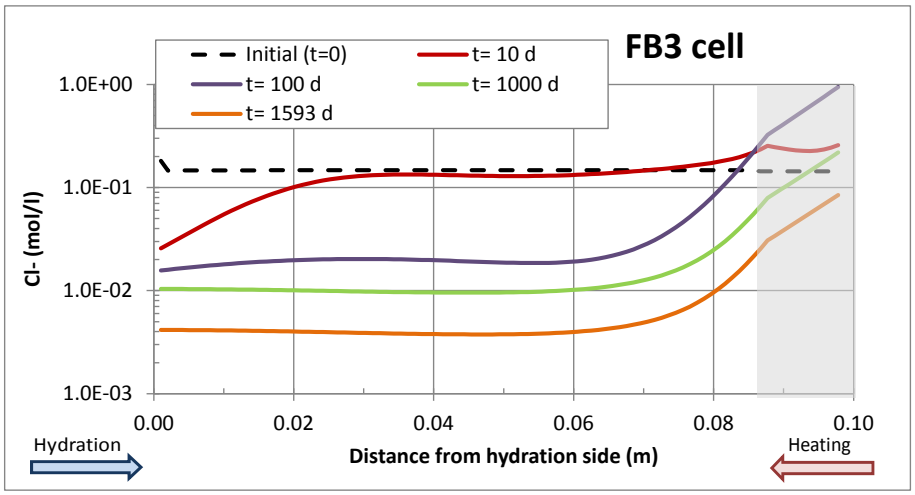

Figure 5-33. Spatial distribution of the computed concentration of dissolved Cl^- at selected times in the corrosion test on the FB3 cell.

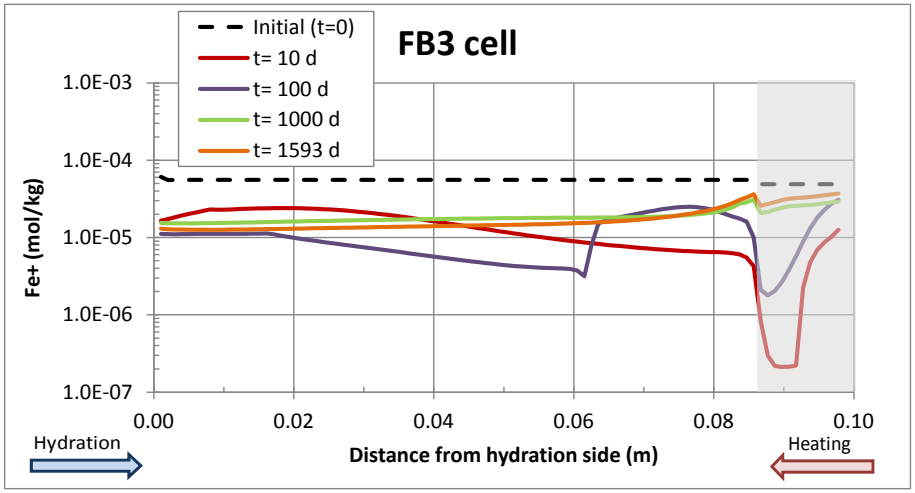

Figure 5-34. Spatial distribution of the computed concentration of dissolved Fe^{2+} at selected times in the corrosion test on the FB3 cell.

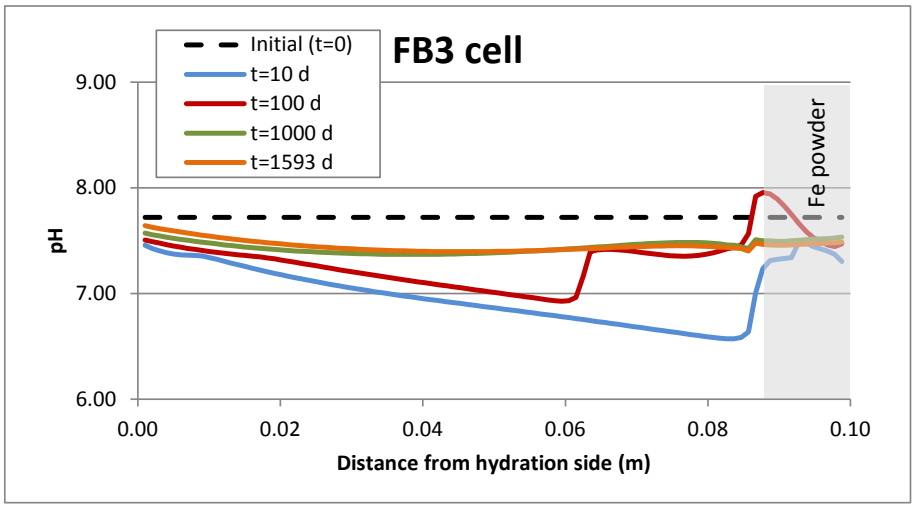

Figure 5-35. Spatial distribution of the computed pH at selected times in the corrosion test on the FB3 cell.

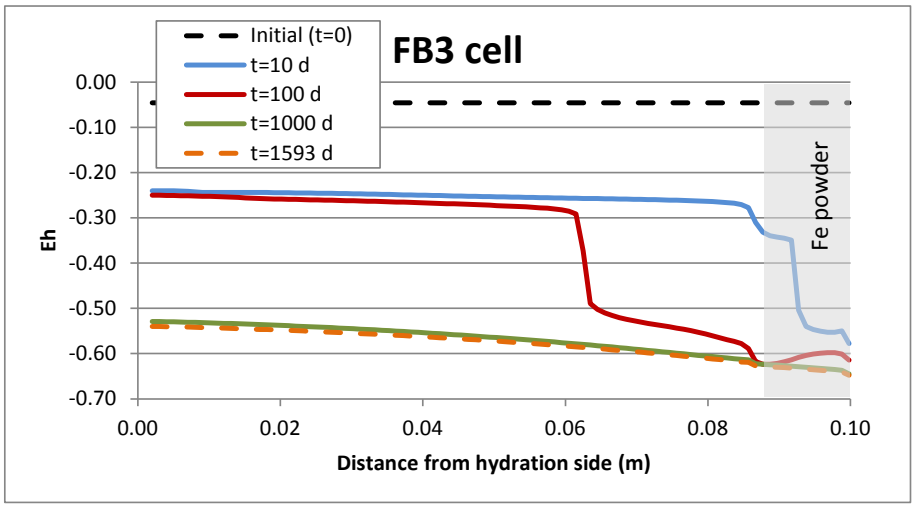

Figure 5-36. Spatial distribution of the computed Eh at selected times in the corrosion test on the FB3 cell.

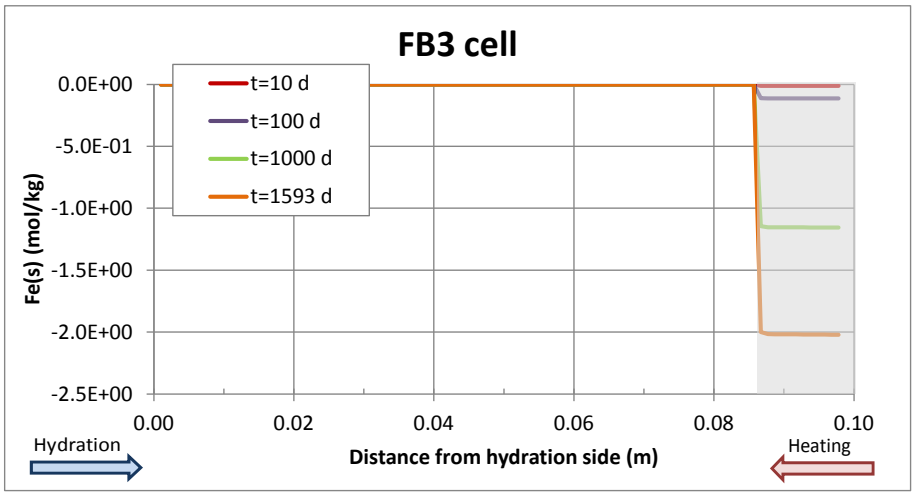

Figure 5-37. Spatial distribution of the computed cumulative dissolution of Fe(s) at selected times in the corrosion test on the FB3 cell.

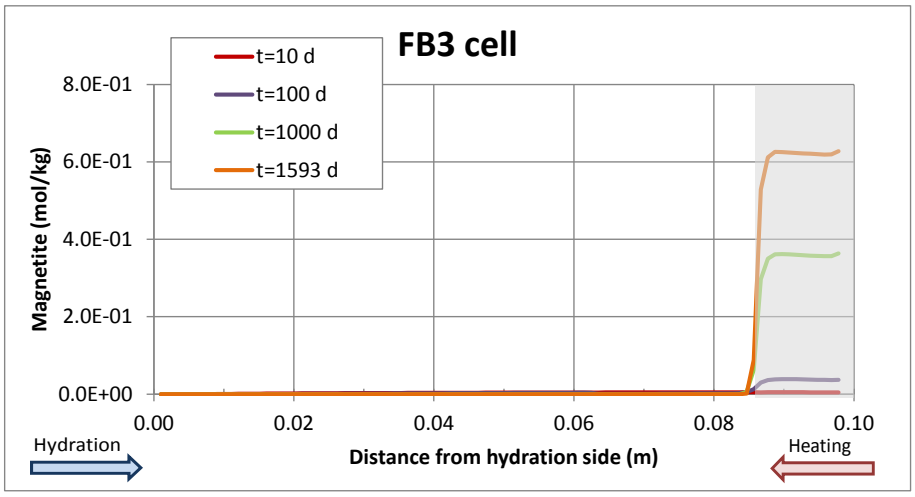

Figure 5-38. Spatial distribution of the computed cumulative precipitation of magnetite at selected times in the corrosion test on the FB3 cell.

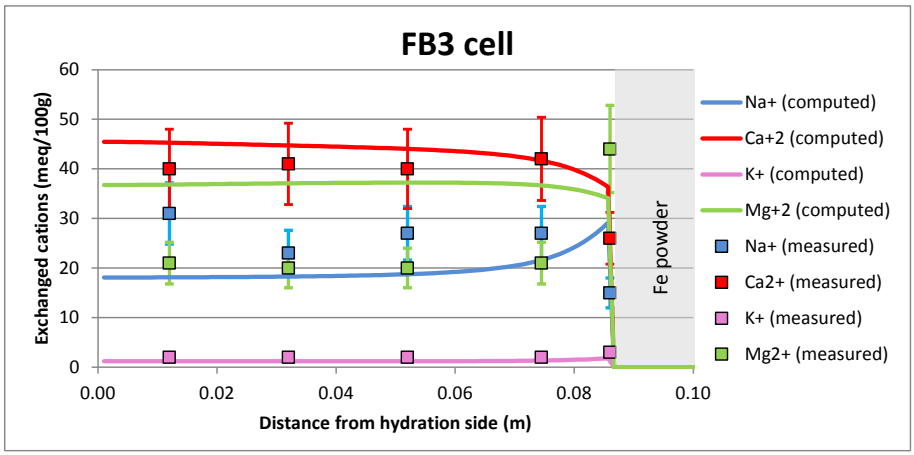

Figure 5-39. Spatial distribution of the computed (lines) and measured (symbols) concentration of the exchanged cations at the end of the corrosion test on the FB3 cell.

5.4 Conclusions

The corrosion tests carried out by CIEMAT have been modelled by UDC with coupled THCm models. Model results of the small cell experiments indicate that:

1) Magnetite and $Fe(OH)_2(s)$ precipitate and compete for Fe^{2+} precipitation. These corrosion products penetrate a few mm into the bentonite.
2) Fe^{2+} is sorbed by surface complexation.
3) Fe^{2+} cation exchange is less relevant than Fe^{2+} sorption.
4) The numerical results fit the measured data of the iron weight for the tests performed at 25º, 50º and 100ºC.

6 THC(m) model of the concrete-bentonite interactions in the HB4 cell

6.1 Introduction

Several sets of tests were performed to study the interactions of concrete and bentonite. The first set of tests aim at studying the interactions of concrete and bentonite porewaters at the conditions prevailing in the EBS during the early hydration stage. This set of tests are denoted as HB and were performed on medium-size cells containing a 7.15 cm thick bentonite sample in contact with a 3 cm thick piece of concrete. The cell was hydrated at a constant pressure at the top of the cell through the concrete while the temperature was maintained constant at 100ºC at the bottom of the cell. This chapter presents the model of test HB4 which lasted for 4.5 years.

6.2 Test description

HB tests were performed on medium-size cells containing a 7.15 cm thick bentonite sample in contact with a 3 cm thick piece of concrete. The cells are cylindrical with and internal diameter of 7 cm and an inner length of 10 cm (see Figure 6-1 from Turrero et al., (2011)). The cells were placed in a Teflon coverture to prevent the lateral heat conduction and the swelling of bentonite. A temperature of 100ºC was imposed at the bottom of the cells and the hydration water had an ambient temperature of 25ºC. The cells contain concrete and bentonite.

The concrete block is 3 cm length. The concrete material is sulfo-resistant ordinary Portland cement (CEM I-SR). The dry density of the concrete was 2.22 g/cm^3 and initial water content was 2.6%. The block of bentonite has a length of 7.15 cm. The FEBEX bentonite has an initial dry density of 1.65 g/cm^3 and a gravimetric water content of13.3%. The HB4 cell was hydrated with the synthetic Spanish Reference Clay porewater (RAF water) at a constant injection pressure of 600 kPa applied on the top of the cell.

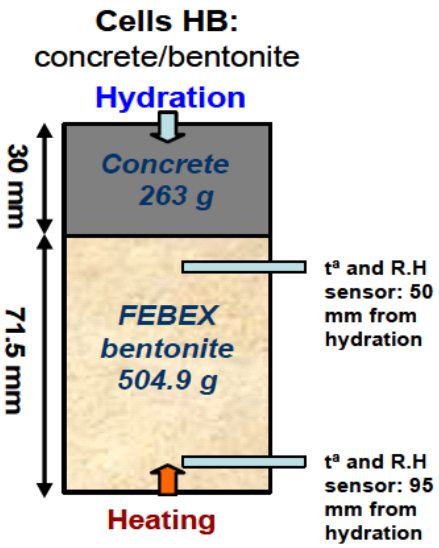

Figure 6-1. Sketch of the concrete-bentonite test on HB4 cell (Turrero et al., 2011).

6.3 Available data

The available measured data are listed in PEBS Project Deliverable 3.3-3-1 (Turrero et al., 2011). Water content and dry density were measured along the cell at the end of the test. Relative humidity and temperature were measured in two sensors during the tests. Sensor 1 was located near the hydration zone (50 mm from hydration) and sensor 2 was near the heater zone (95 mm from hydration side). In the sensor located near the heater system the relative humidity measured values show large data than expected. These data could be affected by vapour which flows throughout the sensor.

The aqueous extract test (AET) method was used to obtain the porewater chemistry of the compacted bentonite. AET is a method to quantify the total content of soluble salts of a clay sample. An 1:R AET consists on adding to a mass Ms of powdered clay sample a mass of distilled water equal to R times Ms. Clay sample and water are stirred during a period of time of usually 2 days during which equilibration of water and clay sample is allowed. Chemical analyses are performed on supernatant solution after phase separation by centrifugation (Sacchi et al., 2001). In addition to dilution, several chemical reactions take place during porewater extraction from clay samples which change the concentrations of dissolved species in a complex nonlinear manner. This makes it difficult to derive the chemical composition of the original (before aqueous extraction) clay porewater from aqueous extract data (Bradbury and Baeyens, 1998; Sacchi et al. 2001). The inference of

dissolved concentration for reactive species requires geochemical modeling based on mineralogical data (Bradbury and Baeyens, 1997, 1998, 2003; Pearson et al., 2003; Fernández and Rivas, 2005; Zheng et al., 2008). Due to that, these measured aqueous species concentration were not considered in the model calibration.

The main experimental observations on the mineral patterns in the concrete and the bentonite at the end of the HB4 test were compared with the computed values of dissolved/precipitated mineral phases.

6.4 Model description

The model includes two materials, concrete (from 0 to 3 cm), and the bentonite (from 3 to 10.15 cm). The model was performed with a 1D mesh (Figure 6-2).

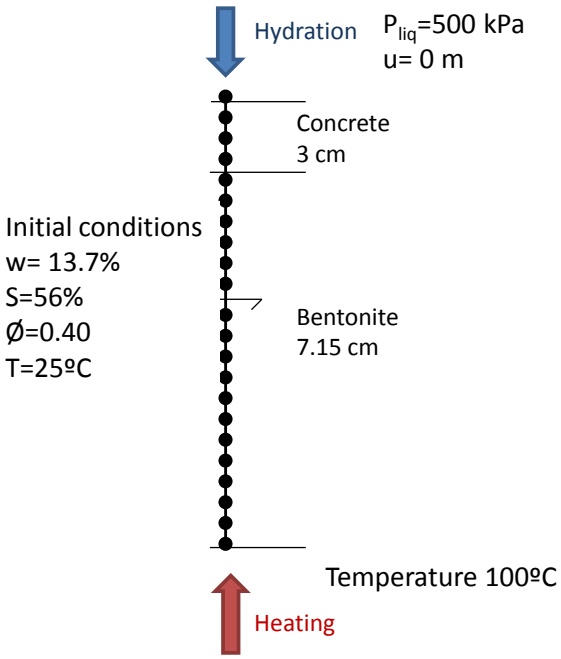

Figure 6-2. One dimensional finite element mesh and boundary conditions for the numerical model for the HB4 tests.

A preliminary model of the HB4 cell was performed first. The model considered a simplify geochemistry system and not considered the concrete as a THM material. The geochemical system did not considered Al^{3+} primary and secondary species and Al^{3+} minerals. This preliminary model showed some conclusions such as:

1) Convergence problems occur at the contact bentonite-concrete, and the the hydration and heater boundaries.

2) The increase in the convergence tolerance aggravates the convergence problems
3) An initial speciation of the initial pore water composition should always be performed to improve the convergence.
4) A mesh with more than 150 nodes increases a lot the CPU time

After this firs attempt a more complex model was performed for the HB4 test. This model includes aqueous aluminium species and aluminium minerals. The concrete was considered as a distinct material with its physical, thermal and mechanical properties. Bentonite parameters were taken from those of the CT23 model (Zheng et al., 2010). The parameters for the concrete were derived from laboratory experiments (Villar et al., 2012; Villar, 2013) and from the model of El Cabril (Ayora et al., 2007). Hydro-thermal-mechanical parameters for bentonite and concrete are listed in Tables from Table A1-1 to Table A1-4. The vertical displacement of the concrete is considered null and the movement and swelling of the bentonite is allowed.

An ambient temperature of 22ºC was imposed in the node where is applied the water injection and a temperature of 100ºC is imposed in the heater side. The numerical models account for the heating as well as for the cooling phase during two days. There were two sensors installed in the tests at x = 5 and x = 95 cm from hydration boundary. Heat dissipation was modelled with a Cauchy condition according to which the heat outflux, Q_c, is computed from

$$Q_c = \alpha_T (T - T^*) \tag{29}$$

where α_T is the thermal coefficient (calibrated to a value of 1016 W/ºC) and T^* is the external temperature which is equal to the mean temperature measured in the thermal sensors.

The initial porosity of the bentonite is 0.4 and the initial water content is 13.3%, which corresponds to a saturation of 57% and a suction of $1.27 \cdot 10^8$ Pa.

The concrete has a porosity of 0.125, a gravimetric water content of and 2.2% and a saturation of 45%. The initial temperature is 22ºC along the cell.

The gas pressure is the atmospheric pressure during the test.

The initial stress assumed uniform and isotropic and is equal to $2.5 \cdot 10^5$ Pa.

The liquid pressure in the injection tank was equal to 500 kPa initially. However, there were some evidences such as a decrease in relative humidity after 400 days,

which indicates that the water injection could have decreased. For this reason the pressure was imposed to be smaller than the initial measured. The liquid pressure at the injection boundary was prescribed at 100 kPa.

A Neuman transport boundary condition was used for solute transport according to which solute flux is equal to the product of water flux times solute concentration of inflow water. The thermo-osmosis was considered in the model. The thermo-osmosis permability was derived from Zheng et al. (2010) and is equal to $4.2 \cdot 10^{-13}$ $m^2/K/s$. The effective diffusion coefficient for all species was considered equal to $2 \cdot 10^{-10}$ m^2/s, except to the Cl^-, which is considered $9.2 \cdot 0^{-11}$ m^2/s.

The chemical composition of the bentonite, concrete and hydration water is listed in Table A2-1 of Appendix A. The porewater composition of the bentonite at a water content of 13.3% was derived from Fernández et al. (2001). The initial chemical composition of the concrete porewater for the HB4 test was derived from Yang et al. (2008). It is assumed that the concentration of dissolved Ca^{2+} is controlled by local chemical equilibrium with respect to portlandite, HCO_3^- is at equilibrium with respect to calcite, Mg^{2+} with brucite, SO_4^{2-} with ettringite and SiO_2(aq) with C1.8SH. The hydration water has the composition of the synthetic Spanish Reference Clay porewater (Turrero et al., 2011).

The initial mineral volume fractions in the bentonite and in the concrete are listed in Table 6-1. Secondary minerals in the model include: anhydrite, sepiolite, anorthite and C0.8SH. The dissolution/precipitation of portlandite, ettringite, C1.8SH, C0.8SH, quartz and cristobalite is kinetically controlled. The following kinetic rate law was used:

$$r_m = k_m e^{-\frac{Ea}{RT}} (\Omega_m{}^{\theta} - 1)^{\eta} (a_{H^+})^n \qquad (30)$$

where r_m is the dissolution/precipitation rate ($mol/m^2/s$); k_m is the kinetic rate constant ($mol/m^2/s$) at 25ºC, Ω_m is the ratio between the ion activity product and the equilibrium constant (dimensionless) and θ and η are parameters of the kinetic law. $e^{-\frac{Ea}{RT}}$ is the thermodynamic factor, which takes into account the apparent activation energy of the reaction, Ea, and R and T are the gas constant and the absolute temperature, respectively. $(a_{H^+})^n$ is the proton activity raised to the power n.

The kinetic parameters of portlandite, ettringite, C1.8SH, C0.8SH, quartz and cristobalite are listed in Table 6-2. The activation energy and the kinetic rate constants were taken from Fernández et al., (2009). The specific surface of the

minerals were calibrated. The only mineral which considers the proton activity term is quartz.

The Gaines-Thomas convention was used for cation exchange. Surface complexation reactions are modeled with triple-site models (Bradbury and Baeyens, 1997). The cation exchange capacity (CEC), the initial concentration of the exchanged cations and the total concentration of sorption sites for the triple-site sorption model in bentonite are listed in Table A2-2 and Table A2-3 in Appendix A. The chemical reactions and their equilibrium constants at 25 ºC for aqueous complexation and mineral dissolution/precipitation as well as selectivity coefficients for exchanged cations and protolysis constants for surface complexation reactions are also listed in Table A2-4 to A2-7 of Appendix A.

Table 6-1. Initial mineral volume fractions (%) for numerical model of the HB4 cell.

Bentonite		**Concrete**	
Calcite	0.36	Calcite	0.1
Gypsum	0.08	Portlandite	7.4
Cristobalite	1.19	Brucite	1.0
		C1.8SH	14.6
		Ettringite	2.2
-	-	Quartz	62.2

Table 6-2. Kinetic parameters for the mineral phases of the numerical model of the HB4 cell (Fernández et al., 2009; Palandri and Kharaka, 2004).

Mineral	**Activation energy (kJ/mol)**	**k_m (mol/m^2/s)**	**θ**	**η**	**n**	**Specific surface (dm^3/kg of soil)**
Portlandite	41.86	$1.0\cdot10^{-8}$	1	1	-	2.0
Ettringite	41.86	$1.0\cdot10^{-8}$	1	1	-	$1\cdot10^{-4}$
C1.8SH	41.86	$1.0\cdot10^{-7}$	1	1	-	$1\cdot10^{-1}$
C0.8SH	41.86	$1.0\cdot10^{-7}$	1	1	-	$1\cdot10^{-1}$
Quartz	95.79	$5.13\cdot10^{-17}$	1	1	0.55	1.0
Cristobalite	65.0	$5.0\cdot10^{-13}$	1	1	-	$2\cdot10^{-2}$

6.5 Model results

6.5.1 Thermo-hydro-mechanical results

Figure 6-3 shows the spatial distribution of the computed and measured volumetric water content at some selected times. Water content increases with time

in the concrete-bentonite interface reaching a maximum value of 0.5 after 7 days while at that time the water content near the heater decreases to 0.1 due to water evaporation. Later, it increases to its initial value at t = 1610 days. The computed water content is slightly smaller than the measured values in the concrete-bentonite interface while the computed water content is larger than measured values near the heater. Figure 6-4 shows the spatial distribution of the computed saturation degree. The concrete saturates completely after a few days. The concrete-bentonite interface shows a similar trend. The bentonite desaturates near the heater reaching a value of 0.39 below its initial value of 0.57. Later, the saturation increases with time in the bentonite.

Figure 6-5 shows the spatial distribution of the computed and measured porosity at some selected times. The porosity of the concrete does not change because deformation is not allowed. Bentonite porosity increases near the concrete-bentonite interface due to bentonite swelling and decreases slightly near the heater. In general, the computed porosity reproduces the measured data in the bentonite.

Steady-state temperatures are reached in a few minutes. Figure 6-6 shows the spatial distribution of the computed and measured temperatures at t = 1610 days. The computed temperature at that time in the hydration side is 25ºC, in the concrete-bentonite interface is 35ºC and near the heater is 90ºC. The computed temperatures reproduce the measured values in the two sensors.

Figure 6-7 shows the spatial distribution of the computed and measured final relative humidity at t = 1610 days. The computed relative humidities fit the measured values.

The time evolution of the computed and measured temperature and relative humidity at the two sensors of the HB4 cell are shown in Figure 6-8 and Figure 6-9. The computed temperatures reproduce well the measured data at the sensors. The computed relative humidities, however, reproduce only the measured data in the sensor near the hydration zone (sensor 1) but not in sensor near the heater (sensor 2). These discrepancies in the sensor 2 could be due to sensor measurement problems during the test.

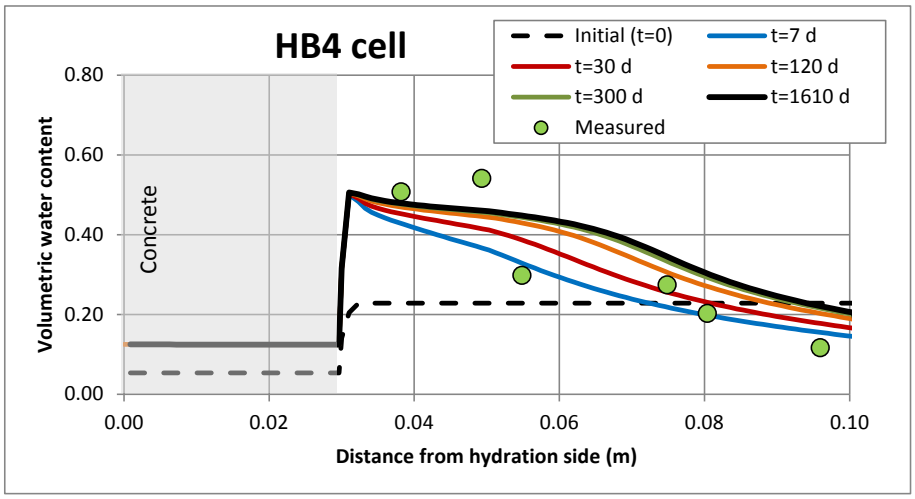

Figure 6-3. Spatial distribution of the computed (lines) and the measured (symbols) volumetric water content of the HB4 cell.

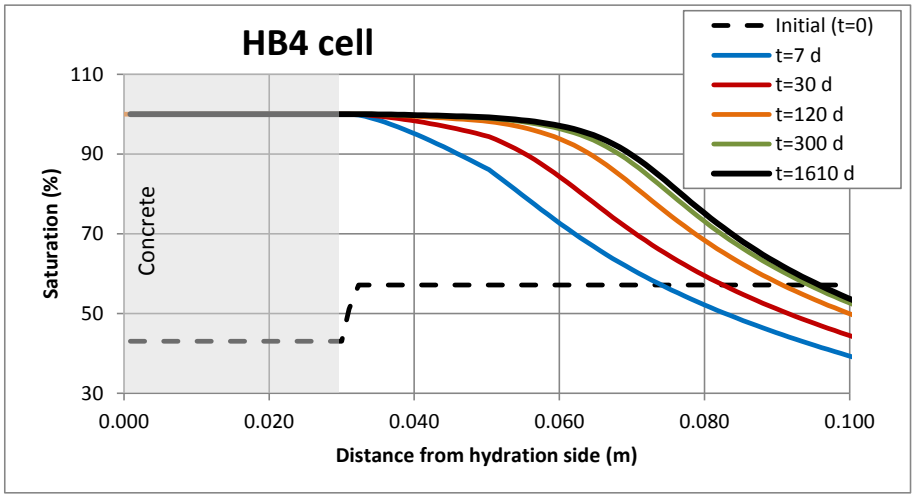

Figure 6-4. Spatial distribution of the computed saturation degree of the HB4 cell at some selected times.

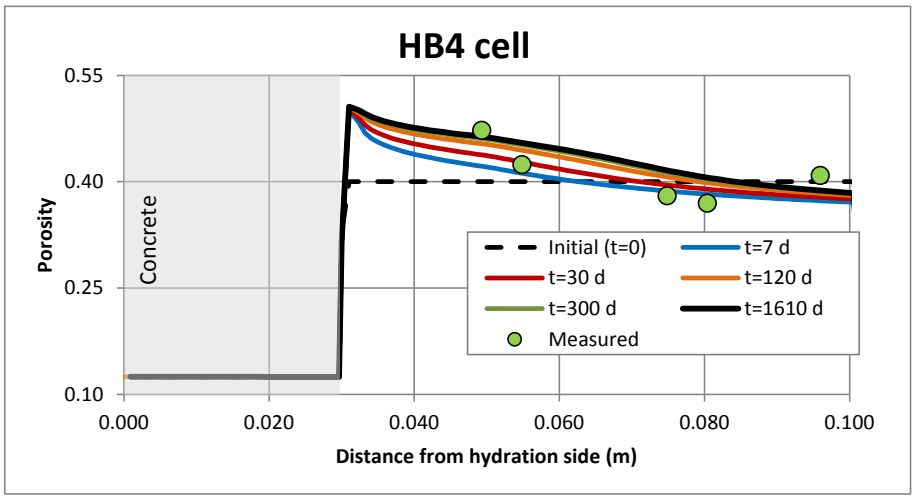

Figure 6-5. Spatial distribution of the computed (lines) and the measured (symbols) porosity of the HB4 cell.

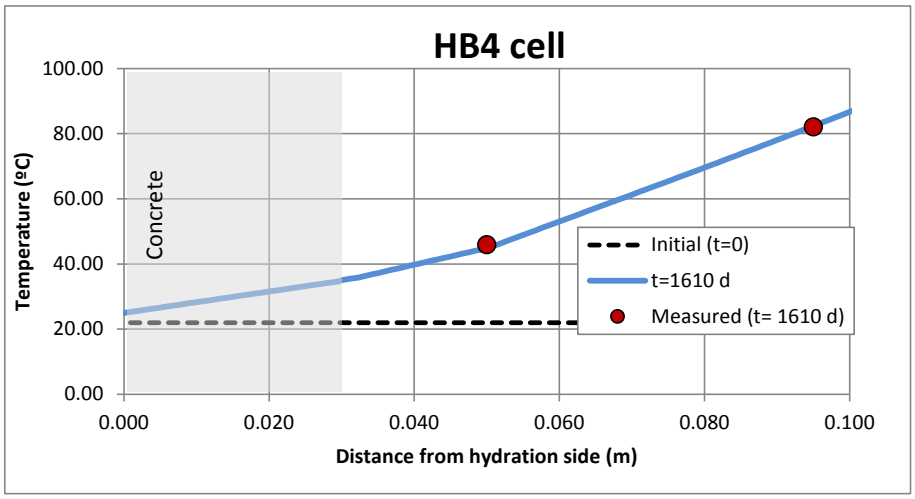

Figure 6-6. Spatial distribution of the computed (lines) and the measured (symbols) temperature of the HB4 cell at the end of the test.

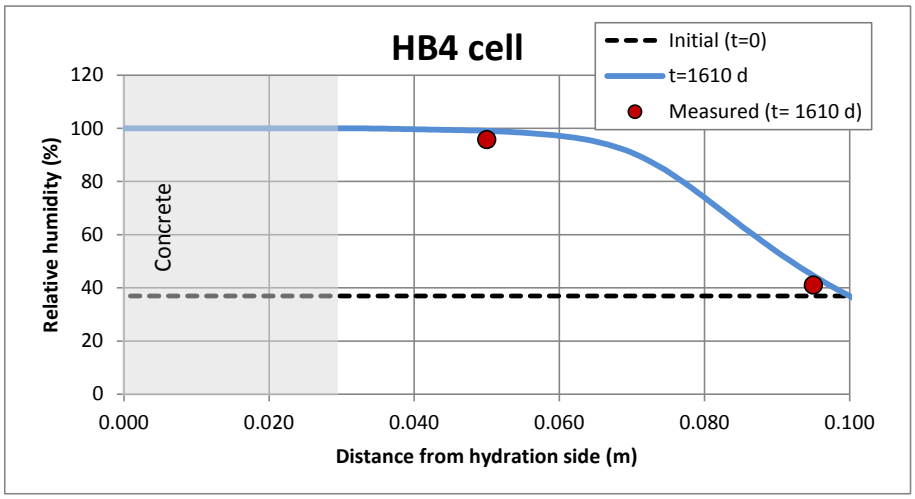

Figure 6-7. Spatial distribution of the computed (lines) and the measured (symbols) relative humidity of the HB4 cell at the end of the test.

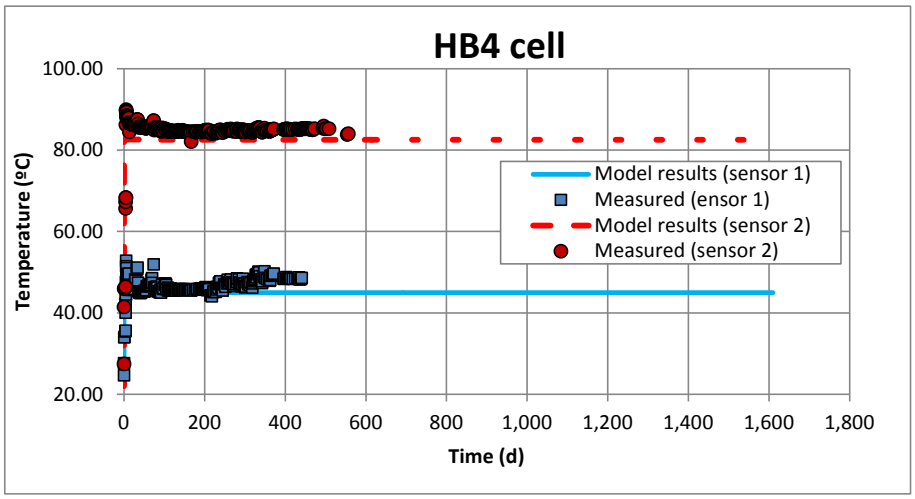

Figure 6-8. Time evolution of the computed (lines) and the measured (symbols) temperature in the sensor 1 (50 mm from hydration) and sensor 2 (94 mm from hydration) of the HB4 cell.

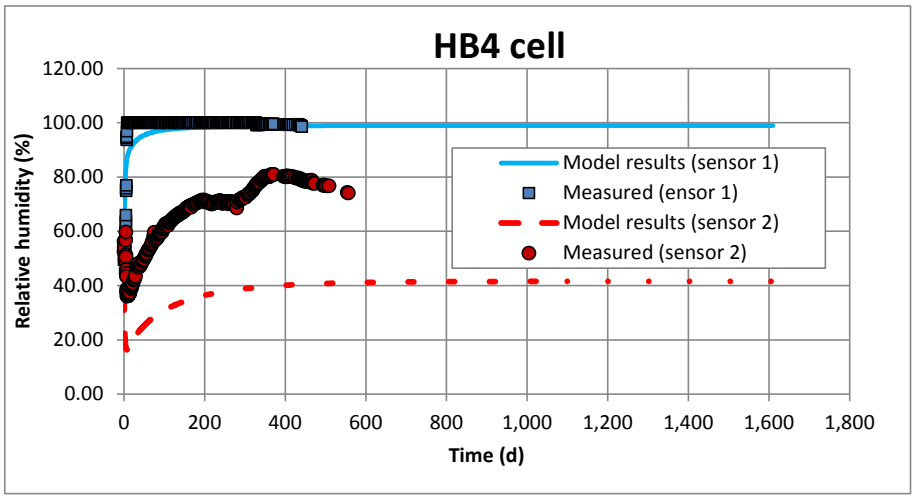

Figure 6-9. Time evolution of the computed (lines) and the measured (symbols) relative humidity in the sensor 1 (50 mm from hydration) and sensor 2 (94 mm from hydration) of the HB4 cell.

6.5.2 Chemical results

One of the main objectives of the THMC model of the HB4 is to test the model results with experimental observations of mineral patterns in the concrete and the bentonite at the end of the test.

Figure 6-10 shows the spatial distribution of the computed cristobalite precipitation/dissolution at t= 1610 days and after the cooling phase. This mineral is initially present only in the bentonite with an initial volume fraction of 1.19%. Its spatial distribution in the bentonite shows some dissolution due to the increase in temperature which is more pronounced near the heater.

Quartz is the main mineral component of the concrete with an initial volume fraction of 62.2% (Figure 6-11). At t = 1610 days this mineral practically does not precipitate or dissolve in the concrete (computed values are in the order of 10^{-14} mol/kg). In the bentonite there is no quartz precipitation.

Figure 6-12 shows the spatial distribution of the computed calcite precipitation/dissolution at t = 1610 days and after the cooling phase. This mineral is initially present in the concrete and in the bentonite with initial volume fractions of 0.1% and 0.36%, respectively. Calcite precipitates slightly in the hydration zone. Calcite precipitation is very large at the concrete-bentonite interface. Calcite dissolves in the rest of the bentonite.

Figure 6-13 and Figure 6-14 show the spatial distribution of the computed portlandite and brucite precipitation/dissolution at t = 1610 days and after the cooling phase. These minerals are initially present only in the concrete with initial volume

fractions of 7.4% and 1.0%, respectively. Portlandite dissolves throughout the concrete, especially near the contact with the bentonite. Brucite precipitates in the hydration zone, in the concrete and especially near the concrete-bentonite interface.

The spatial distribution of the computed gypsum and anhydrite precipitation/dissolution at t = 1610 days and after the cooling phase is presented in Figure 6-15 and Figure 6-16. Gypsum is present initially only in the bentonite with an initial volume fraction of 0.08% while anhydrite is a secondary mineral initially not present. Gypsum precipitates in the bentonite zone in contact with the concrete from t = 7 to t = 30 days while anhydrite starts to precipitate in the bentonite also at t = 7 days producing a precipitation front towards the heater. In the rest of the bentonite, gypsum dissolves until the end of the test. Gypsum precipitates near the heater during the cooling phase.

Figure 6-17 shows the spatial distribution of the computed ettringite precipitation/dissolution at t = 1610 days and after the cooling phase. This mineral is only initially present in the concrete with an initial volume fraction of 2.2%. Ettringite precipitates in the hydration zone and dissolves in the rest of the concrete being more pronounced the mineral dissolution in the contact with the bentonite.

The spatial distribution of the computed C1.8SH and C0.8SH precipitation/dissolution at t = 1610 days and after the cooling phase is presented in Figure 6-18 and Figure 6-19. C1.8SH is present initially only in the concrete with an initial volume fraction of 14.6% while C0.8SH is a secondary mineral not initially considered in the model. C1.8SH precipitates in the concrete near the hydration side (approximately for x < 0.015 m) and dissolves in the rest of the concrete. The largest dissolution rate occurs near the concrete-bentonite interface. C0.8SH precipitates in the concrete in very small amounts.

Figure 6-20 shows the spatial distribution of the computed sepiolite precipitation/dissolution at t = 1610 days and after the cooling phase. This mineral is a secondary mineral not initially considered in the model. Sepiolite precipitates in the bentonite in contact with the concrete. Anorthite, which is another secondary mineral, does not precipitate.

Figure 6-21 shows the spatial distribution of the mineral volume fractions at the final time t = 1610 days. The most abundant minerals initially in the concrete are quartz, C1.8SH and portlandite. In the bentonite the more relevant mineral is

smectite. This mineral is not considered in the model due to its very small dissolution rate.

At the end of the test, the main changes are the increase of the brucite volume fraction in the concrete and in the concrete-bentonite interface and the reduction of the fraction of C1.8SH and portlandite. In the bentonite the most prominent change is the increase of the calcite volume fraction near the contact with the concrete.

Table 6-3 shows a summary of the main experimental observations on the mineral patterns at the end of the HB4 test. For the most part, the numerical model captures the main trends in mineral dissolution/precipitation. However, there are some discrepancies, especially for ettringite and CSH precipitation. For these phases, the numerical model predicts much less precipitation than the observed values.

Figure 6-22 shows the spatial distribution of the porosity changes due to the mineral dissolution/precipitation in the HB4 test. Changes in the porosity occur in three zones of the HB4 cell: (1) The hydration zone, (2) The concrete zone in contact with the bentonite, and (3) The bentonite zone in contact with the concrete. In the hydration zone the porosity decreases mainly due to brucite precipitation. In this zone calcite, ettringite, C1.8SH and C0.8SH precipitation occurs but in a much smaller amount. In the concrete zone in contact with the bentonite, porosity increases due to the combined effect of C1.8SH, portlandite and ettringite dissolution. In the bentonite zone in contact with the concrete, the porosity decreases due to the precipitation of brucite, calcite and sepiolite.

Next, the patterns of the computed concentrations of dissolved species are presented. In order to help the understanding of the chemical evolution of the aqueous species, the concentrations are plotted in natural and logarithmic scales. It is important to point out that the computed concentrations of the aqueous species at t = 0 in the concrete and the bentonite plotted in the figures in Appendix C correspond to the first calculated time once the initial chemical concentration of all aqueous species are equilibrated with the considered initial mineral assemblage. For this reason, the computed concentrations at t = 0 may not coincide with the values listed in Table A2-1 in Appendix A.

Figure 6-23 shows the spatial distribution of the computed Cl^- concentration at some selected times. The computed Cl^- concentration increases with time in the

concrete and decreases in the bentonite. The computed concentrations become uniform in the concrete and the bentonite after 300 days.

The spatial distribution of the computed concentrations of dissolved Na^+, K^+, Ca^{2+}, Mg^{2+}, HCO_3^-, SO_4^{2-}, SiO_2(aq) and Al^{3+} are shown in Appendix C (Figure C-1 to Figure C-8). The computed concentrations of Ca^{2+}, Mg^{2+}, Na^+ and K^+ show similar trends to those of Cl^- (Figure 6-23). In addition to diffusion, these species are subjected to mineral dissolution/precipitation and cation exchange reactions.

The concentration of HCO_3^- in the concrete shows a very large increase at 7 days (Figure C-5). The same effect can be seen in the bentonite zone near the heater. At the other times the profiles are controlled by the dissolution/precipitation of calcite. The distribution of the concentration of SO_4^{2-} is affected by the dissolution/precipitation of portlandite, gypsum, anhydrite, C1.8SH, C0.8SH and ettringite.

The computed SO_4^{2-} concentration at t = 1610 days is the same in the concrete and in the bentonite and equal to 0.1 M.

The computed Al^{3+} concentration increases in the concrete and in the bentonite from 7 to 1610 days reaching finally a uniform profile (Figure C-8). Ettringite dissolution/precipitation governs the concentration of Al^{3+}.

The SiO_2(aq) concentration increases in the concrete due to the dissolution of C1.8SH (Figure C-7) and increases also in the concrete-bentonite interface due to the dissolution of cristobalite.

Figure 6-24 shows the spatial distribution of the computed pH at selected times. The initial pH in the concrete is 12.7 and 7.7 in the bentonite. The pH decreases in the concrete near the contact with the bentonite and increases in the bentonite from 7.7 to 8 at t = 1610 days. The evolution of the alkaline plume can be seen in Figure 6-24. The final pH in the concrete is 12.7 and 11 at the concrete-bentonite interface. It decreases just about from 11 to 8 in the first 2 cm of the bentonite. The pH in the bentonite increases slightly after the cooling phase.

Figure 6-25 to Figure 6-28 show the spatial distribution of the computed and measured concentrations of the exchanged cations at selected times. Cation exchange and sorption reactions are considered only in the bentonite. The computed concentration of exchanged K^+ increases initially in the bentonite near the contact with the concrete and then decreases with time. The computed concentrations of exchanged Ca^{2+} and Na^+ in the bentonite increase with time especially near the

contact with the concrete. The computed concentrations of these three cations reproduce fairly well the measured data. The computed concentrations of exchanged Mg^{2+} decrease with time in the bentonite. The computed values do not match the measured data.

The spatial distribution of the computed concentrations of sorbed species at t = 1610 days is shown in Figure C-9 to Figure C-11 of Appendix C. From the hydration to the heater zone, the concentrations of $S^{s}O^{-}$, $S^{w1}O^{-}$ and $S^{w2}O^{-}$ decrease while those of $S^{s}OH$, $S^{w1}OH$ and $S^{w2}OH$ increase.

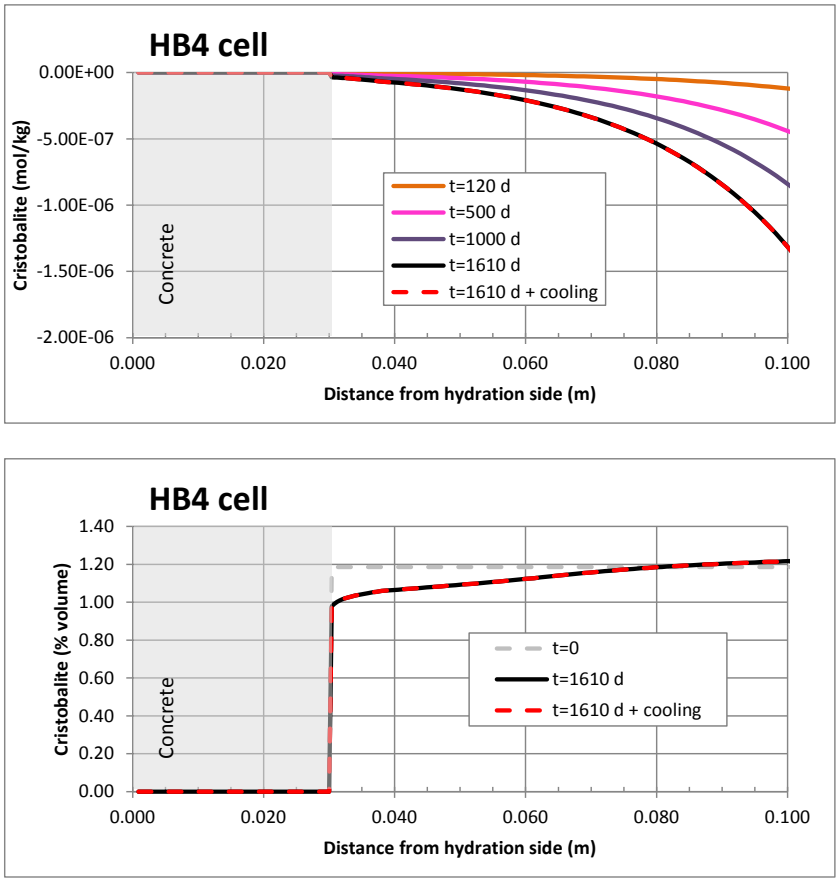

Figure 6-10.Spatial distribution of the computed precipitation/dissolution of cristobalite in the HB4 cell at several times. Cumulative precipitation/dissolution (mol/kg) (top) and volume fraction (bottom). Positive values for precipitation and negative values for dissolution.

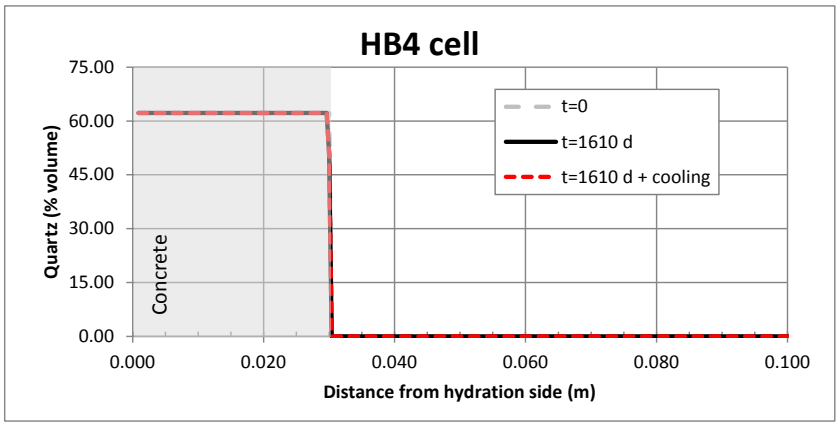

Figure 6-11.Spatial distribution of the computed precipitation/dissolution of quartz in the HB4 cell at several times. Positive values for precipitation and negative values for dissolution.

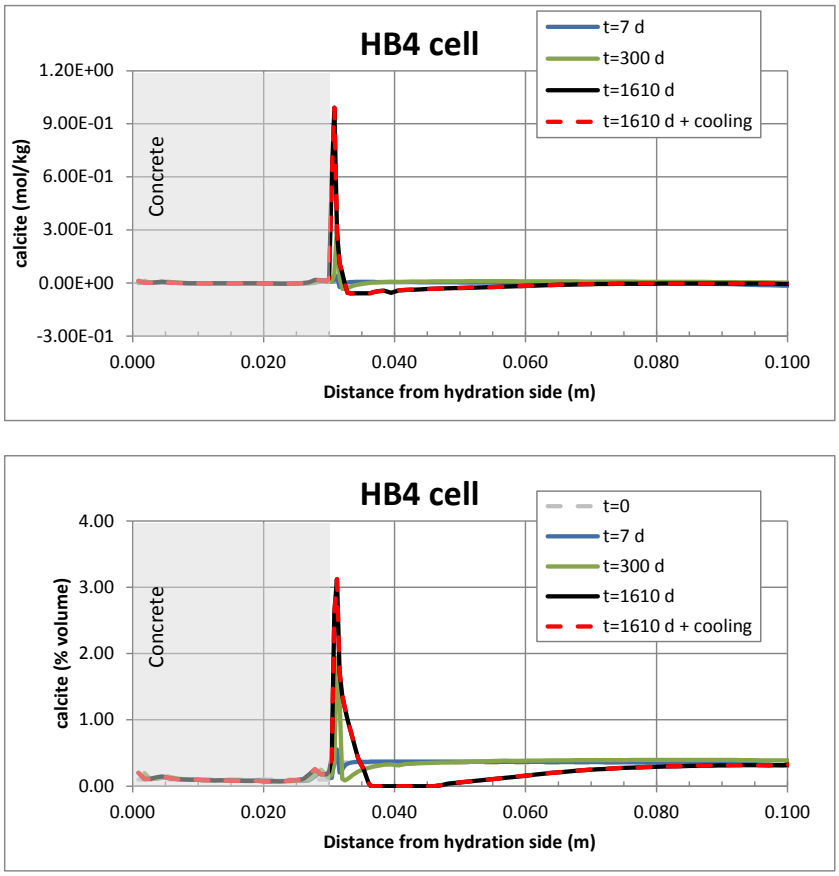

Figure 6-12.Spatial distribution of the computed precipitation/dissolution of calcite in the HB4 cell at several times. Cumulative precipitation/dissolution (mol/kg) (top) and volume fraction (bottom). Positive values for precipitation and negative values for dissolution.

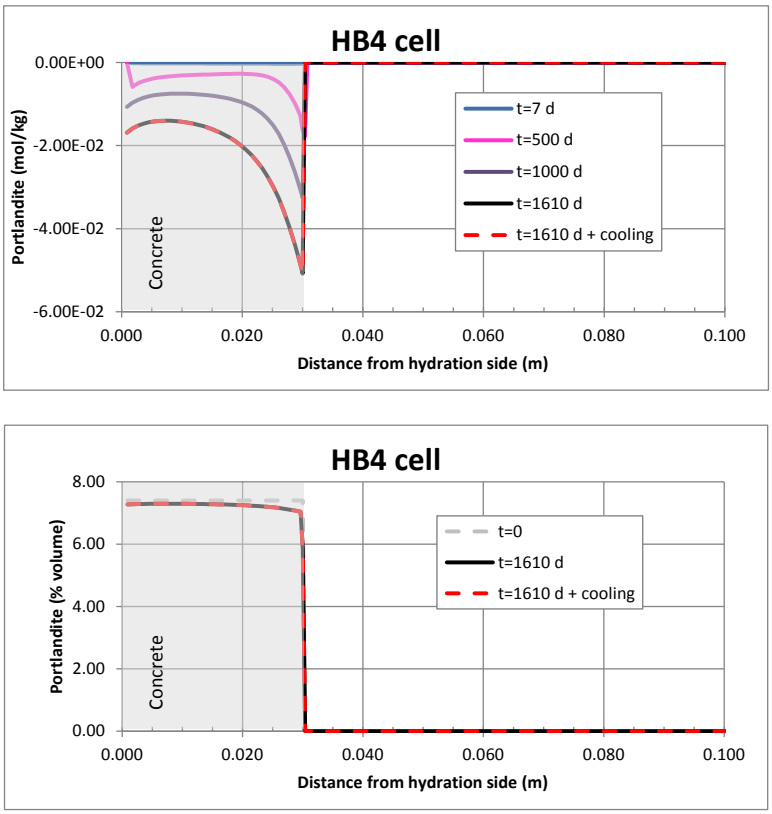

Figure 6-13. Spatial distribution of the computed precipitation/dissolution of portlandite in the HB4 cell at several times. Cumulative precipitation/dissolution (mol/kg) (top) and volume fraction (bottom). Positive values for precipitation and negative values for dissolution.

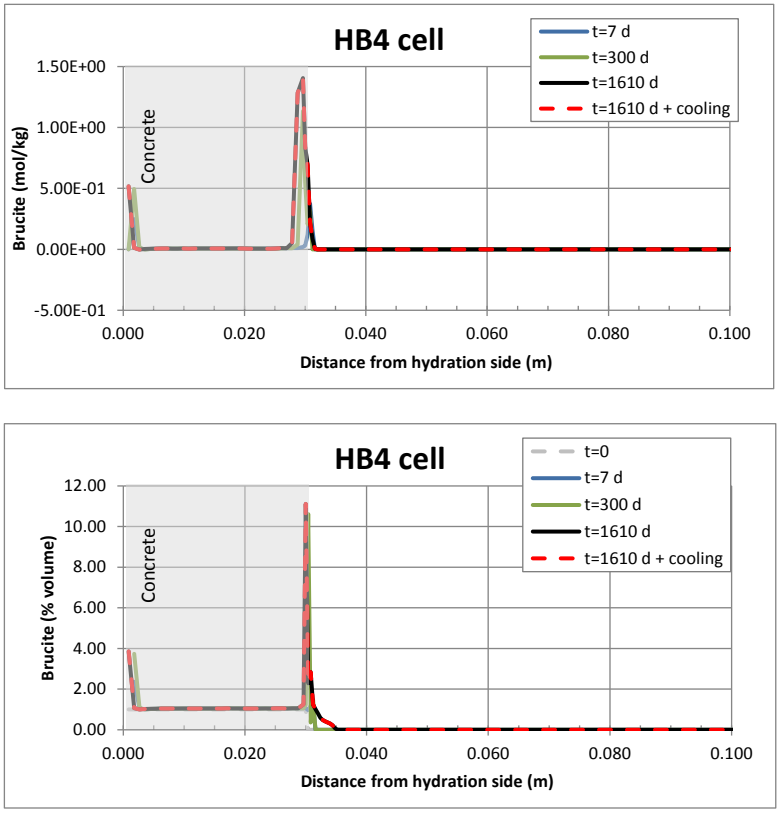

Figure 6-14. Spatial distribution of the computed precipitation/dissolution of brucite in the HB4 cell at several times. Cumulative precipitation/dissolution (mol/kg) (top) and volume fraction (bottom). Positive values for precipitation and negative values for dissolution.

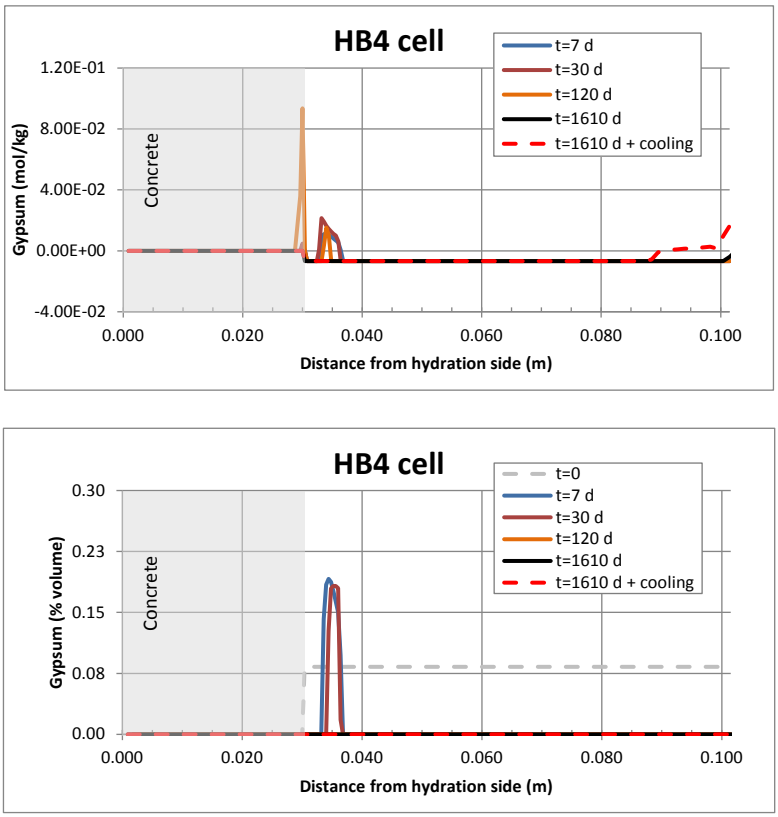

Figure 6-15. Spatial distribution of the computed precipitation/dissolution of gypsum in the HB4 cell at several times. Cumulative precipitation/dissolution (mol/kg) (top) and volume fraction (bottom). Positive values for precipitation and negative values for dissolution.

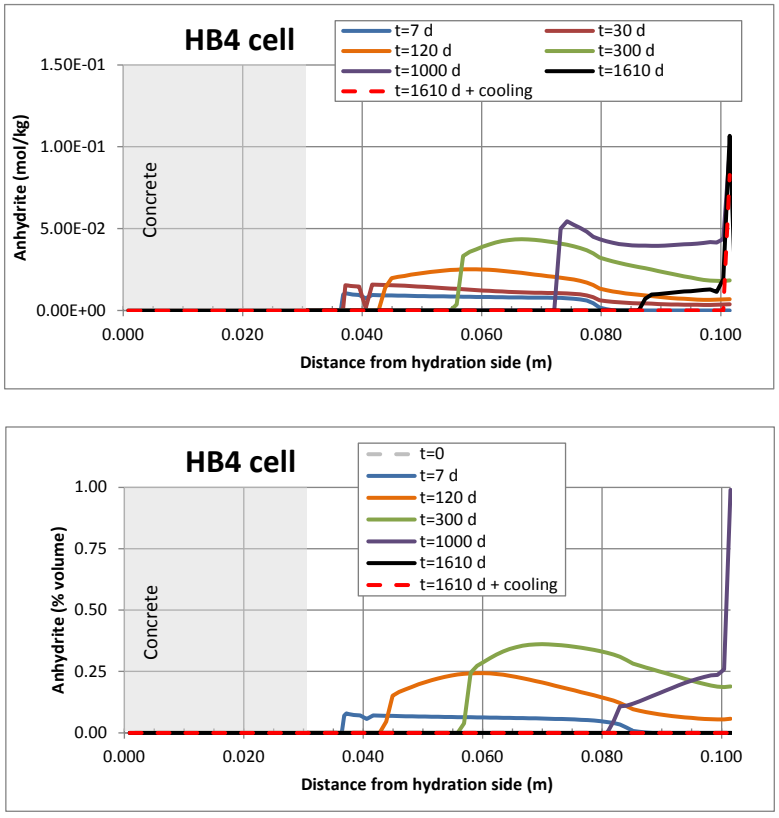

Figure 6-16. Spatial distribution of the computed precipitation/dissolution of anhydrite in the HB4 cell at several times. Cumulative precipitation/dissolution (mol/kg) (top) and volume fraction (bottom). Positive values for precipitation and negative values for dissolution.

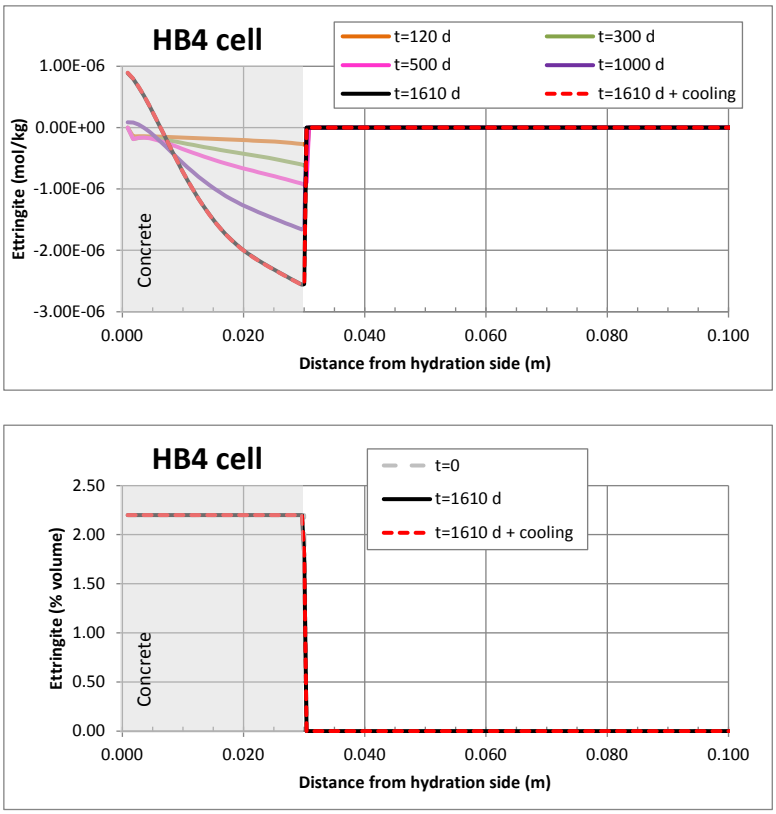

Figure 6-17. Spatial distribution of the computed precipitation/dissolution of ettringite in the HB4 cell at several times. Cumulative precipitation/dissolution (mol/kg) (top) and volume fraction (bottom). Positive values for precipitation and negative values for dissolution.

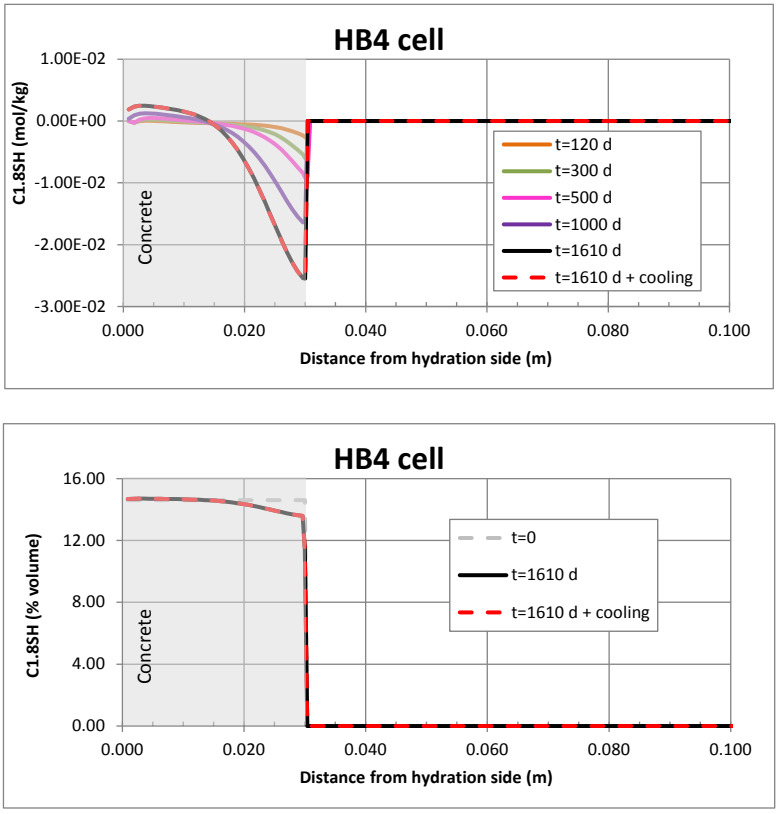

Figure 6-18. Spatial distribution of the computed precipitation/dissolution of C1.8SH in the HB4 cell at several times. Cumulative precipitation/dissolution (mol/kg) (top) and volume fraction (bottom). Positive values for precipitation and negative values for dissolution.

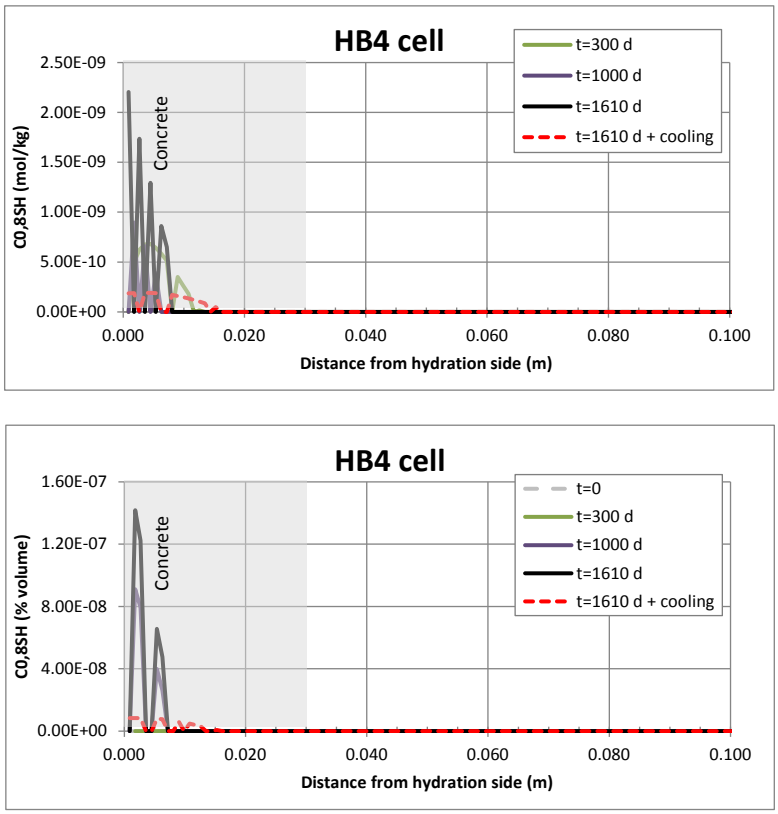

Figure 6-19.Spatial distribution of the computed precipitation/dissolution of C0.8SH in the HB4 cell at several times. Cumulative precipitation/dissolution (mol/kg) (top) and volume fraction (bottom). Positive values for precipitation and negative values for dissolution.

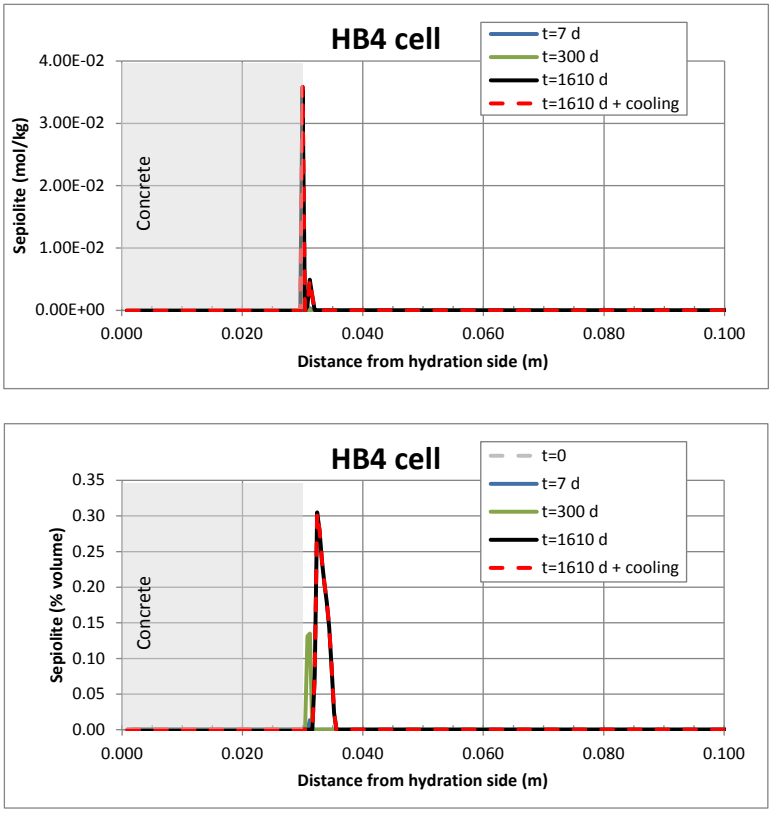

Figure 6-20.Spatial distribution of the computed precipitation/dissolution of sepiolite in the HB4 cell at several times. Cumulative precipitation/dissolution (mol/kg) (top) and volume fraction (bottom). Positive values for precipitation and negative values for dissolution.

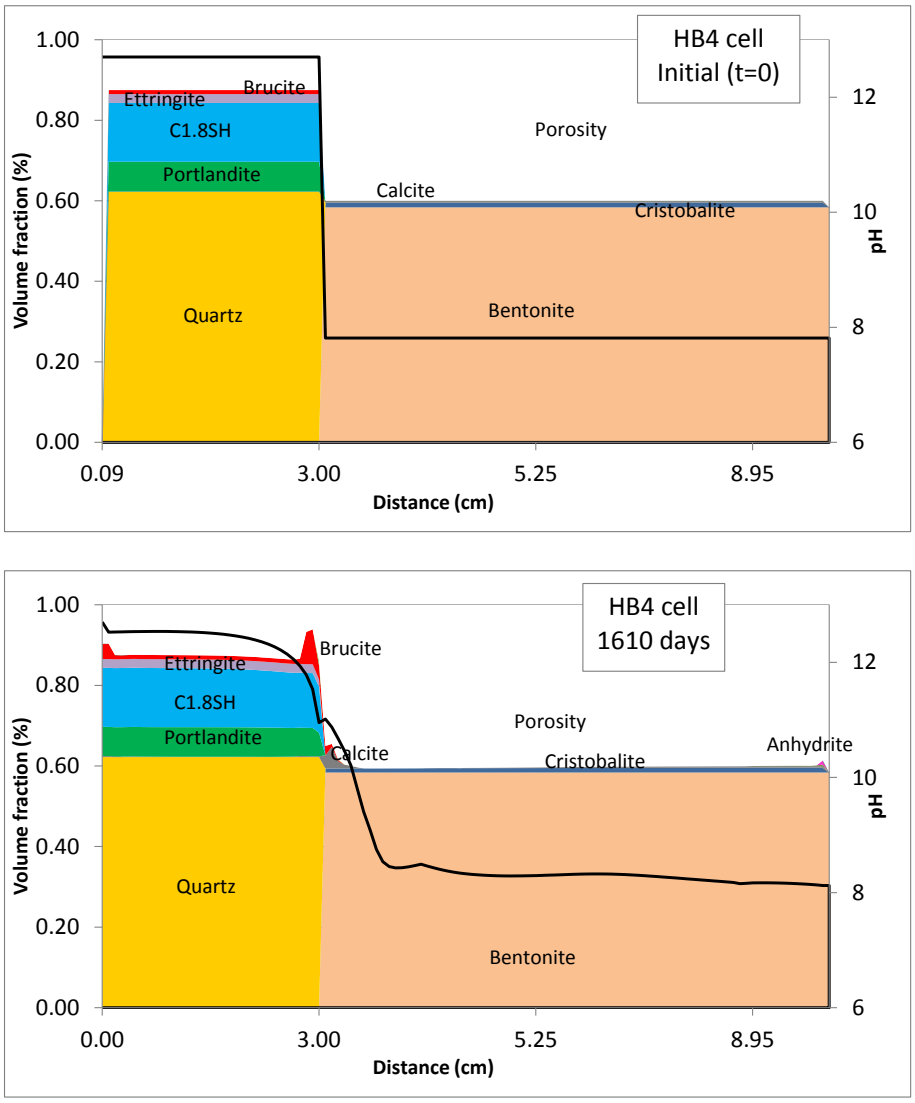

Figure 6-21.Spatial distribution of the volume fraction of the minerals in the HB4 cell at t = 0 (top) and at the end of the test (bottom).

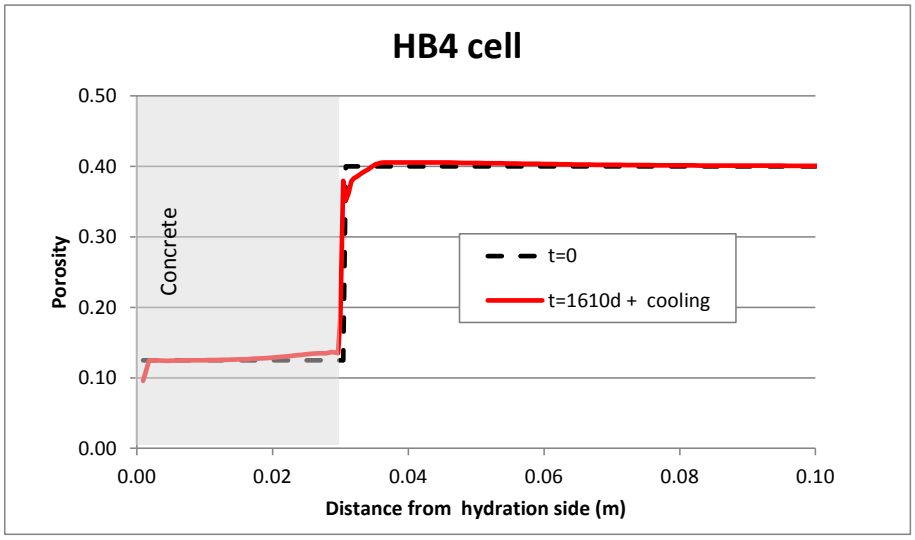

Figure 6-22. Spatial distribution of the porosity in the HB4 cell at the end of the test.

Table 6-3. Experimental observations and THMC model results.

		Observations	Model results
Concrete	Hydration interface	- **Brucite** precipitates - **Calcite** precipitates	- **Brucite** precipitates (2.8 % volume) - **Calcite** precipitates (0.1 % volume)
	Concrete	- **Calcite** precipitates everywhere - **C0.8SH** precipitates - **Ettringite** precipitates everywhere - **Portlandite** is nearly absent	- **Calcite** precipitates everywhere - **C0.8SH** precipitates ($8 \cdot 10^{-9}$ % volume) - **Ettringite** precipitates near the hydration (less than 1% in 1cm thickness) and dissolves in the rest (max of 2% volume in 2 cm thickness) - **Portlandite** dissolves everywhere (max of 1.6% volume in the interface)
	Contact concrete-bentonite	-**Calcite** precipitates more than in the rest of the concrete - **Ettringite** precipitates more than in the rest of the concrete	- **Calcite** precipitates more than in the rest of the concrete (3% volume) - **Ettringite** dissolves near the interface
Bentonite	Contact bentonite-concrete (d<2mm)	- **Calcite**/aragonite precipitates **- Mg-silicates** (sepiolite or saponite) - **C0.8SH** (very low) precipitation - No **ettringite** precipitation - No **anorthite** precipitation	-**Calcite** precipitation - A front of **sepiolite** precipitation (max of 0.3% volume in 0.2 cm from the interface) - A front of **brucite** precipitation (max of 11% volume in the interface) - No **C0.8SH** precipitation - No **ettringite** precipitation - No **anorthite** precipitation
	Bentonite	-**Calcite** dissolves (not clear)	-**Calcite** dissolves (0.35% volume in 30 cm thickness)
	Heating interface	- **Gypsum** and **chloride** precipitation	- **Anhydrite** precipitates (1% volume)

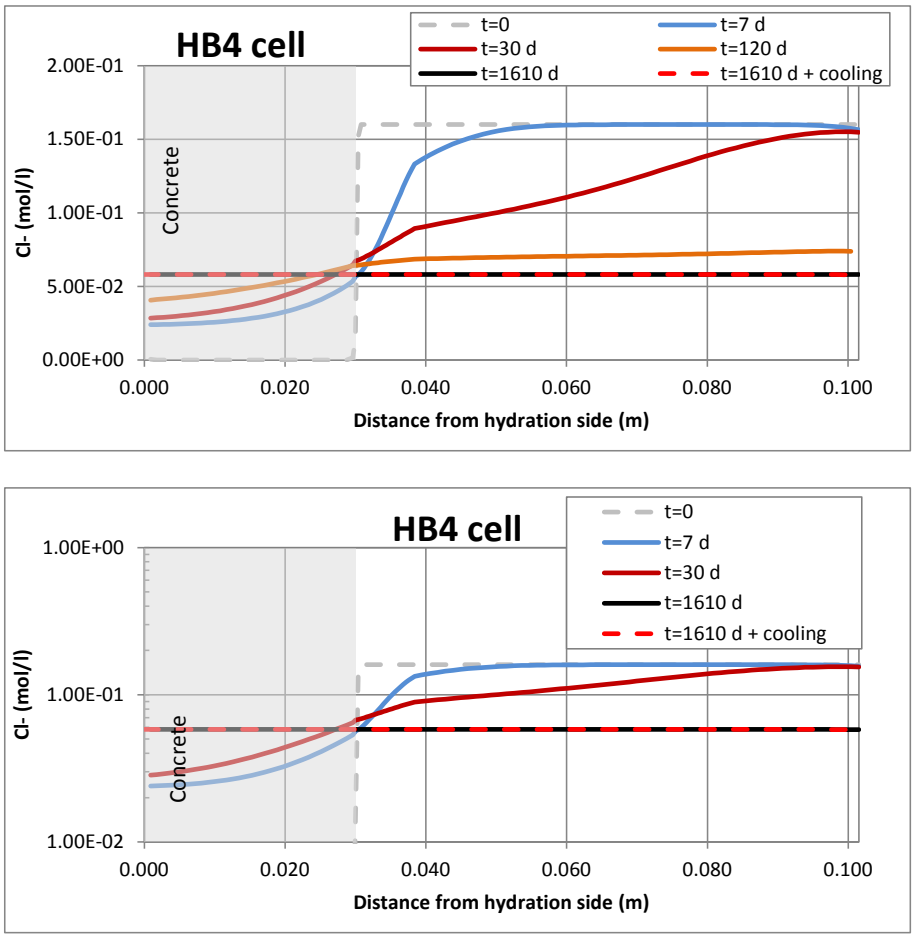

Figure 6-23. Spatial distribution of the computed concentration of dissolved Cl^- in the HB4 cell at several times. Natural scale (top) and logarithmic scale (bottom).

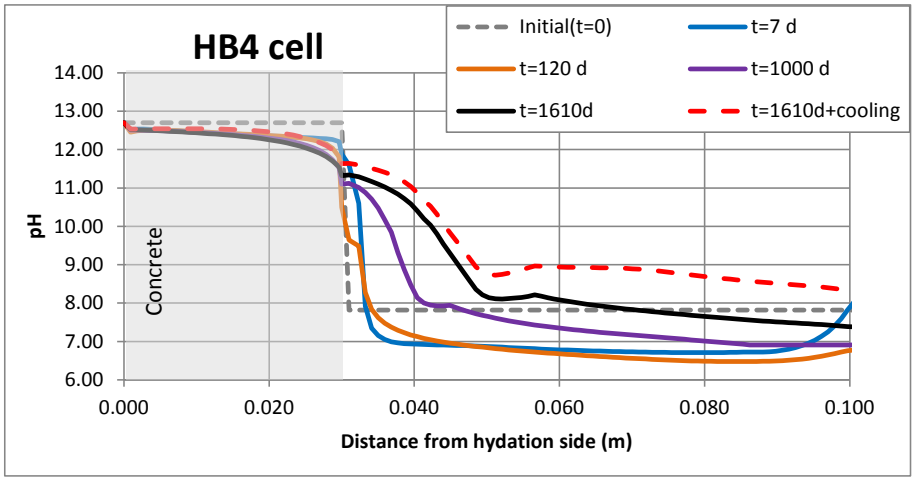

Figure 6-24. Spatial distribution of the computed pH in the HB4 cell at several times.

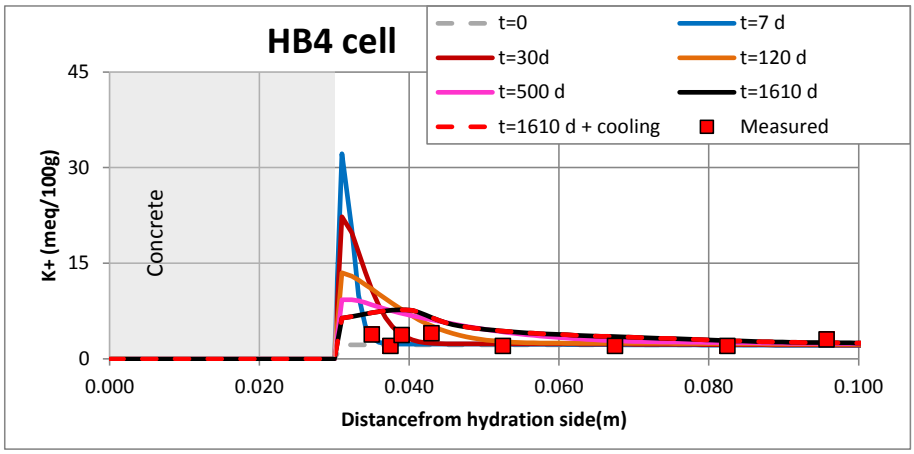

Figure 6-25. Spatial distribution of the computed (lines) and measured (symbols) concentrations of the exchanged K^+ in the HB4 test.

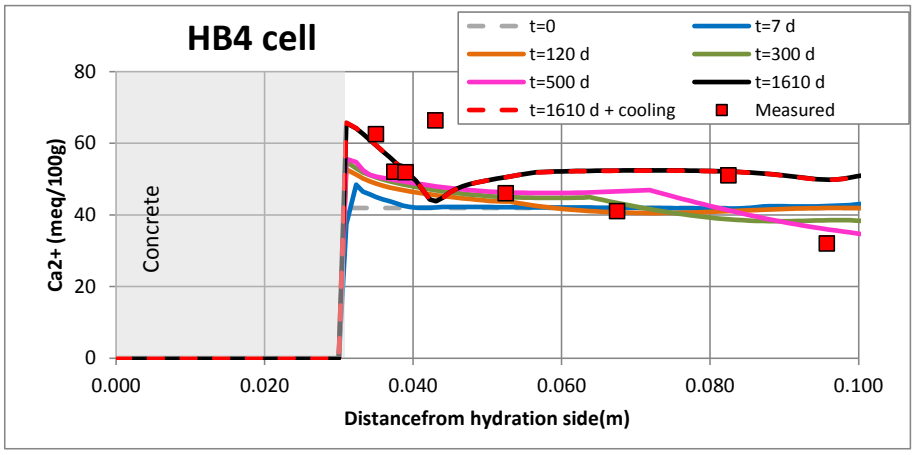

Figure 6-26. Spatial distribution of computed (lines) and measured (symbols) concentrations of the exchanged Ca^{2+} in the HB4 cell.

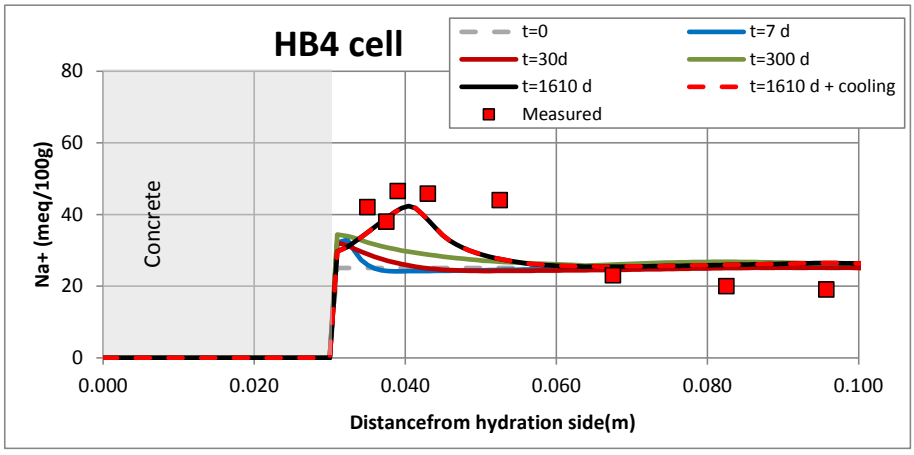

Figure 6-27. Spatial distribution of the computed (lines) and measured (symbols) concentrations of the exchanged Na^+ in the HB4 cell.

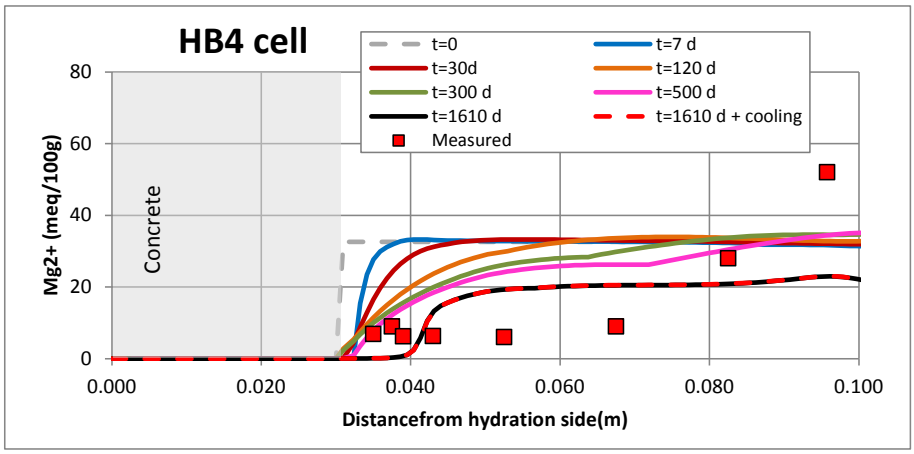

Figure 6-28. Spatial distribution of the computed (lines) and measured (symbols) concentrations of the exchanged Mg^{2+} in the HB4 cell.

6.6 Conclusions

The coupled THCm numerical models of the bentonite-concrete interface tests capture the main observed trends of mineral dissolution-precipitation. The HB4 model, however, do not reproduce the ettringite and CSH precipitation. For these phases, the numerical model predicts much less precipitation than the observed values. The porosity decreases in the bentonite/concrete interface due to the precipitation of minerals and decreases near the hydration boundary due to the dissolution of portlandite and quartz. The lack of thermodynamic data for CASH phases prevented to account for CASH phases in the models.

7 THC(m) model of the double interface tests: mortar-bentonite-magnetite

7.1 Introduction

The double interface cells, 2I, are a 25 mm tests performed by Ciemat with mortar, bentonite and magnetite powder (Cuevas et al., 2013). The cells were hydrated with a synthetic argillaceous water and heated at 60ºC. These tests were performed within the PEBS project. The 2I cells were performed to study the interactions of the corrosion products, the bentonite and the mortar. A THC(m) model was performed for one of the six 2I cells, the 2I3 cell.

7.2 Test description

The tests were designed to reproduce the repository conditions prevailing 1000 to 3000 years after emplacement of the waste, when the bentonite is fully saturated (Cuevas et al., 2013). The six cells were started on May 2012. The dismantling of the cells was performed on September 2012, after 540 days.

The cells are cylindrical with and internal diameter of 7 cm and an inner length of 2.5 cm (Figure 7-1). The cells were placed in a Teflon cylinder to prevent the lateral heat conduction and the swelling of bentonite. They were performed inside a chamber which was fixed at a constant temperature of 60ºC.

The 2.5 cm of inner length of the six cells had a different combination of materials, including either natural or pre-treated FEBEX bentonite, mortar and magnetite. The following six 2I tests were performed:

1) Cell 1: 2.5 cm of pre-treated FEBEX bentonite
2) Cell 2: 2.5 cm of natural FEBEX bentonite
3) Cell 3: 0.5 cm of mortar, 1.8 cm of pre-treated FEBEX bentonite and 0.2 cm of magnetite
4) Cell 4: 0.5 cm of mortar, 1.8 cm of FEBEX bentonite and 0.2 cm of magnetite
5) Cell 5: 0.5 cm of mortar and 2 cm of pre-treated FEBEX bentonite
6) Cell 6: 2.3 cm of pre-treated FEBEX bentonite and 0.2 cm of magnetite

The cells 3, 5 and 6 were performed with a pre-treated FEBEX bentonite obtained from the natural FEBEX bentonite by depleting its exchanged magnesium

content artificially. The concentration of the exchanged Mg^{2+} and Na^{+} was decreased from 33.0 and 25.5 meq/100g, respectively, to 5.5 and 8.9 meq/100g while the exchanged K^{+} concentration was increased from 2.2 to 44.1 meq/100g. The initial concentrations of the exchanged cations of the natural and pre-treated FEBEX bentonites are listed in Table 7-1. The cation exchange capacity in both cases is 102.7 meq/100g.

A lime mortar was used as a surrogate of the product of concrete degradation. It is a paste used in the construction of concrete which is made mainly of quartz aggregates.

The corrosion source was magnetite powder. This mineral is the final corrosion product in the repository. Measurements made in the 2I cells showed that the magnetite did not corrode during the tests.

The dry density and the initial water content of the bentonite were 1.65 g/cm^3 and 13.3%, respectively. The dry density of the mortar was 1.7 g/cm^3 and the initial water content was 2%. The initial water content of the magnetite was 3.2%.

The 2I cells were hydrated with the synthetic Spanish Reference Clay porewater (RAF water) at a constant injection pressure of 600 kPa applied through a bottle installed on the top of the cell.

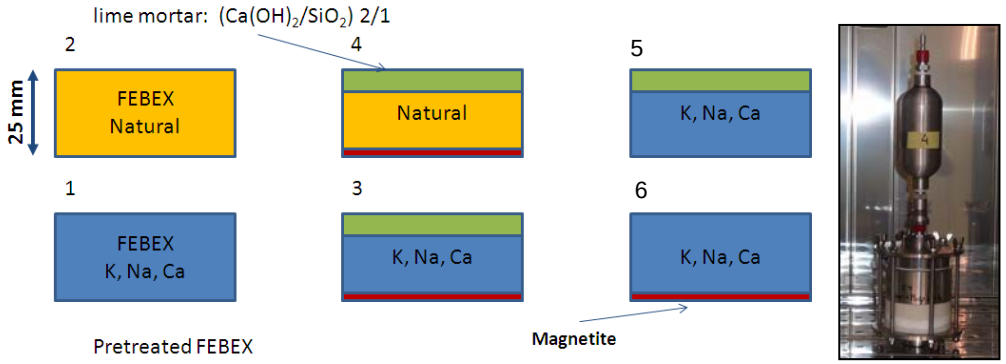

Figure 7-1. Description of the six double interface small cells (Cuevas et al., 2013).

7.3 Analysis of available data

The available measured data include (Cuevas et al., 2013):

1) Water content, water intake, dry density were measured at the end of the test at several points in the bentonite.
2) The chemical composition of the aqueous species and the water volume of the injection bottle were measured at the end of the tests. These data were

useful to know the water leakage from the injection system and to evaluate the possible backwards diffusion of the chemical species towards the hydration system.

3) Mineralogical determinations at the end of the tests

The aqueous extract test (AET) method was used to obtain the porewater chemistry of the compacted bentonite after the test. Changes observed in soluble salts in bentonite were only relevant near the contact with the mortar. Due to the complexity to derive the chemical composition of the original (before aqueous extraction) clay porewater, these measured aqueous species concentration were not considered for model calibration and testing.

The main experimental observations on the mineral patterns in the concrete and the bentonite at the end of the 2I3 test were compared to the computed concentrations of dissolved/precipitated minerals. Neither magnetite dissolution nor new Fe-minerals precipitation were observed in the magnetite/bentonite interface.

7.4 Model description

A THC(m) model was performed for the 2I3 cell. The 2.5 cm of inner length of this cell included 0.5 cm of mortar, 1.8 cm of pre-treated FEBEX bentonite and 0.2 cm of magnetite powder. These three materials were considered in the model (see Figure 7-2).

The hydration of the cell was simulated with a constant injection pressure of 600 kPa applied through a bottle (water tank) installed on the top of the cell connected to the mortar by a small water pipe and a filter (see Figure 7-2).

The measured Cl^- data at the end of some 2I tests indicated that some backwards diffusion occurred. Therefore, it was necessary to include the bottle (inner length of 6 cm), the water pipe (inner length of 4.5 cm) and the filter (inner length of 0.3 cm) in the model. The water pipe porosity value was used to calibrate the Cl^- retro-diffusion. A large value of porosity favours Cl^- backdiffusion.

No backdiffusion was observed in the 2I3 cell. Therefore, a very small porosity of 0.0036 was used for the 2I3 model. It is also important to point out that the bottle was initially fully of water. Therefore, the decrease of the volume of water during the test had to be considered in the model. This effect was simulated by decreasing the water volume of the bottle and the water pressure.

The chemical composition of the aqueous species and the water volume of the injection bottle were measured at the end of the test.

The model was performed with a 1D mesh (Figure 7-2). The model considers the bottle (water tank), the water pipe, the filter, the mortar, the bentonite and the magnetite powder.

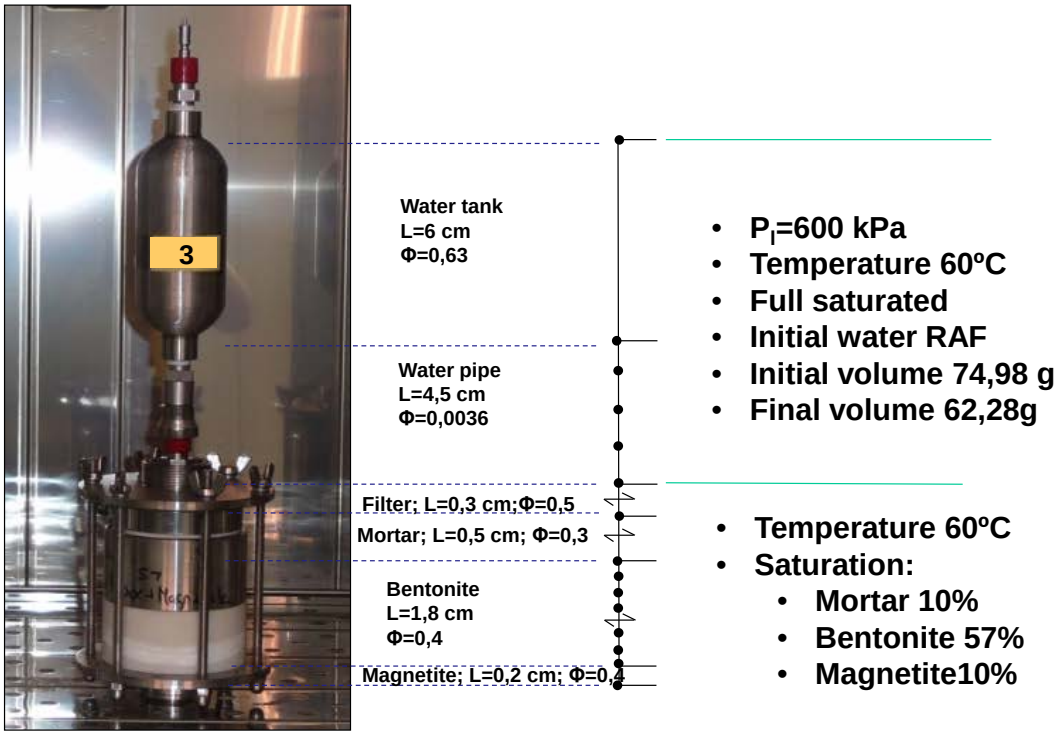

Figure 7-2. One dimensional finite element mesh and boundary conditions used in the numerical model of the 2I3 cell (Cuevas et al., 2013).

Bentonite parameters were taken from those of the calibration of the CT23 model (Zheng et al., 2010). The parameters of the mortar were derived from laboratory experiments (Villar et al., 2012; Villar, 2013), the El Cabril model (Ayora et al., 2007) and the HB4 model (see Chapter 6 of this report). These parameters are listed in Table A1-1 to Table A1-4 in Appendix A. Magnetite powder parameters were taken from those of the Fe powder used in the numerical models of the small corrosion cells (see Chapter 5).

The bottle and the small water pipe (hydration system) were considered fully saturated. The water volume and the water pressure of the bottle were prescribed to decrease with time. The water pressure in the bottle and the pipe was imposed at a value of 600 kPa initially. Then the pressured decreased linearly to 450 kPa. The initially measured volume of water in the tank was 74.98 mL. The volume of water at

the end of the test was 62.28 mL. The filter, which separates the hydration system and the rest of the cell, was also considered fully saturated with a porosity of 0.5.

The vertical displacement of the 2I3 cell was not considered because measured data indicated very small deformation. The temperature was fixed at 60ºC in all the points of the 1D mesh during the entire duration of the test (18 months). The model simulated a cooling phase of 2 days during which the temperature decreased to 25ºC. Finally, the model accounted for additional 60 days of solute distribution.

The initial porosity of the bentonite was 0.4 and the initial water content was 13.3%, which corresponds to a saturation of 57% and a suction of $1.27 \cdot 10^{8}$ Pa. The mortar has a porosity of 0.3, a gravimetric water content of 2% and a saturation of 10%. The magnetite powder has a porosity of 0.6, a gravimetric water content of 3.2% and a saturation of 10%. The initial gas pressure is the atmospheric pressure. The initial stress was assumed uniform and isotropic and equal to $2.5 \cdot 10^{5}$ Pa.

A Neuman transport boundary condition was used for solute transport according to which solute flux is equal to the product of water flux times solute concentration of inflow water. The thermo-osmosis was considered in the model. A thermo-osmosis permeability of $4.2 \cdot 10^{-13}$ $m^2/K/s$ was taken from Zheng et al. (2010). The effective diffusion coefficient for all aqueous species considered in the model was $2 \cdot 10^{-10}$ m^2/s, except in the case of the Cl^- which had a value of $9.2 \cdot 10^{-11}$ m^2/s.

The chemical compositions of the bentonite, mortar and hydration waters are listed in Table A2-1 of Appendix A. The porewater composition of the bentonite at a water content of 13.3% was derived from Fernández et al. (2001). The hydration water is a synthetic Spanish Reference Clay pore water (Turrero et al., 2011). The initial chemical composition of the mortar pore water for the 2I3 test was assumed equal to the composition of the hydration water except for the dissolved Ca^{2+} which was derived from chemical equilibrium with respect to portlandite and SO_4^{2-} with derived by imposing equilibrium with respect to gypsum.

The initial mineral volume fractions in the bentonite, the mortar and the magnetite powder are listed in Table 6-1. The magnetite was considered not reactive in the model. The secondary minerals which were allowed to precipitate include: anhydrite, brucite, sepiolite, ettringite, C1.6SH and C1.2SH. The dissolution/precipitation of portlandite, brucite, sepiolite, ettringite, C1.8SH, C0.8SH, quartz and cristobalite were simulated with kinetics by using the following kinetic rate law:

$$r_m = k_m e^{-\frac{Ea}{RT}}({\Omega_m}^{\theta} - 1)^{\eta}(a_{H^+})^n \quad (31)$$

where r_m is the dissolution/precipitation rate (mol/m^2/s); k_m is the kinetic rate constant (mol/m^2/s) at 25ºC, Ω_m is the ratio between the ion activity product and the equilibrium constant (dimensionless) and θ and η are parameters of the kinetic law; $e^{-\frac{Ea}{RT}}$ is the thermodynamic factor, which takes into account the apparent activation energy of the reaction, Ea, R and T are the gas constant and the absolute temperature, respectively; $(a_{H^+})^n$ is the proton activity raised to the power n.

The kinetic parameters of portlandite, brucite, sepiolite, ettringite, C1.8SH, C0.8SH, quartz and cristobalite are listed in Table 6-2. The activation energy and the kinetic rate constants were taken from Fernández et al. (2009). It is important to point out that the specific surface of the minerals were calibrated. The only mineral which considers the proton activity is quartz.

The Gaines-Thomas convention was used for cation exchange. The cation exchange capacity and the initial composition of the exchanged cations of the natural and pre-treated FEBEX bentonite are listed in Table 7-1 Surface complexation reactions were modeled with triple-site models (Bradbury and Baeyens, 1997). The total concentration of sorption sites for the triple-site sorption model in bentonite are listed in Table A2-2 in Appendix A. The chemical reactions and their equilibrium constants at 25 ºC for aqueous complexation and mineral dissolution/precipitation as well as the selectivity coefficients for exchanged cations and protolysis constants for surface complexation reactions are listed in Table A2-4 to Table A2-7 in in Appendix A.

Table 7-1. Initial concentration of exchanged cations (in meq/100g) of the double interface 2I tests.

Cations	**Ca^{2+}**	**Mg^{2+}**	**Na^{+}**	**K^{+}**	**CEC**
Natural FEBEX bentonite	42.0	33.0	25.5	2.2	102.70
Pre-treated FEBEX bentonite	44.5	5.2	8.9	44.1	102.70

Table 7-2. Initial mineral volume fractions (%) of the numerical model of the 2I3 test.

Bentonite		**Mortar**		**Magnetite powder**	
Calcite	0.36	Portlandite	23.0	Magnetite	100
Gypsum	0.08	Gypsum	1.0		
Cristobalite	1.19	Quartz	46.0		

Table 7-3. Kinetic parameters of minerals considered in the numerical model of the 2I 3 cell (Fernández et al., 2009).

Mineral	Activation energy (kJ/mol)	k_m (mol/m^2/s)	θ	η	n	Specific surface (m^2/ m^3 medium)
Portlandite	41.86	$1.0 \cdot 10^{-8}$	1	1	-	66
Brucite	60.00	$1.0 \cdot 10^{-6}$	1	1	-	$1.16 \cdot 10^{-4}$
Sepiolite	60.00	$1.0 \cdot 10^{-15}$	1	1	-	1.65
Ettringite	41.86	$1.0 \cdot 10^{-8}$	1	1	-	16.5
C1.6SH	41.86	$1.0 \cdot 10^{-7}$	1	1	-	$5 \cdot 10^{-2}$
C1.2SH	41.86	$1.0 \cdot 10^{-7}$	1	1	-	$5 \cdot 10^{-2}$
Quartz	95.79	$5.13 \cdot 10^{-17}$	1	1	0.55	13.2
Cristobalite	65.0	$5.0 \cdot 10^{-13}$	1	1	-	$1.65 \cdot 10^{-2}$

7.5 Model results

7.5.1 Thermo-hydro-mechanical results of

Figure 7-3 shows the spatial distribution of the initial and the computed and measured volumetric water content and at the end of the 2I3 test. The initial water content values in the mortar, bentonite and magnetite powder are 2%, 22% and 5%, respectively. The final water contents are 30% in the mortar, 41% in the bentonite and 60% in the magnetite powder. The computed water content reproduces the measured data in the three materials.

The spatial distribution of the computed saturation degree at the end of the 2I3 test is shown in Figure 7-4.

Figure 7-5 shows the time evolution of the computed and measured water intake. The computed water intake does not reproduce the measured values during the first 50 days. However, the computed water intake after 300 days fit the measured data.

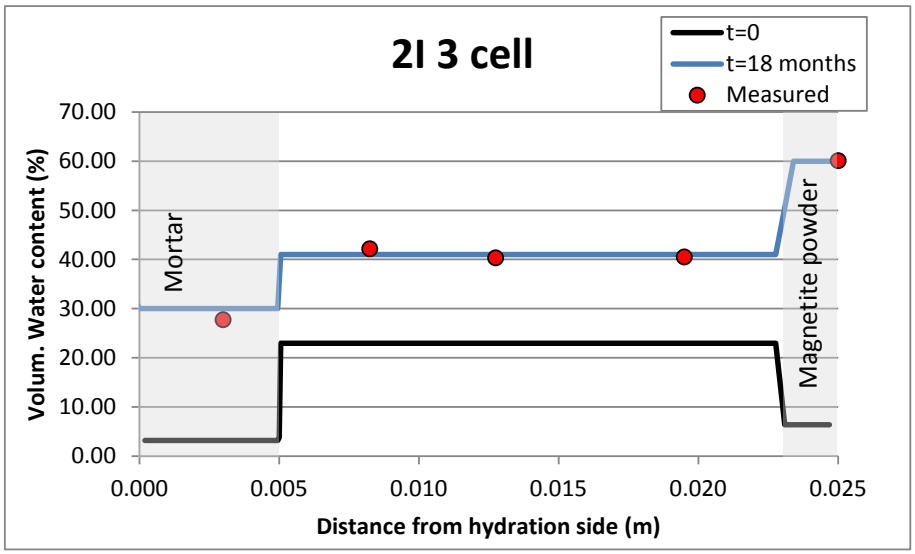

Figure 7-3. Spatial distribution of the computed (lines) and measured (symbols) volumetric water content initially and at the end of the 2I3 test.

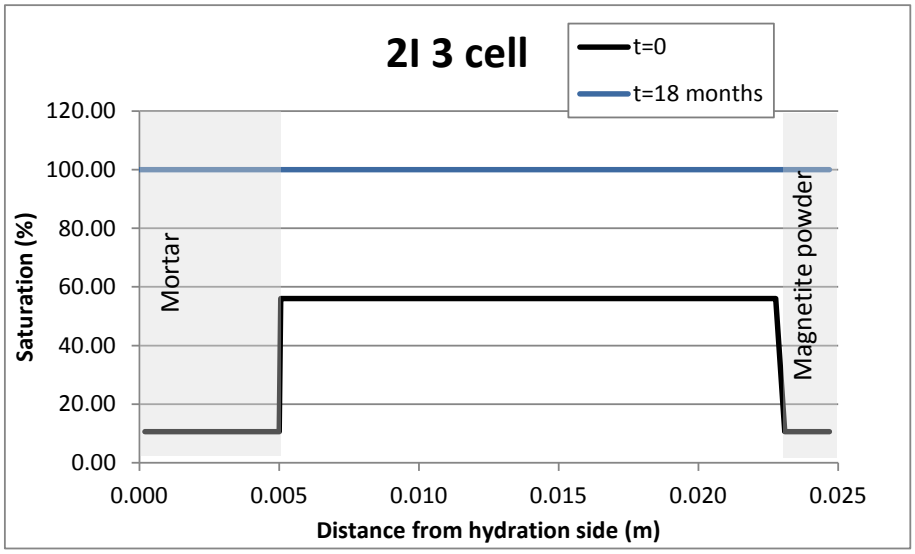

Figure 7-4. Spatial distribution of the computed saturation degree initially and at the end of the 2I3 test.

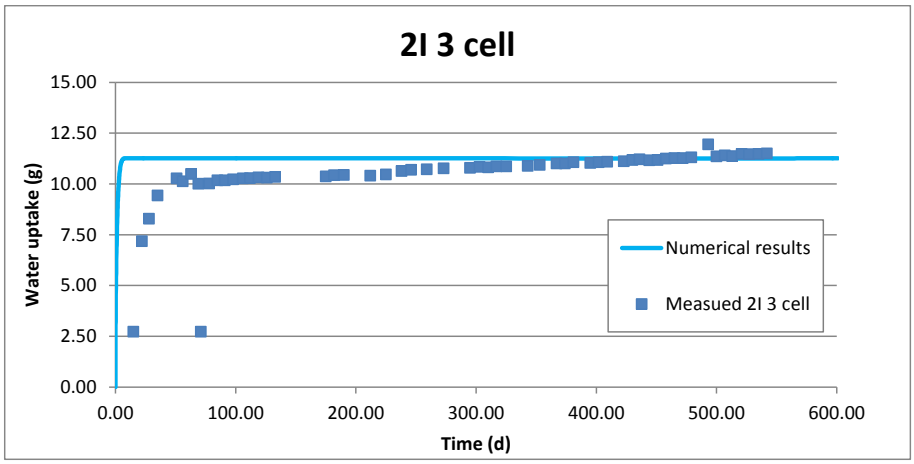

Figure 7-5. Time evolution of the computed (line) and measured (symbols) cumulative water intake in the 2I3 test.

7.5.2 Chemical results

Similar to the HB4 test, one of the main objectives of the THMC model of the 2I3 is to test the model results with experimental observations of mineral patterns in the mortar and the bentonite at the end of the test.

Figure 7-6 shows the spatial distribution of the computed cristobalite precipitation/dissolution at t = 18 months and after the cooling phase. This mineral is present initially only in the bentonite with an initial volume fraction of 1.19%. Its spatial distribution in the bentonite presents a dissolution process with time. In the mortar there is no cristobalite precipitation. Quartz is the main component of the mortar with an initial volume fraction of 46% (see Figure 7-7). After 18 months this mineral practically does not precipitate nor dissolve in the mortar. Actually, the computed values are in the order of 10^{-14} mol/kg. There is no quartz precipitation in the bentonite.

Figure 7-8 shows the spatial distribution of the computed calcite precipitation/dissolution at t = 18 months and after the cooling phase. This mineral is present initially only i in the bentonite with an initial volume fraction of 0.36%. Calcite precipitates in the mortar-bentonite interface and in the first 5 mm of the bentonite while it dissolves in the rest of the bentonite.

Figure 7-9 and Figure 7-10 show the spatial distribution of the computed portlandite and brucite precipitation/dissolution at t= 18 months and after the cooling phase. Portlandite is present initially only in the mortar with an initial volume fraction of 23%. Portlandite dissolves in the mortar. Brucite precipitates in the hydration zone,

in the mortar, in the mortar-bentonite interface and in the first 5 mm of the bentonite. The brucite precipitation is more pronounced in the hydration zone.

The spatial distribution of the computed gypsum and anhydrite precipitation/dissolution at t = 18 months and after the cooling phase is presented in Figure 7-11 and Figure 7-12. Gypsum is initially present in the mortar and in the bentonite with initial volume fractions of 1% and 0.08%, respectively while anhydrite is a secondary mineral not initially present in the system. At a temperature of 60ºC anhydrite is less soluble than gypsum. For this reason, anhydrite precipitates and gypsum dissolves in the mortar at the final time of the test. The cooling produces anhydrite dissolution and gypsum precipitation in the mortar due to the decrease of temperature. In the bentonite anhydrite precipitates slightly at early times (Figure 7-6) and gypsum dissolves.

Figure 7-13 shows the spatial distribution of the computed ettringite precipitation/dissolution at t = 18 months and after the cooling phase. This mineral is a secondary mineral not initially present in the model. Computed results show a precipitation front at the mortar-bentonite interface at t = 1 month. After this time, the front moves towards the bentonite while the maximum concentration of precipitated ettringite decreases. The cooling phase produces a change in the location and in the maximum value of the ettringite precipitation front.

The spatial distribution of the computed C1.6SH and C1.2SH precipitation/dissolution at t = 18 months and after the cooling phase is presented in Figure 7-14 and Figure 7-15. These two minerals are secondary minerals not initially present in the system. C1.6SH precipitates in the hydration zone, the mortar, the mortar-bentonite interface and the first 7-8 mm of the bentonite. C1.2SH precipitates at 7 days and 1 month in the hydration zone and in the mortar while at 6 months it precipitates only within the bentonite. At t = 18 months there is no C1.2SH precipitation.

Figure 7-16 shows the spatial distribution of the computed sepiolite precipitation/dissolution at 18 months and after the cooling phase. This mineral is a secondary mineral not initially considered in the system. Sepiolite precipitates in the hydration zone, the mortar and the mortar-bentonite interface. There is no sepiolite precipitation in the bentonite.

Figure 7-17 shows the spatial distribution of the volume fractions of the minerals at t = 0 and t = 18 months in the model of the 2I3 cell. Initially, the most abundant

minerals in the mortar are quartz and portlandite. The major mineral of the bentonite is the smectite. This mineral is not considered in the model because its dissolution rate is very small. The main changes in mineral phases after 18 months include: (1) The increase of brucite and anhydrite and the decrease of portlandite and gypsum volume fractions in the whole mortar, (2) The increase of brucite and calcite volume fractions in the mortar-bentonite interface, and (3) The slight decrease of gypsum and calcite volume fractions in the bentonite.

Table 7-4 presents a comparison between a summary of the main experimental observations on the mineral patterns in the mortar and the bentonite at the end of the 2I3 test and the computed values of dissolved/precipitated mineral phases considered in the model. For the most part, the numerical model captures the main trends in mineral dissolution/precipitation. However, there are some discrepancies, especially for ettringite in the mortar and in the bentonite (precipitation is observed in the test), and brucite precipitation at the mortar-bentonite interface and in the bentonite (not observed in the test).

Figure 7-18 shows the spatial distribution of the porosity changes due to the mineral dissolution/precipitation in the 2I3 test. It can be seen that the changes in porosity of the mortar and the bentonite are small. The porosity only increases slightly in the mortar zone in contact with the bentonite and near the hydration zone due to the dissolution of portlandite and gypsum.

Figure 7-19 shows the spatial distribution of the computed pH at different times. The initial pH is 11.3 in the mortar and 7.72 in the bentonite. The pH decreases with time in the hydration zone, the concrete and near the contact with the bentonite and increases with time in the bentonite. The evolution of the alkaline plume can be seen in this figure following the pH front penetration in the bentonite. The final pH in the concrete and in the mortar-bentonite interface is around 9.8. It decreases from 9.8 to 7.7 in the first 10 mm of the bentonite. After the cooling phase, the pH increases slightly in the mortar and in the mortar-bentonite interface.

It should be pointed out that the computed concentrations of dissolved species at t = 0 in the concrete and bentonite in the figures of Appendix D correspond to the first calculated time once the initial concentration of aqueous species are equilibrated with the considered initial mineral assemblage. For this reason, the concentrations at t = 0 may not coincide with those listed in Table A2-1 in Appendix A.

Figure 7-20 shows the spatial distribution of the computed Cl^- concentration at different times. The computed Cl^- concentration increases with time in the mortar and decreases in the bentonite. The computed concentrations become uniform in the concrete and the bentonite after a few days, reaching a concentration value of 0.06 mol/L. These calculated values are larger than the measured data in the bentonite.

The spatial distribution of computed concentration of dissolved Na^+, K^+, Ca^{2+}, Mg^{2+}, HCO_3^-,SO_4^{2-}, SiO_2(aq) and Al^{3+} are shown in Appendix D (Figure D-1 to Figure D-8). The computed concentrations of Ca^{2+}, Mg^{2+}, Na^+ and K^+ show similar trends to those of Cl^- (Figure 7-20). In addition to diffusion, these species are subjected to mineral dissolution/precipitation and cation exchange reactions.

Figure D-5 shows the spatial distribution of the computed HCO_3^- concentration at different times. This species shows a front moving from the bentonite zone in contact with the mortar towards the other side of the bentonite. The peak concentration decreases as the front moves through the bentonite. The effect of the cooling phase in the HCO_3^- concentration can be clearly seen in the bentonite (from 15 mm to the magnetite powder zone). The decrease of temperature produces an increase in the maximum value of the HCO_3^- front due to calcite dissolution.

The time evolution of the SO_4^{2-} concentration (Figure D-1) is affected by the dissolution/precipitation of portlandite, gypsum, anhydrite, C1.6SH, C1.2SH and ettringite. The computed SO_4^{2-} concentration decreases with time. At the final time of the experiment (18 months) the SO_4^{2-} computed concentration is the same in the mortar and in the bentonite. The concentration increases in the bentonite and the mortar during the cooling phase.

The Al^{3+} computed concentration increases in the mortar and in the bentonite from 7 days to 18 months reaching a uniform profile at the end of the test (Figure D-8). Ettringite dissolution/precipitation governs the concentration of Al^{3+}.

The SiO_2(aq) concentration decreases with time in the mortar and in the bentonite (Figure D-7).

Figure D-9 to Figure D-12 show the spatial distribution of the computed and measured concentration of the exchangeable cations at different times. Cation exchange and sorption are considered in the bentonite. The computed concentrations of exchanged Ca^{2+} and K^+ increase with time in the bentonite while those of Mg^{2+} and Na^+ decrease.

The spatial distribution of computed concentrations of sorbed species at t = 18 months is shown in Figure D-13 to Figure D-15 of Appendix D. The concentrations of S^sO^-, $S^{w1}O^-$ and $S^{w2}O^-$ decrease from the bentonite-mortar interface to the bentonite-magnetite interface while the concentrations of S^sOH, $S^{w1}OH$ and $S^{w2}OH$ increase.

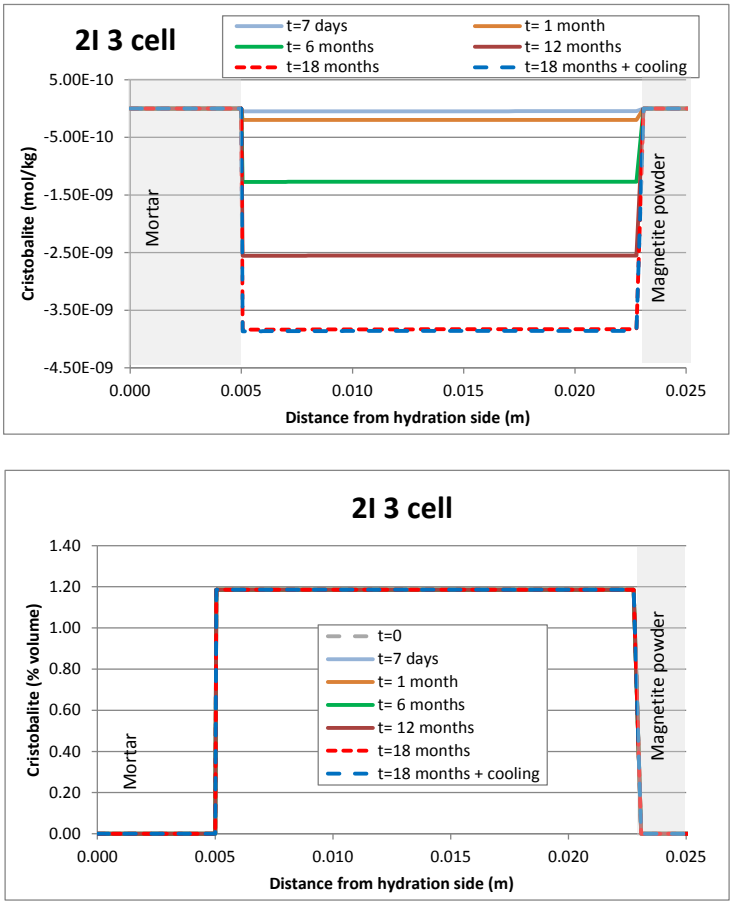

Figure 7-6. Spatial distribution of the computed dissolution of cristobalite in the double interface 2I3 test. Cumulative precipitation/dissolution (mol/kg) (top) and volume fraction (bottom). Positive values for precipitation and negative values for dissolution.

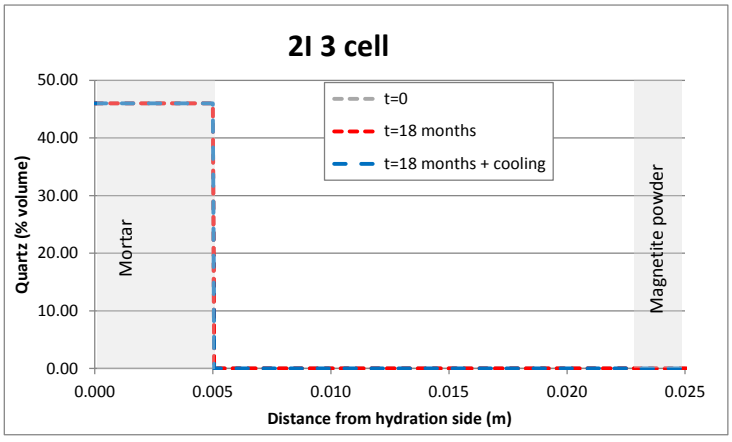

Figure 7-7. Spatial distribution of the computed dissolution of quartz in the double interface 2I3 test. Positive values for precipitation and negative values for dissolution.

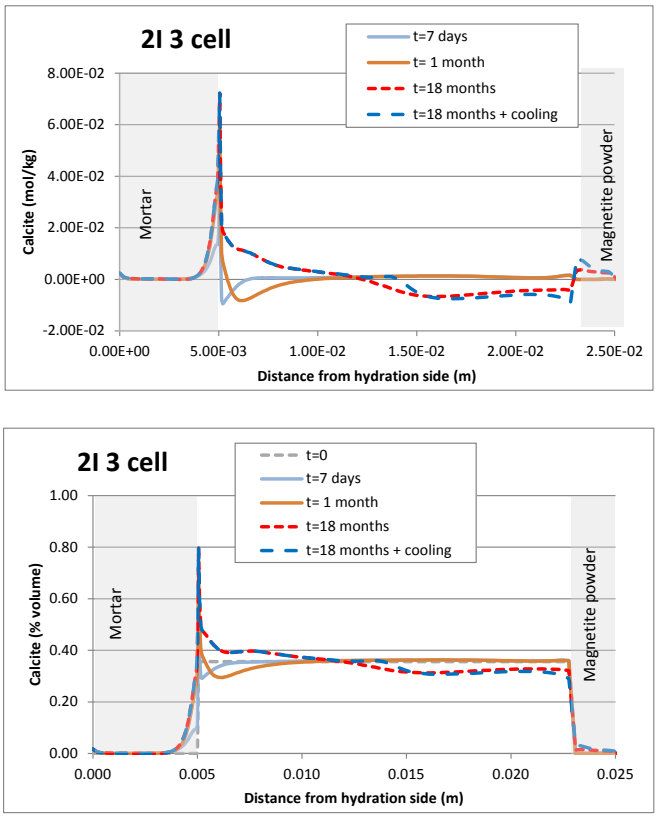

Figure 7-8. Spatial distribution of the computed volumetric fraction of calcite in the double interface 2I3 test. Cumulative precipitation/dissolution (mol/kg) (top) and volume fraction (bottom). Positive values for precipitation and negative values for dissolution.

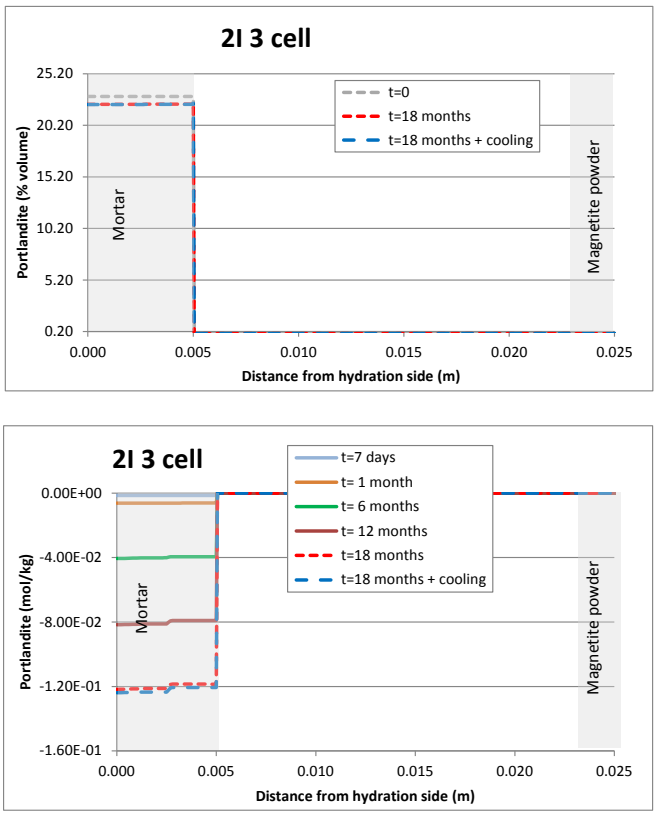

Figure 7-9. Spatial distribution of the computed dissolution of portlandite in the double interface 2I3 test. Cumulative precipitation/dissolution (mol/kg) (top) and volume fraction (bottom). Positive values for precipitation and negative values for dissolution.

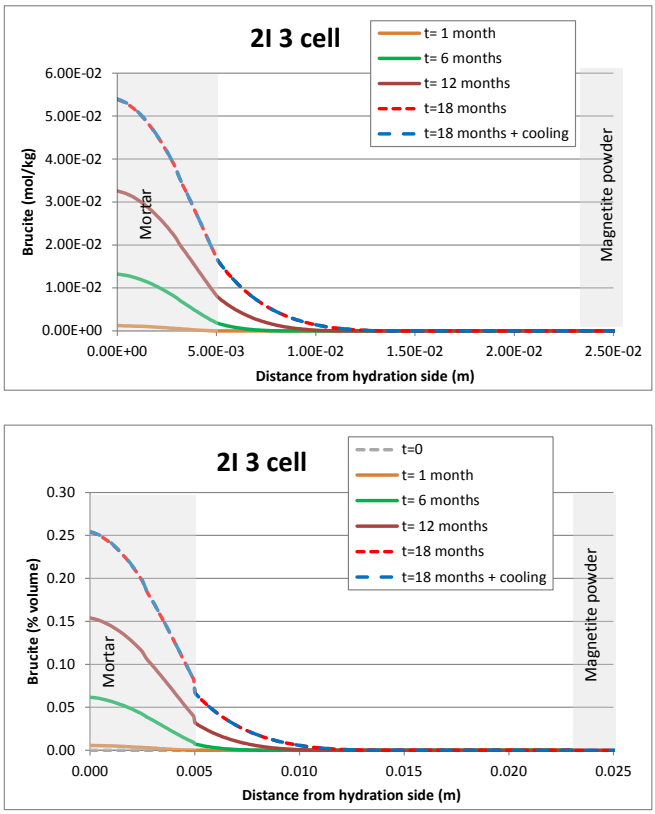

Figure 7-10. Spatial distribution of the computed volumetric fraction of brucite in the double interface 2I3 test. Cumulative precipitation/dissolution (mol/kg) (top) and volume fraction (bottom). Positive values for precipitation and negative values for dissolution.

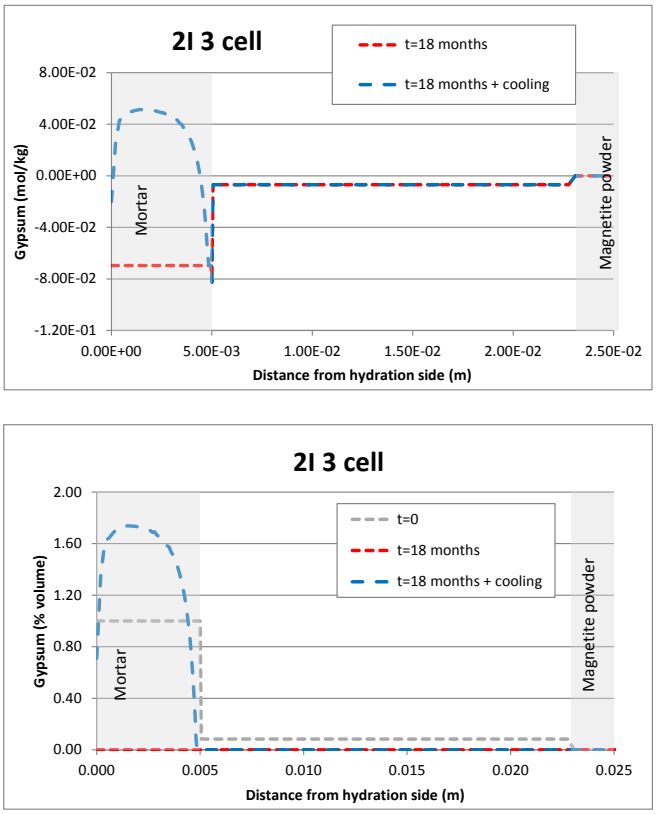

Figure 7-11. Spatial distribution of the computed volumetric fraction of gypsum i in the double interface 2I3 test. Cumulative precipitation/dissolution (mol/kg) (top) and volume fraction (bottom). Positive values for precipitation and negative values for dissolution.

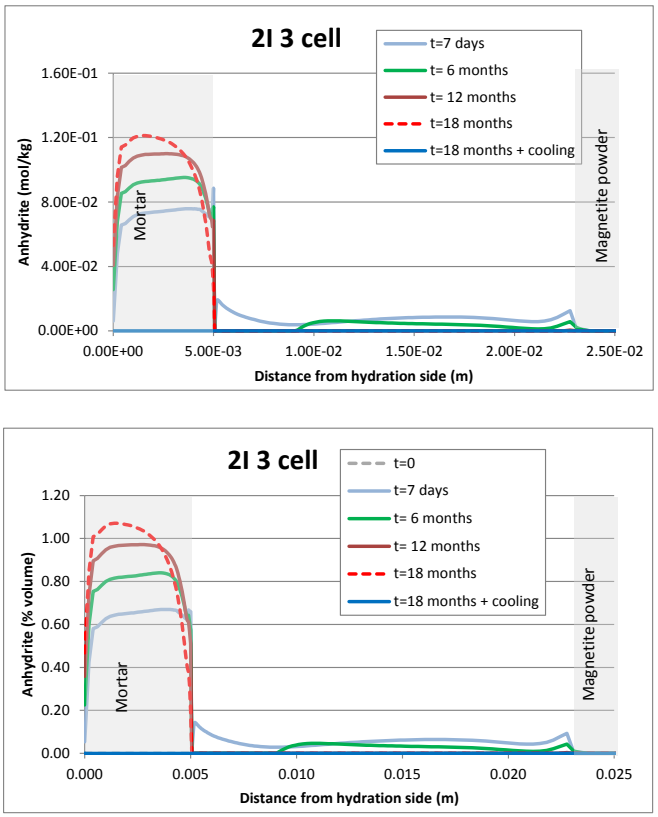

Figure 7-12. Spatial distribution of the computed volumetric fraction of anhydrite in the double interface 2I3 test. Cumulative precipitation/dissolution (mol/kg) (top) and volume fraction (bottom). Positive values for precipitation and negative values for dissolution.

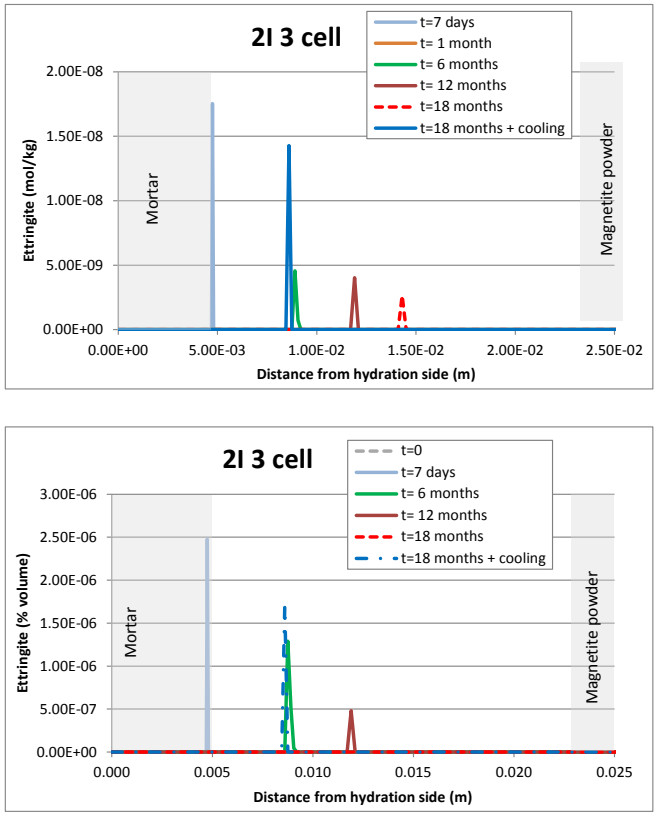

Figure 7-13. Spatial distribution of the computed volumetric fraction of ettringite in the double interface 2I3 test. Cumulative precipitation/dissolution (mol/kg) (top) and volume fraction (bottom). Positive values for precipitation and negative values for dissolution.

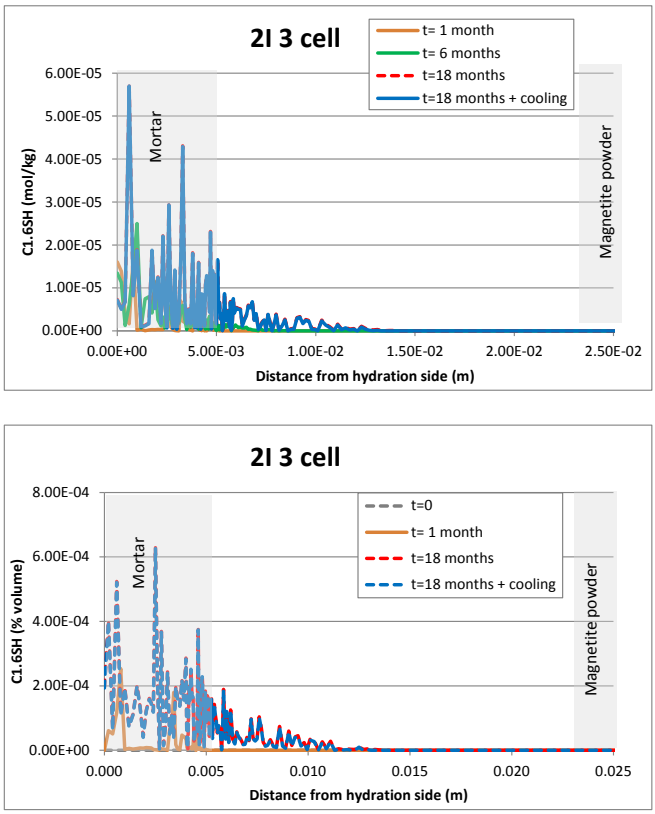

Figure 7-14. Spatial distribution of the computed volumetric fraction of C1.6SH in the double interface 2I3 test. Cumulative precipitation/dissolution (mol/kg) (top) and volume fraction (bottom). Positive values for precipitation and negative values for dissolution.

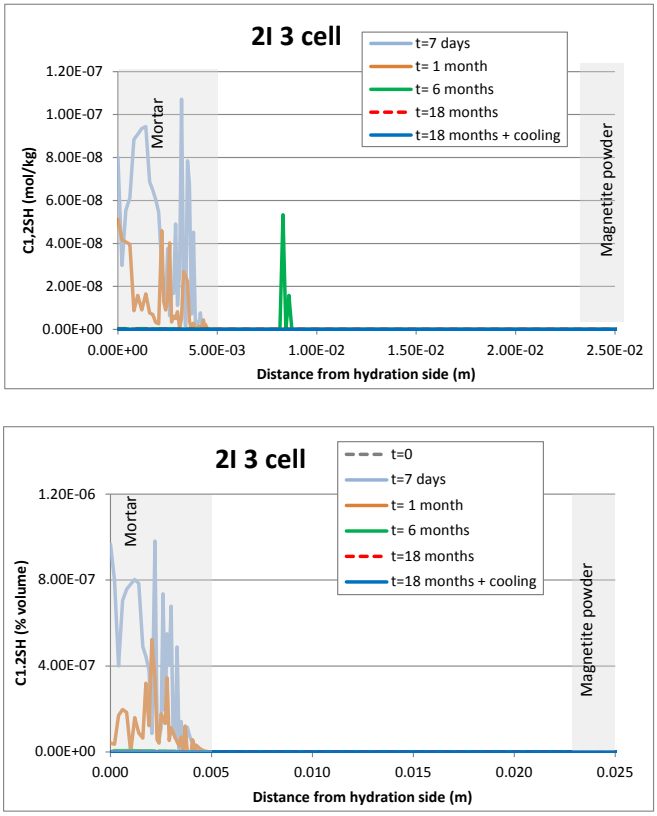

Figure 7-15. Spatial distribution of the computed volumetric fraction of C1.2SH in the double interface 2I3 test. Cumulative precipitation/dissolution (mol/kg) (top) and volume fraction (bottom). Positive values for precipitation and negative values for dissolution.

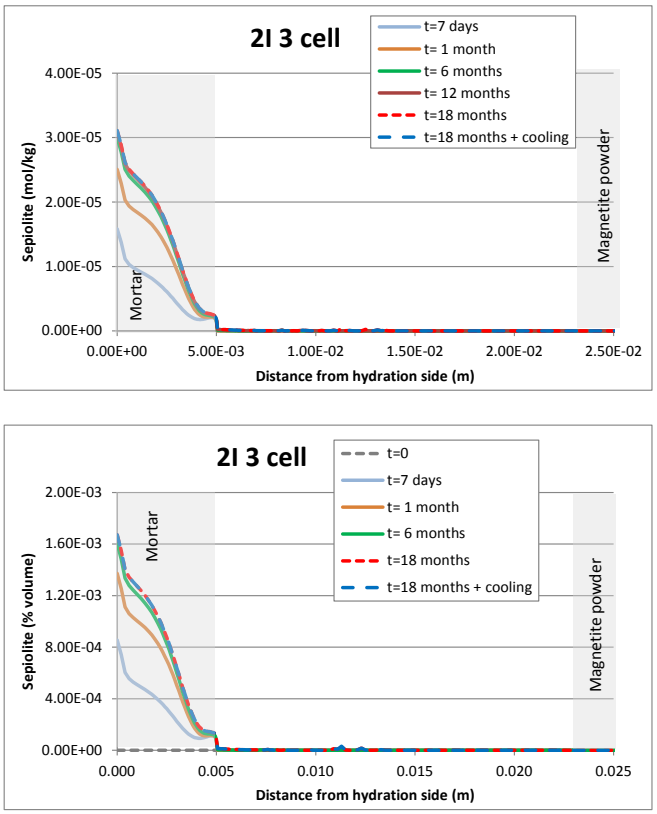

Figure 7-16. Spatial distribution of the computed volumetric fraction of sepiolite in the double interface 2I3 test. Cumulative precipitation/dissolution (mol/kg) (top) and volume fraction (bottom). Positive values for precipitation and negative values for dissolution.

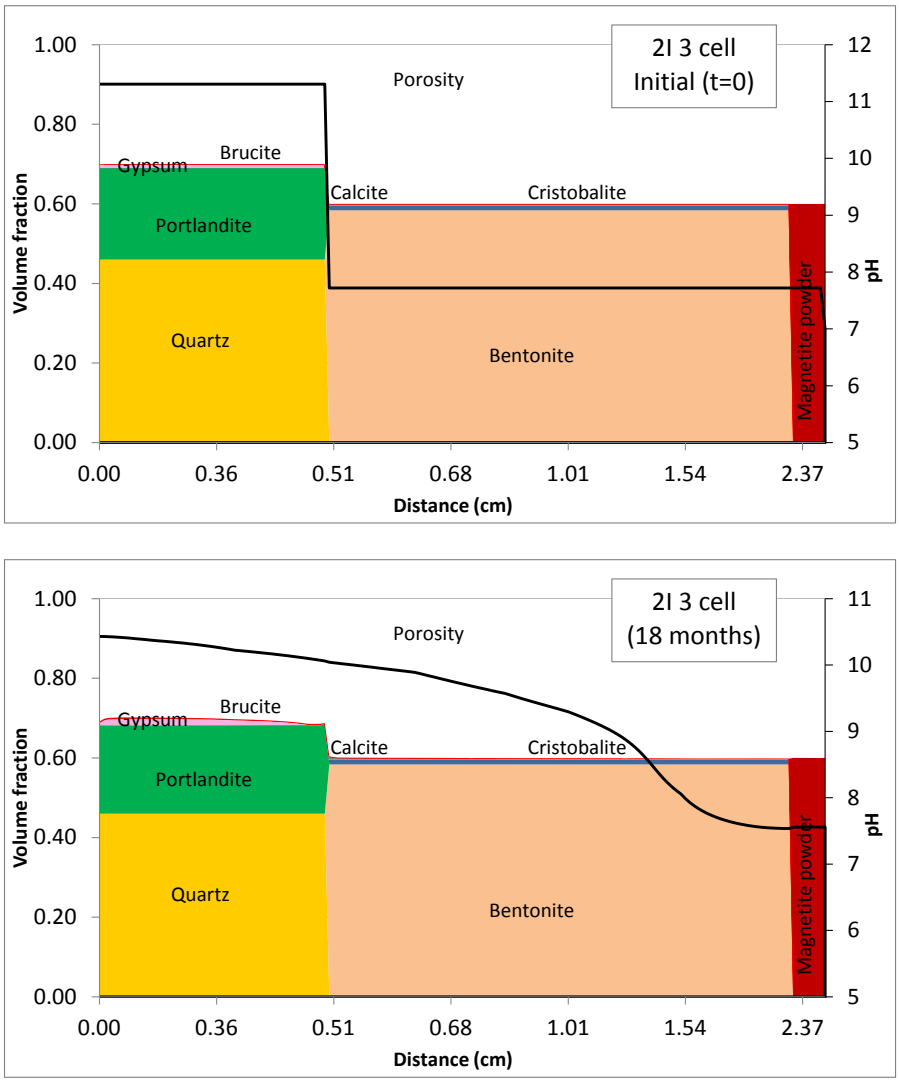

Figure 7-17. Spatial distribution of mineral fraction volume in the double interface 2I3 test. Initial mineral volume (top) and at the end of the test (bottom).

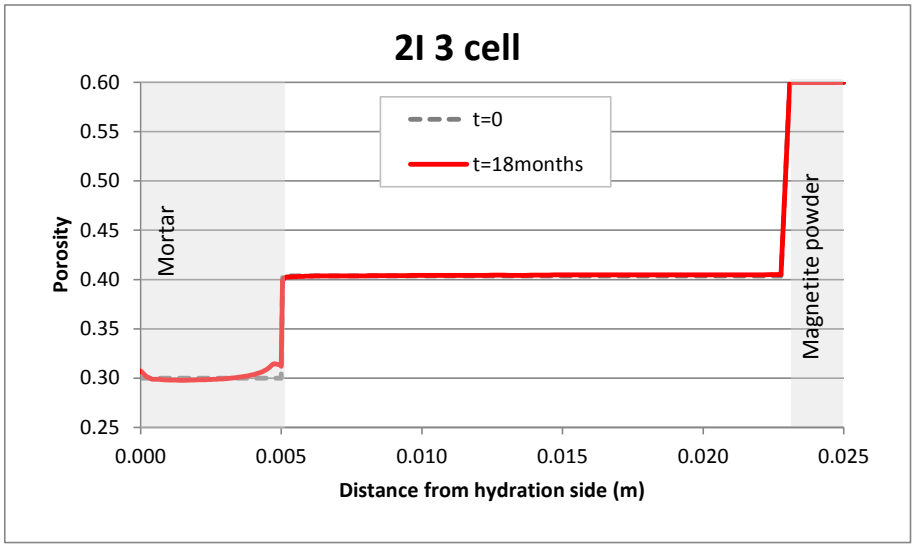

Figure 7-18. Spatial distribution porosity in the double interface 2I3 test at the end of the test.

Table 7-4. Experimental observations and THMC model results for the 2I3 test.

		Observations	THC model result
Mortar	Hydration interface	- **Gypsum** precipitates - **Brucite** precipitates - **Portlandite** dissolves	**- Gypsum** precipitates (0.8% volume) - **Brucite** precipitates (0.25% volume) **- Sepiolite** precipitates ($1.6 \cdot 10^{-3}$ % volume) - **Portlandite** dissolves (1% volume)
	Mortar	- **Ettringite** precipitates - **Portlandite** dissolves - No **carbonates**	**-** No **Ettringite** precipitation **- Portlandite** dissolves (1% volume) - **Calcite** precipitates (0.4% volume)
	Contact mortar-bentonite	- **CSH** precipitates	- **CSH** precipitates ($3.8 \cdot 10^{-4}$ % volume)
Bentonite	Contact bentonite (d<3 mm)	- No **sulphate** precipitation - **Sepiolite** precipitation - **CSH** precipitates - **Ettringite** precipitates	- No **Gypsum** precipitates - No **Anhydrite** precipitates **- Brucite** precipitates (0.06% volume) - **Sepiolite** precipitates ($1.0 \cdot 10^{-4}$ % volume) - **CSH** precipitates ($1.2 \cdot 10^{-4}$ % volume) **-** No **Ettringite** precipitation
	Bentonite (d>3 mm)		

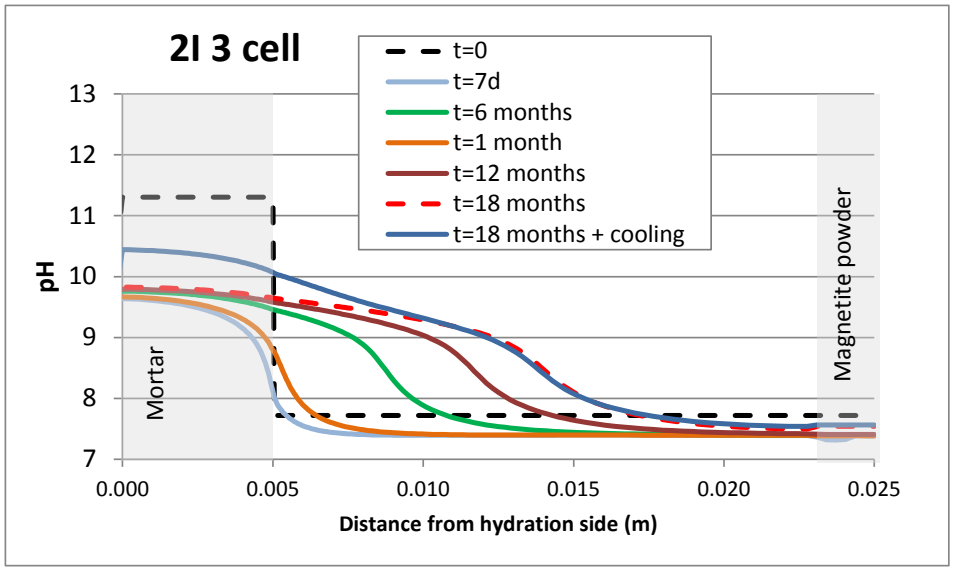

Figure 7-19. Spatial distribution the computed pH in the double interface 2I3 test at several times.

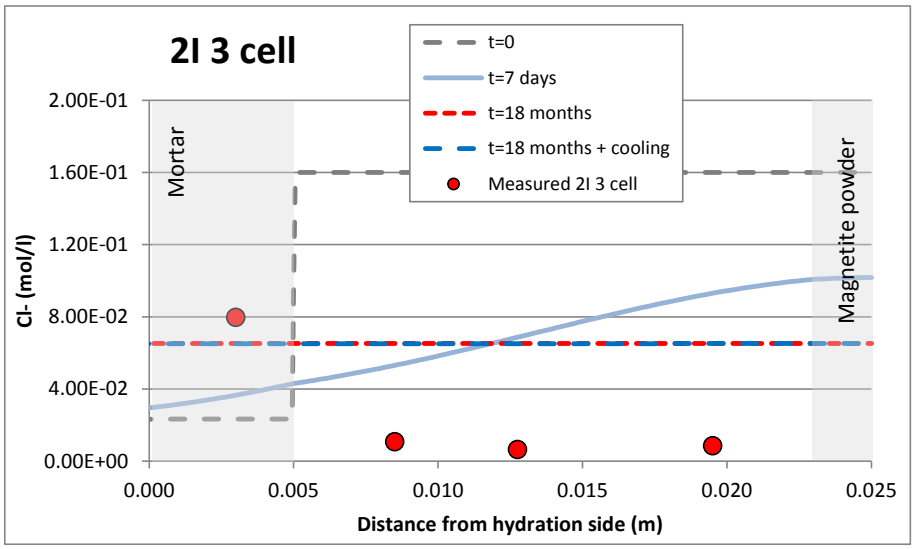

Figure 7-20. Spatial distribution of the computed concentration at several times (lines) and measured (symbols) of dissolved Cl^- in the double interface 2I3 test.

7.6 Conclusions

The numerical model of the double interfaces (concrete-bentonite and bentonite-corrosion products) tests reproduce the measured water content and water intake. For the most part, the numerical model captures the main trends in mineral dissolution/precipitation. However, there are some discrepancies, especially for ettringite in the mortar and in the bentonite (precipitation is observed in the test), and brucite precipitation at the mortar-bentonite interface and in the bentonite (not observed in the test). The lack of thermodynamic data for CASH phases prevented to account for CASH phases in the models.

8 Conclusions

Advanced multiple-continua models for clay barriers have been developped by improving the previous THC(m) models. Such improvements include:

1) Accounting for different types of waters (free, adsorbed and interlayer) in clays and different types of pores (macropores, Interaggregate and Interaggregate pores) in multiple-continua models.
2) Incorporating mechanical and geochemical couplings to account for porosity changes caused by swelling phenomena. This leads to fully coupled THMC models.
3) Improvements in the chemistry of gaseous species such as O_2(g), CO_2(g) and H_2(g).

Model improvements were implemented in the INVERSE-FADES-CORE code developed at the University of A Coruña (Zheng et al., 2010).

The improved models have been tested with data from:

1) The FEBEX mock-up test
2) Heating and hydration tests on 60 cm long cells
3) Heating and hydration corrosion tests
4) Heating and hydration tests with concrete and bentonite
5) Heating and hydration tests with two interphases: magnetite-bentonite and concrete-bentonite

8.1 Model testing with data from the FEBEX mock-up test

The FEBEX mock-up model results have been tested with measured data collected from 2007 till 2012. The computed water intake reproduces the measured intake data. A slight deviation is observed at t = 5000 days. Figure 2 shows the computed and relative humidity at the sensors located at 0.22, 0.37, 0.55 and 0.70 m. The computed relative humidities reproduce the measured data at the external sensors (r = 0.55 and r = 0.70 m), but underestimate the measured data after 1500 days at the internal sensors (r = 0.22 and r = 0.37 m). A double porosity model could overcome these discrepancies.

8.2 Modeling the 60 cm long heating and hydration tests

The testing of the THMC models with data from the 60-cm long heating and hydration tests (CG cells) show that the model captures the main trends of the measured data of the CG0.5, CG0.5b, CG1, CG1b, CG2 and CG2b tests. However, model results show some discrepancies which indicate the need to calibrate some model parameters. The following parameters were calibrated:

1) The vapour tortuosity. Its initial value of 0.3 was adjusted. ts optimum value is 0.4 for the CG0.5, CG1 and CG2 cells and 0.2 for the CG7.6 cell.
2) The lateral heat dissipation parameters. While lateral heat dissipation was not considered for model testing, measured temperature data indicate that heat dissipation must be taken into account. Heat dissipation was modelled with a Cauchy condition according to which the heat outflux, Q_c, is computed from:$Q_c = \alpha_T(T - T^*)$, where α_T is the thermal coefficient (calibrated to a value of 1016 W/ºC) and T^* is the external temperature which is equal to the mean temperature measured in the thermal sensors.
3) The selectivity coefficients of the cation exchange. The initial values were taken from Zheng et al., (2010). However, they were calibrated to reproduce the measured cation exchange data.

After model calibration, the numerical model reproduces the measured porosity data for the CG0.5, CG0.5b, CG1, CG1b, CG2, CG2b and CG7.6 tests. The computed gravimetric water content and saturation fit the measured data, especially the fitting is improved near the neater. The numerical results reproduce the measured water intake of all the tests. Computed concentration of Cl^- and exchanged cations fit the measured data for the CG0.5, CG1 and CG2 tests. Computed concentration of Cl^-, Mg^{2+}, Ca^{2+}, Na^+, K^+, SO_4^{2-}, HCO_3^- and pH reproduced well the results of CGM for the CG7.6 test.

8.3 Modeling corrosion tests

The results of the coupled THCm models of the corrosion tests indicate that:

1) Magnetite and $Fe(OH)_2(s)$ precipitate and compete for Fe^{2+} precipitation. These corrosion products penetrate a few mm into the bentonite.
2) Fe^{2+} is sorbed by surface complexation.
3) Fe^{2+} cation exchange is less relevant than Fe^{2+} sorption.

8.4 Modeling concrete-bentonite interface tests

The coupled THCm numerical models of the bentonite-concrete interface tests capture the main observed trends of mineral dissolution-precipitation. The HB4 model, however, do not reproduce the ettringite and CSH precipitation. For these phases, the numerical model predicts much less precipitation than the observed values. The porosity decreases in the bentonite/concrete interface due to the precipitation of minerals and decreases near the hydration boundary due to the dissolution of portlandite and quartz. The lack of thermodynamic data for CASH phases prevented to account for CASH phases in the models.

8.5 Modeling the double interface tests

The numerical model of the double interfaces (concrete-bentonite and bentonite-corrosion products) tests reproduce the measured water content and water intake. For the most part, the numerical model captures the main trends in mineral dissolution/precipitation. However, there are some discrepancies, especially for ettringite in the mortar and in the bentonite (precipitation is observed in the test), and brucite precipitation at the mortar-bentonite interface and in the bentonite (not observed in the test). The lack of thermodynamic data for CASH phases prevented to account for CASH phases in the models.

9 References

Ayora, C., Soler, J. M., Saaltink, M. W., Carrera, J., 2007. Modelo de transporte reactivo sobre la lixiviación del hormigón por agua subterránea en la Celda 16 de El Cabril. Techn. Publ. ENRESA PT 05-2007.

Bradbury, M.H., Baeyens, B., 1997. A mechanistic description of Ni and Zn sorption on Na-montmorillonite. Part II: modelling. J. Contam. Hydrol. 27, 223–248.

Bradbury, M.H., Baeyens, B., 1998. A physicochemical characterisation and geochemical modelling approach for determining pore water chemistries in argillaceous rocks. Geochim. Cosmochim. Acta 62, 783–795.

Bradbury, B., Baeyens, B., 2003. Pore water chemistry in compacted resaturated MX-80 bentonite. J. Contam. Hydrol. 61, 329–338.

Cuevas, J., Turrero, M.J., Torres, E., Fernández, R., Ruiz, A.I., Escribano, A., 2013. Deliverable D2.3-3-2 of PEBS Project. Laboratory tests at the interfaces. Results of Small Cells with mortar-bentonite-magnetite. CIEMAT.

De Vries, D.A., 1963. Thermal properties of soils. In: Van Wijk, W.R. (Ed.), Physics of Plant Environment. North-Holland Publishing Company, Amsterdam, pp. 210–235.

Dai, Z., Samper, J., 2004. Inverse problem of multicomponent reactive chemical transport in porous media: formulation and applications. Water Resour Res 40, W07407.

Dai, Z., Samper, J., 2006. Inverse modeling of water flow and multicomponent reactive transport in coastal aquifer systems. J. Hydrol. 327 (3-4), 447–461.

Dai, Z., Samper, J., Ritzi, R., 2006. Identifying geochemical processes by inverse modeling of multicomponent reactive transport in Aquia aquifer. Geosphere 4 (4), 210–219.

De Windt, L. and Torres, E., 2009. Modélisation d'expériences en cellule reproduisant les conditions THC d'une alvéole de déchets HAVL. Rapport Technique R201009LDEWI. Accord spécifique IRSN/ARMINES.

De Windt, L. and Torres, E., 2010. Interactions béton/argile sous gradient thermique et réhydratation : modélization d'experiénce en cellule. Rapport Technique R301110LDEWI. Accord spécifique IRSN/ARMINES.

ENRESA, 2000a. Full-scale engineered barriers experiment for a deep geological repository in crystalline host rock FEBEX Project. EUR 19147 EN, European Commission.

ENRESA 2000b. Evaluación del comportamiento y de la seguridad de un almacenamiento de combustible gastado en una formación granítica. ENRESA Informe 49-1PP-M-15-01. Madrid, 2001.

ENRESA 2004. Evaluación del comportamiento y de la seguridad de un almacén geológico profundo de residuos radiactivos en arcilla. PT 49-1PP-M-A1-01.

ENRESA, 2005, Phenomenological description. Reference Concept (Spent Fuel-Carbon Steel Canister-Bentonite-Granite). NF-PRO Integrated Project. Deliverable D5.1.1. Part 1. Final version.

ENRESA, 2006a. Full-Scale Engineered Barriers Experiment: Updated Final Report. ENRESA Tech. Publ. PT 05-02/2006, 589 pp.

ENRESA, 2006b. FEBEX: Final report on thermo-hydro-mechanical modelling. ENRESA Techn. Publ. PT 05-2/2006, 163 pp

ENRESA, 2006c. FEBEX: Final THG modelling report. ENRESA Techn. Publ. PT 05-3/2006, 155 pp

Fernández A.M., Cuevas, J. and Rivas, P., 2001. Pore water chemistry of the FEBEX bentonite. Mat. Res. Soc. Symp. Proc. 663,573-588

Fernández A.M., Bayens, B., Bradbury, M. and Rivas, P., 2004. Analysis of pore water chemical composition of a Spanish compacted bentonite used in an engineered barrier. Phys. Chem Earth (29), 105-118.

Fernández, A.M., Rivas, P., 2005. Analysis and distribution of waters in the compacted FEBEX bentonite: pore water chemistry and adsorbed water properties. In: Alonso, E.E., Ledesma, A. (Eds.), Advances in Understanding Engineered Clay Barriers. A.A. Balkema Publishers, Leiden, The Netherlands, pp. 257–275.

Fernández, R., Cuevas, J. and. Mäder, U. K, 2009. Modelling concrete interaction with a bentonite barrier. Eur. J. Mineral., 21, 177-191.

Fernández A. M., and Villar, M.V., 2010. Geochemical behaviour of bentonite barrier in the laboratory after up to 8 years of heating and hidrating. Applied Geochemistry 25 809-824.

Fredlund, D.G., Rahardjo, H., 1993. Soil Mechanics for Unsaturated Soils.Wiley-IEEE. 517 pp.

Galíndez, J.M., Molinero, J., Samper, J., Yang, C.B., 2006. Simulating concrete degradation processes by reactive transport models. J. Phys. IV France 136, 177–188.

Keijzer, T.J.S., Kleingeld, P.J., Loch, J.P.G., 1999. Chemical osmosis in compacted clayey material and the prediction of water transport. Eng. Geol. 53, 151–159.

Keijzer, T.J.S., Loch, J.P.G., 2001. Chemical osmosis in compacted dredging sludge. Soil Sci. Soc. Am. J. 65, 1045–1055.

Lloret, A., Alonso, E.E., 1995. State surfaces for partially saturated soils. In: Proceedings of the International Conference on Soils Mechanics and Foundation Engineering, Balkema, pp. 557–562.

Martín, P.L., Barcala, J.M., 2005. Large scale buffer material test: mock-up experiment at CIEMAT. Eng. Geol. 81, 298–316.

Martín, P.L., Barcala, J.M., and Huertas, F., 2006. Large-scale and long-term coupled thermo-hydro-mechanic experiements with bentonite: the FEBEX mock up test. J. Iberian Geol. 32 (2), 259-282.

Molinero, J., Samper, J., Zhang, G., Yang, C., 2004. Biogeochemical reactive transport model of the redox zone experiment of the Äspö hard rock laboratory in Sweden. Nucl. Technol. 148, 151–165.

Molinero, J., Samper, J., 2006. Modeling of reactive solute transport in fracture zone of granitic bedrocks. J. Cont. Hydrol. 82, 293–318.

Navarro, V., 1997. Modelo de comportamiento mecánico e hidráulico de suelos nosaturados en condiciones no isotermas. Ph.D. Dissertation, Universidad Politécnica de Cataluña, 329 pp. (in Spanish).

Navarro, V. and Alonso, E.E., 2000. Modelling swelling soils for disposal barriers. Compt. Geotech. 27,19-43.

Nguyen, T.S., Selvadurai, A.P.S., Armand, G., 2005. Modelling the FEBEX THM experiment using a state surface approach. Int. J. Rock Mech. Min. Sci. 42 (5–6), 639–651.

Palandri, J. L., Kharaka, Y. K., 2004. A compilation of rate parameters of water-mineral interaction kinetics for applications to geochemical modelling. U.S. Geological Survey.

Pearson, F.J., Arcos, D., Bath, A., Boisson, J.Y., Fernández, A.M., Gäbler, H.-E., Gaucher, E., Gautschi, A., Griffault, L.,Hernán, P., Waber, H.N., 2003.

Geochemistry of Water in the Opalinus Clay Formation at the Mont Terri Rock Laboratory.Swiss Federal Office for Water and Geology Series Nº 5.

Pollock, D.W., 1986. Simulation of fluid flow and energy transport processes associated with high-level radioactive waste disposal in unsaturated alluvium. Water Resour. Res. 22 (5), 765–775.

Tang, A.M., Cui, Y.J., Le, T.T., 2008. A study on the thermal conductivity of compacted bentonites. Appl. Clay Sci. 41 (3–4), 181–189.

Torres, E., Turrero, M. J., Peña, J., Martín, P.L., Escribano, A., Alonso, U., Villar, M.V., 2008. Deliverable 2.3.2 of component 2 NF-PRO project. Interaction iron-compacted bentonite: corrosion products and changes in the properties of the bentonite, 2008. CIEMAT

Torres, E., Turrero, M.J., Escribano, A., 2013. Synthesis of corrosion phenomena at the iron/bentonite interface under unsaturated condictions. Thecnical Note CIEMAT/DMA/2G210/02/2013. PEBS Project.

Turrero, M. J., Villar, M. V., Torres, E., Escribano, A., Cuevas, J., Fernández, R., Ruiz, A. I., Vigil de la Villa, R., del Soto, I., 2011. Deliverable 2.3-3-1 of PEBS Project. Laboratory tests at the interfaces, Final results of the dismantling of the tests FB3 and HB4, 2011. CIEMAT.

Sacchi, E., Michelot, J.L., Pitsch, H., Lalieux, P., Aranyossy, J.F., 2001. Extraction of water and solution from argillaceous rock for geochemical characterisation: methods, processes, and current understanding. Hydrol. J. 9, 17–33.

Samper, J., Yang, C., Montenegro, L., 2003. CORE2D version 4: a code for non-isothermal water flow and reactive solute transport. Users Manual. University of La Coruña, Spain.

Samper, J., Dai, Z., Molinero, J., García-Gutiérrez, M., Missana, T., Mingarro, M., 2006. Inverse modeling of tracer experiments in FEBEX compacted Ca-bentonite. Phys. Chem. Earth 31, 640–648.

Samper, J., Yang, C., 2006. Stochastic analysis of transport and multicomponent competitive monovalent cation exchange in aquifers. Geosphere 2, 102–112.

Samper, J., Zheng, L., Montenegro, L., Fernández, A.M., Rivas, P., 2008a. Testing coupled thermo-hydro-chemical models of compacted bentonite after dismantling the FEBEX in situ test. Appl. Geochem. (23/5), 1186–1201.

Samper, J., Zheng, L., Fernández, A.M., Montenegro, L., 2008b. Inverse modeling of multicomponent reactive transport through single and dual porosity media. J.

Cont. Hydrol.

Samper, J., Mon, A., Pisani, B., Montenegro, L., 2011. Report on integration of available data for bentonites from different scales and scaling laws and extrapolation for long-term analyses for clay barriers. Deliverable 3.5-1 of PEBS Project.

Soler, J.M., 2001. The effect of coupled transport phenomena in the Opalinus clay and implications for radionuclide transport. J. Contam. Hydrol. 53, 63–84.

Villar, M.V, Fernández, A.M., Martín, P.L., Barcala, J.M., Gómez-Espina, R. and Rivas, P., 2008a. Effect of heating/hydration on compacted bentonite: test in 60 cm long cells. Colección Documentos CIEMAT.

Villar, M.V., Sánchez, M., Gens, A., 2008b. Behaviour of a bentonite barrier in the laboratory: experimental results up to 8 years and numerical simulation. Physics and Chemistry of the Earth, Vol. 33, Supplement 1, pp. S476-S485.

Villar, M. V., Martín, P. L., Romero, F. J., Gutiérrez-Rodrigo, V., Barcala, J. M., 2012. Gas and Water Permeability of Concrete. Informes técnicos CIEMAT.

Villar, M. V., 2013. Long-term Performance of Engineered Barrier Systems PEBS. Summary of concrete hydraulic properties determined at CIEMAT. Technical Note CIEMAT/DMA/2G210/01/13.

Wollery, T.J., 1992. EQ3/3. A software package for geochemical modeling of aqueous system: package overview and installation guide version 7.0. UCRL-MA-110662-PT-I, Lawrence Livermore National Laboratory, Livermore, California.

Xu, T., Samper, J., Ayora, C., Manzano, M., Custodio, E., 1999. Modeling of non-isothermal multi-component reactive transport in field scale porous media flow systems. J. Hydrol. 214 (1–4), 144–164.

Yang, C., Samper, J., Molinero, J., Bonilla, M., 2007. Modeling geochemical and microbial consumption of dissolved oxygen after backfilling a high level radioactive waste repository. J. Contam. Hydrol. 93, 130–148.

Yang, C., Samper, J., Montenegro, L., 2008. A coupled non-isothermal reactive transport model for long-term geochemical evolution of a HLW repository in clay. Environ. Geol. 53, 1627–1638.

Zhang, G., Samper, J., Montenegro, L., 2008. Coupled thermo-hydro-bio-geochemical reactive transport model of the CERBERUS heating and radiation experiment in Boom clay. Appl. Geochem. (23/4), 932–949.

Zheng, L., Samper, J., 2004. Formulation of the inverse problem of non-isothermal multiphase flow and reactive transport in porous media. Comput. Meth. Water Resour. XV, 1317–1327.

Zheng, L and Samper, J., 2005. A dual continuum coupled multiphase flow model with mixed second order water transfer term for structured soils. Jornadas de la Zona no Saturada 2005, VII, 301-306.

Zheng, L., 2006. Coupled thermo-hydro-mechanical-geochemical models for structured deformable porous media. Ph.D. Dissertation, Universidad de A Coruña, A Coruña, Spain, 439 pp.

Zheng, L. and Samper, J., 2008. A coupled THMC model of FEBEX mock-up test. Physics and Chemistry of the Earth 33, S486-S498

Zheng, L., Samper, J. and Montenegro, L., 2008a. Inverse hydrochemical model of aqueous test. Physics and Chemistry of the Earth 33,1009-1018

Zheng, L., J. Samper, L. Montenegro & J.C. Mayor, 2008b, Flow and reactive transport model of a ventilation experiment in Opallinus clay, Physics and Chemistry of the Earth, Vol. 33, S486–S498. doi:10.1016/j.pce.2008.05.012

Zheng, L., Samper, J., Montenegro, L. and Fernández, A.M., 2010. A coupled model of heating and hydration laboratory experiment in unsaturated compacted FEBEX bentonite. Journal of hydrology 386, 80-94.

Zheng L J Samper and L Montenegro, 2011, A coupled THC model of the FEBEX in situ test with bentonite swelling and chemical and thermal osmosis, J of Contaminant Hydrology 126:45–60. doi:10.1016/j.jconhyd.2011.06.003

Appendix A. Tables of parameters and chemical reactions and constants

A.1. Thermo-hydro-mechanical parameters

Table A1-1. Water flow parameters (ENRESA, 2006a; Zheng et al., 2010, Villar et al., 2012; Villar, 2013).

	Bentonite	Concrete/ Mortar	Fe powder/ Magnetite powder
Intrinsic permeability of the liquid, k^{il} (m^2) as a function of porosity	with $\emptyset_o$=0.40 k_o= $2.75 \cdot 10^{-21}$	$k^{il} = k_0 \frac{\emptyset^3}{(1-\emptyset)^2} \frac{(1-\emptyset_0)^2}{\emptyset_0^3}$ with $\emptyset_o$=0.125 concrete with $\emptyset_o$=0.3 mortar k_o= $3.6 \cdot 10^{-18}$	with $\emptyset_o$=0.40 Fe powder with $\emptyset_o$=0.20 magnetite powder k_o= $2.75 \cdot 10^{-19}$
Liquid relative permeability k^{rl} as a function of liquid saturation S_l	$k_{rl} = S_l^3$		
Retention curve: liquid saturation S_l as a function of suction Ψ (Pa)	$S_l = \frac{(1 - 9.1 \cdot 10^{-7}\Psi)^{1.1}}{[(1 + 5 \cdot 10^{-5}\Psi)^{1.22}]^{0.18}}$	$S_l = 1 + \frac{(1 - 0.2)}{[(1 + (3.8 \cdot 10^{-3}\Psi)^{1.23}]^{0.19}}$	$S_l = \frac{(1 - 9.1 \cdot 10^{-7}\Psi)^{1.1}}{[(1 + 5 \cdot 10^{-5}\Psi)^{1.22}]^{0.18}}$
Liquid viscosity (kg/m·s) as a function of temperature T (ºC)	$0.6612 \cdot (T - 229)^{-1.562}$		
Liquid density (kg/m^3) as a function of liquid pressure p^l and temperature	$998.2 \cdot e^{[5 \cdot 10^{-5} \cdot (p^l - 100) - 2.1 \cdot 10^{-4} \cdot (T - T_{ref})]}$		
Reference temperature, T_{ref} (ºC)	22		
Gas intrinsic permeability (m^2)	$5 \cdot 10^{-10}$		
Gas relative permeability k^{rg}	$k_{rl} = (1 - S_l)^3$		
Vapour tortuosity	0.3	0.3	1.0
Gas viscosity (kg/m·s)	$1.76 \cdot 10^{-5}$		
Solid density (kg/m^3)	$2750 \cdot e^{[-2 \cdot 10^{-5} \cdot (T - T_{ref})]}$	$2360 \cdot e^{[-2 \cdot 10^{-6} \cdot (T - T_{ref})]}$	$2785 \cdot e^{[-2 \cdot 10^{-6} \cdot (T - T_{ref})]}$
Reflection coefficient for chemical osmosis	0.2		
Thermo-osmotic permeability (m^2/K/s)	$4.2 \cdot 10^{-13}$		

Table A1-2. Thermal parameters (ENRESA, 2006a; Zheng et al., 2010).

	Bentonite	Concrete/ Mortar	Fe powder/ Magnetite powder
Specific heat of the liquid (J/kg·ºC)	4202		
Specific heat of the air (J/kg·ºC)	1000		
Specific heat of the vapour (J/kg·ºC)	1620		
Specific heat of the solid (J/kg·ºC)	835.5	480	789
Reference temperature (ºC)	22		
Thermal conductivity of the liquid (W/m·ºC)	1.5		
Thermal conductivity of the air (W/m·ºC)	$2.6 \cdot 10^{-2}$		
Thermal conductivity of the vapour (W/m·ºC)	$4.2 \cdot 10^{-2}$		
Thermal conductivity of the solid (W/m·ºC)	1.23	50.16	1.56
Vaporization enthalpy (J/kg)	$2.45.10^6$		

Table A1-3. Solute transport parameters(ENRESA, 2006a; Zheng et al., 2010).

	Bentonite	**Concrete/ Mortar**	**Fe powder/ Magnetite powder**
Molecular diffusion coefficient in water $D_0(T)$ in m^2/s as a function of T and the molecular diffusion coefficient at the reference temperature T_{ref} (ºC), $D_0(T_{ref})$	$D_o(T) = D_o(T_{ref})\frac{T}{T_0}\frac{\mu_0^l}{\mu^l}$ $D_o(T_{ref}) = 2 \cdot 10^{-10}$, (except Cl^-, $D_o(T_{ref}) = 9 \cdot 10^{-11}$)		
Longitudinal dispersivity (m)	0.001	0.02	0.01
Solute tortuosity τ as a function of volumetric water content θ and porosity ϕ	$\tau = \frac{\theta^{7/3}}{\emptyset^2}$		

Table A1-4. Mechanical parameters (ENRESA, 2006a; Zheng et al., 2010).

	Bentonite	**Concrete/ Mortar**	**Fe powder/ Magnetite powder**
Water mechanical compressibility (Pa^{-1})		$5 \cdot 10^{-7}$	
Water thermal expansion (K^{-1})		$2.1 \cdot 10^{-4}$	
Solid thermal expansion (K^{-1})	$2 \cdot 10^{-5}$		$2 \cdot 10^{-6}$
State surface parameters	$e = A + B \cdot ln\sigma' + C \cdot \ln(\Psi + P^a) + D \cdot ln\sigma' \cdot \ln(\Psi + P^a)$ A=0.76; B=-0.052446; C=-0.0406413; D=0.00479977	-	-

A.2. Chemical parameters

Table A2-1. Chemical composition of the initial porewater in bentonite, concrete and mortar, and the hydration boundary water used in the UDC THCm models.

	Initial bentonite porewater (Fernández et al., 2001)	Initial concrete[(1)] porewater	Initial mortar[(2)] porewater	Synthetic Spanish Reference clay porewater (Turrero et al., 2011)	Grimsel hydration water (Turrero et al., 2011)	Granitic hydration water for the CG tests (Villar et al., 2008)
Na^+	$1.3\cdot10^{-1}$	$1.6\cdot10^{-2}$	$1.3\cdot10^{-1}$	$1.3\cdot10^{-1}$	$3.7\cdot10^{-4}$	$4.8\cdot10^{-4}$
Ca^{2+}	$2.2\cdot10^{-2}$	$4.4\cdot10^{-3}$	$1.4\cdot10^{-2}$	$1.1\cdot10^{-2}$	$1.8\cdot10^{-4}$	$1.1\cdot10^{-3}$
Mg^{2+}	$2.3\cdot10^{-2}$	$1.8\cdot10^{-8}$	$9.1\cdot10^{-3}$	$8.2\cdot10^{-2}$	$1.6\cdot10^{-5}$	$3.9\cdot10^{-4}$
K^+	$1.7\cdot10^{-3}$	$1.0\cdot10^{-1}$	$8.0\cdot10^{-4}$	$8.2\cdot10^{-4}$	$2.2\cdot10^{-5}$	$2.6\cdot10^{-5}$
SO_4^-	$3.2\cdot10^{-2}$	$1.6\cdot10^{-2}$	$5.8\cdot10^{-2}$	$7.0\cdot10^{-2}$	$6.1\cdot10^{-5}$	$1.5\cdot10^{-4}$
Cl^-	$1.6\cdot10^{-1}$	$1.0\cdot10^{-5}$	$2.3\cdot10^{-2}$	$2.3\cdot10^{-2}$	$2.3\cdot10^{-5}$	$3.7\cdot10^{-4}$
$SiO_2(aq)$	$1.0\cdot10^{-4}$	$2.0\cdot10^{-5}$	$3.0\cdot10^{-4}$	$2.7\cdot10^{-4}$	$1.9\cdot10^{-4}$	$1.9\cdot10^{-4}$
HCO_3^-	$5.8\cdot10^{-4}$	$1.7\cdot10^{-5}$	$1.8\cdot10^{-3}$	$1.8\cdot10^{-3}$	$3.9\cdot10^{-4}$	$2.3\cdot10^{-3}$
Al^{3+}	-	$1.8\cdot10^{-5}$	$1.8\cdot10^{-5}$	$1.0\cdot10^{-8}$	-	-
Fe^{2+}	$6.6\cdot10^{-5}$	-	-	-	$1.8\cdot10^{-8}$	-
pH	7.72	13.25	11.30	7.54	9.7	8.3

[(1)] concrete pore water was calculated with EQ3 based on the concrete pore water of ENRESA, 2004 and equilibrated with portlandite, calcite, brucite, ettringite and C1.8SH

[(2)]mortar pore water was calculated with EQ3 based on the RAF water and equilibrated with portlandite and gypsum.

Table A2-2. Site capacities (mol/kg) for FEBEX bentonite (Bradbury and Bayens, 1997) and bentonite with corrosion products.

Type of site	Bentonite		Bentonite and corrosion	
	Surface complex	**Site capacity (mol/kg)**	**Surface complex**	**Site capacity (mol/kg)**
S^SOH	$S^SOH_2^+$ S^SO^-	$1.5\cdot10^{-3}$	$S^SOH_2^+$ S^SO^- S^SOFe^+ S^SOFeOH $S^SOFe(OH)_2^-$	$1.5\cdot10^{-3}$
$S^{w1}OH$	$S^{w1}OH_2^+$ $S^{w1}O^-$	$30.5\cdot10^{-3}$	$S^{w1}OH_2^+$ $S^{w1}O^-$ $S^{w1}OFe^+$	$30.5\cdot10^{-3}$
$S^{w2}OH$	$S^{w2}OH_2^+$ $S^{w2}O^-$	$30.5\cdot10^{-3}$	$S^{w2}OH_2^+$ $S^{w2}O^-$	$30.5\cdot10^{-3}$

Table A2-3. Initial concentration of exchanged cations (in meq/100g) for FEBEX bentonite (Fernández et al., 2004) and for bentonite with corrosion products.

	Ca^{2+}	**Mg^{2+}**	**Na^+**	**K^+**	**Fe^{2+}**	**CEC**
Bentonite	34.62	34.01	31.18	1.94	-	102
Bentonite-CP	42.0	33.0	25.5	2.2	0.5	102.70

Table A2-4. Chemical reactions and equilibrium constants for aqueous complexes at 25ºC of (Wolery, 1992) for bentonite, the additional reaction of bentonite with corrosion products and with concrete interactions.

Aqueous complexes	Log K
$CaCO_3(aq) + H^+ \Leftrightarrow Ca^{2+} + HCO_3^-$	7.0017
$CaHCO_3^+ \Leftrightarrow Ca^{2+} + HCO_3^-$	-1.0467
$CaSO_4(aq) \Leftrightarrow Ca^{2+} + SO_4^{2-}$	-2.1111
$CaCl^- \Leftrightarrow Ca^{2+} + Cl^-$	0.6956
$CO_2(aq) + H_2O \Leftrightarrow H^+ + HCO_3^-$	-6.3447
$CO_3^{2-} + H^+ \Leftrightarrow HCO_3^-$	10.3288
$KSO_4^- \Leftrightarrow K^+ + SO_4^{2-}$	-0.8796
$MgCO_3(aq) \Leftrightarrow Mg^{2+} + CO_3^{-2}$	-2.9789
$MgHCO_3^+ \Leftrightarrow Ca^{2+} + HCO_3^-$	-1.0357
$MgSO_4(aq) \Leftrightarrow Mg^{2+} + SO_4^{2-}$	-2.4117
$MgCl^- \Leftrightarrow Mg^{2+} + Cl^-$	0.1349
$NaHCO_3(aq) \Leftrightarrow Na^+ + HCO_3^-$	-0.1541
$NaSO_4^- \Leftrightarrow Na^+ + SO_4^{2-}$	-0.8200
$NaCO_3^- + H^+ \Leftrightarrow Na^+ + HCO_3^-$	9.8367
$NaCl^-(aq) \Leftrightarrow Na^+ + Cl^-$	0.7770
$H_3SiO_4^- + H^+ \Leftrightarrow SiO_2(aq) + 2H_2O$	9.8120
$OH^- + H^+ \Leftrightarrow H_2O$	13.9951
Corrosion-bentonite cells (SC and FB3 cells)	
$HS^- + 2O_2(aq) \Leftrightarrow H^+ + SO_4^{2-}$	138.31
$Fe^{3+} + 0.5\ H_2O \Leftrightarrow H^+ + 0.25\ O_2 + Fe^{2+}$	-8.2077
$FeHCO_3 \Leftrightarrow Fe^{2+} + HCO_3^-$	-1.98
$FeCO_3(aq) + H^+ \Leftrightarrow Fe^{2+} + HCO_3^-$	5.67
$FeCl^+ \Leftrightarrow Fe^{2+} + Cl^-$	0.154
$FeCl^{2+} + 0.5\ H_2O \Leftrightarrow Fe^{2+} + H^+ + 0.25\ O_2 + Cl^-$	-7.50
$FeOH^+ + H^+ \Leftrightarrow Fe^{2+} + H_2O$	10.7
$FeOH^{2+} \Leftrightarrow Fe^{2+} + 0.5H_2O + 0.25\ O_2$	-3.95
$Fe(OH)_2(aq) + 2H^+ \Leftrightarrow Fe^{2+} + H_2O$	20.2
$Fe(OH)_3(aq) + 2H^+ \Leftrightarrow Fe^{2+} + 0.25\ O_2 + 2.5H_2O$	3.96
$Fe(OH)_4^- + 3H^+ \Leftrightarrow Fe^{2+} + 0.25\ O_2 + 3.5H_2O$	13.0
$Fe(OH)_2^+ + H^+ \Leftrightarrow Fe^{2+} + 0.25\ O_2 + 1.5H_2O$	-2.7424
$Fe(SO_4)_2^- + 0.5H_2O \Leftrightarrow Fe^{2+} + H^+ + 2SO_4^{2-} + 0.25O_2$	-11.4
$FeSO_4(aq) \Leftrightarrow Fe^{2+} + SO_4^{2-}$	-21.9
$FeHSO_4^{2+} + 0.5H_2O \Leftrightarrow Fe^{2+} + 2H^+ + SO_4^{2-} + 0.25O_2$	-9.7477
$Fe_2(OH)_2^{4+} \Leftrightarrow 2Fe^{2+} + H_2O + 0.5\ O_2$	-9.3067
$KOH(aq) + H^+ \Leftrightarrow K^+ + H_2O$	14.4
$HSO_4^- \Leftrightarrow H^+ + SO_4^{2-}$	-2.0366
$H_2(aq) + 0.25O_2 \Leftrightarrow H_2O$	46.10
$NaHSiO_3(aq) + H^+ \Leftrightarrow H_2O + Na^+ + SiO_2(aq)$	8.3040
$HSiO_3^- + H^+ \Leftrightarrow H_2O + SiO_2(aq)$	9.9525
$MgH_3SiO_4^+ + H^+ \Leftrightarrow 2H_2O + Mg^{2+} + SiO_2(aq)$	8.5416
Concrete/mortar-bentonite cells(HB4 cell and 2I3 cell)	
$CaCl_2(aq) \Leftrightarrow Ca^{2+} + 2Cl^-$	0.6436
$Ca(H_3SiO_4)_2(aq) + 2H^+ \Leftrightarrow Ca^{2+} + 2SiO_2(aq) + 4H_2O$	15.0532
$CaH_2SiO_4(aq) + 2H^+ \Leftrightarrow Ca^{2+} + SiO_2(aq) + 2H_2O$	18.5616
$CaH_3SiO_4^+ + H^+ \Leftrightarrow Ca^{2+} + SiO_2(aq) + 2H_2O$	8.7916
$MgOH^+ + H^+ \Leftrightarrow Mg^{2+} + H_2O$	11.607
$Mg_4(OH)_4^{4+} + 4H^+ \Leftrightarrow 4Mg^{2+} + 4H_2O$	39.750
$MgH_2SiO_4(aq) + 2H^+ \Leftrightarrow Mg^{2+} + SiO_2(aq) + 2H_2O$	17.4816
$MgH_3SiO_4^+ + H^+ \Leftrightarrow Mg^{2+} + SiO_2(aq) + 2H_2O$	8.5416
$NaHSiO_3(aq) + H^+ \Leftrightarrow H_2O + Na^+ + SiO_2(aq)$	8.6616
$KOH(aq) + H^+ \Leftrightarrow K^+ + H_2O$	14.4600
$KCl^+(aq) \Leftrightarrow K^+ + Cl^-$	1.4946
$KHSO_4(aq) \Leftrightarrow H^+ + K^+ + SO_4^{2-}$	-0.8136
$H_2SiO_4^{2-} + 2H^+ \Leftrightarrow 2H_2O + SiO_2(aq)$	22.9116
$H_4(H_2SiO_4)_4^{4-} + 4H^+ \Leftrightarrow 8H_2O + 4SiO_2(aq)$	35.7464

$HSiO_3^- + H^+ \Leftrightarrow H_2O + SiO_2(aq)$	9.9525
$H_6(H_2SiO_4)_4^{2-} + 2H^+ \Leftrightarrow 8H_2O + 4SiO_2(aq)$	13.4464
$HCl^+(aq) \Leftrightarrow H^+ + Cl^-$	0.6700
$HSO_4^- \Leftrightarrow H^+ + SO_4^-$	1.9791
$Al(OH)_4^- + 4H^+ \Leftrightarrow Al^{3+} + 4H_2O$	22.1477
$Al(OH)_3(aq) + 3H^+ \Leftrightarrow Al^{3+} + 3H_2O$	16.1577
$Al(OH)_2^+ + 2H^+ \Leftrightarrow Al^{3+} + 2H_2O$	10.0991
$AlOH^{2+} + H^+ \Leftrightarrow Al^{3+} + H_2O$	5.0114

Table A2-5. Chemical reaction and equilibrium constants for minerals at 25ºC of (Wolery, 1992) for bentonite, the additional reaction of bentonite with corrosion products and with concrete interactions.

Minerals	**Log K**
$Calcite + H^+ \Leftrightarrow Ca^{2+} + HCO_3^-$	1.8487
$Anhydrite \Leftrightarrow Ca^{2+} + SO_4^{2-}$	-4.3064
$Gypsum \Leftrightarrow Ca^{2+} + SO_4^{2-} + 2H_2O$	-4.4823
$Chalcedony \Leftrightarrow SiO_2(aq)$	-3.7281
$Cristobalite \Leftrightarrow SiO_2(aq)$	-3.4488
Corrosion-bentonite cells (SC and FB3 cells)	
$Magnetite + 6H^+ \Leftrightarrow 3Fe^{2+} + 0.5O_2(aq) + 3H_2O$	-6.5076
$Siderite + H^+ \Leftrightarrow Fe^{2+} + HCO_3^-$	-0.1920
$Goethite + 2H^+ \Leftrightarrow Fe^{2+} + 1.5H_2O + 0.25O_2(aq)$	-7.9555
$Fe(OH)_2(s) + 2H^+ \Leftrightarrow Fe^{2+} + 2H_2O$	12.156
Concrete/mortar-bentonite cells(HB4 cell and 2I3 cell)	
$Quartz \Leftrightarrow SiO_2(aq)$	-3.9993
$Portlandite + 2H^+ \Leftrightarrow Ca^{2+} + 2H_2O$	22.5552
$Brucite + 2H^+ \Leftrightarrow Mg^{2+} + 2H_2O$	16.2980
$Sepiolite + 8H^+ \Leftrightarrow 4Mg^{2+} + 6SiO_2(aq) + 11H_2O$	30.4439
$C1.8SH + 3.6H^+ \Leftrightarrow 1.8Ca^{2+} + SiO_2(aq) + 2.8H_2O$	32.4814
$C0.8SH + 1.6H^+ \Leftrightarrow 0.8Ca^{2+} + SiO_2(aq) + 1.8H_2O$	10.8614
$C1.6SH + 3.2H^+ \Leftrightarrow 1.6Ca^{2+} + H_4SiO_4(aq) + 2.18H_2O$	28.0022
$C1.2SH + 2.4H^+ \Leftrightarrow 1.2Ca^{2+} + H_4SiO_4(aq) + 1.26H_2O$	19.3013
$Ettringite + 12H^+ \Leftrightarrow 2Al^{3+} + 3SO_4^{2-} + 6Ca^{2+} + 38H_2O$	60.8127
$Anothite + 8H^+ \Leftrightarrow Ca^{2+} + 2Al^{3+} + 2SiO_2(aq) + 4H_2O$	24.8686

Table A2-6. Chemical reaction and equilibrium constants for surface complexation at 25ºC of (Wolery, 1992) or bentonite, the additional reaction of bentonite with corrosion products and with concrete interactions.

Surface complexation reactions	**Log K**
$\equiv S^SOH^{2+} \Leftrightarrow \equiv S^SOH + H^+$	-4.5
$\equiv S^SO^- + H^+ \Leftrightarrow S^SOH$	7.9
$\equiv S^{W1}OH^{2+} \Leftrightarrow \equiv S^{W1}OH + H^+$	-4.5
$\equiv S^{W1}O^- + H^+ \Leftrightarrow \equiv S^{W1}OH$	7.9
$\equiv S^{W2}OH^{2+} \Leftrightarrow \equiv S^{W2}OH + H^+$	-6.0
$\equiv S^{W2}O^- + H^+ \Leftrightarrow \equiv S^{W2}OH$	-10.5
Corrosion-bentonite cells (SC and FB3 cells)	
$\equiv S^SOFe^{2+} + H^+ \Leftrightarrow \equiv S^SOH + Fe^{2+}$	0.6
$\equiv S^SOFeOH + 2H^+ \Leftrightarrow \equiv S^SOH + Fe^{2+} + H_2O$	10.0
$\equiv S^SOFe(OH)_2^- + 3H^+ \Leftrightarrow \equiv S^SOH + Fe^{2+} + 2H_2O$	20.0
$\equiv S^{W1}OFe^{2+} + H^+ \Leftrightarrow \equiv S^{W1}OH + Fe^{2+}$	3.3

Table A2-7. Chemical reaction and equilibrium constants for cation exchange at 25ºC of (Wolery, 1992) or bentonite, the additional reaction of bentonite with corrosion products and with concrete intaractions.

Cation exchange	$K_{Na\text{-}cation}$
$Na^+ + X\text{-}K \Leftrightarrow K^+ + X\text{-}Na$	0.1456
$Na^+ + 0.5\ X_2\text{-}Ca \Leftrightarrow 0.5\ Ca^{2+} + X\text{-}Na$	0.3265
$Na^+ + 0.5\ X_2\text{-}Mg \Leftrightarrow 0.5\ Mg^{2+} + X\text{-}Na$	0.3766
Corrosion-bentonite cells (SC and FB3 cells)	
$Na^+ + 0.5\ X_2\text{-}Fe \Leftrightarrow 0.5\ Fe^{2+} + X\text{-}Na$	0.5

Appendix B. Plots of model results for the corrosion tests

B.1. THC(m) model results of the corrosion tests performed on small cells

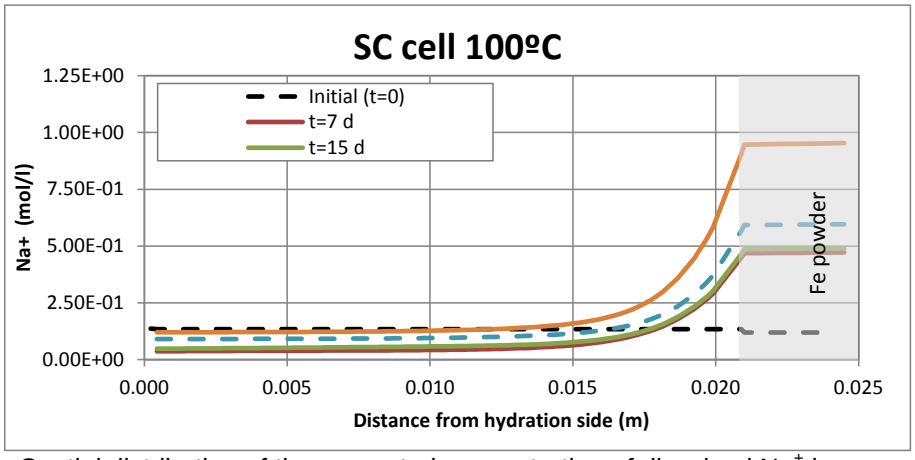

Figure B1-1. Spatial distribution of the computed concentration of dissolved Na^+ in corrosion tests on small cells at 100ºC at several times.

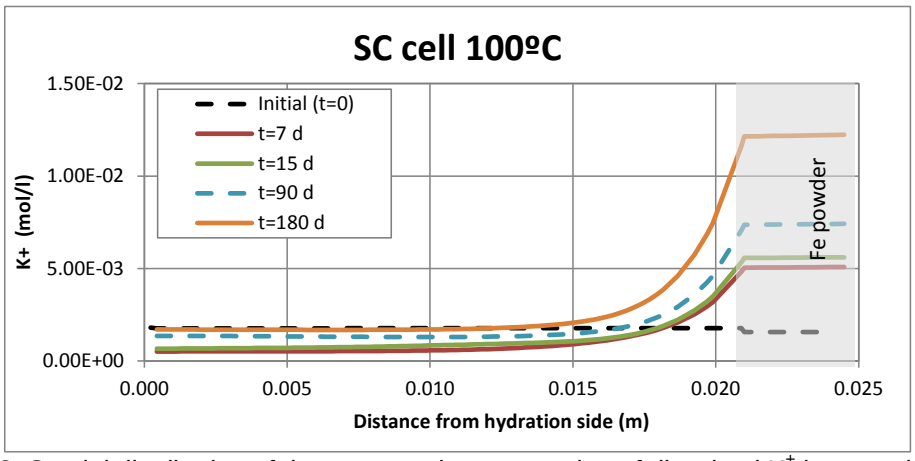

Figure B1-2. Spatial distribution of the computed concentration of dissolved K^+ in corrosion tests on small cells at 100ºC at several times.

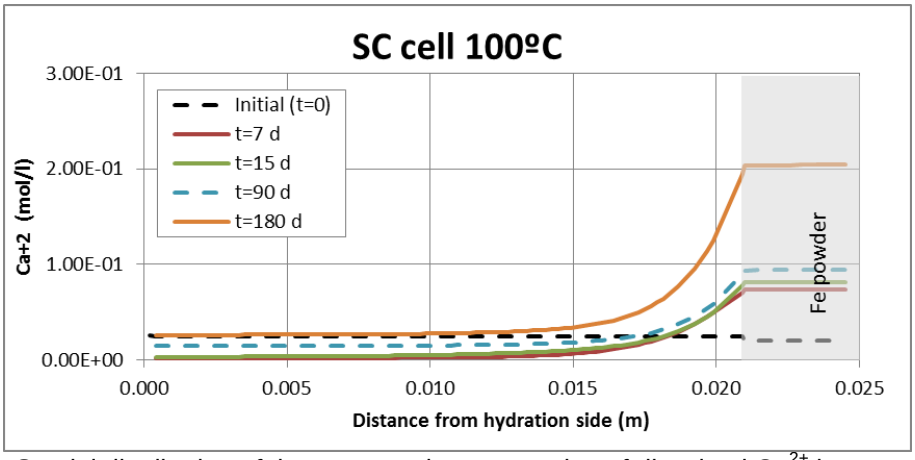

Figure B1-3. Spatial distribution of the computed concentration of dissolved Ca^{2+} in corrosion tests on small cells at 100ºC at several times.

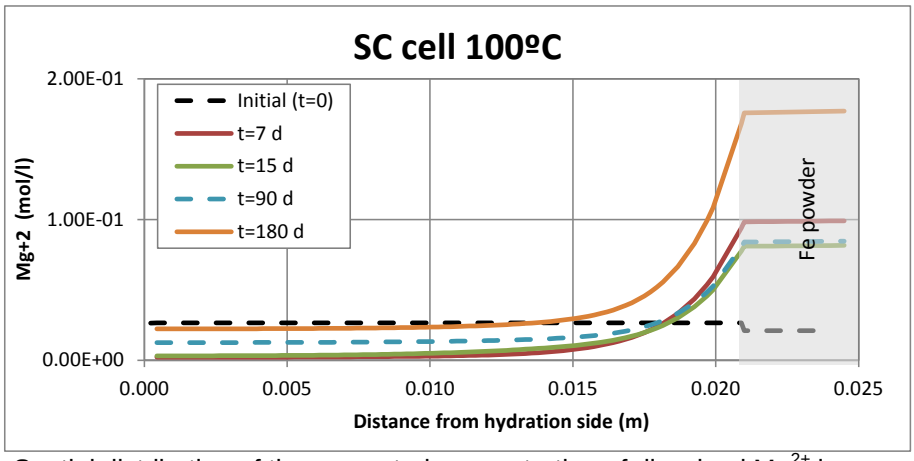

Figure B1-4. Spatial distribution of the computed concentration of dissolved Mg^{2+} in corrosion tests on small cells at 100ºC at several times.

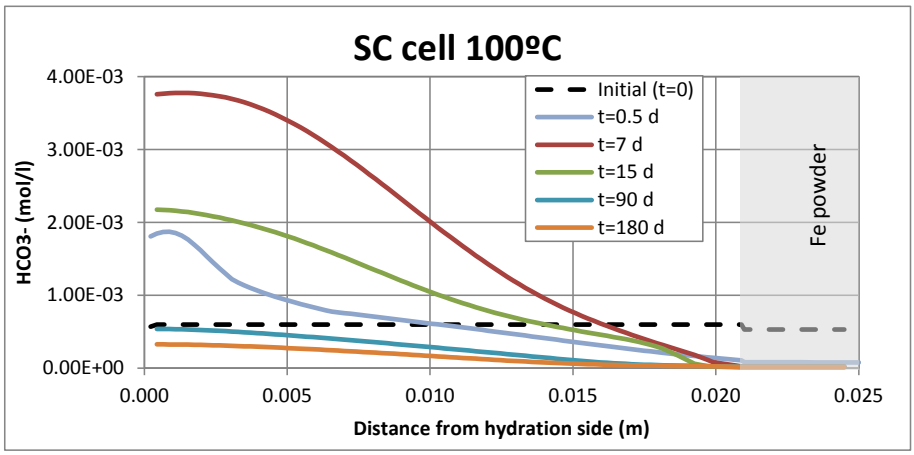

Figure B1-5. Spatial distribution of the computed concentration of dissolved HCO_3^- in corrosion tests on small cells at 100ºC at several times.

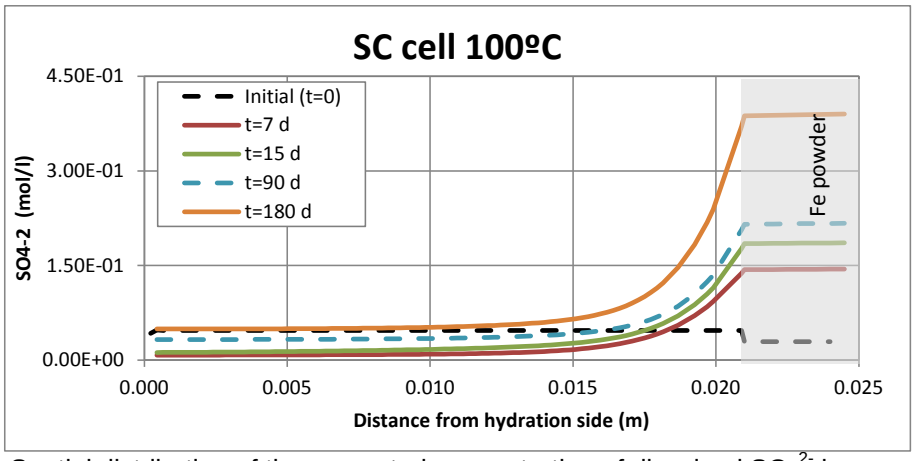

Figure B1-6. Spatial distribution of the computed concentration of dissolved SO_4^{2-} in corrosion tests on small cells at 100ºC at several times.

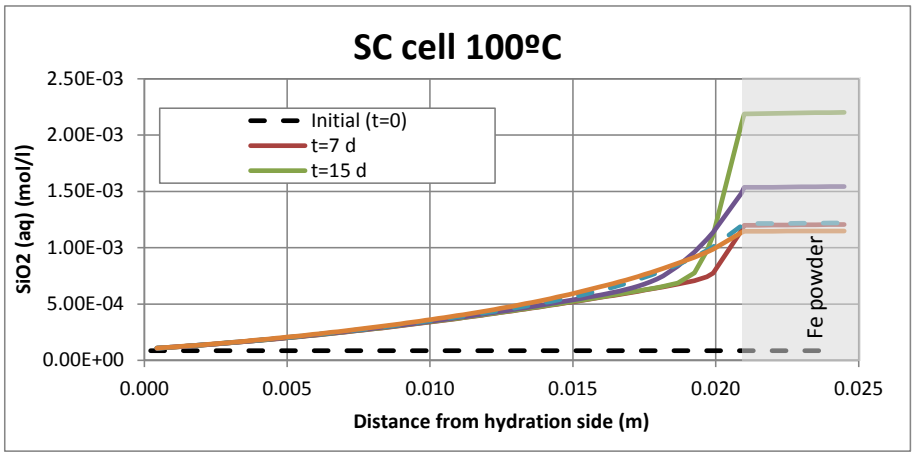

Figure B1-7. Spatial distribution of the computed concentration of dissolved SiO_2(aq) in corrosion tests on small cells at 100ºC at several times.

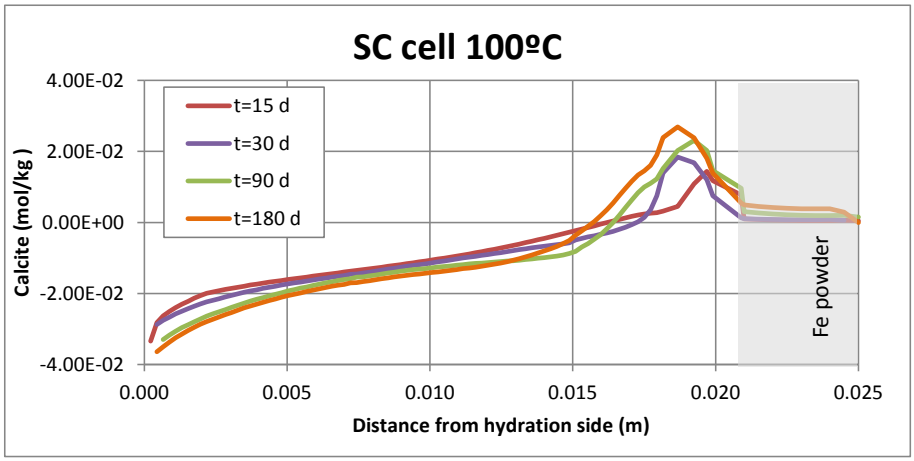

Figure B1-8. Spatial distribution the computed cumulative precipitation/dissolution of calcite in corrosion tests on small cells at 100ºC at several times.

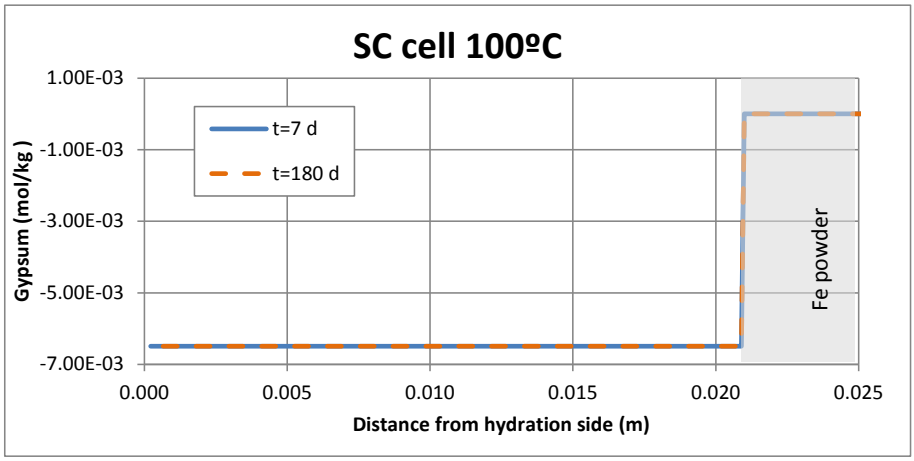

Figure B1-9. Spatial distribution the computed cumulative precipitation/dissolution of gypsum in corrosion tests on small cells at 100ºC at several times.

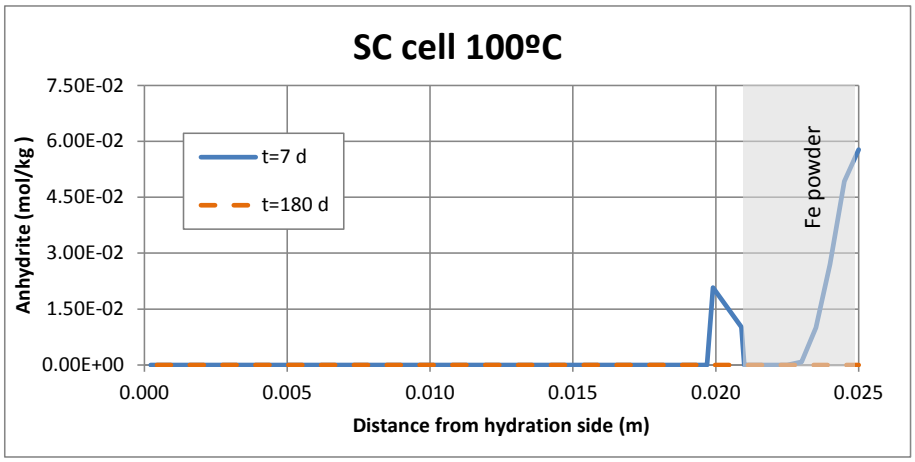

Figure B1-10. Spatial distribution the computed cumulative precipitation/dissolution of anhydrite in corrosion tests on small cells at 100ºC at several times.

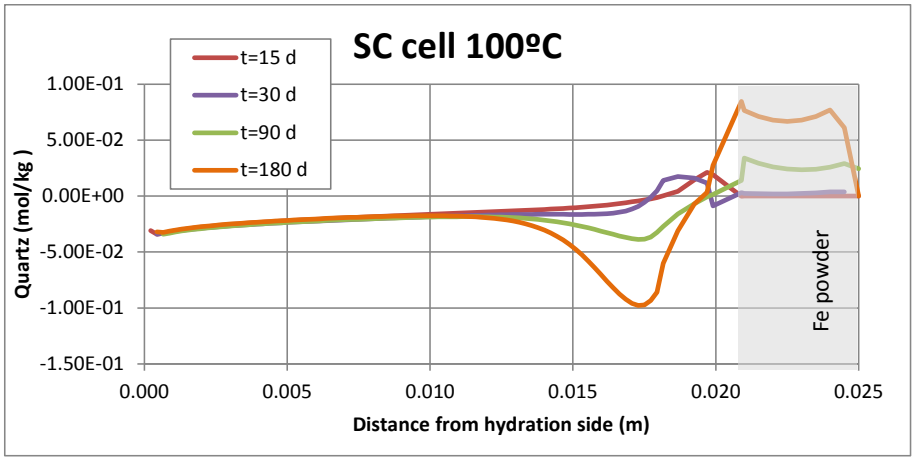

Figure B1-11. Spatial distribution the computed cumulative precipitation/dissolution of quartz in corrosion tests on small cells at 100ºC at several times.

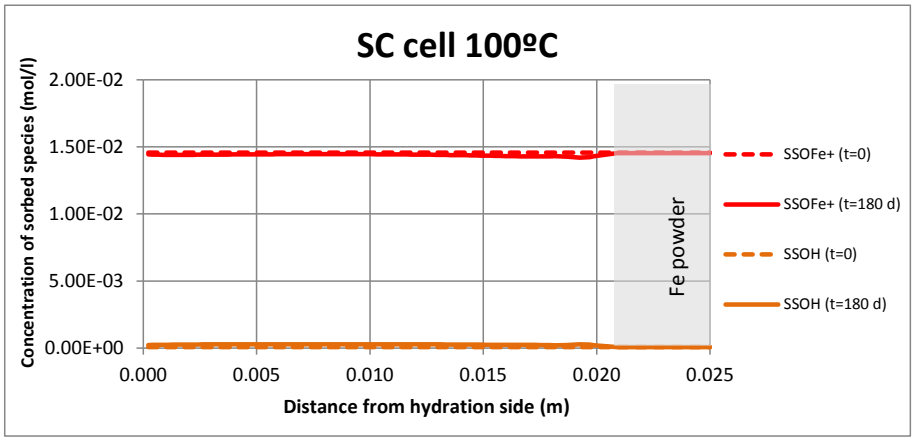

Figure B1-12. Spatial distribution of computed concentrations of sorbed species in strong sorption site at the end of the test.

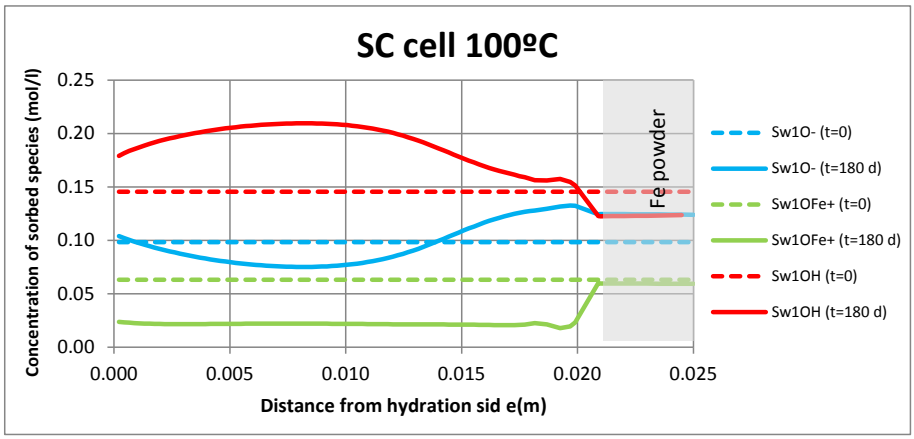

Figure B1-13. Spatial distribution of computed concentrations of sorbed species in weak 1 sorption site at the end of the test.

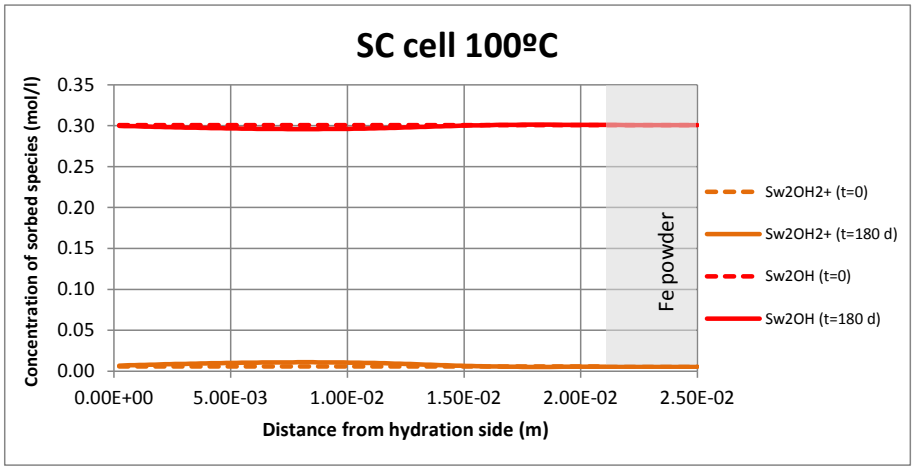

Figure B1-14. Spatial distribution of computed concentrations of sorbed species in weak 2 sorption site at the end of the test.

B.2. THC(m) model results of the corrosion tests performed on medium cells

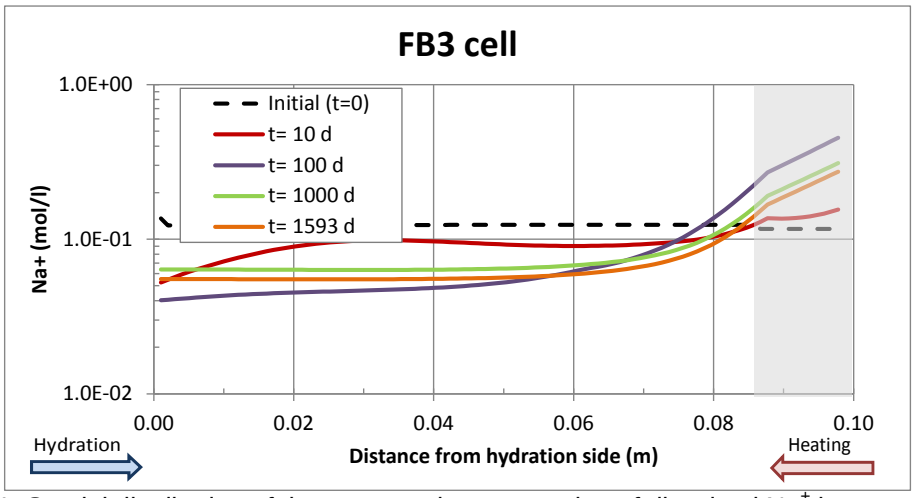

Figure B2-1. Spatial distribution of the computed concentration of dissolved Na^+ in corrosion test on the FB3 cell at several times.

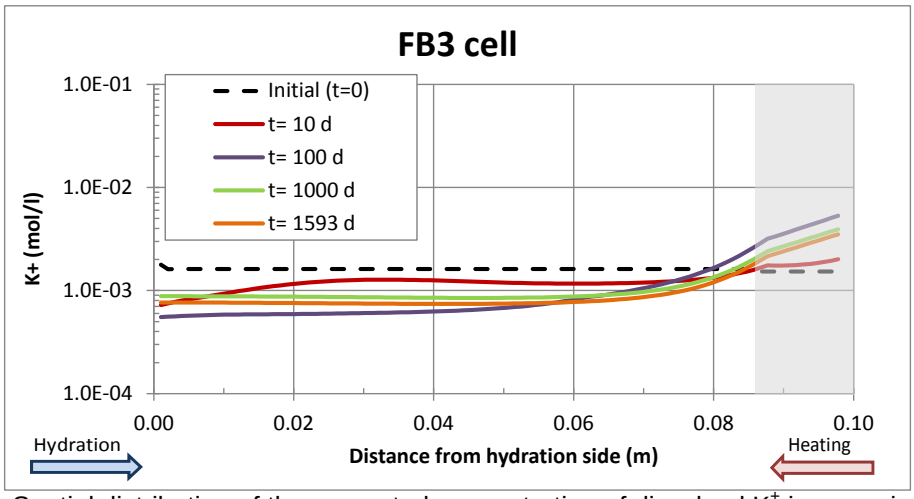

Figure B2-2. Spatial distribution of the computed concentration of dissolved K^+ in corrosion test on the FB3 cell at several times.

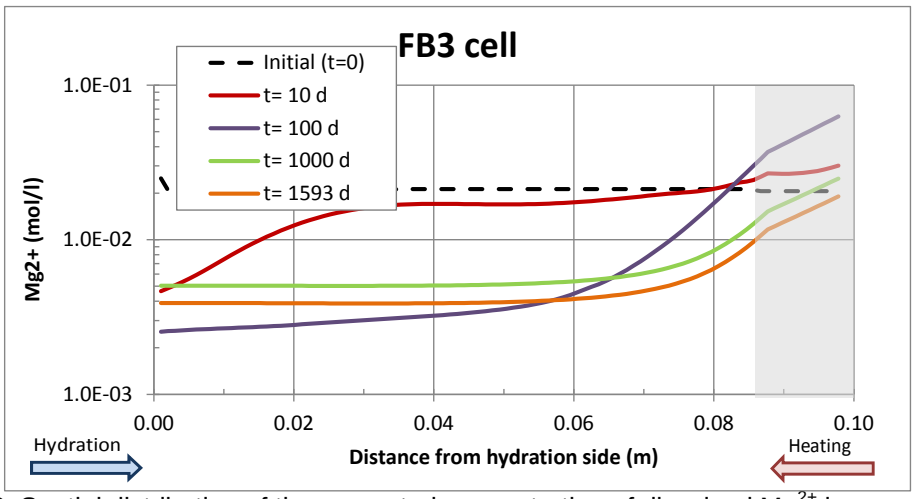

Figure B2-3. Spatial distribution of the computed concentration of dissolved Mg^{2+} in corrosion test on the FB3 cell at several times.

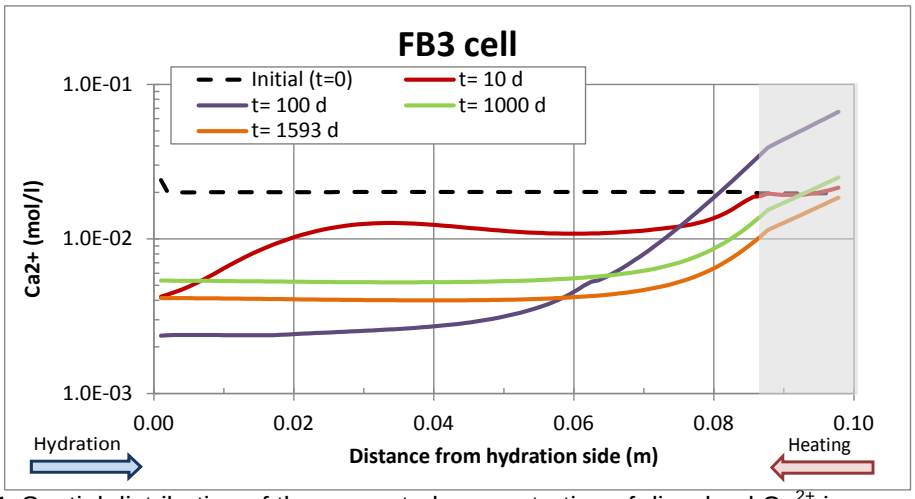

Figure B2-4. Spatial distribution of the computed concentration of dissolved Ca^{2+} in corrosion test on the FB3 cell at several times.

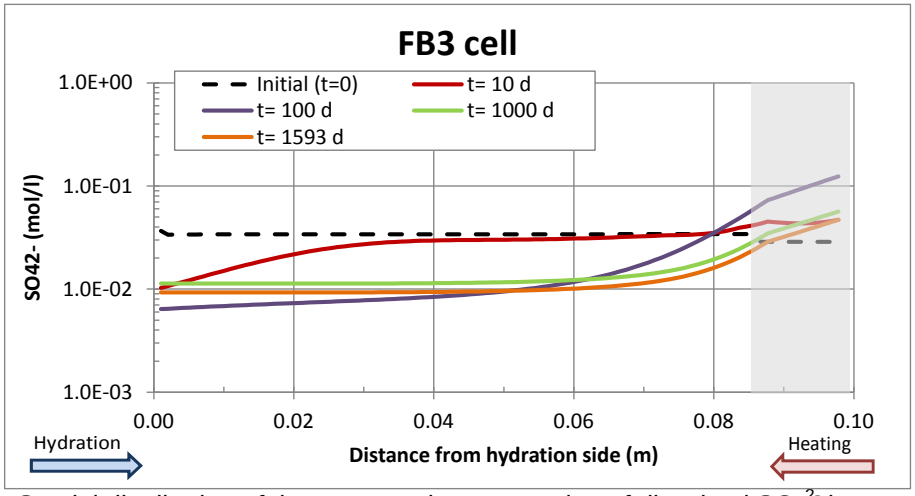

Figure B2-5. Spatial distribution of the computed concentration of dissolved SO_4^{2-} in corrosion test on the FB3 cell at several times.

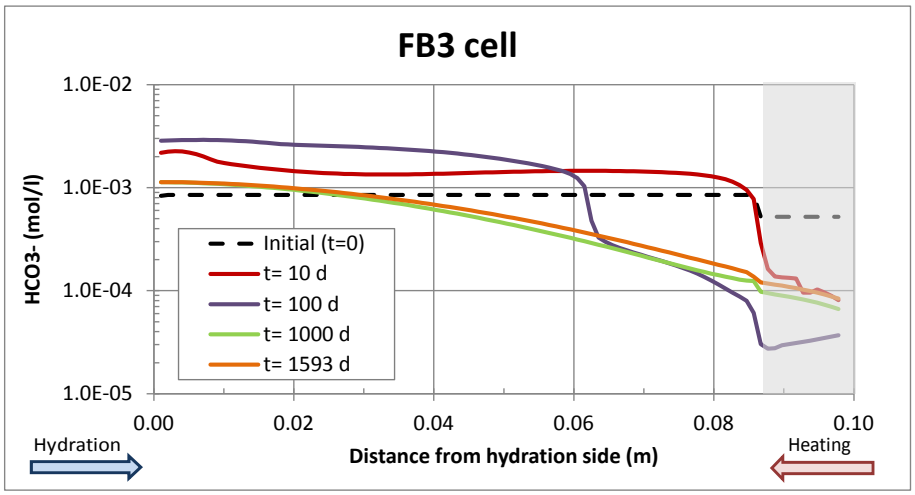

Figure B2-6. Spatial distribution of the computed concentration of dissolved HCO_3^- in corrosion test on the FB3 cell at several times.

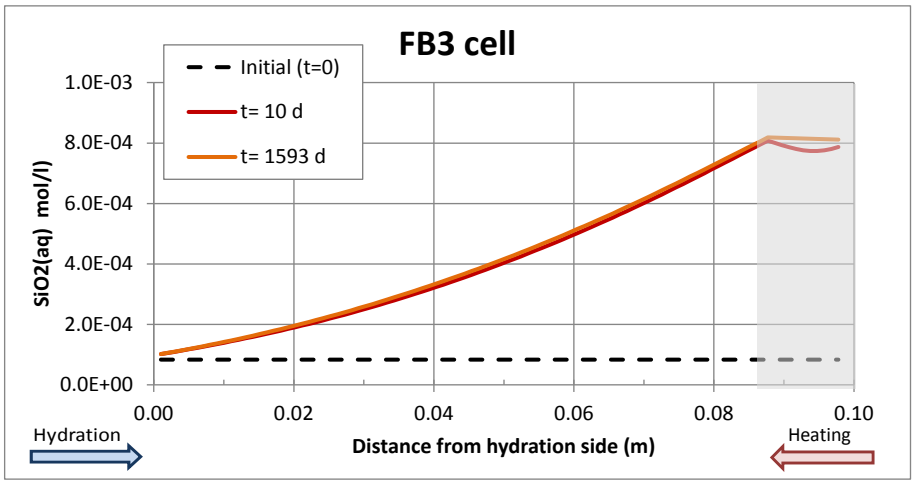

Figure B2-7. Spatial distribution of the computed concentration of dissolved $SiO_2(aq)$ in corrosion test on the FB3 cell at several times.

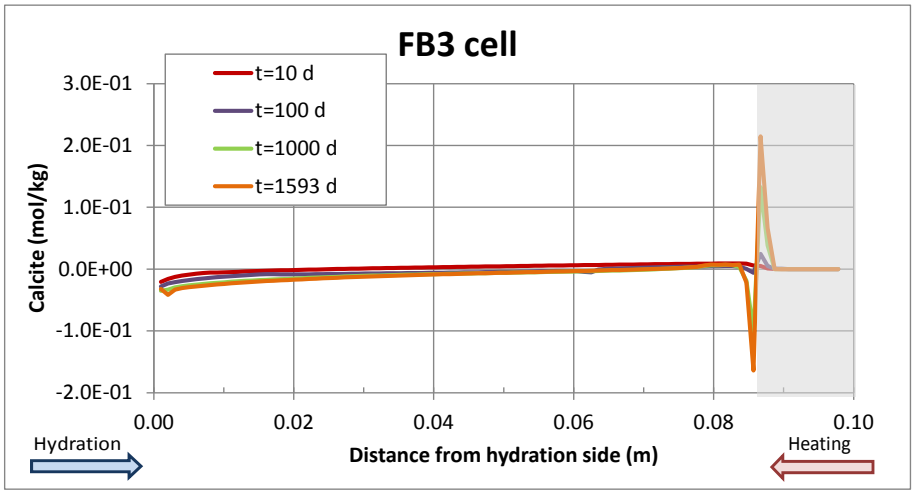

Figure B2-8. Spatial distribution of the computed cumulative precipitation/dissolution of calcite in corrosion test on the FB3 cell at several times.

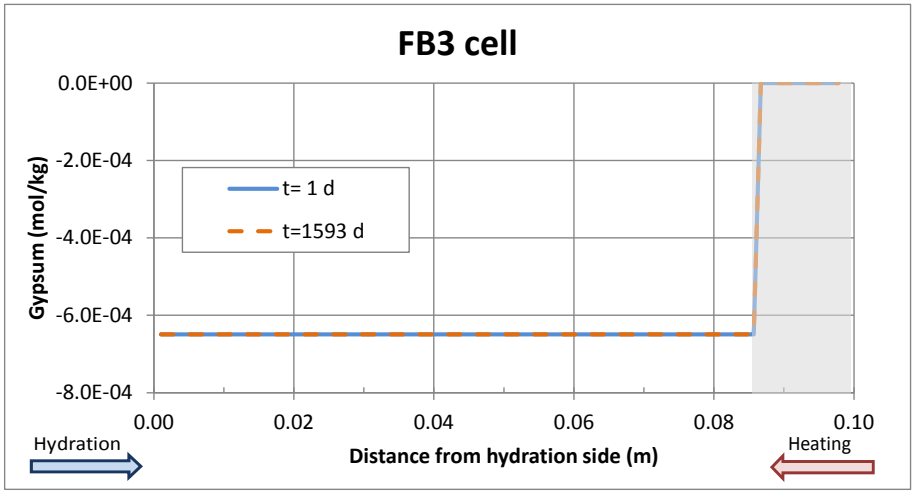

Figure B2-9. Spatial distribution of the computed cumulative precipitation/dissolution of gypsum in corrosion test on the FB3 cell at several times.

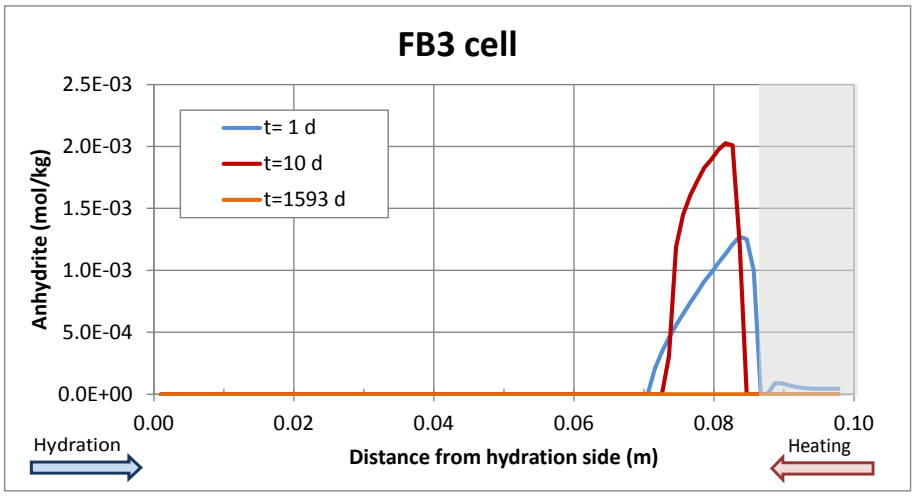

Figure B2-10. Spatial distribution of the computed cumulative precipitation/dissolution of anhydrite in corrosion test on the FB3 cell at several times.

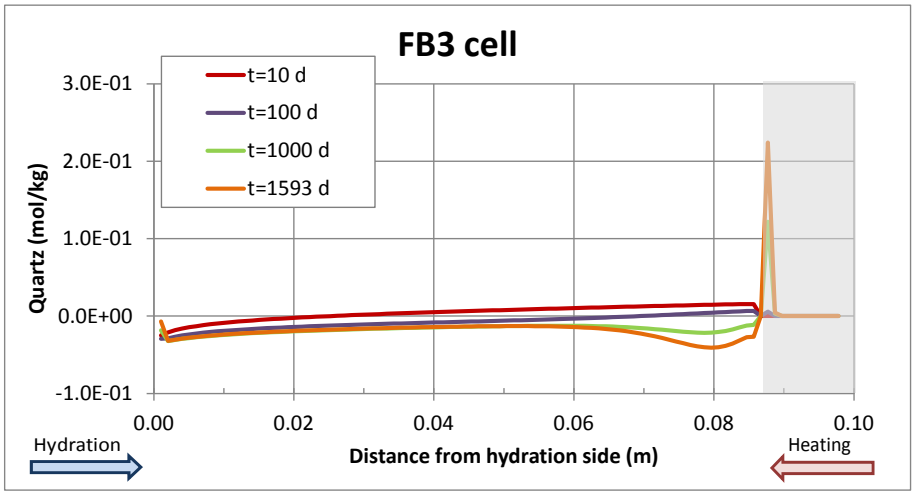

Figure B2-11. Spatial distribution of the computed cumulative precipitation/dissolution of quartz in corrosion test on the FB3 cell at several times.

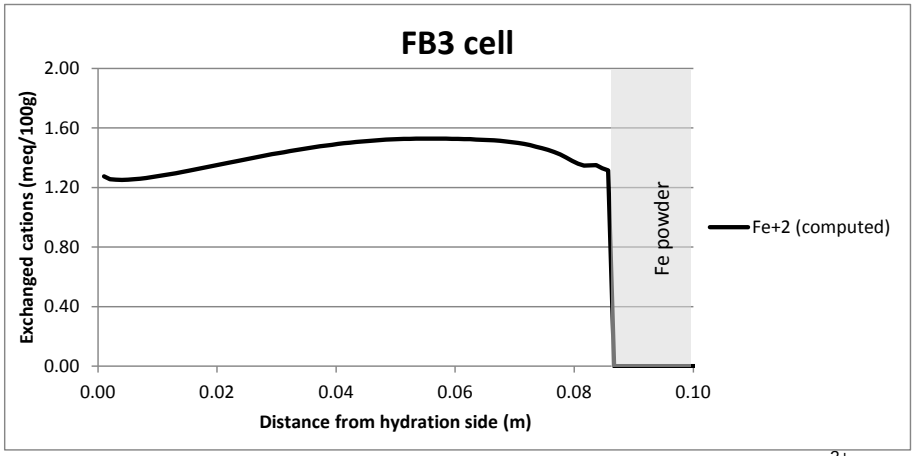

Figure B2-12. Spatial distribution of the computed concentration of exchanged Fe^{2+} in corrosion test on the FB3 cell at the end of the test.

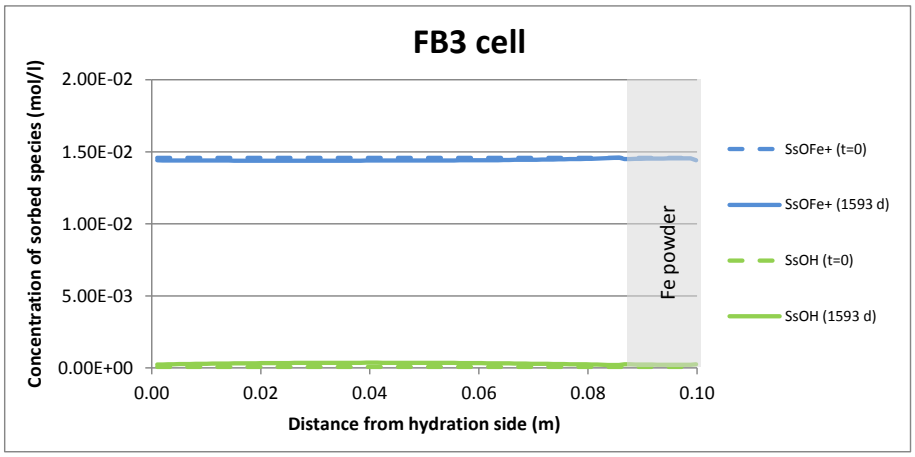

Figure B2-13. Spatial distribution of the computed concentration of sorbed species in strong sorption site in corrosion test on the FB3 cell at the end of the test.

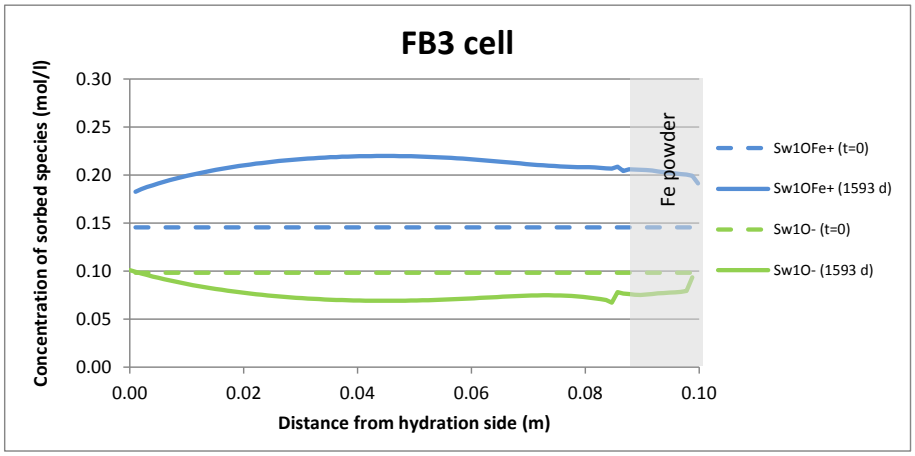

Figure B2-14. Spatial distribution of the computed concentration of sorbed species in weak 1 sorption site in corrosion test on the FB3 cell at the end of the test.

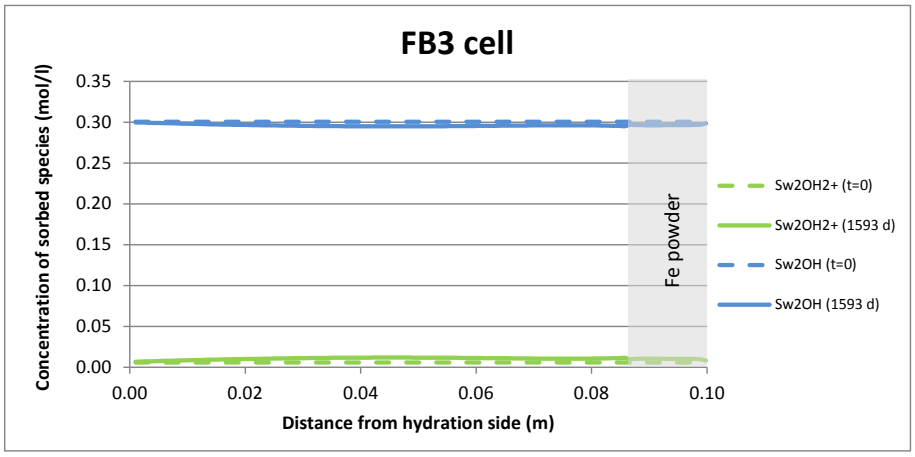

Figure B2-15. Spatial distribution of the computed concentration of sorbed species in strong sorption site in corrosion test on the FB3 cell at the end of the test.

Appendix C. THC(m) model results of the HB4 concrete-bentonite interface test

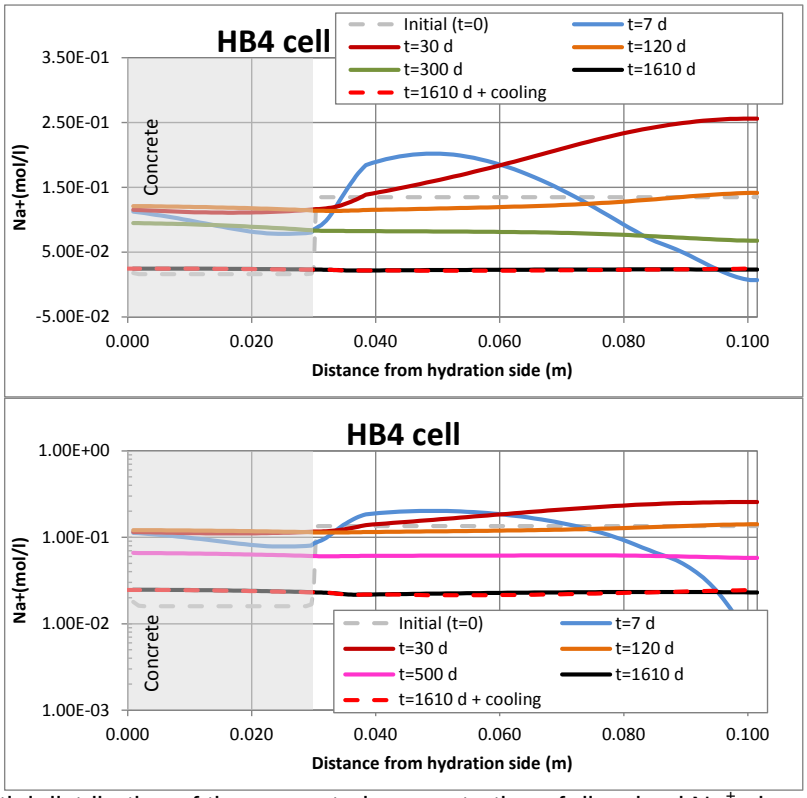

Figure C-1.Spatial distribution of the computed concentration of dissolved Na^+ along the HB4 cell at several times. Natural scale (top) and logarithmic scale (bottom).

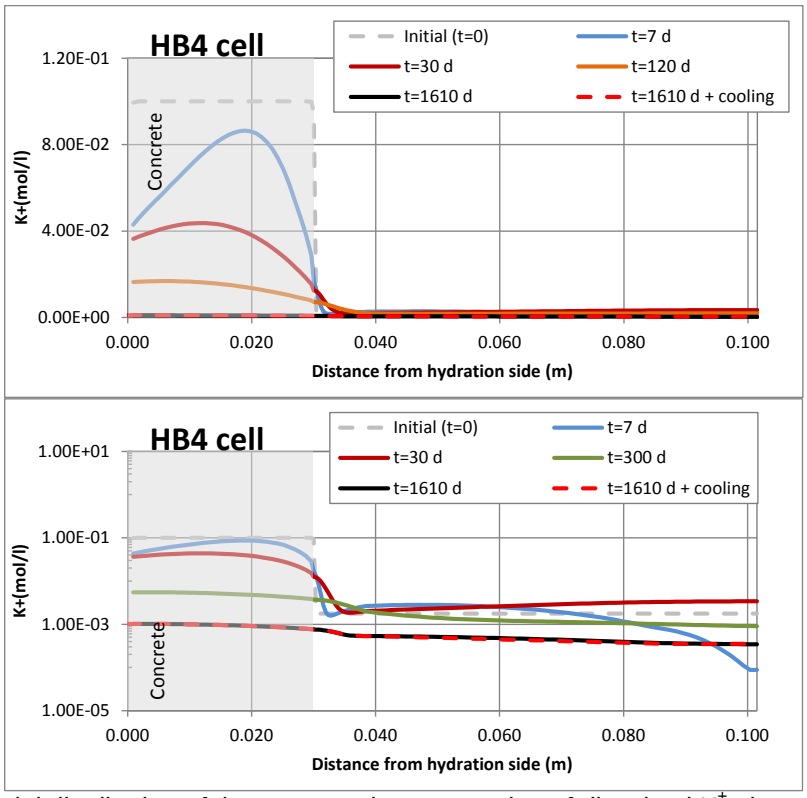

Figure C-2.Spatial distribution of the computed concentration of dissolved K^+ along the HB4 cell at several times. Natural scale (top) and logarithmic scale (bottom).

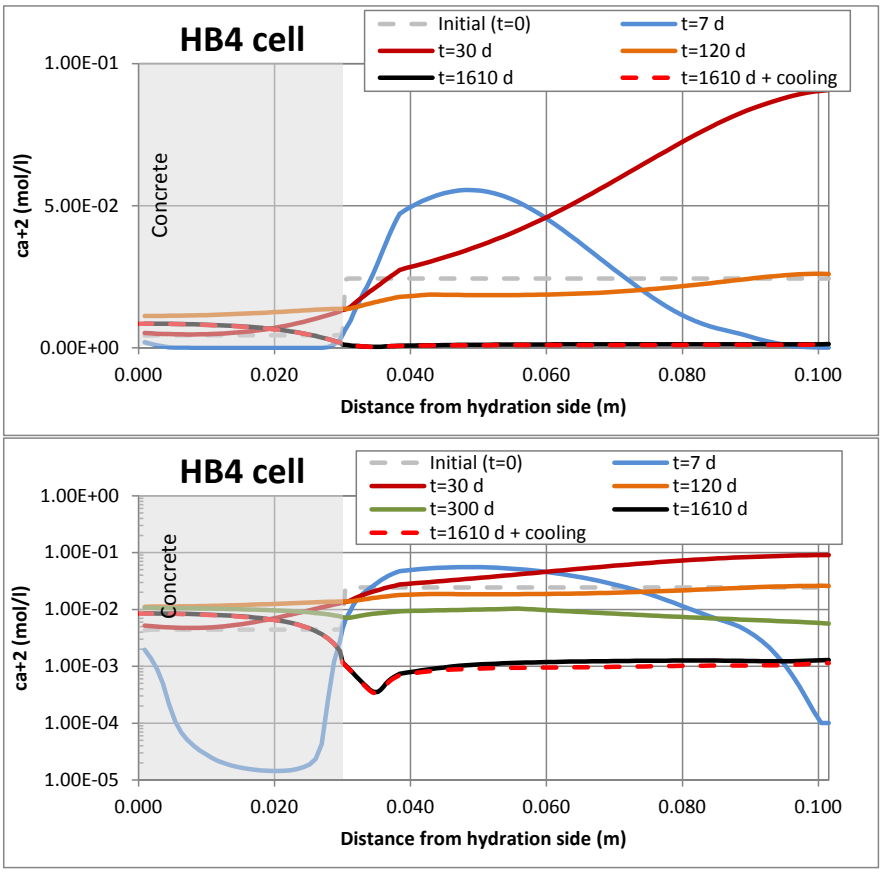

Figure C-3.Spatial distribution of the computed concentration of dissolved Ca2+ along the HB4 cell at several times. Natural scale (top) and logarithmic scale (bottom).

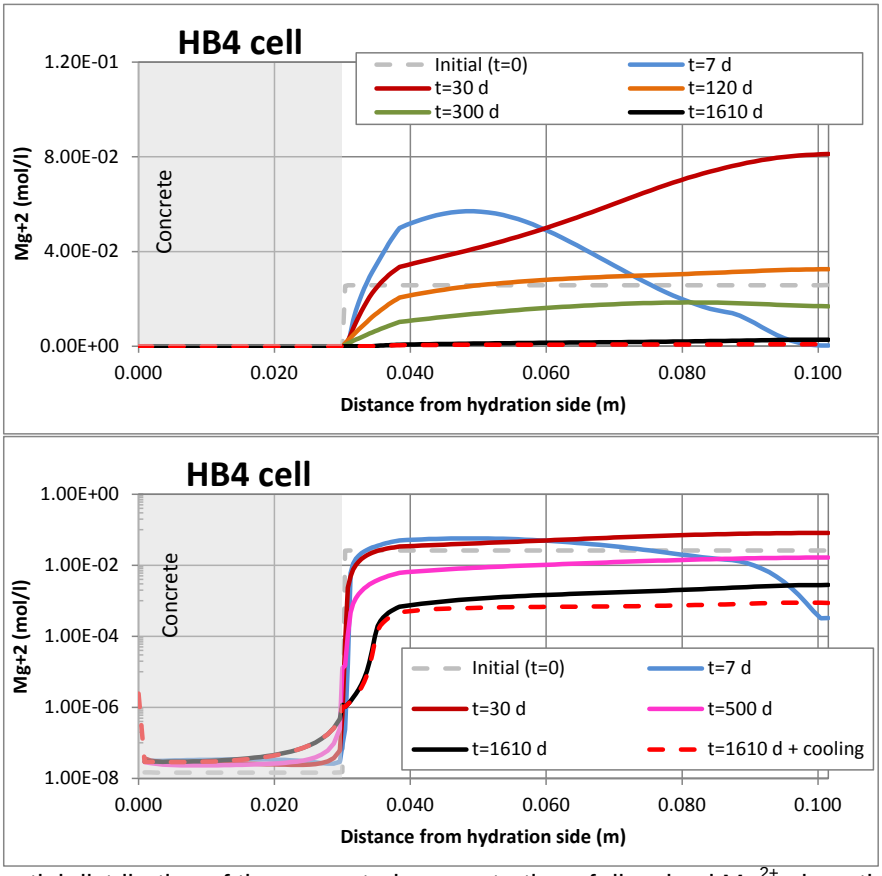

Figure C-4.Spatial distribution of the computed concentration of dissolved Mg^{2+} along the HB4 cell at several times. Natural scale (top) and logarithmic scale (bottom).

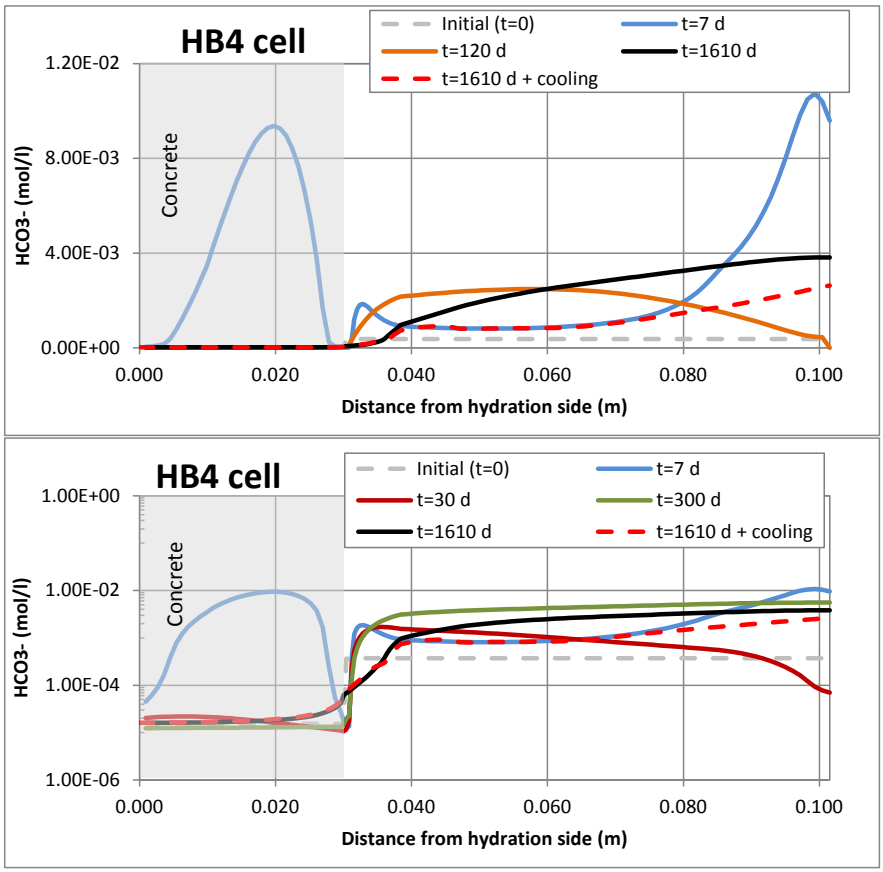

Figure C-5. Spatial distribution of the computed concentration of dissolved HCO_3^- along the HB4 cell at several times. Natural scale (top) and logarithmic scale (bottom).

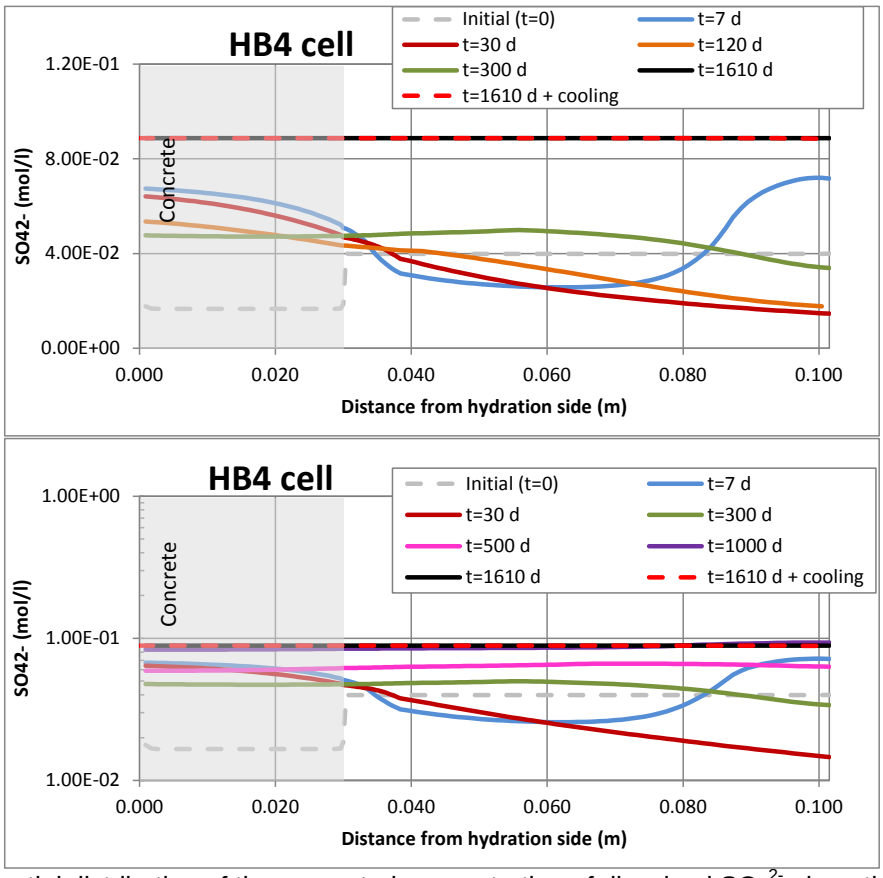

Figure C-6.Spatial distribution of the computed concentration of dissolved SO_4^{2-} along the HB4 cell at several times. Natural scale (top) and logarithmic scale (bottom).

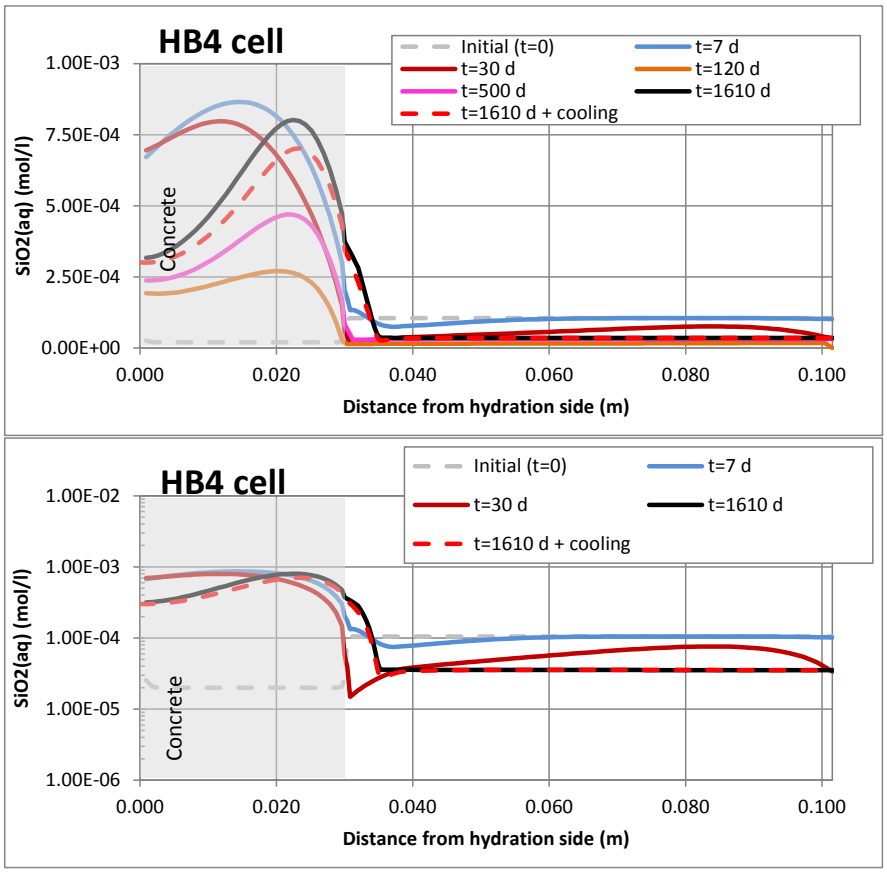

Figure C-7.Spatial distribution of the computed concentration of dissolved SiO_2(aq) along the HB4 cell at at several times. Natural scale (top) and logarithmic scale (bottom).

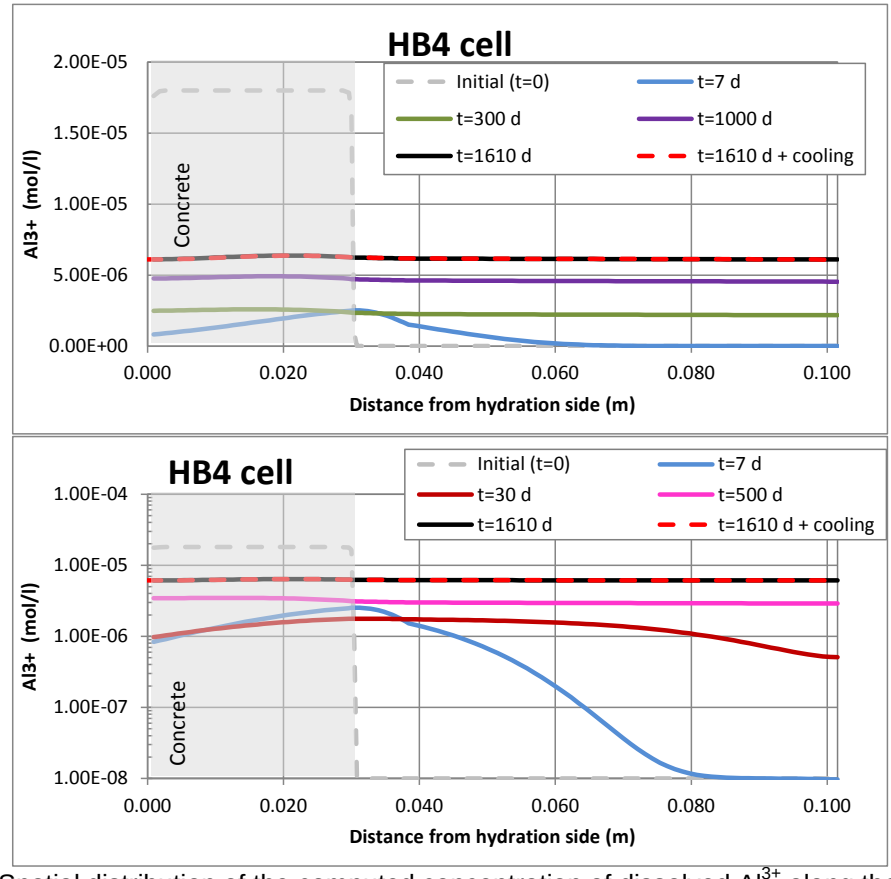

Figure C-8.Spatial distribution of the computed concentration of dissolved Al^{3+} along the HB4 cell at several times. Natural scale (top) and logarithmic scale (bottom).

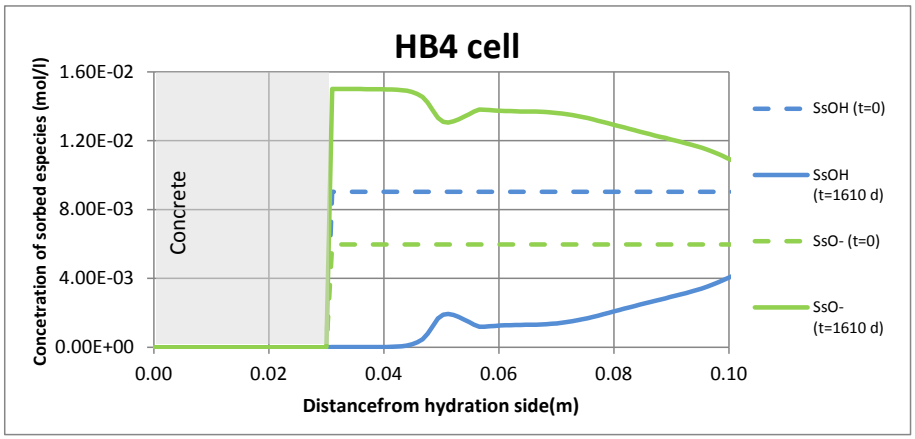

Figure C-9. Spatial distribution of the computed concentration of sorbed species in strong sorption site along the HB4 cell at the end of the test.

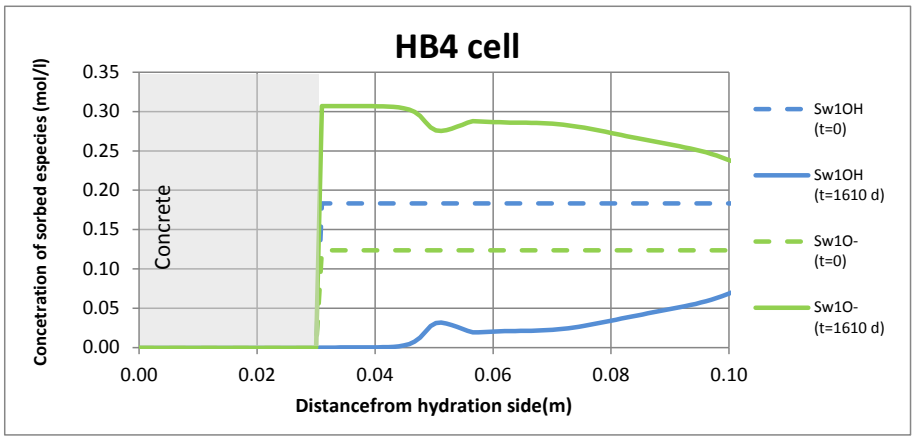

Figure C-10. Spatial distribution of computed concentrations of sorbed species in weak 1 sorption site along the HB4 cell at the end of the test.

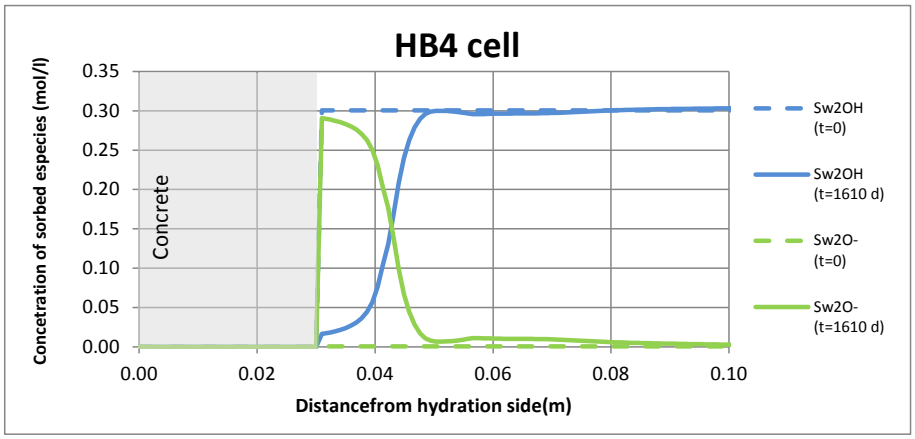

Figure C-11. Spatial distribution of computed concentrations of sorbed species in weak 2 sorption site along the HB4 cell at the end of the test.

Appendix D. THC(m) model results of the double interface mortar-bentonite-magnetite tests

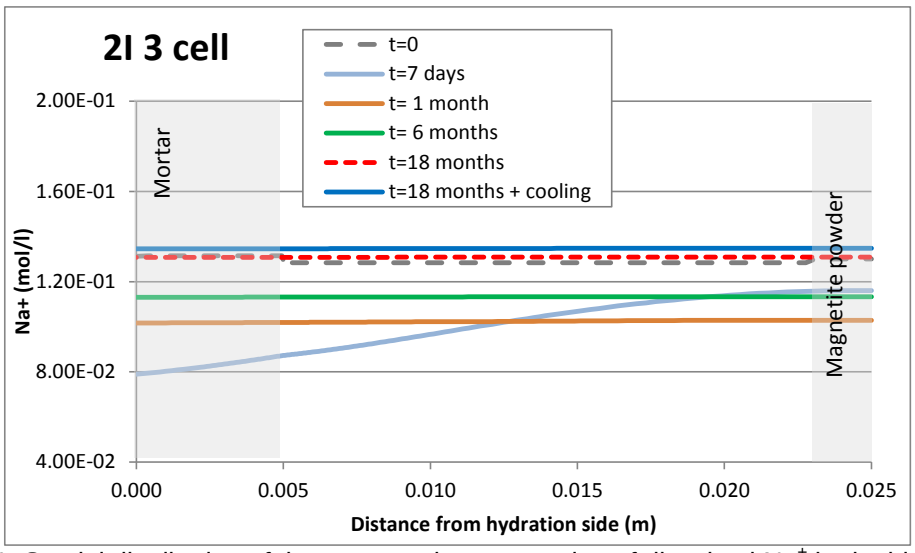

Figure D-1. Spatial distribution of the computed concentration of dissolved Na^+ in double interface tests on 2I 3 cell at several times.

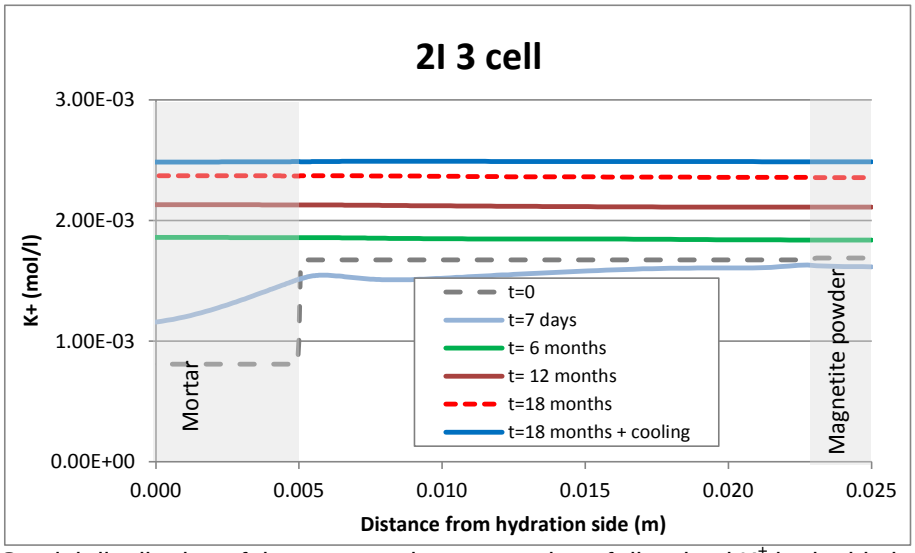

Figure D-2. Spatial distribution of the computed concentration of dissolved K^+ in double interface tests on 2I 3 cell at several times.

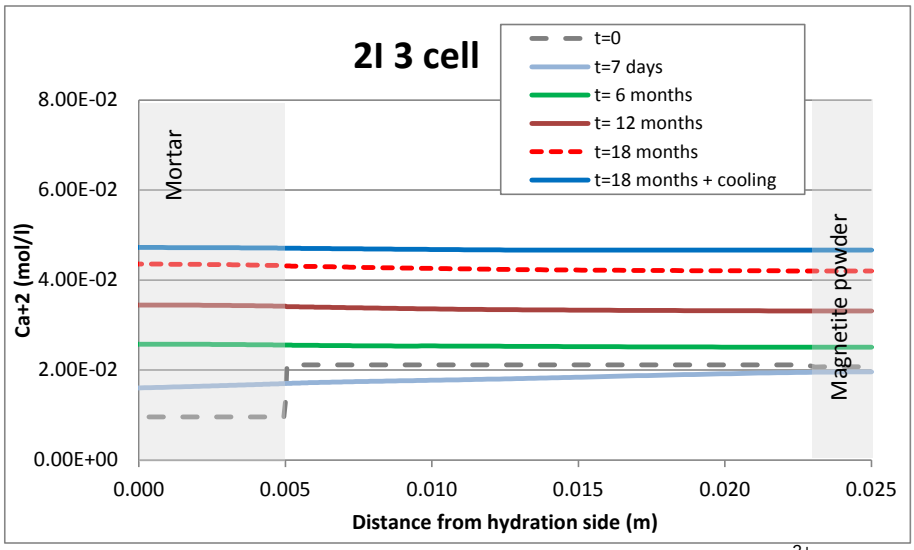

Figure D-3. Spatial distribution of the computed concentration of dissolved Ca^{2+} in double interface tests on 2I 3 cell at several times.

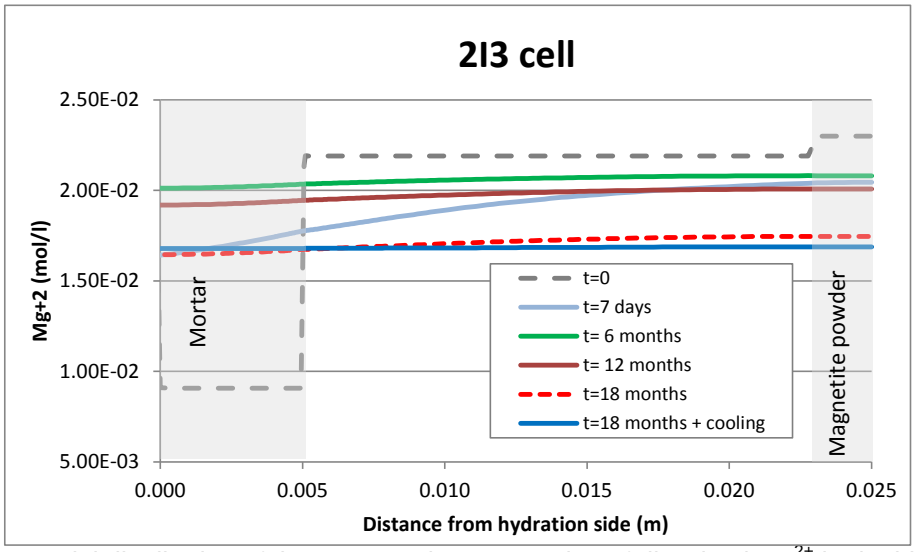

Figure D-4. Spatial distribution of the computed concentration of dissolved Mg^{2+} in double interface tests on 2I 3 cell at several times.

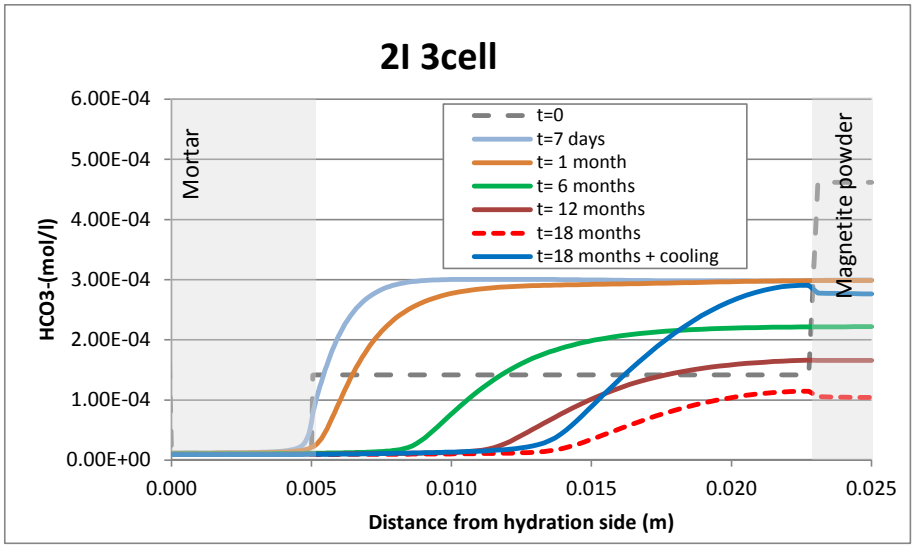

Figure D-5. Spatial distribution of the computed concentration of dissolved HCO_3^- in double interface tests on 2I 3 cell at several times.

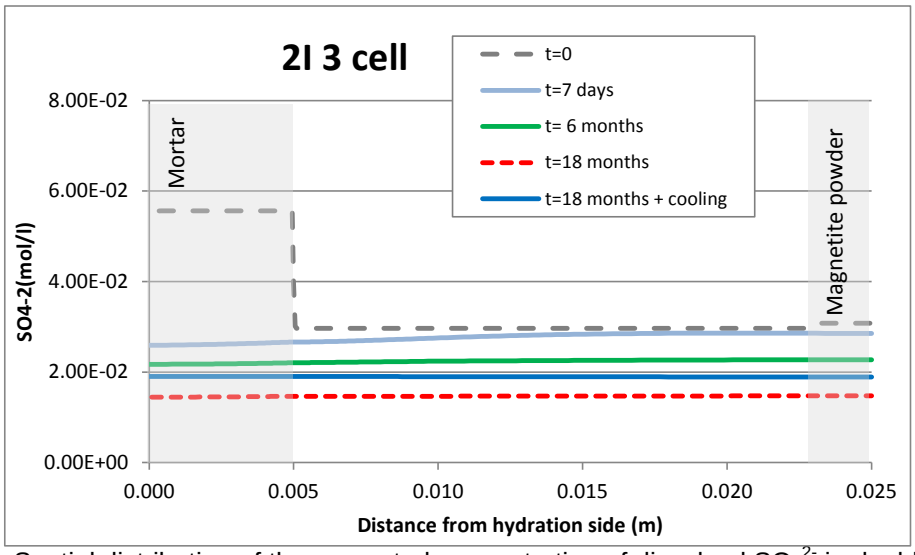

Figure D-6. Spatial distribution of the computed concentration of dissolved SO_4^{2-} in double interface tests on 2I 3 cell at several times.

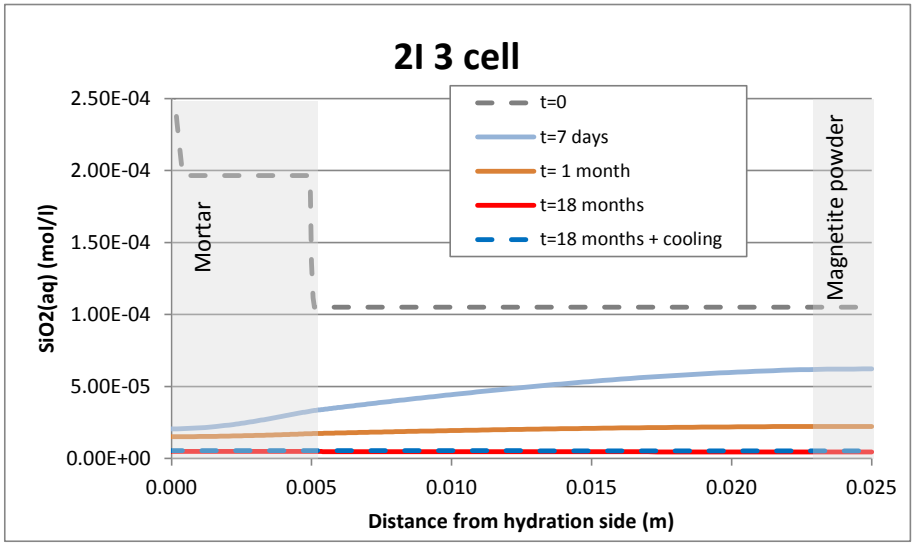

Figure D-7. Spatial distribution of the computed concentration of dissolved $SiO_2(aq)$ in double interface tests on 2I 3 cell at several times.

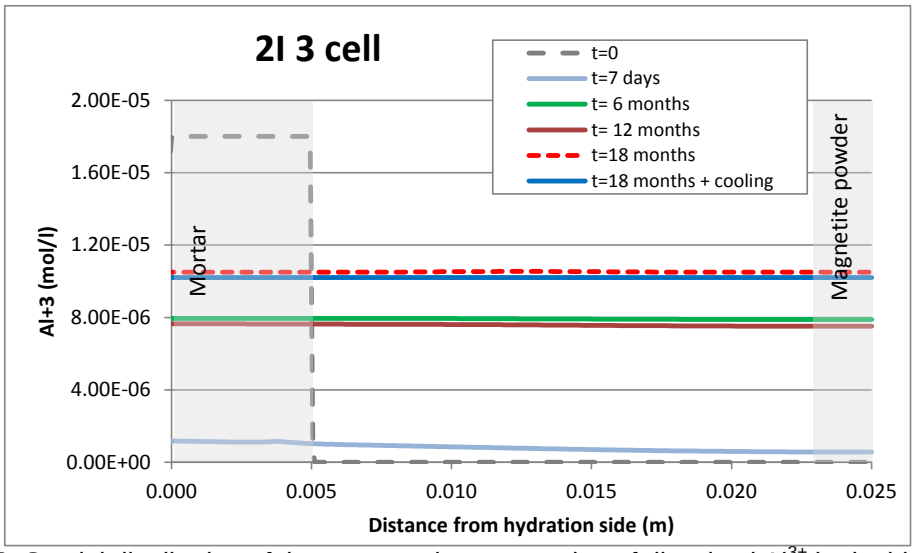

Figure D-8. Spatial distribution of the computed concentration of dissolved Al^{3+} in double interface tests on 2I 3 cell at several times.

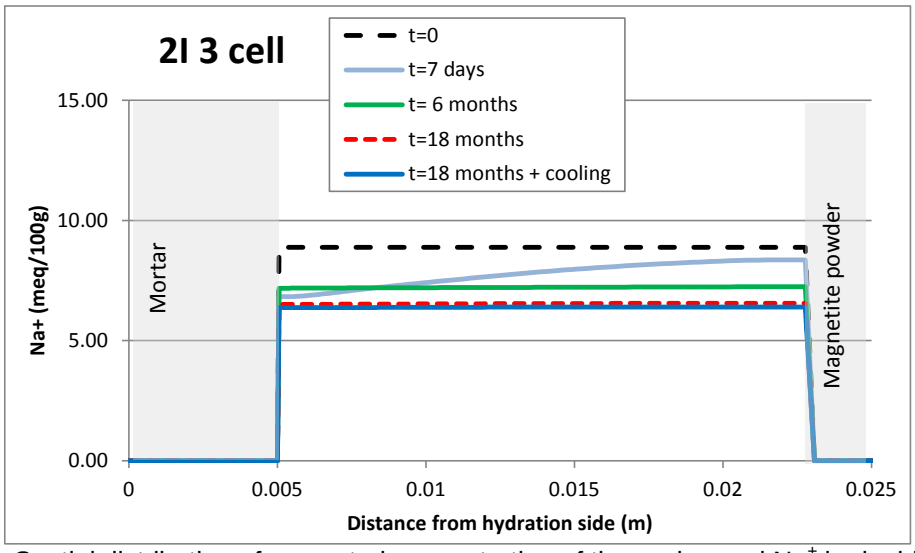

Figure D-9. Spatial distribution of computed concentration of the exchanged Na^+ in double interface tests on 2I 3 cell at several times.

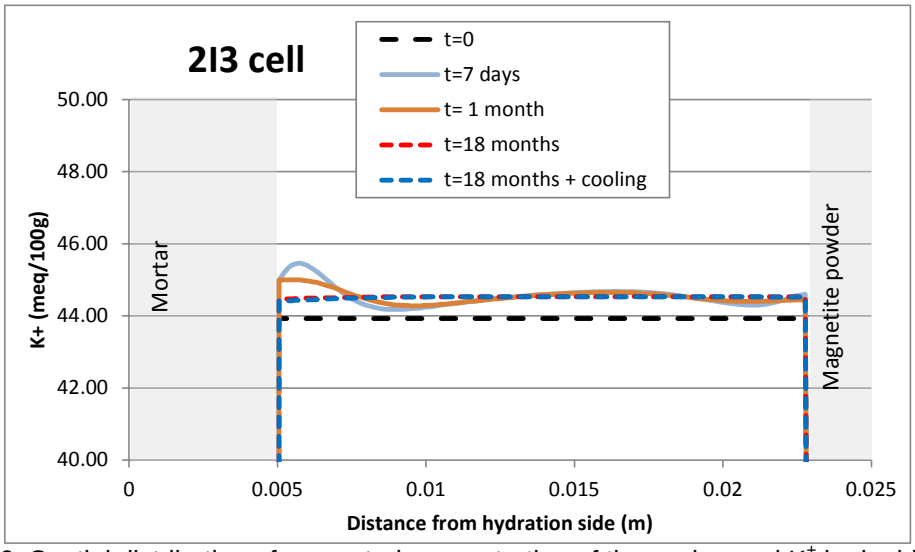

Figure D-10. Spatial distribution of computed concentration of the exchanged K^+ in double interface tests on 2I 3 cell at several times.

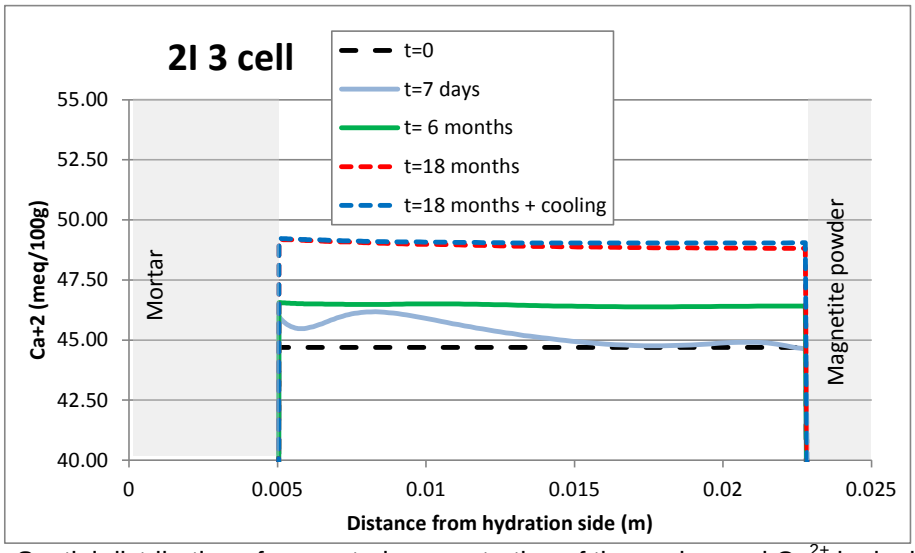

Figure D-11. Spatial distribution of computed concentration of the exchanged Ca^{2+} in double interface tests on 2I 3 cell at several times.

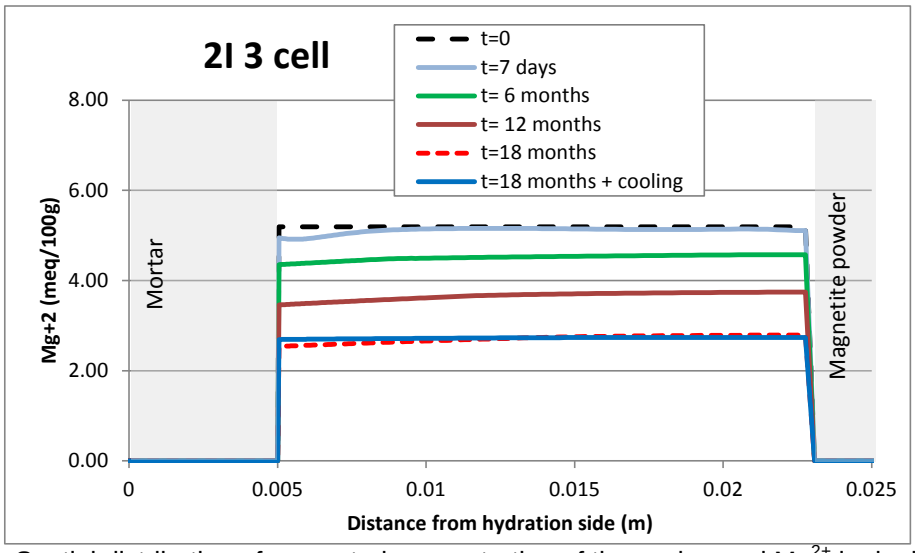

Figure D-12. Spatial distribution of computed concentration of the exchanged Mg^{2+} in double interface tests on 2I 3 cell at several times.

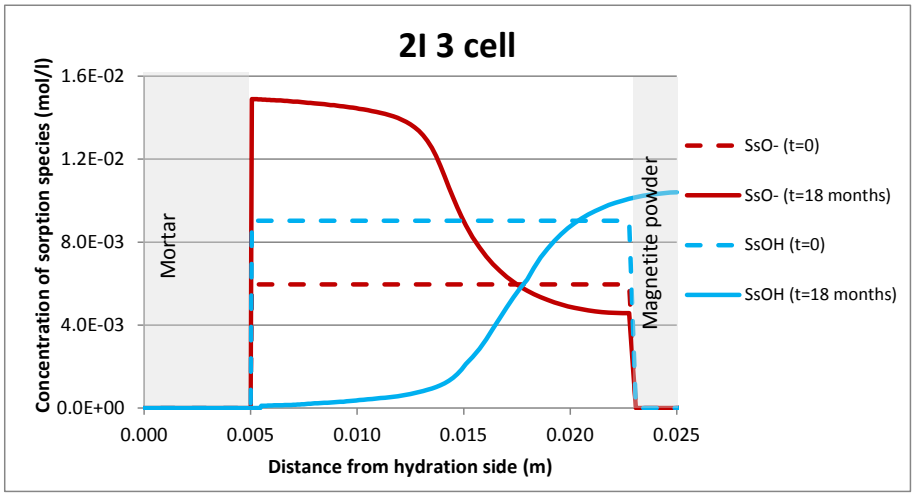

Figure D-13. Spatial distribution of computed concentrations of sorbed species in strong sorption site in double interface tests on 2I 3 cell at the end of the test.

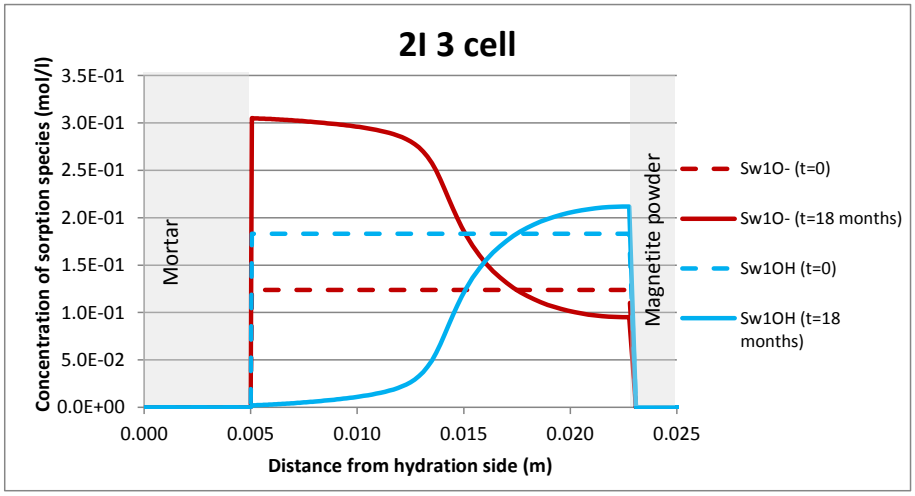

Figure D-14. Spatial distribution of computed concentrations of sorbed species in weak 1 sorption site in double interface tests on 2I 3 cell at the end of the test.

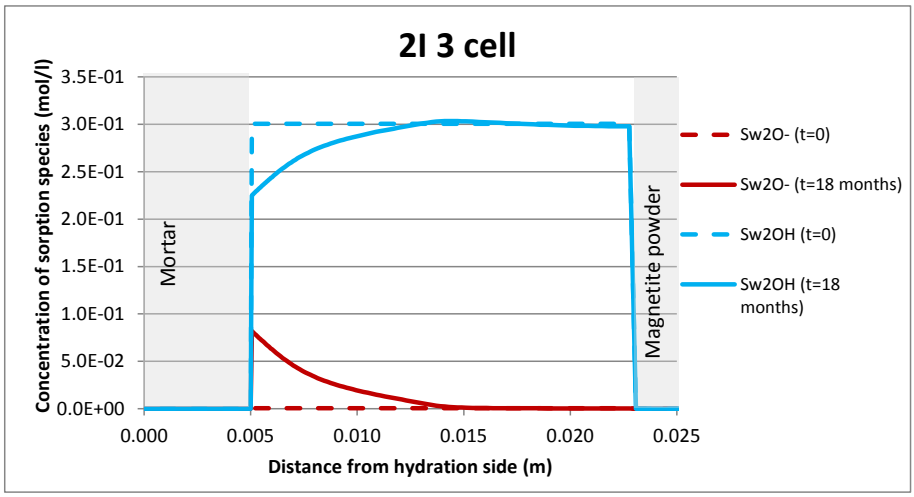

Figure D-15. Spatial distribution of computed concentrations of sorbed species in weak 2 sorption site in double interface tests on 2I 3 cell at the end of the test.